LEABHARLANN CHOLÁISTE NA TRÍONÓIDE, BAILE ÁTHA CLIATH | TRINITY COLLEGE LIBRARY DUBLIN
Ollscoil Átha Cliath | The University of Dublin

Terms and Conditions of Use of Digitised Theses from Trinity College Library Dublin

Copyright statement

All material supplied by Trinity College Library is protected by copyright (under the Copyright and Related Rights Act, 2000 as amended) and other relevant Intellectual Property Rights. By accessing and using a Digitised Thesis from Trinity College Library you acknowledge that all Intellectual Property Rights in any Works supplied are the sole and exclusive property of the copyright and/or other IPR holder. Specific copyright holders may not be explicitly identified. Use of materials from other sources within a thesis should not be construed as a claim over them.

A non-exclusive, non-transferable licence is hereby granted to those using or reproducing, in whole or in part, the material for valid purposes, providing the copyright owners are acknowledged using the normal conventions. Where specific permission to use material is required, this is identified and such permission must be sought from the copyright holder or agency cited.

Liability statement

By using a Digitised Thesis, I accept that Trinity College Dublin bears no legal responsibility for the accuracy, legality or comprehensiveness of materials contained within the thesis, and that Trinity College Dublin accepts no liability for indirect, consequential, or incidental, damages or losses arising from use of the thesis for whatever reason. Information located in a thesis may be subject to specific use constraints, details of which may not be explicitly described. It is the responsibility of potential and actual users to be aware of such constraints and to abide by them. By making use of material from a digitised thesis, you accept these copyright and disclaimer provisions. Where it is brought to the attention of Trinity College Library that there may be a breach of copyright or other restraint, it is the policy to withdraw or take down access to a thesis while the issue is being resolved.

Access Agreement

By using a Digitised Thesis from Trinity College Library you are bound by the following Terms & Conditions. Please read them carefully.

I have read and I understand the following statement: All material supplied via a Digitised Thesis from Trinity College Library is protected by copyright and other intellectual property rights, and duplication or sale of all or part of any of a thesis is not permitted, except that material may be duplicated by you for your research use or for educational purposes in electronic or print form providing the copyright owners are acknowledged using the normal conventions. You must obtain permission for any other use. Electronic or print copies may not be offered, whether for sale or otherwise to anyone. This copy has been supplied on the understanding that it is copyright material and that no quotation from the thesis may be published without proper acknowledgement.

Micromechanical Inking and Printing of Nano-objects using a Nanoindenter and Electromechanical Testing of Nanomaterial Films

Evelyn M. Doherty

A thesis submitted for the degree of
Doctor of Philosophy

Centre for Research on Adaptive Nanostructures and Nanodevices (CRANN)
&
School of Physics
Trinity College
University of Dublin
2012

TRINITY COLLEGE
2 4 MAY 2013
LIBRARY DUBLIN

Thesis 9843

DECLARAT ION

I declare that this thesis has not been submitted as an exercise for a degree at this or any other university and it is entirely my own work.

I agree to deposit this thesis in the University's open access institutional repository or allow the library to do so on my behalf, subject to Irish Copyright Legislation and Trinity College Library conditions of use and acknowledgement.

Acknowledgements

I wish the thank everyone who helped and supported me for the duration of my PhD. I especially wish to thank my supervisor Prof. Graham Cross. Thank you for always believing in me and pushing me to be better than I thought I could be. I have gained an incredible amount of knowledge and understanding as a result of your guidance and perhaps more importantly I have learned the skills I need to be successful at any scientific endeavour. I also wish to thank Prof. Werner Blau who gave me the opportunity of a PhD position at Trinity College and who has always been a positive and supportive mentor. Additionally I wish to thank Prof. Jonathan Coleman for the great support he has provided over the years.

I would also like to thank my friends and family who helped me along the way. To Anna (and Luke) and Valeria for their support and great sense of fun, and using their knowledge of chemistry to create the legendary LAVE nights. To Sophie who has been indeed a great friend to me always. To Roseanne and all of groups Cross, Coleman and Blau, we have some great memories together (think X-factor). I'd also like to thank "Team Bergman" for all the support, encouragement and belief in me. Thank you for coming into my life and opening my eyes and my heart. I am awed by your extraordinary talent and insight. Finally I would like to thank my family, both in Ireland and in the USA for loving me no matter what and for the Dr. BB jokes. The collective sense of humour of my family is one of the greatest gifts I have experienced in my life.

Abstract

Micromechanical Inking and Printing of Nano-objects using a Nanoindenter and Electromechanical Testing of Nanomaterial Films

As research changes focus from traditional silicon based electronic devices towards new materials with exotic capabilities such as carbon nanotubes, nanowires and graphene, the ability to create, pick up and place devices and materials becomes all the more vital. A recently developed and effective method of doing so is to use an elastomeric stamp to pick and place objects. This method is inexpensive and requires no additional chemical processes making it a very attractive option for industry to assemble materials that have otherwise unknown or incompatible processing requirements.

Using a nanoindenter with a microscopic elastomer indenting tip, we have successfully demonstrated and studied kinetic transfer of silver nanowire and single-walled carbon nanotube films. We have found each of these materials has a unique transfer mechanism as a result of how they interact within a network. We discovered that the silver nanowire films behave like low-cohesively bonded networks of discrete objects which can be peeled from the substrate once a critical crack velocity is reached. The carbon nanotubes however display highly cohesive behaviour and act like a thin film. The film peels from the substrate also but requires an additional stress from the stamp to fracture it before inking of the tip can occur. This stress occurs at a velocity much higher than that for peeling the film and the size of the inked region can be controlled by the peak load.

We have demonstrated the measurement of the relevant forces and deformation geometry during transfer in unprecedented detail. Using this knowledge the ultra-thin porous films (50 nm – 300 nm thick) can be controllably manipulated in a manner never demonstrated previously. Materials can be picked and placed with micron level accuracy. This technique presents a major potential contribution to the field of transfer and includes new modes such as shape and size selection, and multiple stacking of nanomaterial layers. Using the nanoindenter provides a powerful tool for conducting transfers and represents a new direction in the field of contact mechanics.

We have also developed a completely novel technique for effectively measuring the contact area using the small amplitude dynamic mode (CSM) feature of the nanoindenter. This provides a powerful way of calculating the contact area critical to the study of adhesion and contact mechanics in the absence of conventional optical detection. We have found that existing theories of contact mechanics require modification to fully describe our unique system, opening up new possibilities in the current understanding of adhesion.

Finally we have demonstrated our ability to print nanomaterials on a range of substrates, including glass, plastic and a gold circuit deposited on a silicon oxide chip. This presents opportunities for creating devices using materials with novel properties, and which were previously difficult to manipulate, for sensor applications and nanoscale assembly techniques. These can be potentially scaled up for mass production. We also conducted electromechanical testing of the materials using a tensile tester and two point probe system, showing that even after many cycles of bending and stretching the materials demonstrate high conductivity, making them ideal for flexible electronics applications.

Summary

We used a nanoindenter to facilitate the transfer of nanomaterial networks from one surface to another. The nanomaterials included silver nanowires and single-walled carbon nanotubes. These were dispersed in organic solvents before being deposited onto ceramic porous membranes using vacuum filtration. Once dry, the films could be transferred to other surfaces using an elastomeric stamp, either by hand for bulk films or by using the nanoindenter for smaller sections.

Elastomer stamps were created for the nanoindenter by mounting 1 mm diameter silicon spheres onto nanoindenter mounts. These spheres then had elastomer spin-coated on while it was in its liquid form. Once cured, the stamps could be used to conduct transfer experiments in the nanoindenter.

An experimental method was designed and created for the nanoindenter which involved a very sensitive surface-find segment followed by a load program, which allowed the user to specify the peak load applied by the stamp to the film, the rate of loading and the rate of unload. Investigations were conducted to examine the role of peak load and unload rate on transfer events including the possibility of transfer, the size and shape of the transferred film. The transfer experiments were supported by low-level optical observations which showed how the rate of unload and peak load influenced the behaviour of the elastomer during transfer. This behaviour dictated the size and shape of the transferred films. It was found that behaviours were different for silver nanowires films and for carbon nanotube films. Whereas the silver nanowires films exhibited low cohesion as a network, the carbon nanotube films were highly cohesive. This meant that the silver nanowire films needed only a critical velocity between the stamp and the substrate in order to initiate peeling and ink the stamp. However the carbon nanotube film required additional stresses as it need to be fractured from the rest of the film before it could ink the stamp. This level of stress was only observed at the end of the test, as the PDMS disengaged from the underlying substrate.

We were able to conduct contact mechanics studies of the elastomer/nanomaterial interaction using the small amplitude dynamic mode (CSM) feature of the nanoindenter. It was possible to track the change in the contact area without optical measurements, by correlating the stiffness of the nanoindenter to the size of the contact. To our knowledge this technique has never before been used and it meant we could measure the contact area of opaque and microscopic materials without a microscope.

We also demonstrated the use of the nanoindenter to print the films onto desirable substrates such as PET, glass and silicon oxide chips with gold contacts. We found that in most cases heat

was a mediating factor in facilitating printing, though in the case of the silicon oxide chips no heat was needed. We were able to pass an electrical current through the transferred nanowire and nanotube films demonstrating that the materials were still conductive even after transfer had been completed.

The bulk films were transferred by hand to plastic for use in electromechanical testing. Testing was done using a tensile tester with a two point probe system operating in parallel. Gold contacts were evaporated on either end of a strip of the nanomaterial and fitted into custom clamps for the tensile tester. The films were then compressed to a specific bend radius and subsequently relaxed to the original bend radius. A nanomaterial film coating the outside of the plastic during bending allowed for tensile tests to be conducted while a current was passed through the nanomaterial. If the film was coating the inside of the plastic during bending, compression tests were conducted. The tests were repeated hundreds of times to test their electrical response to the stress subjected on them. It was found that for CNTs and AgNWs, the conductivity of the films were reduced by only a few per cent even after a thousand cycles making these materials highly suitable for flexible electronics applications.

Glossary of Useful Terms and Abbreviations used Throughout this Thesis

a - Contact radius: radius of contact between the nanoindenter stamp and the receiving substrate

AgNW – silver nanowires

a_{ink} – the contact radius at which inking of a nanomaterial is initiated

a_{max} – the maximum contact radius from a test

CF – Calibration Factor: the factor allowing the contact radius throughout the test to be calculated from the stiffness data. It depends on a knowledge of the maximum contact radius and the peak stiffness value of the contact

CI – Contact Impression: the optically visible residue left from excess cross-linker in the PDMS tip which allows the maximum contact radius during the test to be measured

CNT – carbon nanotubes

CSM – Continuous Stiffness Measurement. This is a mode in the nanoindenter whereby a small oscillation is applied to the stiffness measurement which allows the stiffness to be measured throughout the test

D – Displacement: the amount the material moves as a result of the force applied to it by the nanoindenter.

E – Young's modulus of a material, in most of this thesis this will refer to the Young's modulus of PDMS

E^* - Reduced Young's modulus which takes the Poisson ratio of the material into account such that $\frac{1}{E^*} = \frac{(1-\nu^2)}{E}$.

G – the energy release rate, or crack propagation rate. It is a measure of the energy involved at the interface of an opening or closing crack

Inking – the process whereby a material is adhered to the PDMS stamp

JKR – Johnson, Kendall, Roberts theory. A contact mechanics formulation based on the Hertz theory which takes adhesion between materials into account

L – Load: a force applied to the nanoindenter tip as it makes contact with a test material

L-D curve – Load-Displacement curve – a characteristic nanoindenter curve for examining the relationship between the applied and measured load and the resulting material displacement.

PA – Peak Adhesion Force: the value measured at the minimum on an L-D curve which show the peak adhesive force measured during the test. It is measured in Newtons.

PDMS – Polydimethylsiloxane. A cross-linked elastomer which is used in this thesis to transfer nanomaterials from one place to another

PET – polyethylene terephthalate : a transparent plastic material commonly used in industry

Printing – the process whereby a material is transferred from the PDMS stamp to a receiving substrate

S – Stiffness: a channel recorded by the nanoindenter which measures the stiffness of a contact between the nanoindenter tip and the test material

S-L curve: Stiffness-Load curve – a characteristic nanoindenter curve which allows the relationship between the contact stiffness and the applied and measured load of the test to be examined

v – crack velocity: The velocity at which a crack is opening or closing at an interface between two materials. In this thesis this refers either to the crack opening between the PDMS stamp and the material it is contacting, or between the nanomaterial and its underlying substrate.

v_{ink} – the crack velocity during a test at which inking of a nanomaterial is initiated

Glossary of Nanoindenter Curves

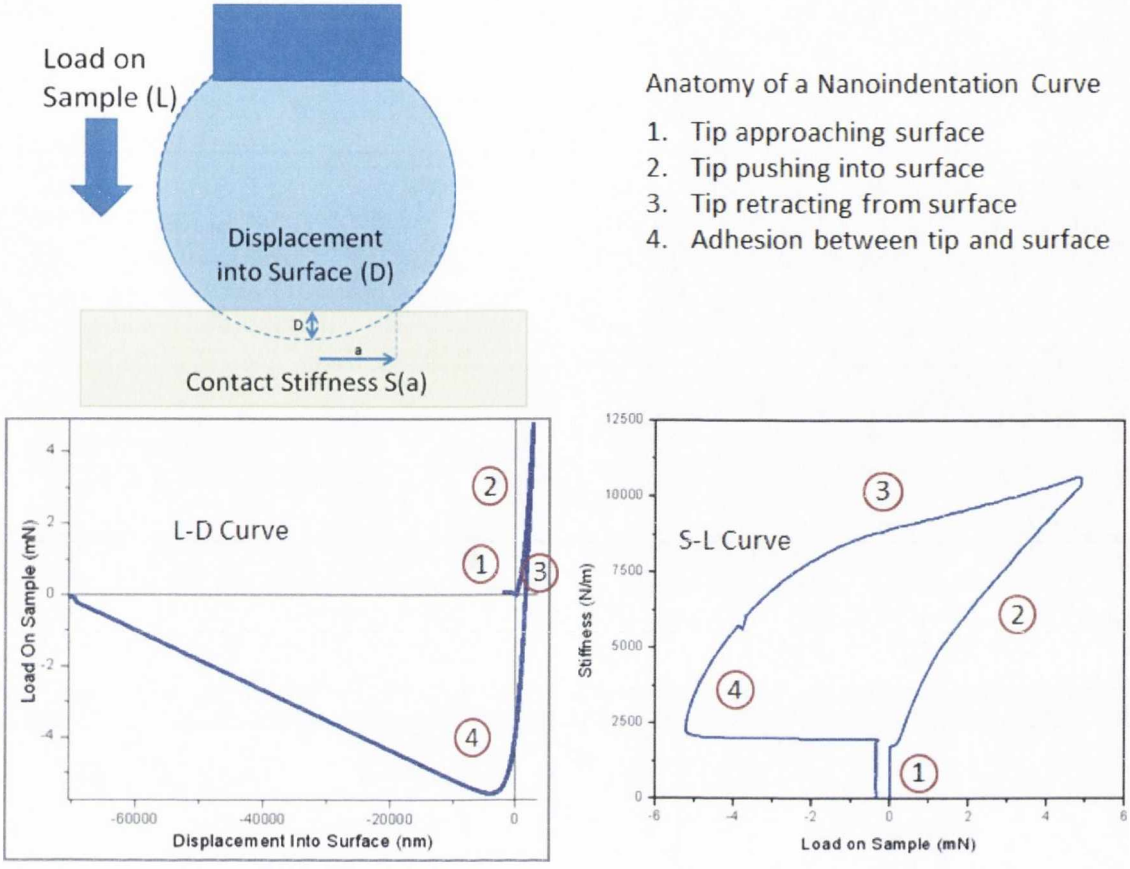

Figure 1. Schematic of a nanoindentation test and subsequent nanoindentation curves. Shown here are a Load-Displacement curve (L-D) and a Stiffness-Load curve (S-L). Further explanation is provided in the text.

Figure 1 shows a schematic of a nanoindentation test done using the PDMS stamp coming into contact with the substrate. There are three main parameters or channels which are directly measured by the nanoindenter in these tests. There is the Load on Sample (or Load) which is the force applied to the nanoindenter tip as it comes into contact with the test. This force becomes negative when there is adhesion between the tip and the sample. The Displacement into Surface (Displacement) in this case refers to the amount the PDMS stamp is compressed and stretched during loading and unloading of the tip with the sample. The Stiffness refers to the contact stiffness between the nanoindenter tip and the contacted sample. Typical ways of viewing this data is using Load-Displacement (L-D) and Stiffness-Load (S-L) curves.

There are four regions illustrated in these tests. 1 indicates the approach of the nanoindenter tip towards the sample where Load, Displacement and Stiffness are all equal to zero. 2 is where the tip has come into contact with the sample and begins to load up to value specified by the user. The Load is applied by the tip and a resulting Displacement and Stiffness is measured. 3 is where the tip reverses direction and begins to withdraw from the surface. If there is adhesion between

the tip and surface, this is shown by 4 where the load and displacement do not return immediately to zero. The load takes negative values in this region and the displacement can also take negative values. The stiffness is always positive because a negative stiffness would be non-physical.

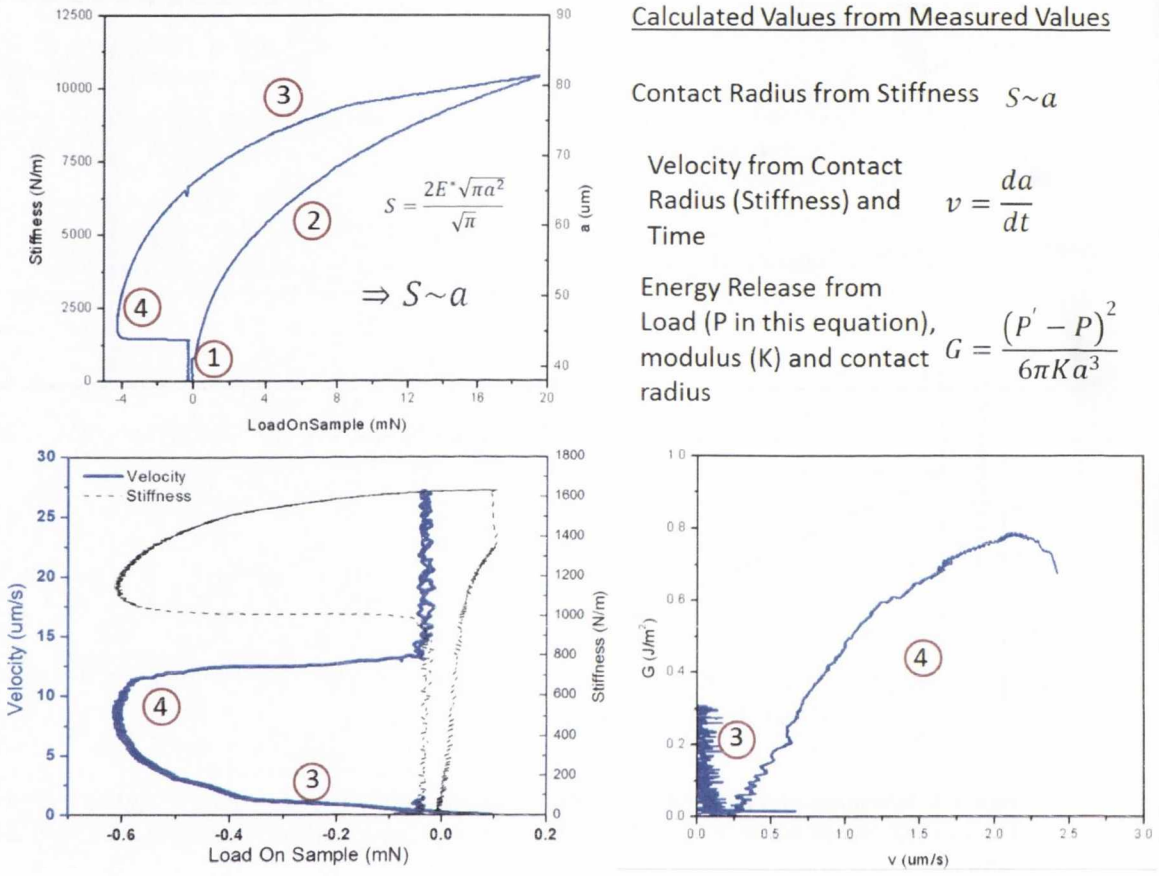

Figure 2. From the values measured by the nanoindenter, further values can be calculated. So using Sneddon's equation (which is described in more detail in Chapter 3) the contact radius a can be found from the Stiffness data. From this, the crack velocity v can be found. The energy release rate G can be found from the Load (shown as P in this equation), the modulus (K) and the contact radius.

The channels measured by the nanoindenter can then be used to calculate further parameters such as contact radius a, crack velocity v and energy release rate G. These curves and the equations used to calculate them are shown in Figure 2. The theory behind these calculations are described in more detail in Chapters 2 and 3 and examples of this data on alumina, CNTs and AgNWs are described in Chapters 4, 5 and 6.

Chapter 1 Adhesion and Transfer 1

1.1 Introduction 1

1.2 Brief Literature Overview 3

1.3 Kinetic Control of Transfer Printing 4

1.4 Calculating *G* for a Spherical Contact 7

1.5 Printing of Films 9

Chapter 2 Contact Mechanics, Adhesion and Transfer Theory 11

2.1 Materials Theory 11

Contact Mechanics in Linear Elastic Materials 12

Adhesion 15

2.2 Contact Mechanics Models 18

Hertz Theory of Contact 18

JKR Theory of Contact Mechanics 19

DMT Model 21

DMT-M Model 23

Stress Distributions 24

Surface Roughness 25

2.3 Viscoelastic Considerations 28

Viscoelasticity in Contact Mechanics 31

Adhesion Hysteresis in Viscoelastic Contact 31

2.4 Experimental Applications of Contact Mechanics 34

Extended JKR Theory 34

2.5 Failure Modes of Adhesive Contact 38

Cavitation with Flat Punch Tests 39

Fracture of Adhesive Film during JKR Tests 41

2.6 Conclusions 46

Chapter 3 Experimental Devices & Methods 48
3.1 Introduction 48
3.2 Nanoindenter Structure & Use 48
Nanoindenter Design and Structure 49
AC Modulation Technique 52
Phase Angle Surface Detection 54
3.3 General Description of Mechanical Tests 57
Nanoindenter Method 57
Mechanical Data Curves 60
Video Imaging Capability during Nanoindenting Experiments 63
3.4 Stiffness and Contact Radius Correlation 64
Kink in Data at S = 6000 N/m 65
Displacement Data 70
3.5 Experimental Materials Preparation 71
Tip Preparation Method 71
PDMS Preparation 71
3.6 Mounting Samples 72
3.7 Preparation of Nano-network Films 73
Ag Nanowire Film Creation 73
Filtration of Nanomaterial Films 74
Creation of CNT films 75
3.8 Conclusion 75
Chapter 4 Contact Mechanics and Adhesion Studies on Alumina 77
4.1 Introduction 77
4.2 Measuring the Contact Radius 77
Contact Impression 77
"Halo Effect" in Contact Impression 79

Defining the Contact Radius Stiffness Correlation 80
Measuring the Contact Radius Directly 83
Contact and Surface Forces During Approach 87
Possible Origin of the Contact "Halo" during Initial Contact 89
Measurement of Jump to Contact 92
4.3 Adhesion and Contact Mechanics Studies 94
Adhesion Studies on Alumina 94
Mechanical Tests for Different Peak Loads 94
Peak Adhesion and Work of Adhesion 96
Location Testing & Adhesion 97
Unload Rate and Adhesion 100
4.4 Contact Mechanics of the Interface 102
Correcting for Viscoelasticity in the JKR Theory 108
4.5 PDMS Layer Thickness 111
Experimental Results for PDMS of Different Thickness 112
4.6 Chapter Summary 117
4.7 Conclusions 118
Chapter 5 Transfer of Silver Nanowires 120
5.1 Introduction 120
5.2 Nanowire Inking Test 121
5.3 Kinetic Control of AgNW Inking 131
5.4 Comparing Adhesion between Interfaces 134
Mechanical Data from the AgNW Tests 135
Correlation of Peak Load and Ink Size 143
5.5 Chapter Summary 144
Chapter 6 Transferring Carbon Nanotube Films 147
6.1 Introduction 147

6.2 Inking of CNT films 148
6.3 Stacking of Carbon Nanotubes 157
CNT Film Extension and Failure 166
6.4 CNT "Seeding" Events 170
6.5 Summary 174
Chapter 7 Printing and Applications 176
7.1 Printing Using a Bulk PDMS Stamp 176
7.2 Printing Using Heat in the Nanoindenter 177
7.3 Printing for Electrical Devices 180
7.4 Electromechanical Testing of AgNW and CNT films 182
7.5 Experimental Set-up 183
7.6 Results 187
7.7 Conclusions 191
Chapter 8 Conclusions and Future Work 192
Conclusions 192
Stiffness to Contact Area Correlation 195
Transfer of AgNW films 196
Transfer of CNT Films 196
Printing and Applications 197
Future Work 197
References 199

Chapter 1 Adhesion and Transfer

1.1 Introduction

"The best way to predict the future, is to invent it"

-Alan Kay, Computer Scientist

The future of modern life, as in the present will be intimately tied to technology. The huge advances in technology of the last century have caused a major change in the way people live their everyday lives. It has changed how the world operates, how economies flow and how information is shared and used. It has allowed people to become educated about their own communities and the impact that the global family has on their lives. Perhaps never in the known history of humanity have such fundamental changes and transitions in how people live their lives been experienced, as has been experienced in the last 50 years. Even in the last five years there has been a communication revolution on the back of technological advances, as more people have access to the internet on smartphones and tablets which are light, powerful and easily transported. It is a common occurrence in the daily news to see news footage of current events captured on a witness's smart phone and uploaded to their local newspaper and in many ways this feature alone can change the tide of world history.

Technology is advanced through the better understanding of how materials interact with one another, both on a macroscopic level and on an atomic and even sub-atomic level. A major concern of scientists improving current technologies and creating the technology of the future lies in the creation and manipulation of materials which surpass the current state of the art. It is always desirable to find materials that can create devices which are smaller, lighter, more powerful and which use lower energy, either in processing or in creation. In the future-conscious world that we live in today, renewable materials which are inexpensive and environmentally friendly are much sought after as the mining resources of the planet begin to dwindle. At present many of the materials used in technology are rare and expensive and come from non-renewable sources. Many need to be mined and processed in ways which damage the environment and, either directly or indirectly, the people that provide these materials for use. An example of this would be indium. Indium is a major component of indium-tin-oxide (ITO), a transparent, electrically conducting material which is commonly used in flat panel displays on television sets, computer screens and smartphone screens. Although valued for its high electrical conductivity-to

optical-transparency -ratio and for the ease in which it can be deposited onto materials for use in devices, ITO is becoming increasingly expensive as the world supply of indium begins to dwindle. It is also a brittle material which creates limitations in how it can be used in electronics applications. It cannot be rolled or folded and even though touchscreens are used ever more commonly, they have a limited lifetime due to potential fracture of the ITO in the screen.

Materials scientist have therefore been considering and testing alternative materials for use in electronics applications. For example carbon nanotube films, silver nanowire films and graphene have all been pitched as replacements for ITO. Not only do these materials display superior electrical conductivity but they are also mechanically very flexible. This opens up a whole new realm of possibilities in the creation of *e*-paper or flexible tablets that can be rolled up for transporting. In dealing with these novel nanomaterials a major concern regards the deposition of the materials for electronics applications. Research has been conducted on different methods of accomplishing this, including spraying, inkjet printing and using an elastomer stamp to pick up and place the materials.

The aim of this thesis is to describe the research conducted on transferring nanomaterials using an elastomeric stamp, from their place of processing to devices used in electronics research. The thesis will describe work done on films made from single walled carbon nanotubes and silver nanowires. A major study is conducted on the picking up or *inking* of the elastomeric stamp using a nanoindenter to better understand the processes involved in such a transfer. There is also work done on the putting down or *printing* of the nanomaterials onto a desirable substrate such as plastic, glass or silicon oxide. There will be a brief description of how the materials can be used potentially and their performance during electromechanical testing.

Before describing in detail the research done for this thesis we will describe some of the work already done in inking and printing materials. This will be followed in Chapter 2 with a description of contact and fracture mechanics and the mathematical formulations used to describe the contact of materials. Chapter 3 is the experimental chapter where the processing of materials, the use of the nanoindenter and the experimental methods will be described in detail. Chapters 4, 5 and 6 describe the experiments done on various materials including carbon nanotube films and silver nanowire films. Finally Chapter 7 will describe the printing of the materials, their potential uses in devices and the electromechanical testing of the printed materials for use as large-scale flexible displays.

It is important at this juncture to say a word about the nature of the films created with the silver nanowires and the carbon nanotubes. The literature described below considers two categories of materials for transfer; discrete objects such as pollen or silicon microstructures and continuous

thin films such as gold or polymer films only hundreds of nanometres thick. Although the theory of peeling is the same for continuous films and discrete objects the continuous films may have an additional requirements regarding transfer. If a continuous film is being peeled from the substrate the theory is the same. If however as in our case, a section of film is being cut out from the whole film then fracture of the film will be required. In the case of the AgNW films consisting of loosely bound nanowires, the discrete formulation appears to be the most applicable whereas the CNT film behaves like a cohesive membrane, requiring the fracture analysis of the continuous film case. This will be discussed in more detail throughout the thesis but it is useful to bring it to the reader's attention at this point.

1.2 Brief Literature Overview

In 2006 a paper written by Prof. George Grüner *et al* was published in Applied Physics Letters [2] describing the transfer of carbon nanotube (CNT) films from one substrate to another for use in electronic large area displays. The carbon nanotubes were dispersed in surfactants and water and were vacuum filtered onto porous alumina membranes. A stamp was created from a silicon based viscoelastic elastomer called polydimethylsiloxane (PDMS) and contact was made between the stamp and the carbon nanotube film. The film was transferred to the PDMS stamp. The authors mention that this is a process mediated by surface energies but do not describe how this mechanism works. They note that the PDMS stamp has a relatively low surface energy of 19.8 mJ/m^2 but state the nanotubes ink the stamp as they are sitting loosely on the alumina membrane. The authors then describe printing the film on the PDMS stamp onto various materials with higher surface energies such as polyethylene terephthalate or PET (surface energy = 44.6 mJ/m^2), glass (47 mJ/m^2) and silicon which had been treated with an oxygen plasma and vapour salinization. The printing situation in each case was mediated by gentle heating of the receiving substrate to 80°C. Figure 3 shows an example of a film on PET which was transferred in this manner. The authors transferred films which were as thin as 10 nm, making them optically transparent and were able to show that they were conductive, paving a way for replacing ITO in flexible electrodes.

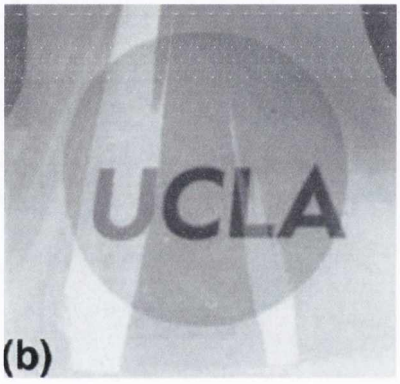

Figure 3. CNT film transferred from an alumina membrane to polyethylene terephthalate (PET) plastic using a polydimethylsiloxane (PDMS) stamp [2].

This compelling piece of work promised exciting new possibilities for using novel materials such as carbon nanotubes which were previously difficult to process and apply to useful substrates such

as PET and silicon. Understanding the process behind transfer opened up new possibilities for using these and other exceptional materials such as silver nanowire (AgNW) films or even graphene. There existed an opening for understanding exactly the kinds of dynamics needed to mediate transfer with elastomeric stamps. Using the superior sensitivity and control provided by a nanoindenter seemed like an ideal and exciting way to conduct research on transferring these exceptional materials of the future.

There were two approaches to the formalisation of this problem. One was to investigate the process of transfer itself, be it inking a stamp or printing from the stamp. In order to further our understanding of these processes additional considerations were needed regarding the stamp itself and how it interacted with different types of materials. Understanding the contact of PDMS with various interfaces could provide valuable information on the most important parameters facilitating transfer. Those parameters could then potentially be used to facilitate transfer of any material on a micro or macro scale.

Literature searches yielded many excellent research papers on contact and adhesion experiments with PDMS, including work by Schwarz [3], Barthel [4-11], Wahl [12-14], Creton [15-20]and Hui [19,21-31] which took the foundations of their research from the pivotal work by Johnson [32-34], Kendall [33,35,36] and Roberts [33], Maugis [37,38], Barquins [38] and Gent [39-44]. Two outstanding authors in particular who used the theories of adhesion and contact mechanics to describe the transfer of materials, and whose research was used heavily in this thesis work are Prof. John Rogers [45-55] of the University of Illinois and Prof. Ken Shull [1,15,17,20,25,56-63] of Northwestern University. Prof. Shull [59] also wrote a very comprehensive review of contact mechanics and adhesion, much of which is used in Chapter 2 when describing the theory in detail. We will now provide a brief overview of the research done by these authors which was most relevant to the work in this thesis.

1.3 Kinetic Control of Transfer Printing

The first author to be reviewed is Prof. John Rogers [46,52]. In his work he demonstrates the *kinetic control* of transfer using an elastomeric stamp. His work relates the energy release rate G of a material to the velocity v at which an interface opens between the stamp and the target material, or the target material and its underlying substrate.

When considering inking or printing of a material we must consider the *interfaces* involved. There is the underlying substrate, the target material (which is to be inked) and the elastomeric stamp. A schematic of their configuration is shown in Figure 4 In order to transfer the film the elastomer

is *peeled* back from the underlying substrate. In this schematic there is an interface between the substrate and the film, and the film and the stamp. When the stamp *inks* the film, a crack opens between the substrate and the film. When the stamp fails to ink the film or is *printing* the film, a crack opens between the stamp and the film. These cracks have a velocity v which may or may not be constant throughout the peeling event.

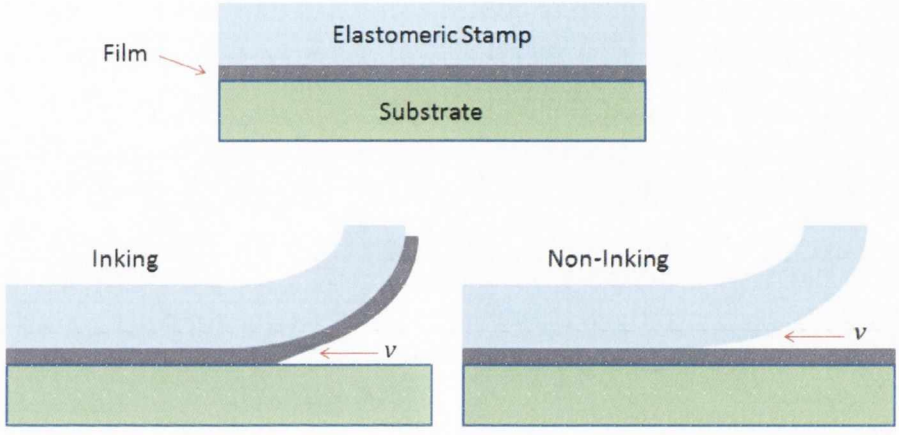

Figure 4. Schematic showing the interfaces involved in an inking problem[46]. For an inking event a crack is created between the film and the substrate with a velocity *v*. For a non-inking or printing event the crack is formed between the elastomer and the film.

When a crack is formed between interfaces there is an energy release rate G associated with it. For a steady state problem the energy release rate is given by the peeling force F and the width w of the stamp

Equation 1

$$G = \frac{F}{w}$$

For this problem G represents the energy of the breaking of adhesive bonds between the stamp and substrate and also accounts for viscoelastic dissipation at the crack front. The Griffith crack criterion [64] defines a critical energy release rate, G_{crit} at which there is a steady propagation of the crack.

Figure 4 shows the competition between crack formation in inking and printing of a continuous film. For an inking event the crack is formed between the film and the underlying substrate. For a non-inking event, or for a printing event the crack forms between the elastomer stamp and the film. The critical energy release rate for the inking scenario is designated as $G_{crit}^{Film/Substrate}$. This value is a property of the material and is independent of the crack velocity v for elastic substrates and films. For the printing case we have $G_{crit}^{Stamp/Film}$ which is dependent on the crack velocity between the elastomer and the film to account for viscoelastic dissipation in the stamp at the crack tip. An example of an equation describing this relation has the form [44] [38]

Equation 2

$$G = G_0(1 + \left(\frac{v}{v^*}\right)^n)$$

In this case G_0 is a critical value of G at which the crack velocity $v \rightarrow 0$. Its value is dependent on the materials of the interface involved and is assumed to be rate independent and equal to the work of adhesion w. The viscoelastic response of the system is described by the ratio of the crack velocity to a reference velocity v^* which is where the critical energy release rate of the steady state approaches G_0. The scaling parameter n is found experimentally and describes the relationship between G and v.

During an inking event where the film is picked up by the stamp, the energy release rate G between the film and the substrate reaches the critical value $G_{crit}^{Film/Substrate}$ first. If G reaches the critical value $G_{crit}^{Stamp/Film}$ first then the film is printed or left uninked.

- ⇨ For Inking $G_{crit}^{Film/Substrate} < G_{crit}^{Stamp/Film}$
- ⇨ For Printing $G_{crit}^{Film/Substrate} > G_{crit}^{Stamp/Film}$

Figure 5 shows a schematic diagram which illustrates the relationship between the critical energy release rate of the film and substrate as a function of the crack velocity between the film and substrate. This schematic follows the power law relationship predicted by Equation 2 whereby G is

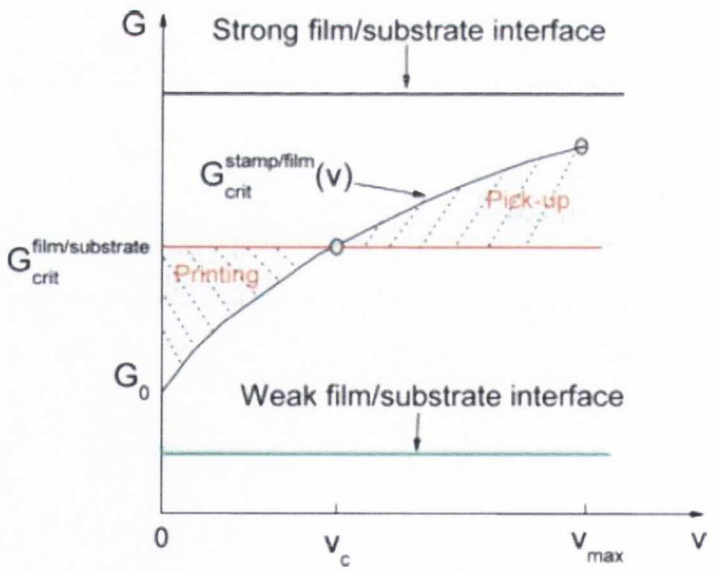

Figure 5. Schematic showing the relationship between $G_{crit}^{film/substrate}$ and crack velocity v in the inking (pick-up) and printing regimes[46].

a function of v. The critical value of G to initiate inking (or pick up) and printing is indicated at $G_{crit}^{Film/Substrate}$ on the schematic. For G values above $G_{crit}^{Film/Substrate}$ a crack opens between the film and the substrate and inking occurs. For values below this the crack opens between the elastomer

and the film and thus printing occurs. This can be for discrete objects or the initiation of the peel of a thin film. The horizontal lines top and bottom represent very strong and very weak film/substrate interfaces respectively which correspond to pick up only and printing only. The

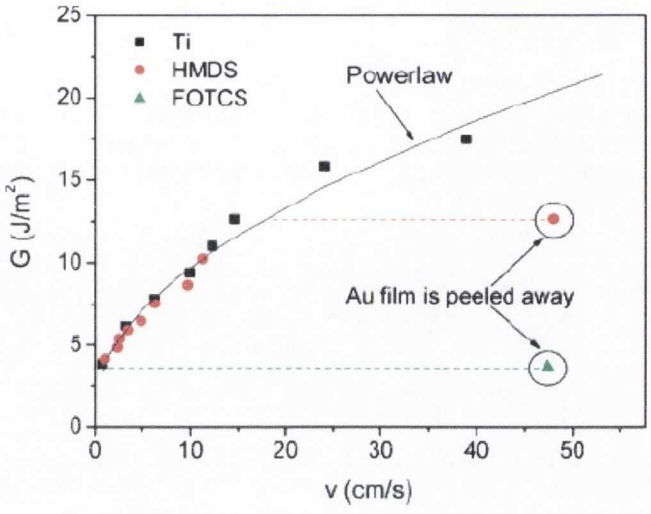

Figure 6. Experimental results for the inking of a PDMS stamp with an Au thin film done by Rogers *et al* [42]. The Au was adhered to a glass substrate with three varying degrees of adhesion. The adhesion of the Au to the glass was mediated by three different surface treatments for the glass, a tricholorosilane (FOTCS) vapour treatment, a hexamethyldisilazane (HDMS) vapour treatment and thirdly an adhesive layer of titanium (Ti).

authors were able to demonstrate experimentally that this schematic worked whereby the peel velocity was kept constant and G was calculated for different values of v.

The interface consisted of a thin film of gold on glass and treatments were used to create three different levels of adhesion between the film and the glass as indicated by the black, red and green symbols. As can be seen in the diagram their work followed the power law very nicely.

1.4 Calculating G for a Spherical Contact

The question is if we are able to kinetically control transfer for the materials studied in this thesis. Our stamp system has a very different geometry from that used by Rogers in that we use a 1 mm diameter silicon sphere, coated with a thin film (approximately 20 um thick) of PDMS. This spherical configuration requires a more complicated approach to calculating G. We use the JKR theory as described by Shull *et al* [63] to calculate G. More details on the JKR theory can be found in Chapter 2. This theory allows G to be calculated using

Equation 3

$$G = \frac{(P' - P)^2}{6\pi K a^3} f G_P\left(\frac{a}{h}\right)$$

where P' is the Hertzian load given by $P' = 16E_S a^3/9$, E is the elastic modulus of the material and a is the contact radius at any given point in the test. $fG_P\left(\frac{a}{h}\right)$ is a finite size correction factor [59] where h is the PDMS thickness which is included in the case where the PDMS layer is confined between two hard surfaces (in our case the silicon indenter sphere and the target substrate). All of these parameters are described in more detail in Chapter 2.

Shull *et al* used a glass indenter sphere with a radius of curvature of 6 mm to pick-up a thin viscoelastic polymer film which had been spin coated onto a bulk PDMS substrate.

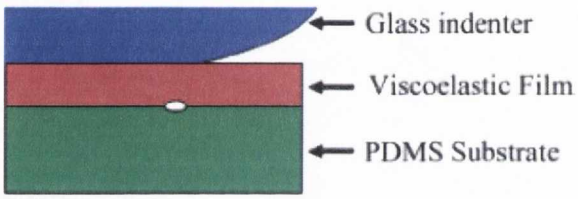

Figure 7. Schematic illustrating the interfaces used in Shull's transfer experiment. A glass indenting sphere was used to pick up a viscoelastic film from a PDMS substrate [1].

Figure 7 shows a schematic of the interfaces used in their work. They used Equation 3 to calculate G for various values of v in the experiment. They were able to image the contacts directly through the transparent PDMS and polymer film which allowed them to directly calculate the crack velocity of the opening interface v. They oxidised the PDMS substrate to increase its adhesion so that the crack would open between the glass indenter sphere and the viscoelastic film and found that the resulting values of G for the crack velocities used fit the power law in Equation 1 very well with fitting parameters of G_0 = 0.1 J/m^2, v^* = 2.5 nm/s and n = 0.5. This showed that using the JKR theory to calculate G was valid for their system.

The paper also investigates the extension of the polymer film during inking. Details are found at the end of Chapter 2 but they were able to relate an extension ratio λ which describes the deformation of the polymer film during transfer to the energy release rate using

Equation 4

$$G = \frac{Eh}{6}\left(\lambda^2 - \frac{3}{\lambda^2} + \frac{2}{\lambda^4}\right)$$

In this case G refers to the energy released as the cohesive polymer film separates from the PDMS substrate and we shall see in Chapter 6 that this formulation is relevant to describing the inking and fracture of CNT films.

1.5 Printing of Films

The vast majority of this thesis work regards the inking aspect of the transfer problem. For completeness Chapter 7 will briefly describe how printing may occur though this research is ongoing at this time. As described in the paper by Grüner [2] above, the printing of CNT films is facilitated by the use of thermal energy. We now briefly describe some of the theory involved in this process using work done by Rogers *et al* [46].

PDMS is in fact a elastomer (which is defined as a viscoelastic polymer) and therefore follows the rate-temperature equivalence

$$G_{critical}^{stamp/film} = G_{critical}^{stamp/film}(va_T)$$

where $\log_{10} a_T = -17.6\frac{T-T_g}{52+T-T_g}$. T_g is the glass transition temperature for the polymer and T is the temperature at which a_T is measured. Further information about the temperature shift parameter a_T and its use in polymer theory is found in Chapter 2. This includes a description of the Williams-Landel-Ferry (WLF) [65] which allows for the construction of a temperature curve for any polymer such that viscosity as a function of temperature can be calculated. It is a consequence of a correlation between time and temperature in [66] polymers whereby effects due to viscoelastic relaxation (such as printing) which would need a long time frame can be expedited by the use of temperature. PDMS has a T_g of -125°C which means it is unlikely to print as a result of viscoelastic relaxation at room temperature. Rogers *et al* tested this out for an Au film at various temperatures using the relation by relating the energy release rate to temperature using

Equation 5

$$G = G_0(1 + (a_T v^* v)^n)$$

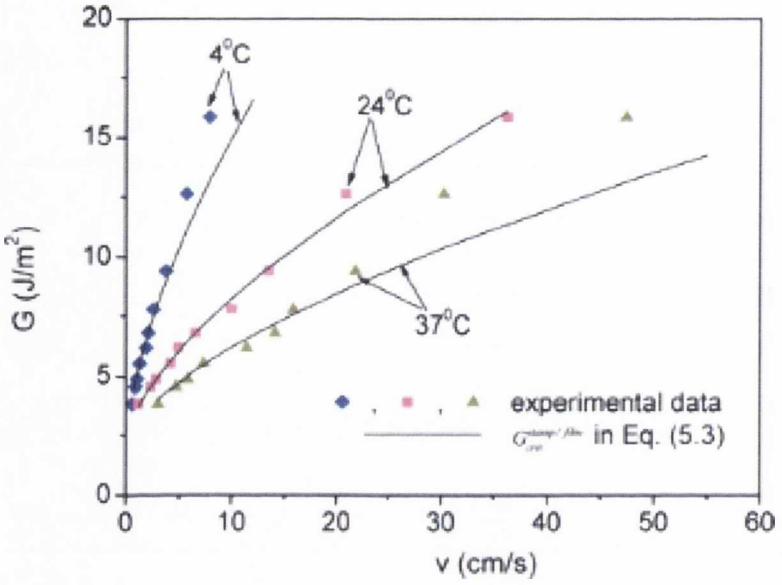

Figure 8. Experimental work by Rogers *et al* [46] showing the rate-temperature dependence for stamp/film interfaces at different temperatures. As can be see the experimental data fits the power law predicted by Equation 1 very well.

Figure 8 shows the experimental data measured by Rogers et al for the interface between the PDMS stamp and a thin Au film. The film was strongly adhered to the glass substrate so that inking could not occur. The data shows that the rate-temperature dependence fits the power law predicted by Equation 1 and Equation 5 very well.

Our printing work is still in the initial stages of experimentation and analysis but we will show that for CNT films printing does occur a higher temperatures but not at room temperature on PET and glass. More details of this and printing of the AgNWs will be described in Chapter 7.

Chapter 2 Contact Mechanics, Adhesion and Transfer Theory

2.1 Materials Theory

The aim of this chapter is to present the theory of micromechanical transfer from the point of view of contact and interfacial fracture mechanics in elastic and viscoelastic materials. Many of the theoretical models and formulations of these fields are described here, including modifications to account for viscoelastic effects. The final part of the chapter describes some applications of the theory to quantify and describe the observed behaviour.

The physical problem we have before us involves using a soft elastomeric material as an adhesive stamp which is brought into contact with a network of nanotubes or nanorods. The nano-network adheres to the stamp which is then withdrawn from the network carrying a fractured portion of the network with it. This *inked* stamp is then contacted to a receiving substrate such as plastic, glass or SiO_2 and deposits the nanomaterials onto it in a *printing* step. This process is mediated by mechanical and surface effects of the materials involved, in how they contact one another and how they separate. It is therefore important to review several fields such as contact mechanics, fracture mechanics and surface physics and chemistry.

Before reviewing these fields in detail it may be useful for the reader to visualise the material interfaces in this problem. Figure 9 shows a schematic of the interfaces in question for the inking portion of the experiment. There are three distinct material interfaces which are numbered on the schematic:

1. A rigid, smooth spherical surface (Si sphere) coated by a film of the elastomer PDMS.
2. The PDMS film in contact with a continuous ultra-thin film network (50-300 nm thick) of nanomaterials.
3. The nanomaterial network as deposited on a porous alumina membrane. The pores of this membrane may range anywhere from 20 – 200 nm in diameter.

The interfaces are the same for the printing regime except that the alumina is replaced by the receiving substrate, e.g. glass.

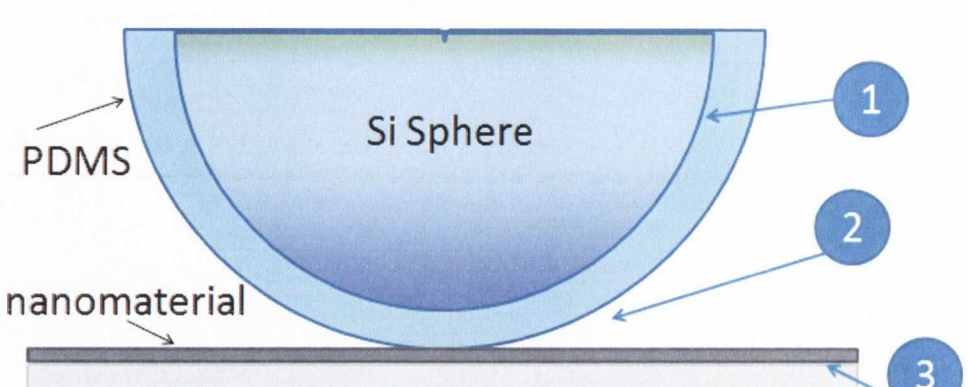

Figure 9. Schematic showing interfaces between materials which are used in the transfer experiments. The interfaces are numbered 1-3 as shown.

Although interface 1 is a consideration, for the analysis in this work it is generally viewed as fixed and not moving throughout the experiment. Its role in the analysis is that is confines the PDMS layer during experiments as the layer is sandwiched between the sphere and the hard substrate material. Aside from that, most of the analysis will be focussed on interfaces 2 and 3.

The transfer of the nanomaterials to the PDMS surface is governed by general considerations of contact mechanics, fracture mechanics and surface effects. Intrinsic material properties of surface energy, elasticity, and inelastic dissipation modes combine with (thermo)mechanical loading dynamics including peak compressive contact load, temperature, time in contact with the sample, rate of load, rate of unload, etc. Also considered are the effects of the materials themselves, such as surface energies, porosity and thickness in forming a picture of the transfer process.

Contact Mechanics in Linear Elastic Materials

The mechanics of contact and fracture between interfaces are well defined for *liner elastic (LE) materials* i.e. materials which obey Hooke's Law with a linear relation between stress and recoverable strain. Although many materials are linearly elastic, some, especially polymers can also be viscoelastic. This means that there is an extra time based component to the material behaviour. This manifests itself in that the materials exhibit simultaneous elastic and viscous behaviour while undergoing deformation. For the present introduction of formulating contact and fracture mechanics only linear elastic materials shall be considered. Later parts of the discussion will introduce viscoelasticity and the modifications to the theories that it requires. A discussion of

stress fields and their contribution to deformation and fracture of the materials will also be outlined.

The basic physical problem discussed in this thesis work can be defined as the *contact* and *fracture* of materials. The contact of two bodies of different materials creates an interface between them. Separating the bodies at that interface can be described as the propagation of a crack leading to adhesive fracture failure between them.

Contact mechanics problems are usually formulated between two bodies in contact; most commonly two elastic spheres or an elastic sphere on an infinitely hard flat material. The circular contact between them has a *contact radius* a, and the sphere has radius R. The applied force on the bodies is designated P and the elastic deformation has a displacement δ. Isotropic linear elastic materials are described by their Young's modulus E and their Poisson ratio ν. For adhesive interactions where the interface supports both tensile and normal tractions, the surface energy γ of the contacting materials can be used to capture this behaviour and is given by the excess energy created by the formation of new surfaces after fracture has occurred.

The energy criterion of fracture mechanics [64] states that crack extension occurs when the crack growth is sufficient to overcome the resistance of the material to the crack extension. This resistance may come from surface energies or other types of energy dissipation in the region of the crack. Griffith [64] and Irwin [67] developed this energy criterion approach by defining the energy release rate G which was introduced in Chapter 1. This is the rate of change of potential energy with the crack area for a linear elastic material. At a certain critical value G_G, fracture occurs and therefore G_C is a measure of fracture toughness. Using the description in Anderson's book *Fracture Mechanics* [68] the energy release rate is given by

Equation 6

$$G = \frac{K_I{}^2}{2E^*}$$

for linear elastic materials. K_I is called the stress intensity factor, a constant which completely characterises the crack tip conditions for this type of material. It refers to a type of loading which causes an opening crack. In LEFM it can be found from the experimental data. There are also stress intensity factors for in-plane shear loading and out of plane shear loading which will not be discussed at this time. E^* is the reduced modulus which is defined by

$$\frac{1}{E^*} = \frac{1-\nu^2}{E_1}$$

where ν is Poisson's ratio of the elastic material. For PDMS in the rubbery state (room temperature) Poisson's ratio is usually taken as 0.5, the incompressible limit.

Another parameter which is relevant to the discussion of materials is the compliance. It may be thought of as the inverse of stiffness, $C = \frac{\delta}{P}$ where δ is the distance from equilibrium. Compliance will factor in our discussion of the theories of contact and fracture mechanics and features as a type of "relaxation factor" in the subject of viscoelasticity. In the next section however, we shall examine some of the theories related to the contact and subsequent separation of materials, specifically in the microscope regime as opposed to the macroscopic.

Adhesion

All materials experience competing forces of attraction and repulsion between the atoms and molecules of the materials. These forces are known as van der Waals forces and include repulsion due to the Pauli exclusion principle, electrostatic forces generated by dioles, the Debye force due to electric polarisation of particles and London dispersion effects from interactions of instantaneous multipoles [69].

Below a certain equilibrium distance between two bodies of atoms z_0 the force is repulsive while above z_0 the force is attractive. The variation of the force per unit area p between two materials as a function of separation z is shown as a Lennard-Jones potential in Figure 10 [32]. By convention, in the compressive (repulsive) regime the force is positive and in the tensile (or attractive) regime it is negative.

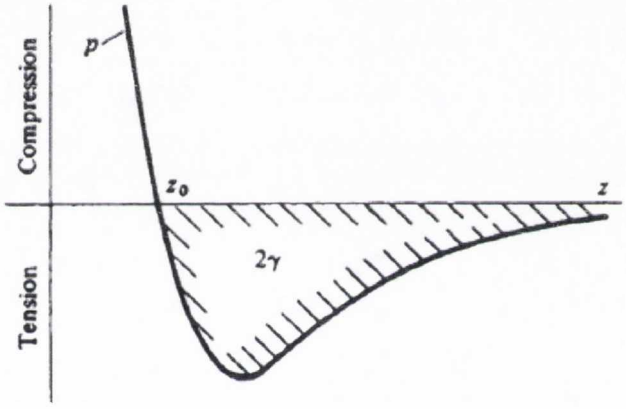

Figure 10 Interaction energy regime as a function of intermolecular distance between surfaces. From Johnson *Contact* Mechanics[32].

This tensile region is also known as the *adhesive* regime where the two materials are experiencing attraction with one another.

The work of adhesion which is the work needed to separate two surfaces can be expressed by the Young-Dupré equation

Equation 7

$$W = \gamma_1 + \gamma_2 - 2\gamma_{12}$$

The surface energy γ is the energy available when new surfaces are created. In Equation 7 γ_1 and γ_2 are the surface energies of the two different materials which are in contact and $2\gamma_{12}$ is the energy of the interaction.

Adhesion forces can be categorised as follows: Chemical adhesion, diffusive adhesion and dispersive adhesion [13]. Chemical adhesion is due to short range attractive forces arising

from chemical bonds between the molecules of contact surfaces. These bonds may be covalent, ionic or hydrogen bonds. The range of these bonds is on the order of Ångströms.

An example of diffusive adhesion is the adhesion between polymers. In this case, sufficiently long chains of molecules in the polymers are able to entangle with one another. The interface between the separate bodies is spanned by polymer chains entangled into both. Uncrosslinked polymers exhibit the strongest diffusive adhesion because they are free to move across a boundary and can entangle easily. Crosslinked polymers possess far less freedom of movement as they are chemically bonded to each other in many places along the polymer chain, and therefore can form only weak diffusively bonded connections.

The third category of adhesion is dispersive adhesion. This is the type of adhesion usually referred to by surface scientists simply as adhesion. Dispersive adhesion is due to *van der Waals* interactions which are interactions between dipoles in the contacting molecules. The dipoles may be permanent (Keesom forces) or temporary and moving (London forces). The forces can have an interaction length of 1-1000 nm [70] depending on the materials present.

A prominent feature of diffusive adhesion is hysteresis, where the work of adhesion to bring surfaces together is less than the work to pull them apart. This is due to the polymer chains having time to diffuse and entangle between materials on the timescale of the experiment. More diffusion leads to greater adhesion since more work will be needed to pull them apart. Hysteresis is also a factor in the non-diffusive adhesion of viscoelastic materials such as elastomers, but for a different reason. Viscoelastic materials behave like a combination of elastic solid and viscous liquid giving a time dependant character to their deformation. Chemical or dispersive adhesion causes an asymmetry in the deformation and deformation rates when bodies are brought into contact and then separated, leading to hysteresis. Viscoelastic materials and their adhesion hysteresis are discussed in more detail in Section 2.3.

In discussing surface forces between two different materials a distinction must be made between *cohesive* and *adhesive* interactions [68]. Cohesive failure implies separation of the molecules and failure of the attractive interactions within the bulk of one particular

material. So for example, the formation of a tear inside an elastomer is an example of cohesive failure. Adhesive failure however refers to the creation of new surfaces between two different materials. So the same elastomer being peeled from a glass slide is an example of adhesive failure. This thesis is mostly concerned with adhesive failure between different materials.

A feature essential to the theory of contact is the contact area. This is the area between the two materials that are in contact and is bounded by the contact line. When the contact area is decreased (due to adhesive failure of the interface) a "crack" forms between the two contact materials. This crack is referred to as a *growing or closing crack* when the contact area is increasing and as a *receding or opening crack* when the contact area is decreasing. The rates at which cracks grow or recede are highly relevant in the contact mechanics formulations discussed in this thesis.

2.2 Contact Mechanics Models

Many theories have been developed to describe contact mechanics problems starting in the late 19th century. An excellent overview of many of theories is contained in a paper by U.D. Schwartz [3] and the following discussion is based on the first half of this paper.

Hertz Theory of Contact

The first theory of the linear elastic contact of bodies was introduced in the 1880s. In contacting two materials, for example two solid elastic spheres (or elastic half spaces), initial contact is at one point on each sphere. As they are pushed together, deformation occurs causing the contact area between them to grow with increasing load. This work was pioneered by Hertz who developed equations for understanding the interaction of half spaces which had been brought into contact.

The theory assumes the bodies are frictionless and therefore transmit no shear stress across the contacting interface, and that the strains remain small ($a << R$). Adhesive traction at the contact is not taken into account, which is major simplification of the model.

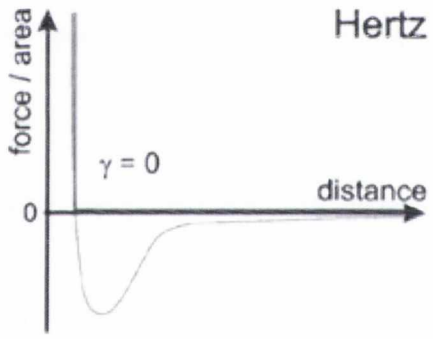

Figure 11. Figure from Schwarz [3] showing the Hertz case on a Lennard-Jones potential plot. There is no work of adhesion in this model.

Figure 11 shows the Hertz formulation on a Lennard-Jones potential taken from Schwarz [3]. The work of adhesion is calculated by finding the integral of the area under the *x*-axis. In this model there is no adhesion which is shown by that area being kept blank. There is no short range or long range attraction whereas a realistic situation would consist of long range and short range forces as outlined in Section 2.2. The Hertz equations of contact mechanics are as follows:

The contact radius of the sphere on flat is

Equation 8

$$a'^3 = \left(\frac{PR}{K}\right)$$

where $\frac{1}{K} = \frac{3}{4E^*}$. (Note this K is an elastic constant not to be confused with the stress intensity factor K_I in Equation 6). The relative displacement of the deformed elastic sphere on contact is given by

Equation 9

$$\delta' = \left(\frac{a^2}{R}\right)$$

The Hertz applied load is given by

Equation 10

$$P' = \frac{Ka^3}{R}$$

and the pressure distribution at a location r in the contact region is defined by

Equation 11

$$p(r) = \frac{3Ka}{2\pi R}\sqrt{1 - \left(\frac{r}{a}\right)^2}$$

Although these equations describe the theory of small strain contact [68] between linear elastic bodies, they are limited by not accounting for adhesion. The Johnson-Kendall-Roberts Theory (JKR) takes adhesive effects into account and therefore is discussed next.

JKR Theory of Contact Mechanics

The Johnson-Kendall-Roberts (JKR) [33] theory of contact mechanics is an extension of the Hertz model which accounts for adhesion in interactions between soft, deformable, elastic materials. It predicts a strong adhesive force acting at the equilibrium distance z_0 which is described by a delta function including area W (or γ as shown in Figure 12). z_o represents the contact area but for distances greater than z_o i.e. outside the contact boundary, the adhesion vanishes to zero. Therefore the JKR theory is only valid for the region inside the contact boundary.

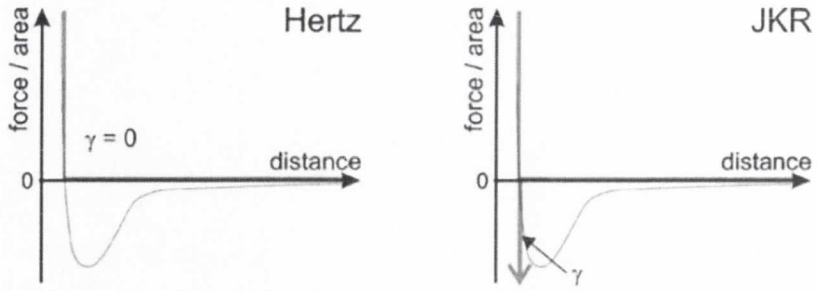

Figure 12. Schematic comparison of Hertz and JKR theories surface energies. Taken from Schwarz [3]

The JKR theory is formulated by coupling the adhesion energy to the contact radius which is then released as elastic energy stored in the deformed material. It assumes that a neck is formed during the deformation of the materials as it separates from the contacting material and this therefore gives it a flat punch configuration [4], [14]. The work of adhesion W can be found from the neck height using [4]

Equation 12

$$2\pi aW = \frac{3}{4}K\delta^2{}_{fp}$$

The full JKR model is described by two governing equations which relate the applied load P, the displacement δ, relative to the undisturbed sample surface and the contact radius a between the two surfaces. For a system where the spherical contacting body has a radius R, these equations are described by

Equation 13

$$a^3 = \frac{R}{K}\left[P + 3\pi RW + \sqrt{6\pi RPW + (3\pi RW)^2}\right]$$

and

Equation 14

$$\delta = \frac{a^2}{R} - \sqrt{\frac{8\pi\gamma a}{3K}}$$

When these equations were originally derived by Johnson *et al* [33] the authors considered the equilibrium case where G is equal to the thermodynamic work of adhesion, W_{TD} which describes the increase in free energy of a system when a single interface between materials is replaced by free surfaces. Maugis and Barquins [38] also developed an approach which is based on mechanical equilibrium between adhesive forces and the bulk deformation of the elastic material in their analysis of the model. By using the equation

Equation 15

$$G = \frac{(P' - P)^2}{6\pi K a^3}$$

which is equivalent to Equation 6 and assuming this mechanical equilibrium approach G can be found at every point along a loading or unloading curve for an elastic material. P' is the Hertz force calculated from Equation 10.

Although this theory accounts for adhesion in contacting materials it does present some drawbacks. Firstly the theory is developed for linear elastic materials contacting an infinitely smooth surface in a vacuum. Our experimental work is done with rough materials and not in a vacuum. Although applicable to soft elastomeric materials such as PDMS, most polymers including PDMS may exhibit some viscoelastic behaviour which might not be accounted for in the theory. Viscoelastic effects and resulting modifications to the JKR theory are considered in Section 2.3.

A second drawback to the JKR theory involves the inherent stress singularity at the contact edge as indicated in Figure 12. This means that only attractive forces inside the contact area are considered while those outside the contact line are disregarded. This is unrealistic because there will still be attraction between surfaces which, although not in contact, are in close proximity to one another. An equation which takes the surface attractions outside the contact area into account is the DMT model.

DMT Model

The Derjaguin-Muller-Toporov (DMT) [71] assumes there is no deviation of the shape of the material

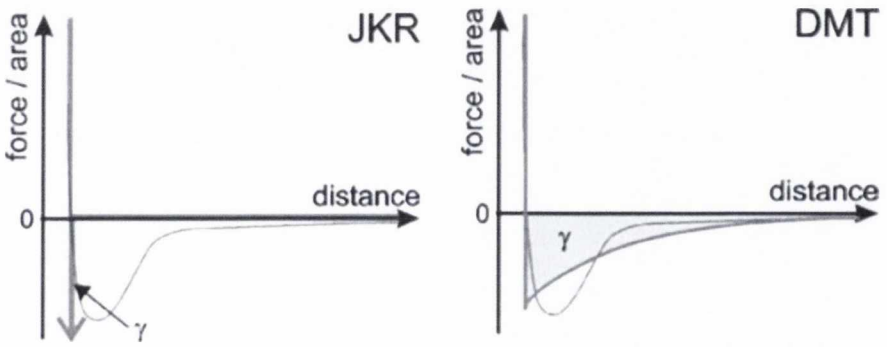

Figure 13. Comparison of surface energies of the JKR and DMT models. Taken from Schwarz [3]

outside the contact zone from the Hertzian profile. Doing this serves to gives a finite adhesive stress outside the contact zone in what is known as the *cohesive zone* but makes it zero inside. It

accounts for long range surface forces such as van der Waals-type attractive forces in the cohesive zone [3].

Figure 13 shows a comparison between the surface energies in the JKR and the DMT models [3].

The model does not account for deformation of the sphere outside the contact zone i.e. there is a stress-discontinuity once the model transitions to the cohesive zone. Therefore the DMT model is applicable for materials much stiffer than the soft elastomers used in this thesis. However viscoelastic effects may make it relevant to discussions involving contact edges as shall be discussed presently. This is because the viscoelasticity of a material resists large fast deformation in the material, which can essentially pin a moving crack front. In this case the local value of E could rise as the material stiffens resulting from resistance to the deformation. This process could be even more significant for elastomers which are thin films where the energy dissipation is restricted compared to a bulk material.

The transition from JKR to DMT behaviour is governed by the Tabor parameter [72]

$$\mu = \left(\frac{RW^2}{E^{*2}z_0^3}\right)$$

where z_0 is the effective range of action of the adhesive force (0.3-0.5 nm). For JKR behaviour, μ is > 5 and for DMT it is < 0.1. The Tabor parameter for elastomers such as PDMS is typically >5 .

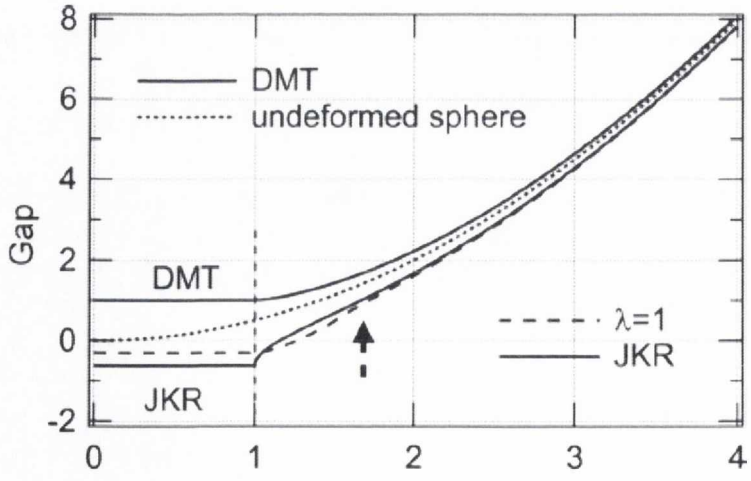

Figure 14. Comparison of DMT and JKR models showing how they deform a sphere. The undeformed sphere is also shown for comparison. From Creton *et al* [15]

Figure 14 [6] shows a schematic comparison of the shape on the deformed contacting spheres at the contact boundary for JKR and DMT theories. The dotted line shows the undeformed sphere for comparison. As can be observed the JKR deformation involves the formation of a neck at the boundary whereas the DMT shows no such configuration. A comparison of the predicted contact radius as a function of load for both tests is illustrated in Figure 14 [4]. This clearly illustrates that the Hertz theory predicts no adhesion (where the load is negative) and that the JKR will exhibit a peak adhesive value followed by a smooth transition back to zero load and contact radius.

DMT-M Model

An approximation to the original DMT model was put forward by Maugis *et al* [37] which proposes a unifying *cohesive zone model* based on the Dugdale-Barenblatt model. It is often known as the DMT-M model [3]. In this model intermolecular forces outside the contact zone are included by requiring the stresses to be bounded at the edge of contact. This serves to remove the singularity of the JKR model and the stress discontinuity of the

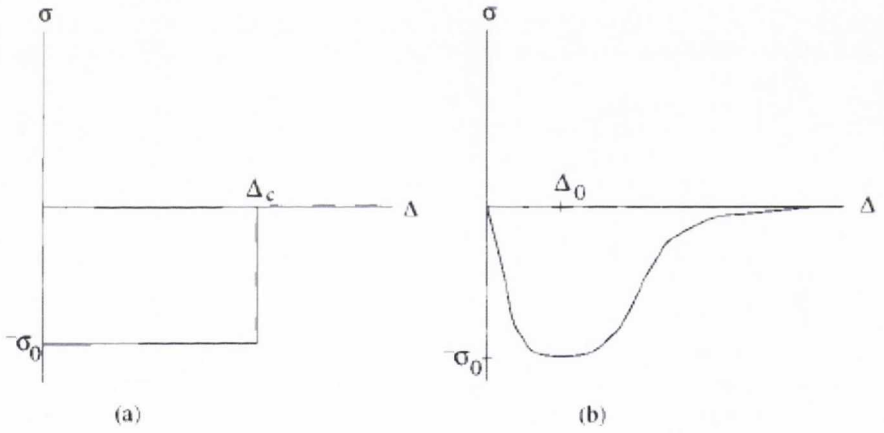

Figure 15. DMT-M model showing the normal stress σ on a material in the cohesive zone and the air gap Δ outside the contact area. (a) shows the Dugdale model upon which DMT-M is based and (b) represents a more realistic distribution. Taken from Schwarz [3]

DMT model. The model relates the normal stress, σ on the material in the cohesive zone to the height of the air gap, Δ outside the contact zone by the relation: $-\sigma = \sum(\Delta)$. The work of adhesion is found from the area under the σ-Δ curve. A diagram showing this Dugdale model and comparing it with a realistic σ-Δ curve is shown in Figure 15.

The work of Maugis [37] makes a connection between the elastic contact problem and LEFM. If we think of the air gap just outside the contact zone as being like an external crack, the pressure P_{tip} at the crack tip is in the form $\sigma \approx \frac{-K_1}{\sqrt{2\pi(a-r)}}$ as $r \to a$. Maugis verifies that this equation which gives a singular stress at the edge of contact is an excellent approximation of the stress

distribution near the edge as long as the cohesive zone is much smaller in size than the contact zone. Therefore a, P (the applied force) and δ in an elastic JKR system depend only on the work of adhesion W for this condition. The adhesion of elastic systems can be completely determined by the knowledge of W.

More realistic cohesive zone models exist which use a simple representation of the intermolecular interactions across surfaces [73] and finite element methods between viscoelastic and elastic materials [74]. However these models are beyond the scope of this thesis.

Stress Distributions

For a complete consideration of the contact mechanics of the linear elastic materials described by these models, the behaviour of the material at the crack edge must also be studied. The stress distribution of the elastic sphere in contact with the rigid flat material will not be homogenous across the contact area. For the Hertz model the stress-distribution can be described by [3]

Equation 16

$$p(r) = \frac{3Ka}{2\pi R}\sqrt{1-\left(\frac{r}{a}\right)^2}$$

where K is again an elastic constant defined by $\frac{1}{K} = \frac{3}{4E^*}$ and r is the position of the stress relative to the contact radius a.

For the JKR theory, taking adhesion into account the stress-distribution becomes

Equation 17

$$p(r) = \frac{3Ka}{2\pi R}\sqrt{1-\left(\frac{r}{a}\right)^2} - \sqrt{\frac{3\gamma K}{2\pi a}}\left(1-\left(\frac{r}{a}\right)^2\right)^{-1/2}$$

Of particular interest is the stress field at the contact edge which becomes relevant in inking of 2-dimensional thin films with a PDMS tip. The stress intensity factor is described by the formula [75]

Equation 18

$$g(a) \cong -\frac{\pi}{4}\sigma_0\sqrt{2a\epsilon_0}$$

where σ_0 is known as the cohesive stress for crack healing and can be described by a simple Dugdale model developed by Maugis [37] which can be formulated as being related to the air gap of

the cohesive zone as shown in Figure 15. $g(a)$ is the mode I stress intensity factor K_I for an outer circular crack in linear elastic fracture mechanics and so $K_I = \frac{2g(a)}{\sqrt{\pi a}}$.

The stress intensity factor can be related to the JKR surface energy using

Equation 19

$$w = \frac{2g(a)^2}{\pi E^* a}$$

and to the neck height in a JKR system by the formula

Equation 20

$$g(a) = \frac{E^*}{2}\delta_{fp}$$

As had been stated previously PDMS displays linear elastic behaviour in the bulk but that viscoelasticity is manifested at the moving crack edge. As stated by Hui *et al* [26]the idea of a universal relation between the stress intensity factor and crack growth rate is an important consideration in fracture mechanics. Therefore these equations may not be adequate for describing the stress distribution at the crack edge. The viscoelastic version of these equations will be considered in Section 2.3.

Surface Roughness

The above models have all been formulated for atomically smooth materials. However one must consider the effect on rough materials as it is rare that the contacting materials are atomically smooth. It has been found that rough surfaces will have increased adhesion compared with smooth ones [76]. The contact models all rely heavily on the contact radius (or contact area) of the materials at the interface. For a rough surface, there is a difference between the *apparent contact area*, A_0 which is the area we can measure with a microscope and the *true contact area*, A which is the area of the material including all the asperities, peaks and troughs which might be found in a rough material.

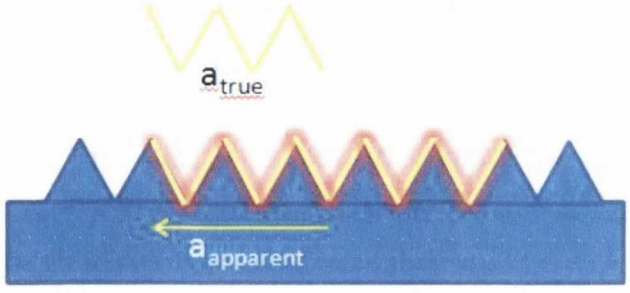

Figure 16. Figure showing how the apparent contact radius, measured by a microscope compares with the true contact radius which incorporates the 3 dimensional roughness of the material.

Figure 16 features a schematic showing how the 2-dimensional apparent radius measured by a microscope compares with the 3-dimensional true radius. Because the microscope takes only a 2-dimensional image of the contact, surface area due to peaks or asperities is not accounted for. The true radius, or more significantly, the true area would incorporate all the 3-dimensional details of the rough surface.

For low roughness materials the Wenzel roughness factor [76] can be defined as

Equation 21

$$r = \frac{A}{A_0}$$

However there are exceptions when the true and apparent area may be the same, for example cleaved mica which can have atomic resolution and low modulus materials such as elastomers which can conform to the surface they are in contact with. This can be borne in mind when considering the conformal contact of PDMS with the materials in this thesis.

Why does the surface roughness affect adhesion however? Let us consider the formula for the energy release rate introduced in Chapter 1.

Equation 22

$$G = G_0 + \psi$$

Following Packham's [76] discussion G_0 is the surface energy term which can be considered as the surface excess energy ΔG per unit area of the surface. Therefore

Equation 23

$$G_0 = {}^{\Delta G}/_{A}$$

As has already been discussed in Section Chapter 0 adhesion, or ΔG may be influenced by chemical or mechanical methods. Chemical effects might increase ΔG by creating more chemically active groups. The adhesion might be mechanically increased by roughening the surface. In this case an atom may rest atop an asperity which means it will have a greater exposed surface area (and therefore more free bonds) than if it was in the plane of the material. Also roughening the surface may alter the stress distribution at the interface which can increase the volume of material involved in the deformation of the materials due to pull-out and scission.

Roughness is an important consideration in this thesis work because the contacting materials include porous alumina, carbon nanotube networks and silver nanowire networks, all of which are very rough materials. The features of this and how they compare with smooth materials is discussed in Chapter 4.

2.3 Viscoelastic Considerations

Viscoelasticity is used to describe materials that exhibit both elastic and viscous behaviour. Viscoelastic materials exhibit time-dependent strain when undergoing deformation and the behaviour of the material in contact mechanics is dependent on the whole loading history of the contact. For an elastic material the contact radius has a unique value for each value of the applied force whereas in viscoelastic materials the contact area depends on the whole loading history of the test. So for viscoelastic materials with an energy release rate $G = \frac{K^2 I}{2E^*}$, the modulus is not uniquely defined everywhere and can range from an instantaneous modulus E_o^* to a long range or relaxed modulus E_∞^*. Whereas elasticity is usually due to stretching of bonds inside a solid, viscoelasticity is due to diffusion of atoms and molecules in a material [69].

The modulus is a very important concept in the mechanics of materials and will now be discussed using Sperling's very comprehensive book *Introduction to Physical Polymer Science* [65]. There are different types of moduli for materials, from the Young's modulus E which is a measure of the stiffness of an elastic material, to the shear modulus G (not to be confused with the energy release rate) which measures a material's resistance to shear strain and the bulk modulus B which measures the compressibility of a material. For elastomers $E \cong 3G$.

The modulus of a material is made up of two parts, the storage modulus E' which is a measure of the bulk elasticity of the material and the loss modulus E'' which measures the energy losses due to viscoelastic energy dissipation which is in the form of heat. The whole modulus is then defined as

Equation 24

$$E = |E^*| = E' + iE''$$

and similar definitions hold for G and B. The relationship between E' and E'' for an ideal polymer for different temperatures, time or frequency of oscillation is illustrated in Figure 17. The relationship between the storage and loss moduli is known as the dynamic mechanical behaviour of the polymer.

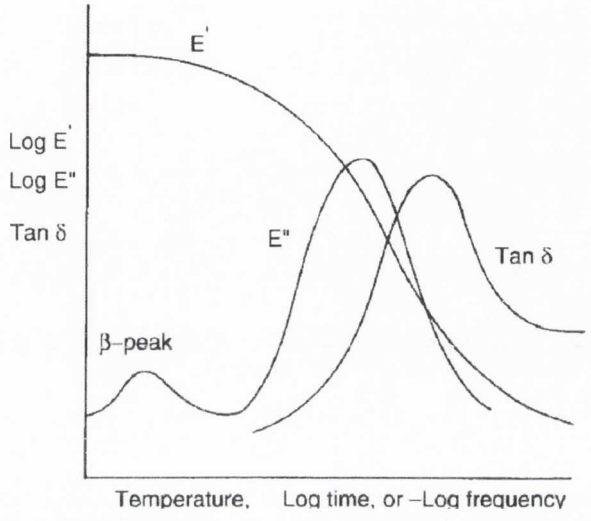

Figure 17. The dynamic mechanical behaviour of an ideal polymer showing the storage and loss moduli. Taken from Sperling *Introduction to Physical Polymer Science* [65].

Tan $\delta = E''/E'$ and is called the loss tangent. Quite often the maxima of E'' and Tan δ are used to define the glass transition temperature, T_g which is the temperature at which a polymer moves from being in a glassy state to being in a rubbery state.

Figure 18 shows the five different regions for viscoelastic polymers based on temperature. Viscoelasticity is based on the time and temperature dependence of a material's mechanical behaviour. Region 1 is the glassy state whereby the polymer is hard and brittle. Region 2 is the glass transition state where the polymer can be described as "leathery". The glass transition temperature can be taken as the point at which the maximum downturn of the modulus occurs, usually at the elbow of the turn as indicated by the vertical dotted line. For PDMS elastomers T_g is measured as -127 °C, far below room temperature. Region 3 is the rubbery plateau region where polymers exhibit rubbery, linear elastic behaviour. The horizontal dotted line indicates the modulus for cross-linked polymers (such as PDMS). As can be seen cross-linked materials do not experience a change in modulus in the last two regions, 4 being the rubbery-flow and 5 being the liquid-flow regions.

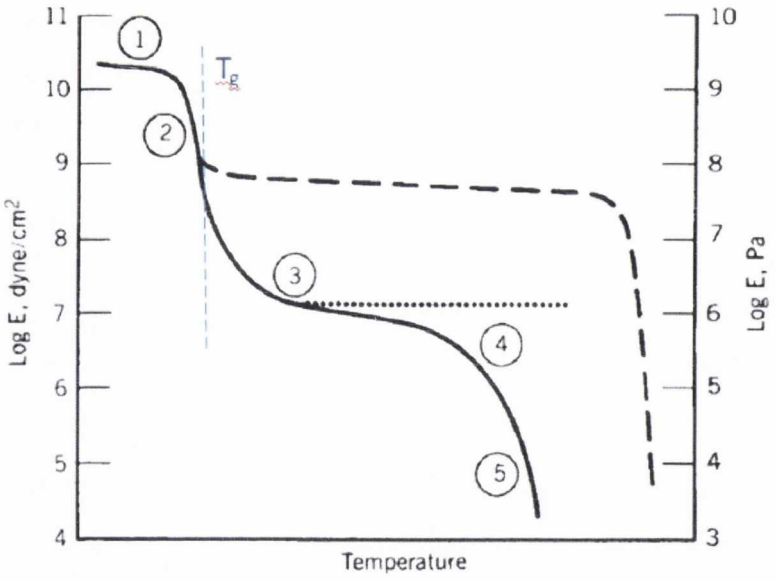

Figure 18. The five regions of viscoelasticity of an ideal polymer as a function of temperature Taken from Sperling *Introduction to Physical Polymer Science* [65].

As is indicated in Figure 18 polymers experience softening and flow above T_g. In order for this to occur a certain amount of free volume is needed which is the unfilled volume found at the end of a polymer chain. The amount of free volume available depends on the number of chains and hence the degree of polymerisation (DP) [77]. Polymer-melt viscosity and free volume can be related to one another by the Williams-Landel-Ferry (WLF) equation

Equation 25

$$\log A_T = -\frac{C_1(T - T_0)}{C_2 + (T - T_0)}$$

where A_T is the temperature based shift factor and C_1 and C_2 are empirical constants. The WLF equation allows for the construction of a temperature curve for any polymer such that viscosity as a function of temperature can be calculated. It is a consequence of the time-temperature superposition principle which is the correlation between time and temperature developed by Andrews and Tobolsky [66]. The consequence of this relationship is that by deforming a polymer, the modulus as a function of temperature illustrated in Figure 18 can be shifted along the x-axis. So for example, deforming the polymer at a particular frequency can cause the viscoelastic regions to shift temperature-wise thus moving the glass transition temperature for the material, or causing it to go into a rubbery state at a higher temperature.

Viscoelasticity in Contact Mechanics

The analysis of viscoelastic theory is challenging as there is no solid theory of viscoelasticity. In adhesion tests there is an interplay of interfacial and bulk contributions. The analysis of Gent and Schultz [44] is often used for describing this. In their analysis, the energy release rate is a combination of surface and bulk effects described by

Equation 26

$$G = G_0(1 + \Phi(a_T v))$$

G_o is again the critical energy release rate above which a crack can form. It is called the interfacial adhesive energy and is assumed to be rate independent and equal to w. This is valid for ideal interfaces which can simply be described by the van der Waals interactions. The bulk viscoelastic response of the system is given by Φ which is called the viscoelastic loss function and is a function of the rate of the propagation of the crack and by the Williams-Landel-Ferry (WLF) shift factor for time temperature superposition, a_T which is described in more detail in the next section. The WLF factor is substrate independent and only applies to the elastomer or polymer in question in the system. Using this formulation the adhesion could be manipulated by changing G_0 through surface modifications or by changing the bulk viscoelastic response.

However more recent work has indicated that this formulation may not be fully accurate. For example Chaudhury and Whitesides [78] have found an interfacial slippage in PDMS which means that their measurements of G are inconsistent with Equation 26. Although we will not describe here how such a formulation is developed, it is important to note that the traditional adhesion analysis based on Gent and Schultz's equation may not be valid for the elastomers used in this thesis. Therefore some more recent work is described in this section including the extended JKR model and a formulation due to Barthel and Frétigny [7].

Adhesion Hysteresis in Viscoelastic Contact

An important observation in viscoelastic materials is that of *adhesion hysteresis*. This is the situation whereby the adhesion in the loading segment of the contact test is different from that during the unload:

$$G(a)_{load} \neq G(a)_{unload}$$

Adhesion hysteresis is often featured in polymer contact experiments and there sources include changes of the material at the interface (such as the surface roughness as described in Section Chapter 0) or due to viscoelastic dissipation effects [4]. These originate from tensile cohesive stresses at the boundary as described by Gent and Schulz [44]. Therefore the cohesive zone should be included in a discussion on viscoelastic contact. Doing so overcomes the stress singularity of

the JKR theory and allows for a finite strain rate. This leads to a *velocity dependent* dissipation as formulated in Equation 26.

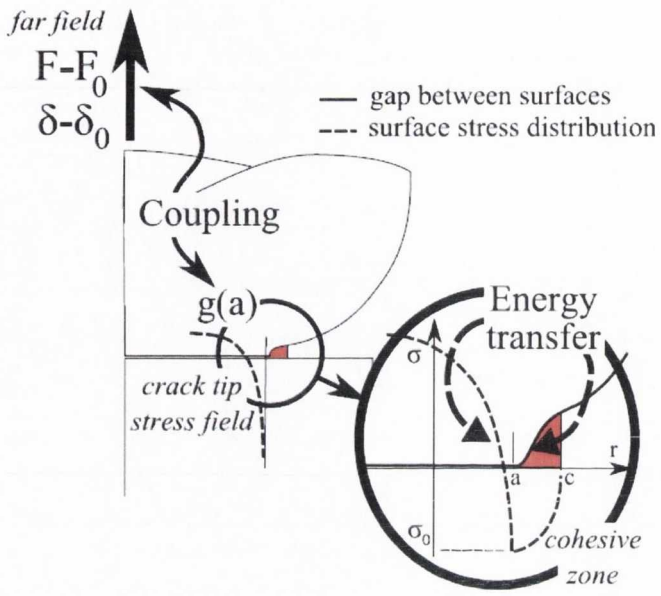

Figure 19. Schematic showing the coupling of local and far field stresses in a viscoelastic. At the crack tip the energy transfer is illustrated using a cohesive zone model. From Barthel *et al* [7].

Barthel and Frétigny [7] propose an approximate expression which accounts for the increase in the adhesion energy due to viscoelastic dissipation in a growing crack. A basic consideration of this theory involves the *coupling* of local stress at the edge of the contact with the far field stress in the bulk material. This is shown in Figure 19 and shows a schematic of the macroscopic contact and the cohesive zone. One can see the coupling of the local stress with the far field and the close-up shows the energy transfer in the cohesive zone at the crack tip. As stated by the authors the formulation for a receding contact (i.e. opening crack = unload segment) is relatively straightforward compared with that of a growing contact (i.e. closing crack = load segment). Receding and growing contacts are schematically illustrated in Figure 20.

An important parameter introduced by Barthel and Frétigny is that of the *dwell time* t_r which is the time taken for a moving crack to cross its own imprint $\epsilon = c - a$. The crack velocity is then defined as $v = \epsilon t_r$. Another important concept is that of the *relaxed modulus* E_∞ which is the long-time response of the material as introduced in discussing the WLF equation in Figure 18. E_0 in contrast is the *instantaneous modulus* (short time response) and an elastomer can be defined as having $E_\infty / E_0 \ll 1$.

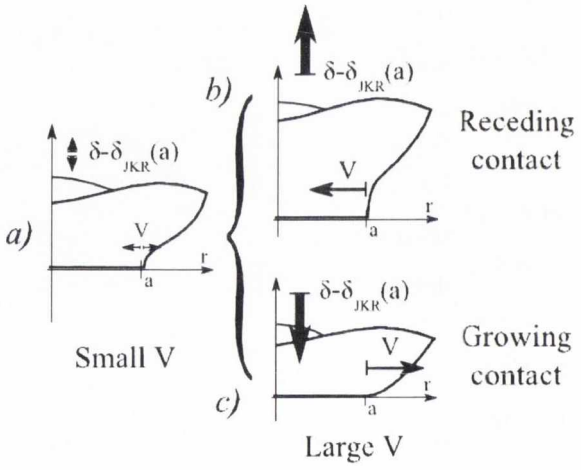

Figure 20. Schematic showing adhesive contact for an elastomer where δ_{JKR} is the elastic JKR penetration for adhesion energy *w*. From Barthel *et al* [7].

It was found that for small velocities the system

is close to equilibrium and the receding and growing contacts are close to the elastic JKR limit when using the relaxed modulus concept. However for large velocities there are strong deviations which are linked to the viscoelastic dissipation process. These are quantified in an *effective adhesion energy*, a concept that was originally introduced by Schapery [79] and Johnson and Greenwood [80]. A schematic illustrating the JKR penetration depth for elastomers with low velocity, and for receding and growing contacts is illustrated in Figure 20.

Extending Sneddon's formulation of the stress intensity factor [75] for the viscoelastic case using the dwell time t_r yields

Equation 27

$$g(a(t), t_r) \cong -\frac{\pi}{4}\sigma_0\sqrt{2a(t)\epsilon(t_r)}$$

and the adhesion energy is given as

Equation 28

$$w = \frac{g(a)^2}{\pi a}\phi_I(t_r)$$

where $\phi_I(t_r)$ is either for opening cracks (receding contact) $\phi_{I,op}(t_r)$ or for closing cracks (growing contact) $\phi_{I,cl}(t_r)$ as defined by

Equation 29

$$\phi_I(t) = \frac{2}{t^2}\int_0^t (t-\tau)\phi(\tau)d\tau$$

$$\phi_I(t) = \frac{2}{t^2}\int_0^t \tau\phi(\tau)d\tau$$

By applying the far-field coupling described in Figure 19 the authors proposed analytic expressions for the effective adhesion of the elastomers which for a receding contact are

Equation 30

$$\frac{G_{eff}}{w} = \frac{\epsilon}{\epsilon_0} = \frac{\phi_I(\infty)}{\phi_I(t_r)}$$

and for a growing contact

$$\frac{G_{eff}}{w} = \frac{\phi_I(\infty)}{\phi_I(t_r)}$$

$$\frac{G_{eff}}{w} = \frac{{\phi_0}^2(t_r)}{\phi_{I,cl}(\infty)\phi_{I,cl}(t_r)}$$

where $\phi_{I,cl}(\infty) = 2/{E^*}_\infty$.

As can be seen in the simulation in Figure 21 there is a large hysteresis in the normalised effective adhesion between load and unload which is low for small crack velocities but grows larger for faster crack velocities until the effective adhesion saturates.

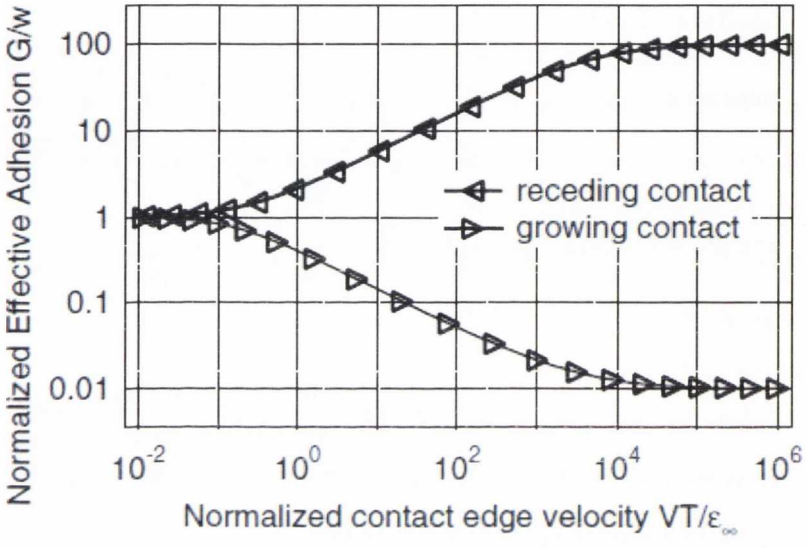

Figure 21. Simulation illustrating the effective adhesion energy as a function of crack velocity in the load and unload segments of a contact test. The crack tip processes were shown to be nearly identical but the resulting effective adhesion is quite hysteretic. From Barthel *et al* [4].

To date experimental verification of this analysis has yet to be performed. In the next section an extension to the JKR based on an effective surface energy will be described. This has been applied to a physical experiment on PDMS spheres which can then be used for comparison with the experimental observations in this thesis.

2.4 Experimental Applications of Contact Mechanics

Extended JKR Theory

A feature of the JKR theory is that it is defined for ideal systems which experience equilibrium contact between elastic materials with a constant surface energy γ. Schapery [79] and Maugis and Barquins [38] were able to apply the JKR theory to non-equilibrium contact by replacing the surface energy with an *apparent surface energy* γ_{app}. This is the energy needed to separate unit area of the adhering surfaces. Soft materials have an apparent surface energy which is dependent on the contact line velocity as formulated by Greenwood and Johnson [80]. This model is known as the

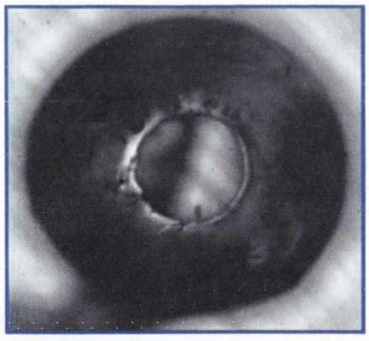

Figure 4. Top view of the contact area.

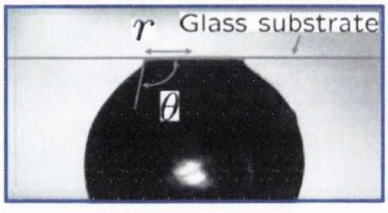

Figure 22. Images from showing the measured contact area and the contact angle of soft PDMS spheres in contact with glass. From Doi *et al* [81]

extended JKR theory and an application of this model to PDMS spheres was conducted by Doi *et al* [81,82].

Spheres made of cross-linked PDMS with a radius of 0.4 mm were contacted against flat glass slides. The contact area was measured as were the contact angles as shown in Figure 22. Using these measurements and applying them to the extended JKR model yield surprising results. Despite the large deformations observed the JKR model fit the experimental data remarkably well, suggesting that PDMS does indeed behave like a linear elastic material. Further tests found that the force-distance data was well reproduced in cyclic experiments indicating that PDMS does behave as an elastic material in the bulk and that any viscoelastic energy dissipation is apparent only in the region near the contact line. Their experimental evidence showed that for the majority of the contact experiment, the contact angle remained constant indicating that the apparent surface energy was only a function of the crack velocity. However in situations where the contact line became pinned and the velocity slowed down or stopped the contact angle changed considerably showing large energy dissipation within the PDMS. At this point the apparent surface energy is no longer a strong function of the surface effects but of the energy dissipation in the region. Therefore the apparent surface energy is a function both of the crack velocity of the interface and of the energy dissipation within the deforming PDMS at a pinned crack.

It is the pinned crack interface at the (viscoelastic) crack boundary that is of the most interest in the inking experiments described in Chapters 5 and 6. Therefore this analysis will be further examined and compared with our experimental data in later chapters.

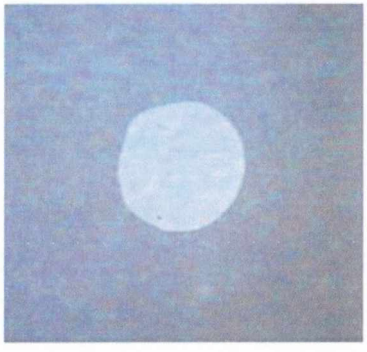

Figure 23. Contact impression left by excess cross-linker on alumina.

As mentioned previously adhesion hysteresis can manifest itself by viscoelastic effects but also by modifications to the surface. Mechanical changes such as surface roughing were discussed previously but the surface can also be changed by chemical means. Changing the chemistry of a surface can allow for more chemical bonds to be formed between the materials thus increasing the adhesion. The longer the materials are in contact that more opportunity there is for bonds to form but also the

rate at which the bonds are broken due to tensile stresses can increase the adhesion substantially. As will be discussed in Chapter 3, PDMS is a crosslinked elastomer. In the experimental work of this thesis, excess cross-linker is not rinsed out before testing begins. This has a useful side effect of leaving a layer of itself behind on the contacted material which allows for the contact radius at the maximum load to be found. We have named this layer the *contact impression*. It must be considered though that this excess cross-linker might chemically change the interfaces thus influencing adhesion. The possible effects this might have on the transfer process will be discussed in more depth in Chapter 5.

We must ask ourselves what the nature of this contact impression is. According to the manufacturer's (Dow Corning) data sheet the cross-linker consists of a platinum-based catalyst in a silica solution. It is not electrically conductive and can be rinsed out of the PDMS elastomer using methanol and toluene. This process takes several days and causes significant swelling of the PDMS which has made it impractical for our purposes. Attempts at removal of the crosslinker from the PDMS caused the PDMS to swell and de-adhere from the silicon sphere, thus rendering the tip useless. It was found that using different thickness PDMS layers as described in Chapter 4 appeared to change the optical contrast of the crosslinker. The thicker the PDMS layer, the optically less opaque the crosslinker. Solid PDMS spheres, or very thick PDMS layers yielded almost no contact impression at all, suggesting that the deposition of excess crosslinker is due to it being squeezed out of the PDMS when the layer is confined between two hard surfaces e.g. the silicon sphere and the alumina membrane. Attempts were made using AFM to characterise the contact impression and measure its thickness. However it was only optically visible on alumina, not on smooth surfaces such as silicon and glass and the roughness of the alumina obscured the measurements. The crosslinker's effect on the nanomaterials will be discussed again in the electrical measurements section in Chapter 8.

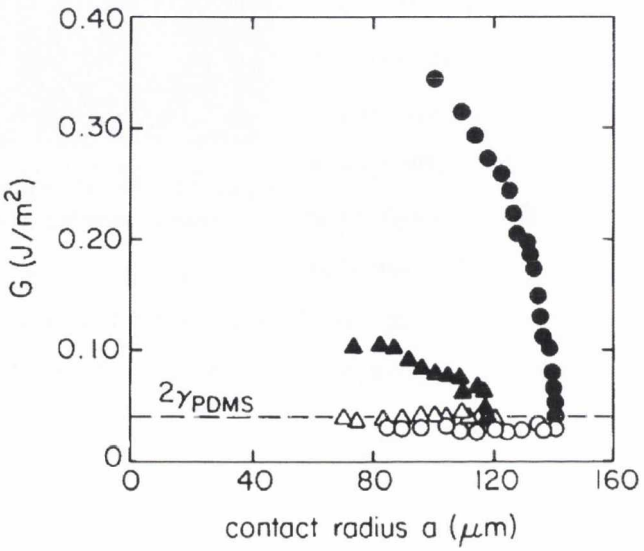

Work done by Perutz *et al* [30] examines the adhesion hysteresis due to excess cross-linker. In this work, the excess in cross-linker (which is a tetrafuctional silane) was carefully controlled and adhesion hysteresis was examined as a function of crack velocity. Figure 25 shows the measured G values as a function of contact radius for PDMS with 10% and 45% excess cross-linker respectively. The open symbols represent the load segment and the closed symbols the unload segment. As can be seen the G values remain constant for all of the load segment and a value of 44 mJ/m^2 was measured which is in good agreement with $G \approx 2\gamma$ where γ_{PDMS}= 22 mJ/m^2. On the unload in both cases the G values increase substantially with a much more significant increase for the tests with the higher level of cross-linker. The load rate was the same as the unload rate for all tests and so the only explanation for this adhesion hysteresis is either viscoelastic effects or changes to the surface energy γ.

25. G as a function of contact radius for PDMS with fferent levels excess cross-linker (triangles = 10%, = 45%). The open symbols represent the load and the ymbols the unload segment. From Perutz *et al* [30].

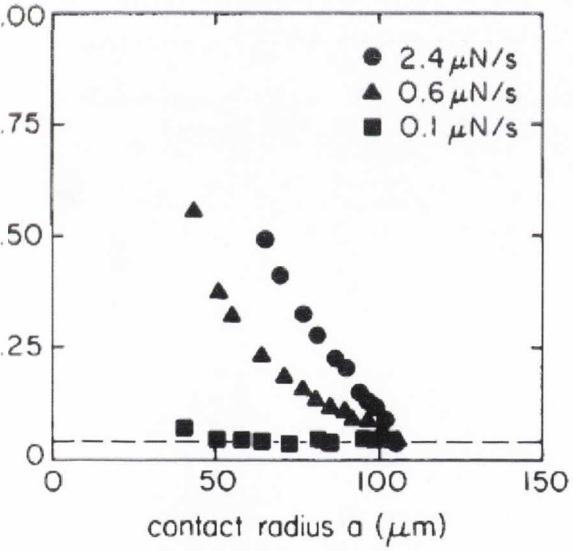

24. Adhesion hysteresis due to changing the unload the contact experiment. From Perutz *et al* [30].

The authors then conducted experiments showing the effect changing the unload rate could have on the adhesion hysteresis and the results are shown in Figure 24. The level of excess cross-linker is 10% for all the tests. As can be seen the amount of adhesion hysteresis scales with the unload rate with the slowest unload rate showing no adhesion hysteresis at all. This test was unloaded at a rate of 0.1 uN/s compared with 2.5 uN/s for the tests in Figure 25. For tests with higher cross-linker the rate at which G became non-hysteretic was even lower. This and the variation of adhesion hysteresis with the amount of cross-linker provide further evidence of how the chemical changes of the material affect the adhesion. The authors claim that the adhesion hysteresis is purely due to chemical effects in this case, as opposed to viscoelastic losses as they argue that viscoelasticity should manifest itself in the load up as well as the unload but they observe a constant G value for the load, regardless of loading rate.

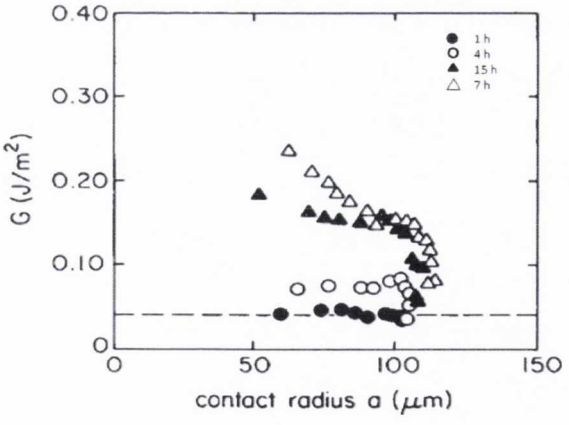

Figure 26 shows the adhesion hysteresis for tests which were held for different peak load times before unloading commenced. Therefore only the unload segment is shown. As can be seen in most cases the adhesion hysteresis increases with greater peak hold time. It was found that after a hold time of 7 hours there was no change in the adhesion hysteresis of the PDMS.

These results are important in considering the causes of adhesion and adhesion hysteresis in tests with PDMS, especially where there is excess cross-linker involved. Comparison of these tests with our experimental data is done in Chapter 4.

Figure 26. Comparisons of adhesion hysteresis with peak hold time before unload commenced. The excess cross-linker was 45% in all cases. From Perutz *et al* [30].

2.5 Failure Modes of Adhesive Contact

In all cases discussed so far the failure of the interface between PDMS and the contacting material has assumed to be a crack which propagates from the outside contact boundary in towards the centre of the contact area. The contacting materials used have also been relatively smooth materials which are rather dissimilar to the porous alumina membranes which are used for a great deal of the work in this thesis. It is necessary therefore to consider if other types of failure can occur due to deformation in adhesive contact as a result of trapped air pockets or asperities in the contacted material. Concepts in the *theory of tack* or adhesion become relevant to this discussion.

There are several classes of deformation and they can be categorised into two general types; those which are governed by the crack propagation rate and those governed by stresses in the layer. The crack propagation rate and the stresses in the layer are related to one another by the degree of lateral confinement. For probe-type adhesion tests this is covered by the ratio of the contact area, a, to the thickness of the adhesive layer. For the peel test, it is related by the length of the stressed area to the thickness of the layer. In brief what follows is the classes of deformation as described by Crosby *et al* [17] and are illustrated in Figure 27.

1) Edge crack propagation (2a). This is simple adhesive failure and the energy applied to

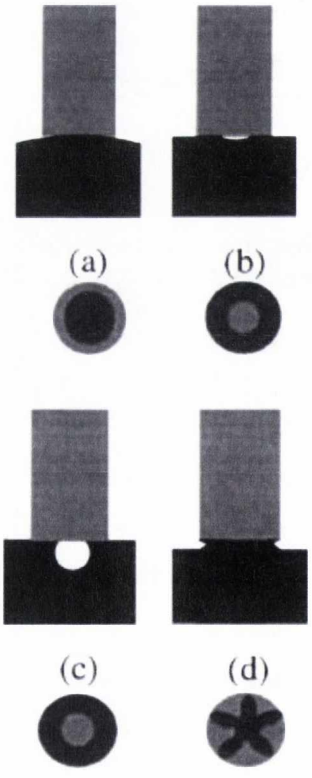

Figure 27: The basic failure modes observed in thin layers under normal loads: a) edge crack propagation; b) internal crack propagation; c) cavitation d) bulk fingering. From Creton *et al* [17].

the system is shared by the propagating interfacial crack and any loss in the viscoelastic compliant layer. For our transfer situation, this type of failure mode is likely to be the most dominant.

2) Internal crack propagation (2b). This is where the hydrostatic pressure in the compliant layers causes the formation of a penny-shaped internal crack which then can propagate in a similar manner to 1) above.
3) Cavitation. This is similar to 2) except that the cavity grows in the bulk instead of propagating at the surface. More details on this process are described below.

Cavitation with Flat Punch Tests

In systems where the adhesive layer is highly constrained, extensive cavitation will occur on the application of negative hydrostatic pressure as outlined by Creton *et al* [16]. Experiments done by Lakrout *et al* [83] show the progression of their formation as outlined in Figure 28.

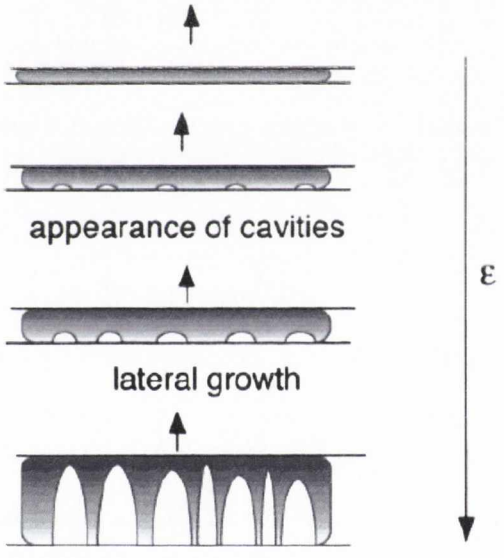

Figure 28: Microscopic deformation mechanisms during the debonding of a soft film from a flat punch. From Creton *et al* [16]

First occurs homogenous deformation of the films as a tensile force is applied. Nucleation of cavities forms at the probe/film interface. These cavities usually form due to trapped air pockets in the interface between the soft film and the probe. As the tensile force is further applied the cavities expand to form interfacial cracks which in turn develop into a fibrillar structure.

Evaluating the stress field near the contact of the flat punch and the adhesive layer requires the use of finite element methods. However, there are two limiting cases which are described in Creton's paper [16]. One case is where the elastic film is infinite and the other is where the elastic film is very constrained.

For an incompressible film the stress distribution is found to be parabolic with a maximum normal stress and hydrostatic pressure at the centre of the probe which is a classic result of fluid mechanics. What the authors also found is that for systems which are very confined and have any a small amount of deviation from incompressibility (ν = 0.49) the stress distribution becomes rather flat. The implication of this is that the cavitation should appear simultaneously and homogeneously over the entire surface of the film upon application of a hydrostatic tensile force.

In reality though, for thin confined layers the propagation of cracks forms from cavitation, not from the edge of the contact area. Gent *et al* [42,84,85] showed that for crosslinked elastomers, cavitation will occur for sustained tensile stress which is higher than approximately E. The development of spherical cavities in the adhesive film is illustrated in Figure 29.

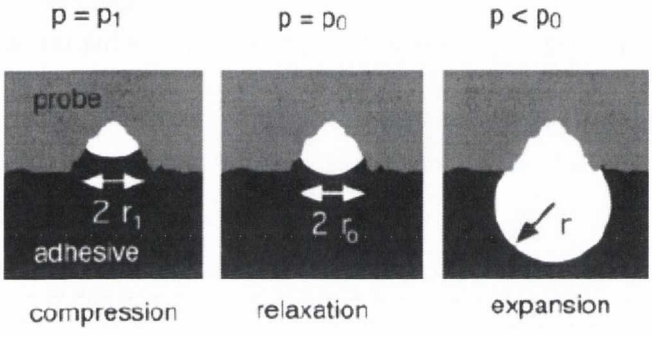

Figure 29: Schematic of compression and expansion of an air bubble trapped at the probe/film interface. From Creton *et al* [62]

If the air inside the trapped air bubble is compressed to a pressure p_1 and then the tensile stress is applied, the internal pressure in the cavity will decrease. The cavity then expands. Expressions have been formed by Gent and Kaelble [86], especially for the viscoelastic case so that the hydrostatic stress near the cavity is given by $\bar{\sigma}(t) = \frac{1}{6}E(t)F_1(\lambda) + \frac{1}{\lambda}\left(\frac{2\gamma}{r_0} - \frac{p_1}{\lambda^2}\right) + p_0$ where $F_1(\lambda) = 5 - \frac{4}{\lambda} - \frac{1}{\lambda^4}$ and p_1 is the initial cavity pressure ($t = 0$), p_0 is the ambient pressure, γ is the surface tension of the film, r_0 is the initial radius of the defect, λ is the expansion ratio of the cavity and $F_1(\lambda)$ is the elastic-energy term. The shortcomings of this model are that it only applies to defects which are smaller than 2-300 nm and it only describes an expansion into the bulk and not the interface. Models based on the local energy balance and include the surface energy such as outlined by Gay and Leibler [87] has shortcomings also including the prediction of a maximum stress which increases with the square root of the elastic modulus, which is in contradiction to experimental data on elastomers. So although these models are useful for examining the initial stages of cavities before they interact with one another, more work is needed before we can understand the process fully.

As can be seen from this overview, there is a large body of work associated with the problems of adhesive contacts and crack formation and propagation. For our system the challenge is to pick out the applicable models and ideas that are in existence and apply them accordingly in a way that supports our experimental observations and those of others. Ultimately our goal is to

understand the system in such a way as we can control the type of fracture and deformation modes observed, thus controlling our transfer process between interfaces.

As noted by Barthel [7] our intuition would tell us that the contact zone for a sharp neck would be small. However this assumption is incorrect because necking is due to the far field and the cohesive zone is relevant only locally at the contact boundary. As he reminds us, the size of the contact zone is directly proportional to the square of the stress intensity factor $g(a)$. Therefore the cohesive zone size is dependent on the crack speed.

Fracture of Adhesive Film during JKR Tests

The aim of understanding the contact mechanics between PDMS and other materials is to better understand the inking and printing of 2-dimensional materials. So far we have considered the contact models involved in adhesive contact, how the variation of surfaces, chemistry and crack velocity affect adhesion. We have also considered the stress fields created during adhesive failure and the affect they have on the contact mechanics of the problem. However referring once again to Figure 9 it is clear that the problem we are presenting is more complicated than PDMS in contact with a rigid material. There also exists a thin layer between them, that of the nanomaterial network. How can one formulate an analysis for the deformation and eventual fracture of such a network during an adhesion test?

Work done by Shull *et al* [63] [1] examines this problem as was discussed in Chapter 1. The contact experiment was described with the JKR model for the energy release rate which is given by Equation 15

$$G = \frac{(P' - P)^2}{6\pi K a^3}$$

The authors extend their analysis to what occurs during deformation and fracture of the 2-dimensional material, which in this case is a viscoelastic block-co polymer. It was found that the interface between the polymer film and the flat PDMS slab it was attached to fracture in the mode of cavity formation. This is illustrated schematically in Figure 30. Using a camera underneath the transparent PDMS the formation and growth of the cavity was observed.

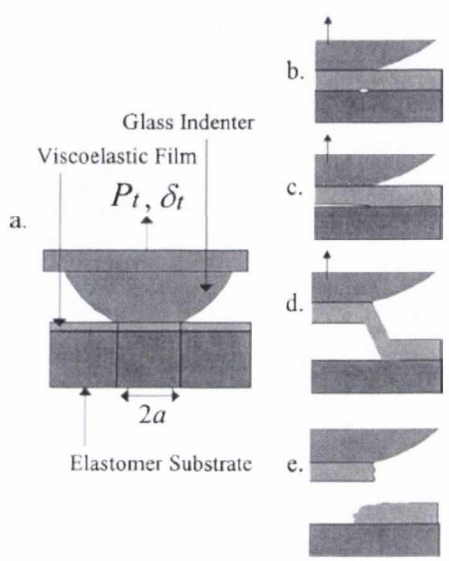

Figure 30. Schematic illustrating cavity formation between the polymer film and underlying PDMS. From Shull *et al* [63].

An analysis follows which describes the deformation and subsequent fracture of the polymer film. Figure 30 shows a schematic of the polymer film in contact with

both the PDMS substrate and the glass indenter after cavity formation and growth between the polymer film and PDMS interface.

As can be seen the membrane is being extended and there are two contact radii. The contact radius of the membrane adhered to the glass sphere is designated a and the contact radius of the membrane de-bonded from the PDMS substrate is designated R_m. The glass sphere is obviously totally solid and so retains its curvature during testing. The height of the sphere above the substrate which is measured by the experimental set-up is designated δ while the height at the edge of the contact is δ_a.

The deformation of the inked membrane is described by an extension ratio

Equation 31

$$\lambda = \sqrt{1 + \Delta^2}$$

which has $\Delta = \frac{\delta_a}{R_m - a}$ and $\delta_a = \delta + R - \sqrt{R^2 - a^2}$ where R = radius of curvature of the glass indenter. In Shull's work an extension ratio of 3 was found which when applied to a large strain theory for this geometry gives $G \approx 0.3$ J/m^2 for the energy release rate needed for crack propagation. This provides a way of quantifying the energy needed to cause cavitation and rupture of the films being inked and as will be seen in Chapters 5 and 6 becomes relevant to the discussions involving the nanomaterial networks involved in this thesis work.

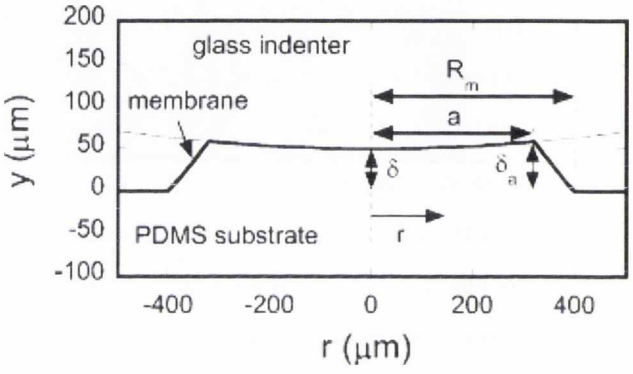

Figure 31. Schematic of the deformation of the thin polymer film during the unload of a glass sphere from PDMS. From Shull *et al* [62]

Nanomaterials Used in This Work

Carbon nanotubes have been studied in great detail since being rediscovered by Sumio Iijima in 1991 [88]. Hollow graphene tubules have been mentioned as far back as 1952 [89] as reported by Monthioux and Kuznetsov [90]. Since their rediscovery, they have generated great interest amongst the academic community due to their extraordinary properties. Their potential lies in their tremendous conducting and tensile abilities and a great many applications have been theorised and tested, including body armour, light-weight super-strong materials and electronics amongst others. It has also been speculated that they could be used instead of the current indium tin oxide films (ITO) that are used in electronics. This would be advantageous as ITO is becoming more

expensive as indium becomes rarer. Another advantage lies in the fact that carbon nanotube films would be flexible, unlike the very brittle ITO, opening up a new range of possibilities in modern electronics and technology.

The aim of this project is to develop and test conductive carbon nanotubes films which can be used instead of ITO and can be used in the next generation of electronics; namely flexible electronic displays. This specific study involves characterising the electromechanical properties of the films.

1.1 Carbon Nanotubes

Carbon nanotubes, simply put, are rolls of graphene. If one could take a sheet of carbon atoms, and roll them up into a cylinder, we would have a carbon nanotube. Apart from being made exclusively of carbon atoms, another distinguishing feature is their aspect ratio which is very high. A typical single-walled nanotube has a diameter of about 1 nm and its length may be many thousands of times longer. There have been recent reports of carbon nanotubes of length in millimetres [91]. There is significant interest in carbon nanotubes due to their extraordinary tensile and conductive properties. Carbon nanotubes (CNTs) have moduli of 1 TPa which compares with the 0.5 GPa of titanium [92]. CNTs are also extremely lightweight with a density of 1500 kg/m^3. Combined with the fact that CNTs can carry currents of 100 MA/cm^2, 1000 times greater than the conductivity of copper, it becomes apparent why they have generated such interest.

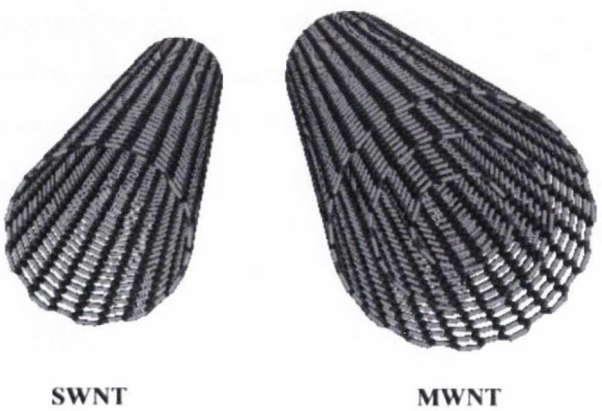

Figure 32: SWCNT and MWCNT [95]

Carbon nanotubes can take on either single-walled (SWCNT) or multi-walled (MWCNT) form, depending on how they are produced. Synthesis of CNTs can be done by laser ablation, chemical vapour deposition or arc-discharge methods. MWCNTs are the most common and may have several tens of shells with an adjacent shell separation of only 0.34 nm [93].

SWCNTs tend to be more difficult to create but have superior conductive and tensile properties over their MWCNT counterparts. This is due to the fact that they contain far fewer defects [94]. Figure 35 [95] illustrates the difference between MWCNTs and SWCNTs.

All carbon nanotubes have a tendency to bundle together in ropes due to van der Waals interactions. This is undesirable as bundling reduces the conductive and tensile properties of the tubes. Therefore, work has been done in order to overcome this bundling by dispersing the CNTs in solvents. Many different solvents can be used and in this work, most of the dispersions will be done in *N*-Methyl-2-pyrrolidone (NMP) as described by Giordani et al [96]. This method consists of sonicating CNTs in the solvent using a sonic tip and a sonic bath. The solution is then centrifuged to remove the larger aggregates and bundles and the supernatant is analysed using ultra-violet visible absorption spectroscopy in order to find the concentration of the CNT in the solution. The concentration is found using the Beer-Lambert law, $A = \alpha lc$ where A is the absorbance, α is the absorption coefficient, l is the path-length of the light beam through the sample and c is the initial concentration of the sample. Adapting this law by noting that α is the same in any optically dilute homogenous system, we can find the concentration using the equation $C_{fin} = C_{\text{int}} \frac{A_f / l}{A_i / l}$ where C_{fin} is the final concentration of the solution, C_{int} is the initial concentration, A_f is the absorbance at a given wavelength after the sample has been centrifuged, A_i is the absorbance of the light at the same wavelength before centrifugation and l is the path length of the light through the sample. For CNT dispersions, the measurements are taken at the 660 nm Van Hove peak which is standard procedure for carbon nanotubes. Sedimentation studies also show a good stability of the dispersion for several weeks.

1.1.1 Optical and Electronic Properties of CNTs

A great deal of work has been done studying the electrical conductivity of CNTs. CNTs are 1-dimensional ballistic conductors [97] with very low scattering which gives their high conductance. The electronic structure of CNTs is governed by many parameters including tube diameter, the presence of defects and tube chirality. The chirality of a CNT is based on the way in which a single roll of graphene can be rolled up and is described by a chiral vector, $\mathbf{C}_H = n\mathbf{a}_1 + m\mathbf{a}_2 \equiv (n, m)$, $\mathbf{a}_i$ signifying the unit vectors. This is illustrated in Figure 33[98].

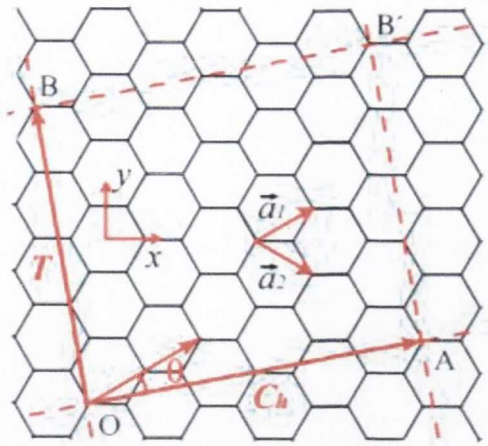

Figure 33: Unrolled Lattice of a Carbon Nanotube [98].

The two components of this vector are given as n and m. Tubes which have $n = m$ i.e. $\mathbf{C}_H = (n, n)$ are known as armchair tubes, those with $C_H = (n, 0)$ are called zigzag tubes and all the other (n, m) tubes are called chiral tubes.

All armchair CNTs have metallic conducting behaviour. Zigzag tubes with $n - m = 3k$ where k is a non-zero integer are semiconducting with a tiny band-gap and so are often classed as metallic. All other tubes are semiconducting with a band-gap that is inversely dependent on their diameter [99].

Generally speaking, there are two thirds semiconducting tubes to one third metallic in any general batch. There are methods of separating the tubes out based on their density as done by Arnold *et al.* [100]. The diameter of the tubes is related to their chirality and the band-gap of semiconducting tubes scales inversely with tube diameter.

Work done on carbon nanotube networks have shown that although perfect nanotubes are extremely conductive, due to their ballistic conductivity and low scattering, the conductivity of the networks can be influenced by several factors including the number of junctions between tubes, the presence of solvents in the network [101] and resistances between the junctions. In some cases, functionalisation of the CNTs can be used to increase their conductivity, which is a path that some of our colleagues in this project are pursuing. The resistance is higher between metallic/semiconducting tubes, than between metallic/metallic or semiconducting/semiconducting tubes [102] because Schottky barriers are formed between them. It has been shown that an increase in the number of connections between tubes causes greater conductivity over larger areas as it increases the number of junctions and paths for the current to flow as well as increasing the chance of a purely metallic tube path being followed by the current.

Silver Nanowires

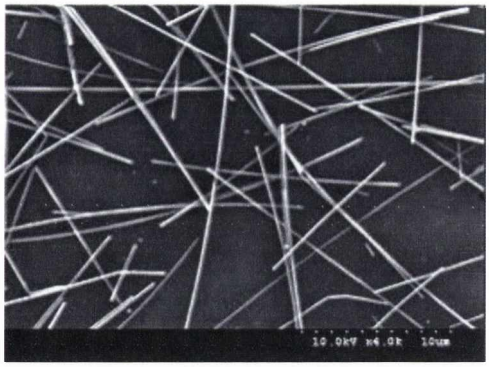

Figure 34. Image from ACS Material of scattered silver nanowires

Silver nanowires unlike organic carbon nanotubes are made of metallic silver. An SEM image is shown in Figure 34 [103]They have average lengths of approximately 6.5 um and diameters of approximately 85 nm [104]. They can be created from either vapour phase or liquid phase approaches. In the vapour phase approach and electron beam is used to grow the wires, but more commonly they are created from liquid phase approaches[105]. This involves growth from a seed in a solvent and growth can be controlled and modified by the rate of injection of the catalyst particles. As with carbon nanotubes they have a tendency to bundle due to Van der Waals effects which lower their electronic and mechanical potential. They are a relatively new material and as such have not been subjected to the same levels of rigorous testing and analysis that carbon nanotubes have. For the work in this thesis, the silver nanowires were bought from Seashell Technologies and arrived dispersed in an aqueous solution with an unknown chemical component, information on which is reserved by the manufacturer. Silver nanowires are not thought to be ballistic conductors and are very strongly influenced by edge effects. It is predicted that conductivity in nanowires would be lower than in a bulk material because of these effects, which become more prominent as the nanowire is scaled down [106]. There is predicted a quantisation of electricity for smaller wires as the electrons have few energy channels to choose from as they pass through the material. However more extensive research is needed on the nanowires to understand exactly the nature of electrical conductivity in them.

Chapter 3 will provide more experimental detail on the processing and preparation of both silver nanowires and carbon nanotubes. They require some special preparation due to bundling effects and it is for this reason that a simple transfer process is so useful. This way materials can be prepared in one place and then potential placed on devices or circuits, eliminating the need to difficult preparation in the region of the device.

2.6 Conclusions

With an overview completed of the physics involved in contacting and fracturing problems completed the stage is now set to apply this knowledge to the system illustrated in Figure 9. Various aspects of contact mechanics have been considered including the definition of adhesion and surface interaction and by describing some of the models developed to describe and predict this behaviour. Although many of the models were designed for linear elastic materials behaving in ideal conditions, experimental studies of them have demonstrated a certain robustness when used in the real world. This combined with the fact that the PDMS elastomer may be considered a linear elastic in the bulk means there is now a framework in place for analysing the bulk behaviour of the materials used in this thesis.

Although there is no full theory of viscoelasticity, modifications to the existing elastic models and consideration of polymer viscoelastic behaviour provides clues as to the correct way to analyse the behaviour of elastomers at the moving crack edge where viscoelasticity tends to manifest itself. This is of great interest as it is the energy dissipation at this moving crack edge which most likely provides the energy of fracture needed to rip a section of nanomaterials from its network.

A brief overview of fracture was provided including descriptions of cavitation and fibrillation. Some experimental work on the fracture of viscoelastic polymer films [63] was described showing how the theory can be applied to a practical inking problem.

The materials for inking in this work have also been introduced. They are of considerable interest due to their superior conductive and mechanical properties and the use of a simple transfer technique as studied in this thesis would be of invaluable help in taking full advantage of their properties.

The next chapter will describe the experimental set-up of the work in this thesis. It will describe material preparation and the use of the nanoindenter. There will also be an overview of the mechanical data measured by the indenter and how it can be interpreted and analysed.

Chapter 3 Experimental Devices & Methods

3.1 Introduction

The concepts outlined in this chapter will become important in the results discussion. An explanation of the mechanical data measured by the nanoindenter will be provided along with an introduction to our interpretation of the data. We also discuss the preparation of the materials used in the experiments including the creation of the PDMS tips and processing of the nanomaterials to create transferrable nanomaterial networks.

3.2 Nanoindenter Structure & Use

The nanoindenter is a device designed to characterize the mechanical properties of small volumes of matter using very sensitive measurements of force and displacement. A typical nanoindenter can measure forces and displacements as small as 0.2 uN and 0.2 nm [107]. Traditionally, measurements are made by prescribing the force on a diamond tip, causing it to be pushed into a material of interest and measuring the resulting displacement. Together with some simple assumptions, parameters such as hardness and Young's Modulus can be found. Our use of the nanoindenter is less conventional: We use it to pick up materials with a soft, sticky tip (henceforth known as *inking* the tip) and to place the same materials down on another substrate (*printing* the materials) while measuring and characterising the mechanical interactions between the tip, the inking materials and the substrate they are resting on. In order to fully understand and explain these processes it is important to understand the workings of the nanoindenter.

Nanoindenter Design and Structure

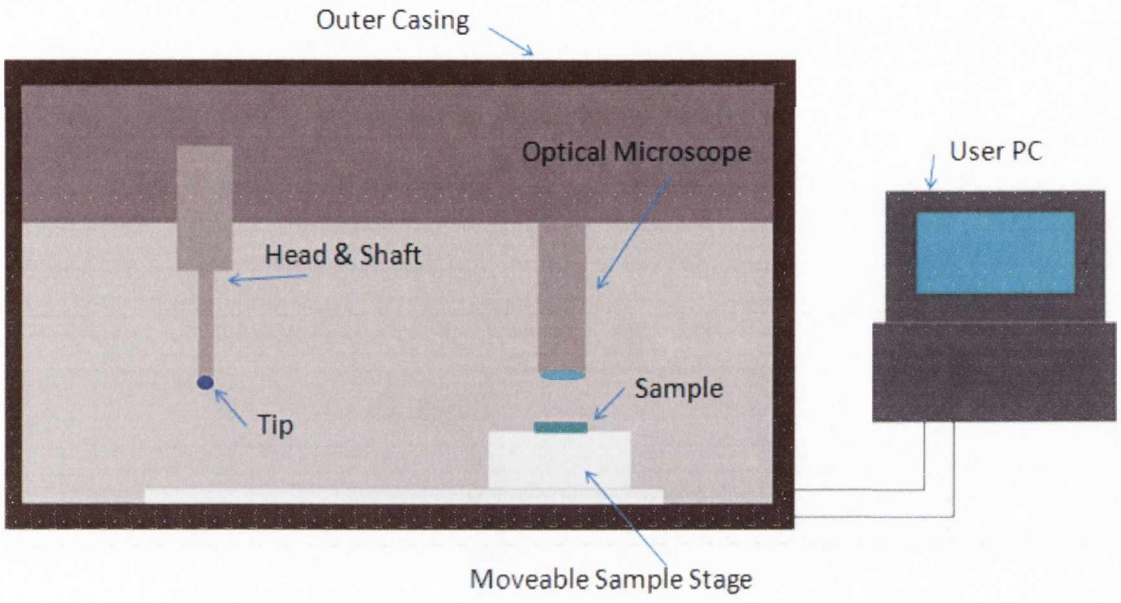

Figure 35. Basic design and layout of Nanoindenter.

The nanoindenter is housed in a casing to protect it from external sources of vibration and noise. The machine is set on a floating table inside this housing so that it is completely isolated from its surroundings. The basic design of the indenter is shown in Figure 35.

The indenter consists of the nanoindenter column onto which the tip is attached. The internal workings of the device are housed inside a cylindrical metal casing. The sample is placed on a stage with a kinematically determinant mounting mechanism which allows for the stage to be taken out and returned so that the sample location will be in precisely the same place. The stage contains metal cylindrical pucks onto which the samples are mounted, usually using crystal bond. These pucks are secured into place on the stage using a screw. In order to avoid crashing the sample into the tip there are guides on the side of the stage showing the optimal height for sample mounting. The stage has a motor which can move it in the x and y directions and so the sample can be driven to a precise location under the tip for the tests. There is also an optical microscope (50X) for use with finding the location on the sample for testing and for calibrating the location of the sample to the tip.

The indenter assembly is controlled by a computer which the user can program methods for conducting experiments. These methods can be written to control the indenter and to measure data channels such as load, harmonic contact stiffness, load on sample, time etc. The methods can also control how the tip approaches the sample, how it makes contact, the rate at which it

loads up, the peak load and the rate of unload. There will be a further discussion on writing and running methods in Section 3.3. The data from the experiments can be analysed using the software provided (Agilent Nanosuite®) or exported for use with other analytical software such as OriginLab® or Matlab®.

The internal structure of the Nanoindenter column is shown in Figure 36.

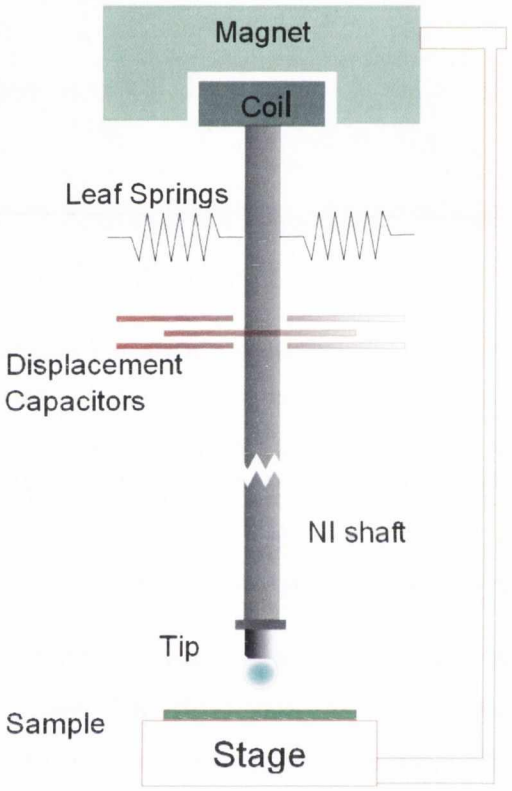

Figure 36. Internal structure of the nanoindenter head and shaft

Electrical current is passed through the coil and this produces an inductive force which can move the shaft in the z-direction. The coil is surrounded by a magnet and the shaft moves in the z-direction and the tip is attached to the end of it. The shaft is connected to a system of leaf springs inside the indenter housing which have a spring constant of 80 N/m. It is also connected to an air-filled parallel plate capacitor which measures the relative displacement of the shaft to its resting position.

The raw data channels such as raw load and raw displacement are measured as voltages which are then digitized. When the tip comes into contact with a sample these raw data channels are used to calculate the Load on Sample and Displacement into Sample channels using formulae

which take the calibration constants, stiffnesses of the leaf springs and frame stiffness into account. Both the load and displacement calibration constants must be found for each individual nanoindenter head and once calibrated will not require recalibration for an extended period of time or unless the head is removed and replaced for repair.

The load calibration is done using known weights which are hung from the indenter mountings. The raw load voltage for each weight in free space is adjusted until the displacement voltage reaches a set value. This is repeated for several different weights. The load voltage versus load has a linear relationship and the calibration constant for the load is found from the slope of this line.

The displacement calibration requires use of Newton's rings interferometry. The nanoindenter is set to move at a constant velocity while attached to the Newton's rings set-up. The motion of the nanoindenter causes a variation in the position of the interference fringes which are then measured with a telescope. The variation in the position of the fringes can be linearly related to the displacement voltage measured by the indenter allowing the displacement calibration constant to be found.

Once the load and displacement calibration constants are found the support spring stiffness can be measured by moving the indenter in free space and measuring the load voltage and corresponding displacement voltage. The support spring stiffness can then be found from these

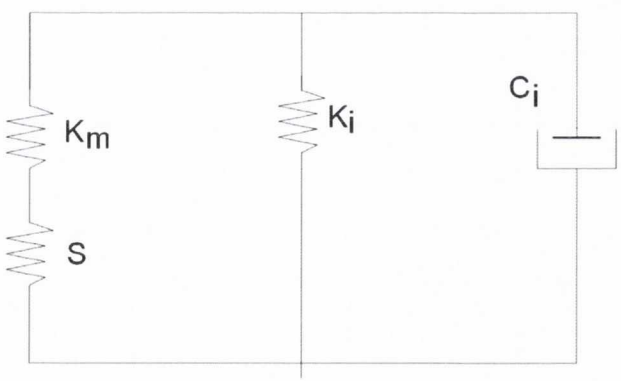

Figure 37. Schematic showing the springs and compliance in the nanoindenter. *S* is the contact stiffness of the sample interaction with the nanoindenter tip. K_m is the spring constant of the indenter head frame and motorised z-drive. K_i is the spring constant of the leaf springs supporting the indenter shaft. C_i is the dampening coefficient of the displacement capacitor.

values using a linear dynamic model.

A schematic of the spring configuration is shown in Figure 37. The leaf springs which shown are designated K_i. These leaf springs support and guide the mass, M which is the mass of the nanoindenter shaft with attached tip. The stiffness due to the rigid head frame and housing of

the indenter is infinite and the stiffness due to the indenter head frame and motorised z-drive is designated K_m. The contact stiffness S is the stiffness of the indenter tip relative to the sample when they are in contact. K_m and S are in parallel with the leaf spring stiffness and so is the displacement capacitance which has a dampening coefficient of C_i. In order to calibrate the support springs stiffnesses indentation experiments are conducted on indium, a material with a well known elastic modulus and Poisson ratio. From these experiments the compliance of the system can be found, which is the inverse of the stiffness. The total compliance of the system, J is given by

Equation 32

$$J = \frac{1}{S_i} = J_f + J_C = J_f + \frac{\pi}{2E^*\sqrt{A}}$$

where S_i is the combined stiffness of the machine and the calibration specimen, J_f is the machine compliance and J_c is the specimen compliance. E^* is the modulus of the specimen and A is the contact area of the tip with the specimen. J_f is found experimentally by conducting a series of indents at different depths and plotting the slope of 1/√A against the measured compliance J. For our indenter the support spring stiffness has been measured to be 80 N/m.

AC Modulation Technique

In principle the nanoindenter should now be ready to use for testing. For deep indents that would certainly be the case, however for more shallow indentation depths or for work with softer or sensitive materials, issues can arise due to thermal drift effects. Thermal drift occurs when the tip and sample are in light contact and tiny movements due to the motion of the machine or the motion of the surface interfaces relative to each other can be recorded by the indenter, thus creating uncertainty in the mechanical curves. In order to overcome this issue a technique was developed known as AC modulation [108]. The use of AC modulation to find the stiffness is extremely sensitive with stiffnesses less than 10 N/m being possible to measure. To put this in context this is sensitive enough to allow the flow of even a few atoms to be found[109].

The other useful application of AC modulation is for the measurement of the stiffness of the sample. The stiffness, $S = \frac{dP}{dD}$ is the slope of the load-displacement curve, however this relation is valid only for the maximum penetration depth. Therefore a different kind of sample stiffness measurement is needed, one that measures the stiffness continuously throughout the experiment. A technique for this is known as *Continuous Stiffness Measurement* or simply CSM.

Again this technique applies a small oscillation on the primary loading signal and then analysis the resultant response. It is extremely useful for films on a substrate where the mechanical properties change with surface penetration and for polymers where the storage and loss moduli are very important. Soft elastomeric materials such as PDMS which is used in this thesis are ideal candidates for use with the CSM.

The basic principle behind AC modulation is to superimpose an oscillatory modulation δP on the quasi-static load, P applied to the indenter and then monitor the amplitude and phase shift of this modulation. The AC Displacement is measured with a lock-in amplifier. A driving force of $F = F_0 \sin \omega t$ is applied. This corresponds to the following equation of motion between the nanoindenter and the nanoindenter head

$$m\ddot{x} + C_i x + kx = F_0 \sin \omega t$$

The solution to this equation is $x = X \sin(\omega t - \varphi)$. X is the amplitude of the displacement oscillation and φ is the phase difference between the displacement and the driving force. The amplitude of the displacement oscillation can then be found from

$$X = \frac{F_0}{\sqrt{(k - m\omega^2)^2 + (C_i \omega^2)}}$$

And the phase angle can be found from

$$\varphi = \tan^{-1} \frac{\omega C_i}{k - m\omega^2}$$

k is the combined spring constant $k = K_i + \frac{1}{\frac{1}{K_m} + \frac{1}{S}}$.

For a sample which is not in contact the contact stiffness $S = 0$ and the values K_i, m and K_m can all be found from the calibration measurements as described previously. Therefore the damping coefficient C_i can be found from the previous equations. Once this is known, the machine can then be calibrated so that the contact stiffness, S can be found when the tip is in contact with a sample. For the CSM the ω value is set and x_O, φ and F_O are measured. This is in contrast to normal oscillation experiments where the spring constant K is fixed and the oscillation frequency ω is measured. When the indenter head is moving in free space the spring constant $K = K_i$. The natural frequency of our nanoindenter head is $\sqrt{K_i/m}$ = 20 Hz.

Figure 38 shows the AC modulation technique schematic. The DC signal is applied to the coil in the indenter head. The output load voltage is passed through a high pass filter which is then passed into the lock-in amplifier.

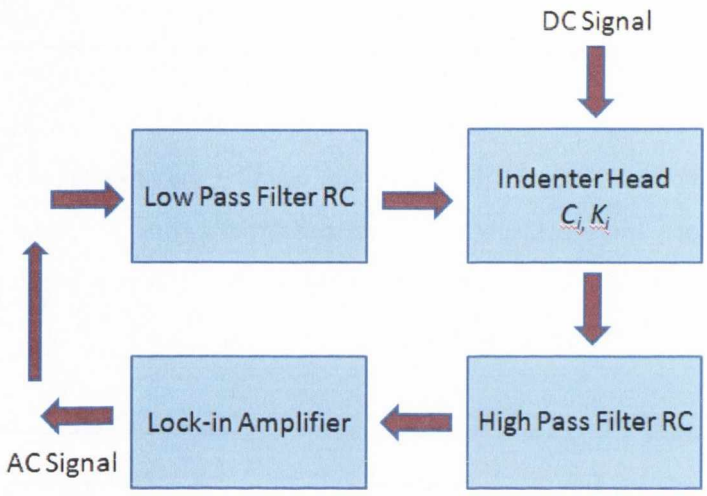

Figure 38. Configuration of AC modulation

A sinusoid AC signal with a known frequency and amplitude is produced by the lock-in amplifier. It is then passed through the low pass filter and onto the coil along with the DC signal. The resultant AC signal is then passed through a high pass filter and is passed back into the lock-in amplifier. This measures the amplitude of the AC signal and the phase difference between the excitation from the source and the resultant signal. In free space, the phase shift is due to the filters and to the damping coefficient, C_i. The damping in the capacitors is usually due to air in the capacitors and C_i varies depending on the position of the middle plate with respect to the fixed parallel outer plates.

Phase Angle Surface Detection

Nanoindentation experiments and calculations are based on knowing the location of the surface of the sample being tested. Many methods using hard nanoindenter tips and/or hard surfaces have a rough surface-find segment whereby the tip is driven to the sample until the stiffness detected becomes twice that of the leaf springs, indicating that the surface has been reached. After this "first touch" the tip will then conduct a more careful surface-find at a driving velocity

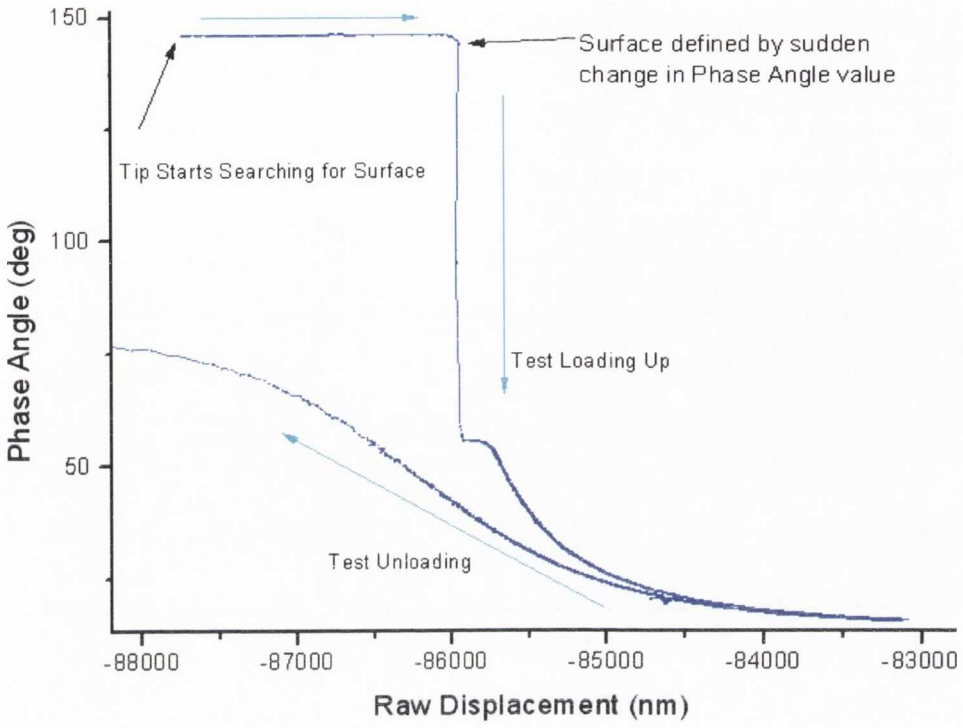

Figure 39. Phase Angle Detect of PDMS tip on SiO_2 surface. When the tip makes contact with the surface its value changes suddenly from the free space value of about 150°.

specified by the user. The initial first touch is generally implemented in nanoindentation systems as an electronic "black box" whereby none of the forces, stiffnesses or displacements are recorded by the indenter. The rough surface-find segment in traditional indenting methods is not suitable for inking experiments however due to the fact that one could have an inking attempt during the surface-find and with the electronic "black box" no mechanical data will be recorded.

Another problem with this rough surface-detect technique is that PDMS tips are very soft and this method is not sensitive enough to detect the initial contact of the tips with the surface. Therefore a more sensitive surface-find must be used which is called *phase angle detection*. This method takes advantage of the AC modulation described above to use a change in the phase angle to detect the surface. The phase angle in free space has very little variation. When a force is detected by the indenter, for example when it comes into contact with something, this phase angle can vary significantly. This is especially useful for soft materials such as PDMS for finding the location of the surface. Although this method gives us a high degree of sensitivity it is doubtful that it is sensitive enough to accurately account for deformation of the PDMS tip itself. There is a distinctive "jump to contact" regime which is shown later in Figure 40. This jump to contact can occur over a distance of up to several hundred nanometres.

Figure 39 shows the phase angle as a function of raw displacement for a single test on SiO_2. As can be seen in this particular test, the phase angle of the tip in free space is an arbitrary 145°. The

jump to contact causes the phase angle to drop rapidly and sharply and the surface is defined as being at the location of this jump as indicated in the figure. In this particular case the surface is defined as being at -85947.5 nm above the zero z-position of the nanoindenter shaft and is used for calculating the load on sample, time on sample and displacement into surface. As can be seen the phase angle drops considerably throughout the whole test.

Using the phase angle detect allows for sensitive location of the surface. In order to avoid inking the tip during the phase angle surface-find, a test is done using a traditional method on a nearby piece of sample where no nano materials are present. This gives an approximate location of the sample and allows us to choose the point at which the tip begins looking for the sample height.

3.3 General Description of Mechanical Tests

Programming the nanoindenter to conduct experiments is done by writing what are known as "methods". A method is like a recipe whereby the user can instruct the indenter on all aspects of how to conduct the test, such as when to tare time, when to establish the tip is in contact, how long to hold for creep and drift effects, how far to push the indenter tip into the sample, what rate to load up or unload the test etc. One can also instruct the indenter the frequency of data acquisition during the test, place segment markers and so forth.

The method used in this thesis work is described and followed by a discussion of the mechanical data measured by the indenter. Interpretation of this data is paramount to our analysis. The mechanical curves are shown and described in detail and a sample data set for PDMS on porous alumina membranes will be explained. Porous alumina is a suitable test material because it is the substrate that the thin (50 – 400 nm thick) nanomaterials are on. Much of the PDMS contact mechanics work done previously is for smooth materials, much smoother than either our alumina or nanomaterials and therefore it is useful to be able to compare the testing method in this thesis with the literature by using smooth materials such as SiO_2 or glass. The difference in mechanical data between the different materials and their significance is outlined in Chapter 4.

Nanoindenter Method

A custom method was developed specifically for the inking tests involving a sensitive phase angle surface-find and high rate of data acquisition. Much of the method was written with the help and expertise of Dr. Erik Herbert of the University of Tennessee, who kindly spent several weeks helping us to refine and improve it. The method can be roughly divided into three separate segments 1) the surface find, 2) load up and peak hold, 3) unload segment. These are described and illustrated in Figure 40 which shows a mechanical data curve demonstrating the change in the Load on Sample as a function of time during the test. Load on Sample is a channel which is calculated by the nanoindenter computer based on the raw data being fed to it from the springs and capacitors. It takes into account the surface height and tares the Load on Sample to zero at that height indicating the beginning of the contact. A similar calculation is done to get the Displacement into Surface and the Time on Sample. Henceforth Load on Sample will simply be

referred to as "Load", Displacement into Surface as "Displacement" and Time on Sample as "Time". Should the raw data channels enter the discussion it will be indicated that they are the raw channels.

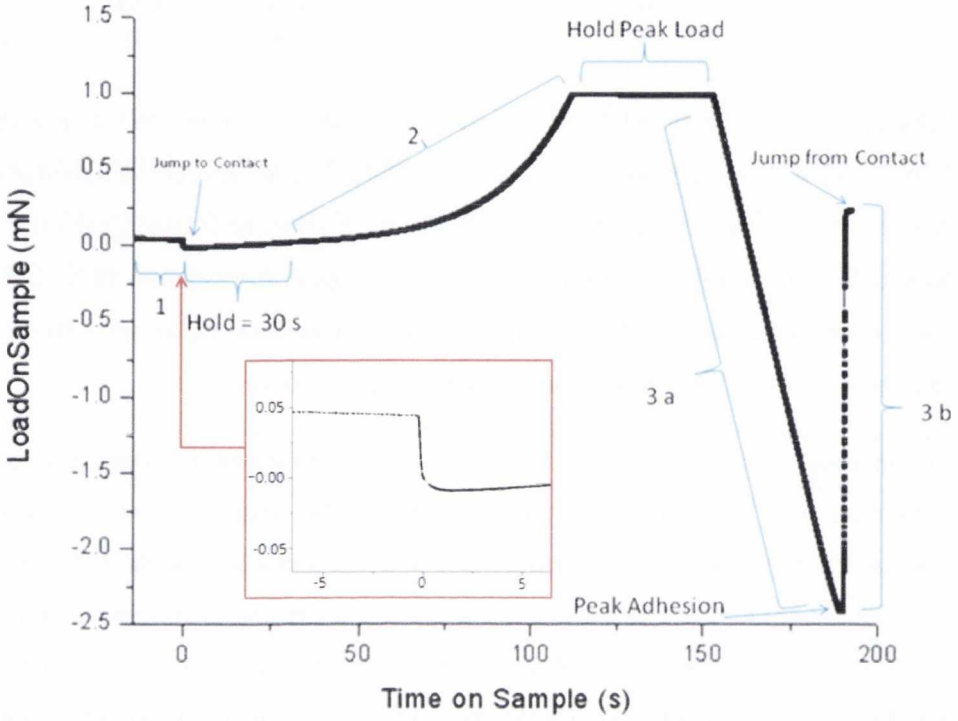

Figure 40. Load on Sample (Load) vs. Time on Sample (Time) for a PDMS tip in contact with a porous alumina membrane. The segments are as follows: (1) Surface-find (2) Load-up and peak hold (3) unload segment. The jumps to and from contact with the surface are also indicated.

The surface-find segment is indicated by (1) on the graph. The load is unchanged (since the tip is not in contact with the sample) during this segment as indicated by the curve being parallel with the x-axis. As indicated in the graph, the tip comes into contact with the surface quite suddenly.

It snaps into contact at what is called the *jump to contact* point. For alumina the jump to contact can measure 100 – 1000 nm in height with a change in load of up to 0.1 mN. The mechanism behind the jump to contact is discussed in Chapters 2 and 4. Once the tip is in contact with the sample, there is a hold period of 30 seconds to allow the CSM to settle. This is necessary because it takes a certain amount of time for the electronics to catch up with the sudden event of contact. 30 seconds was found to be the optimum time to allow the harmonic displacement to settle back to the level which we set at the beginning of the test.

After the initial hold time of 30 seconds, the test is loaded to a specified peak load using a load-up rate also specified by the user. This is followed by a hold at peak load to allow to for creep of the viscoelastic tip. Generally 10-30s hold time is sufficient for our tests. Ideally this hold time would be in the order of hours to allow for full viscoelastic relaxation of the elastomer but this is not practical for our purposes.

The unload rate is again specified by the user and is indicated in the graph by two parts, 3a and 3b. 3a is the unload from peak load to the peak adhesive force. When the load is positive the unload is in the *compressive* region as indicated. Once the load passes through the zero load position it changes sign and is now in the *tensile* or *adhesive* region. This tensile load reaches a maximum value (here of nearly 2.5 mN) which corresponds to the *peak adhesion force* of the test. This is the maximum tensile force experienced between the tip and the sample before it rapidly disengages from the surface. After the peak adhesion has been reached the force changes direction and starts to increase. PDMS exhibits strong deformation during this segment. In this situation the contact area decreases very slowly due to being pinned by viscoelastic resistance to a sudden increase in *v*. The material deforms as it tries to resist the crack edge movement and the PDMS is stretched into a neck as pictured in Figure 41. This image shows a video still of PDMS retracting from contact with alumina. The neck is very clear and will become longer and thinner before popping off the surface. Therefore the unload segment between the peak adhesion force and the jump from contact point will henceforth be referred to as the *rapid deformation unload* segment. This necking behaviour is very typical of materials obeying the JKR theory as outlined in Chapter 2. An essential part of the analysis involves knowing the contact radius throughout the test which will be discussed in the next section where the mechanical data is interpreted in detail.

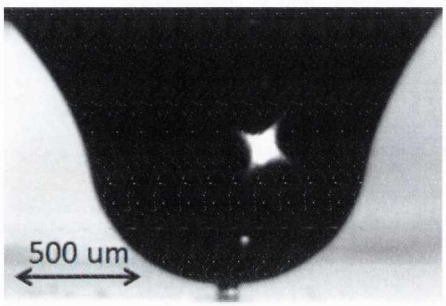

Figure 41. Video still showing the neck formed as PDMS retracts from the substrate.

Mechanical Data Curves

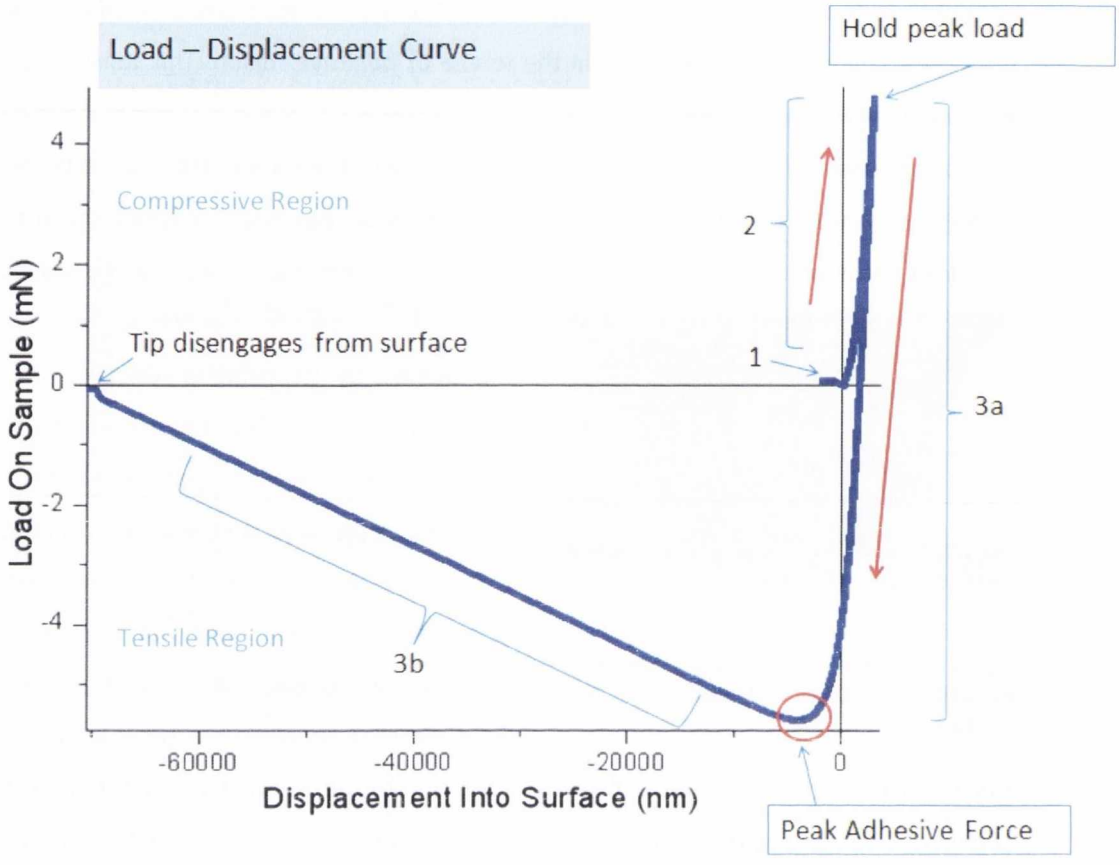

Figure 42. Load-Displacement (L-D) curve for a PDMS tip on Alumina. The red arrows indicate the load and unload directions.

Figure 42 shows a typical Load-Displacement curve for a test on alumina. The segments are numbered as in Figure 40 and the red arrows show the load and unload directions. In traditional nanoindentation experiments a hard tip is pushed into a surface and so the displacement refers to the distance that the tip pushes into the substrate. With the soft PDMS tips however the displacement refers to the distance the PDMS is deformed during the test and so it would be more accurate to refer to it as Displacement into Tip rather than surface. The compressive and tensile (adhesive) regions are indicated.

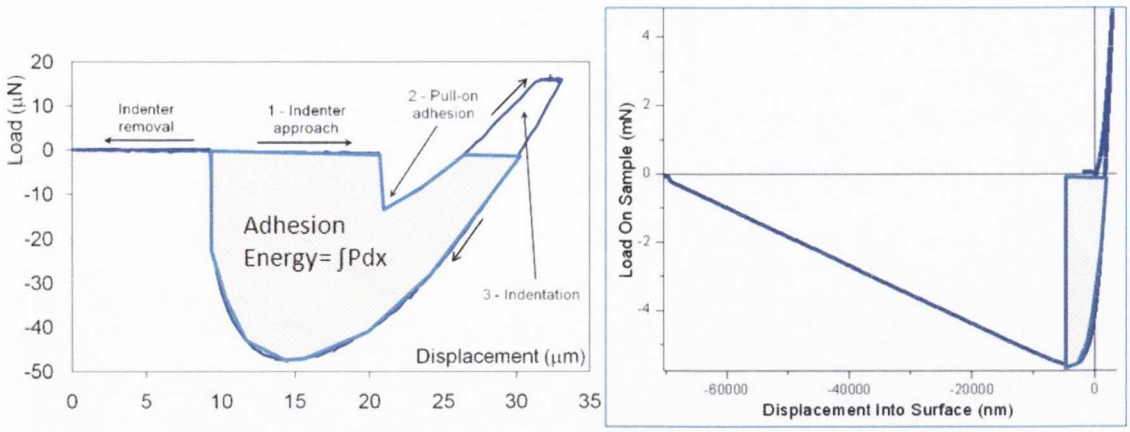

Figure 43. Comparison of a traditional L-D curve [76] with one of our experimental curves. In the traditional curve the unload after the peak adhesion is rounded as the nanoindenter has time to record the relaxation of the material as the tip disengages from it. In contrast our experimental work unloads too rapidly during this segment giving a straight line. This means that unlike the traditional curve, only the area before the peak unload can be used to calculate the adhesion energy.

An important use of the load-displacement curve involves calculating the *adhesion energy* in the test. For this the area under the x-axis is found by taking the integral of this region as illustrated in Figure 43(a). As mentioned previously a problem experienced during the rapid deformation unload segment of the test (3b in the figure) is that the nanoindenter is unable to record good data for this segment as it occurs too quickly. This creates difficulty in calculating the adhesion energy and so the only option is to use the area of the curve before the peak adhesion is reached as illustrated in Figure 51(b). This provides a crude way of comparing the adhesion energies between materials without knowing the absolute values.

Another way in to analyse data is to use the harmonic contact stiffness (S) vs. load on sample curve. Sneddon's equation for elastic materials [75] relates the stiffness to the contact area

Equation 33

$$S = \frac{2E^*\sqrt{A}}{\sqrt{\pi}}$$

where the reduced modulus is $E^* = \frac{1-\nu^2}{E}$ and A is the area of the contact. This means that for an elastic material the stiffness and contact radius a have the relation

$$S \sim a$$

As discussed in Chapter 2 PDMS behaves like an elastic material in the bulk. This means that the viscoelastic properties manifest themselves only at the point of strong deformation such as at a crack edge. For this reason Sneddon can be used as an approximation of the contact radius throughout most of the test by measuring the stiffness curve. Figure 44 shows the Stiffness vs. Load for a test on alumina.

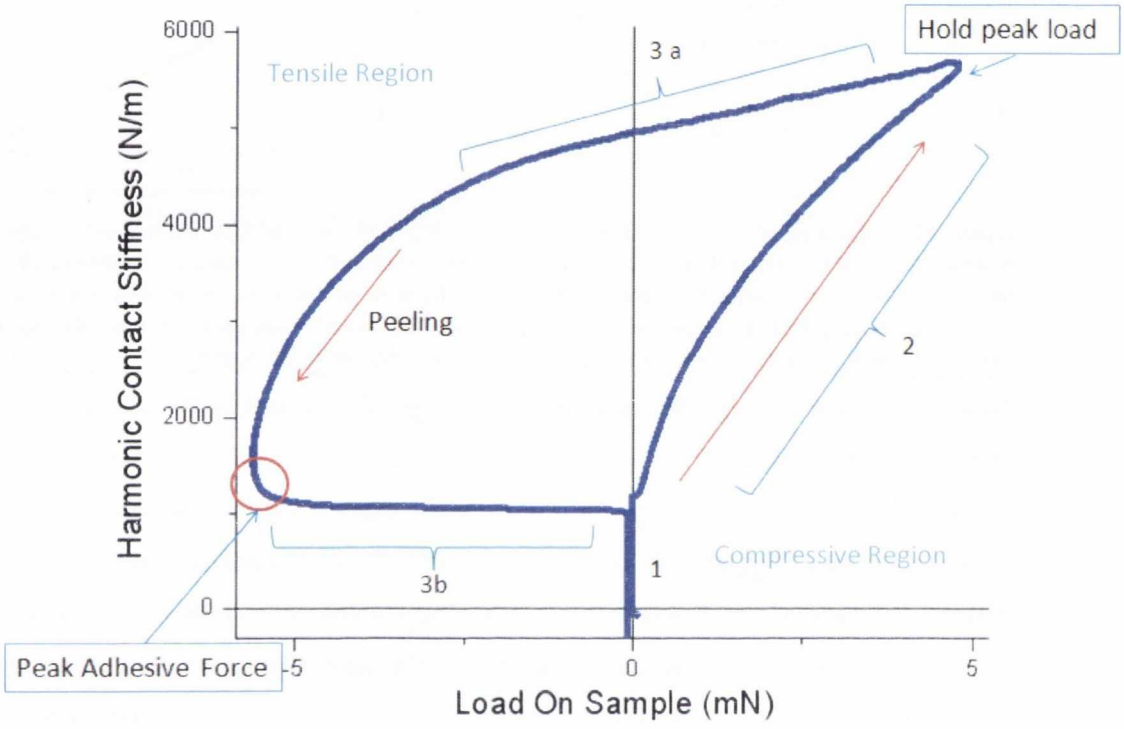

Figure 44. Stiffness-Load (S-L) curve on Alumina corresponding to the L-D curve in Figure 6.

Again the hysteresis between load and unload are very evident in this curve. The shape of the curve in the different segments can provide information about how crack is receding and advancing. In the load-up region (2) the data is quite linear indicating a linear increase in contact area as the load is increased. When the tip begins to unload it is again quite linear though at a different rate than for the load. This is seen in cases also where the load and unload rates are set to the same values . In this particular case, the unload rate is lower than the load up rate The contact peels linearly as it passes from the compressive to tensile regions with a decreasing slowly. Work done by Doi *et al* [81]measured the contact angle during the unload of a PDMS sphere. This experiment is described in more detail in Chapters 2 and 4 but the contact angle result showed that while the contact radius was decreasing slowly, the contact decreased rapidly until it was at 90°. As the test entered the tensile region the contact radius (stiffness) decreases more rapidly as indicated in Figure 44 but the contact angle stops changing and has a value of 90°.

Video Imaging Capability during Nanoindenting Experiments

Although the nanoindenter is unable to accurately measure the stiffness past the peak adhesion point a video camera was able to capture the formation of the neck during this segment (3b). It shows that the contact radius is decreasing reasonably slowly while the PDMS is being deformed indicating that the crack edge is pinned. This is illustrated in Figure 45 and is where viscoelastic effects will appear most prominently in the test. The picture resolution and camera speed is too low for accurate measurement of the contact radius but with better equipment it should be possible to analyse the contact mechanics during this interesting part of the test.

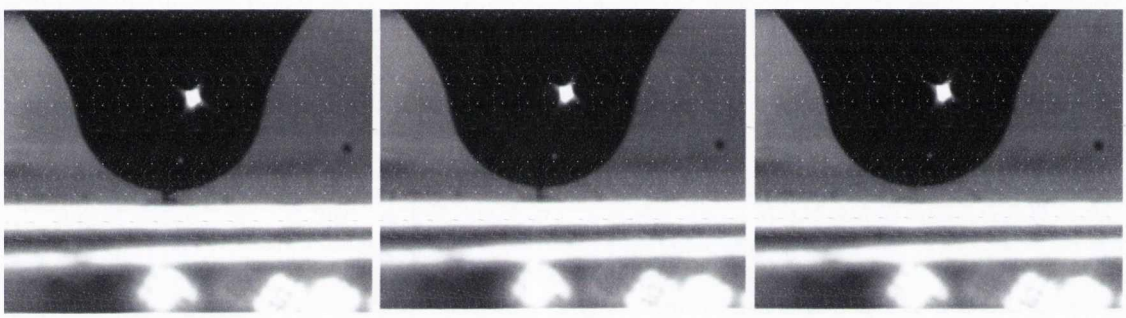

Figure 45. Series of images taken with the video camera showing the neck as the tip disengages from the sample.

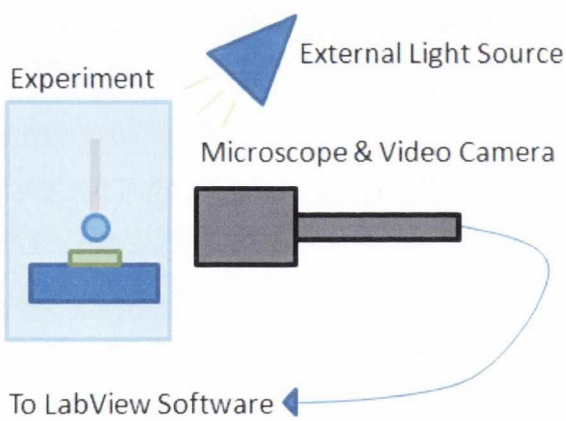

Figure 46. Set up of horizontal microscope and camera relative to sample.

The addition of video capture of the contact experiments provided more insight into the interaction of the PDMS with the various materials being tested. The set-up consists of an optical microscope attached to a video camera on a stand located horizontally from the nanoindenter tip as illustrated in Figure 46.

An external halogen light source is used and the camera is connected to the PC by a coaxial cable and a custom LabView program was written by Prof. John Pethica's group to control the video feed. The video can capture up to 30 frames per second which is rather low but still provides some information about the interaction. As described above and illustrated in Figure 45 information can be gained about the size and geometry of the PDMS when in contact with the various materials. Although we cannot measure absolute dimensions of the tip using this method

we can extrapolate what they are from information about the maximum contact area of the tip on the materials. A program was written by Diego Lionello in our research group which allows us to find the time-stamp of each image within a microsecond scale which can then be matched to the times on the mechanical data. This technique is quite inaccurate at this point as taring the video and nanoindenter is done by hand but it helps piece together a picture of the interaction. For example it is difficult to observe the PDMS necking on smoother materials such as SiO_2 compared to alumina.

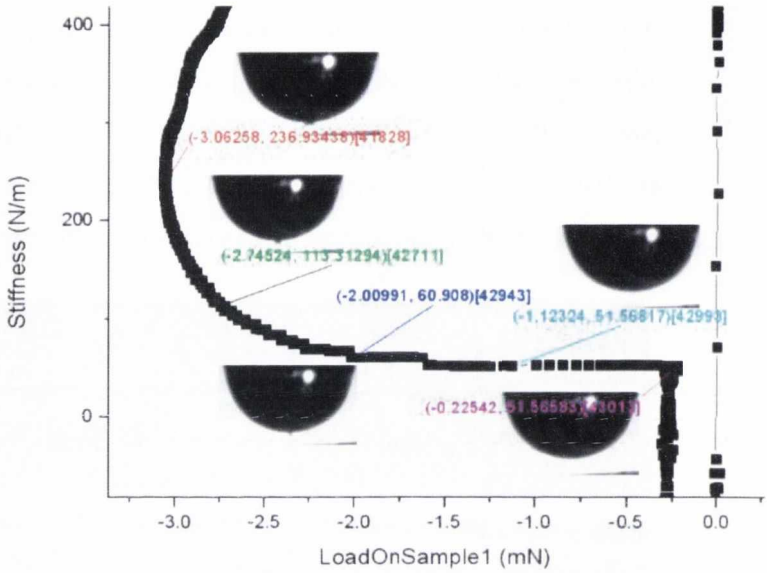

Figure 47. S-L curve showing how the necking of the PDMS can be correlated to the stiffness data during the unload.

Figure 47 shows an example of how the necking events captured by the video could be correlated to the stiffness data during a test. At this point the video and nanoindenter are tared visually by the user and so the correlation is somewhat inaccurate but it is apparent that in the region of the peak adhesion the neck is already well formed. The narrowing of the neck during the final unload segment occurs rapidly until the tip is no longer in contact with the surface. Very rough estimates can be made of the width of neck but the picture resolution is very low. At this time the neck has been measured as having anywhere from 45 – 4 um radius. With better video equipment, picture resolution and superior taring it will be possible to analyse this interesting region where the viscoelasticity is extremely dominant.

3.4 Stiffness and Contact Radius Correlation

Figure 48. PDMS *contact impression* due to excess cross-linker on alumina. This provides a measurement of the contact radius a_{max} at peak load.

Most contact mechanics experiments have some way of imaging the contact area throughout the test usually by placing a camera underneath a transparent sample. Our analysis is

unique because it is not possible to accurately measure the contact area. Therefore Sneddon's equation is used to correlate the stiffness and contact area as described above. In order to successfully do this however it is necessary to accurately measure the contact area at some point during the test. As mentioned in Chapter 2, PDMS rubber is created from liquid PDMS which has been cross-linked. In our experimental set-up we do not rinse any excess cross-linker from the tips and have discovered that when they are in contact with rough materials such as alumina, some of the cross-linker is left behind on the surface as shown in Figure 48. We call this excess cross-linker impression the *contact impression* and measuring its radius gives us the contact area at the peak load of the test. This is the maximum value of the contact a_{max} during the test. The contact impression is usually only visible on rough materials such as alumina and is generally absent on smooth materials such as glass and SiO_2.

Kink in Data at S = 6000 N/m

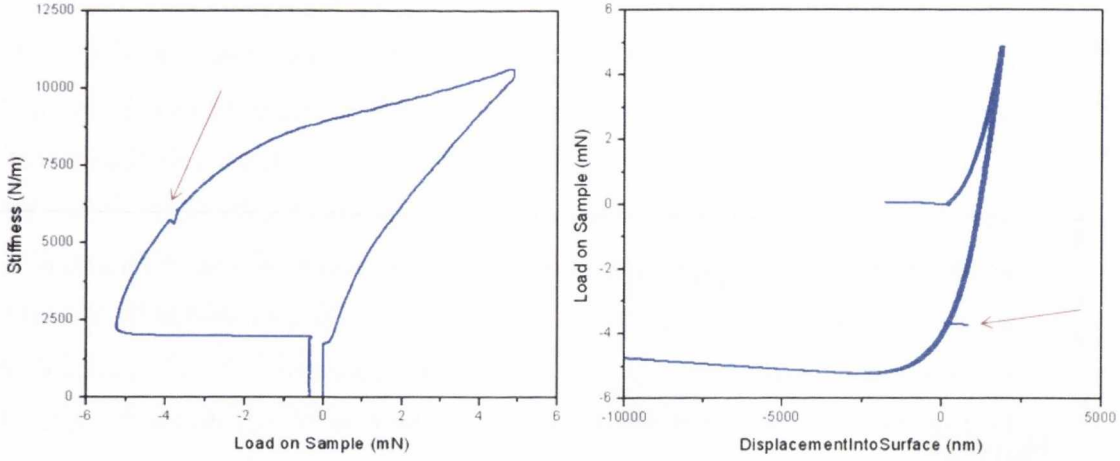

Figure 49. S-L and L-D curves showing a feature which often appears in the data. It is always at a value of just over 6000 N/m on the stiffness channel and is also apparent in the load data. At this point it is unknown what causes it. Notice how in the left-hand figure the Load does not return to 0 after the unload but to a value of approximately -0.4 mN. This is in contrast to an ideal curve as is shown in Figure 39 where the Load returns to a value of zero. At this time it is unknown exactly why this occurs. A correctly calibrated machine should the load to a value of zero. It is most likely there is a discrepancy in the way the load is being recalculated post-test and will require further investigation to rectify.

Before continuing the discussion of the mechanical data, a feature which appears very commonly during the tests should be discussed. It is most apparent in the stiffness data but is also visible in the load data. Figure 49 shows an S-L and L-D curve where the kink is quite apparent. It can appear in tests for any material and for any PDMS thickness. It can appear in both the compressive and adhesive regimes and the only feature that seems to be consistent about it is that it appears for a stiffness value of approximately 6000 N/m. This would suggest that it is a

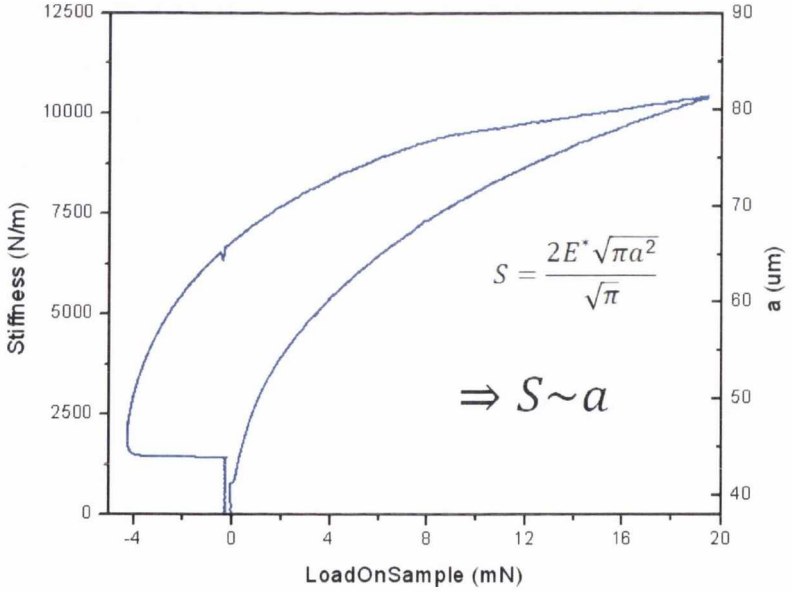

glitch in either the electronics or the inner workings of the indenter. At this point it is unknown what causes it and so it shall not be discussed in most of this thesis.

Figure 50 shows an S-L curve for a test on alumina. Sneddon's equation is used as described in above to find the contact radius a throughout the test. As can be seen the minimum contact radius calculated is 40 um in this case. The reasons for this will be discussed in detail in Chapter 4.

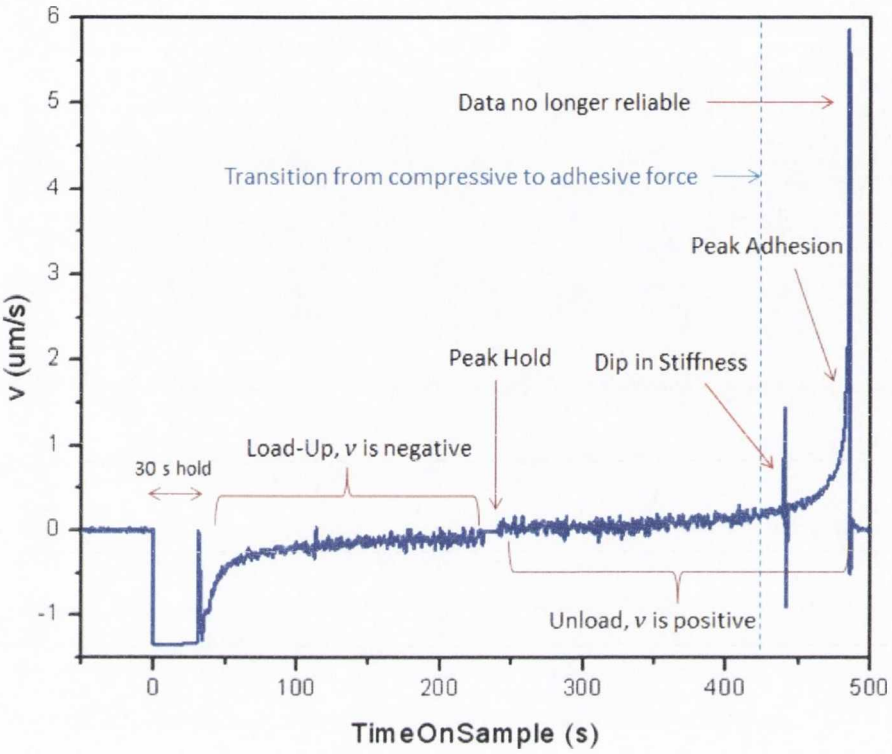

Figure 51. Crack velocity calculated from the time derivative of a. Each of the test segments are indicated and the blue dotted line separates the compressive and tensile regions.

Once the contact radius is known the *crack velocity* v can be found from $v = \frac{da}{dt}$. This is shown vs. time in Figure 51.

Each of the test segments is indicated on the graph. During the load segment the velocity has negative values which switch to positive values for the unload segment. The kink at 6000 N/m apparent in Figure 51 is highlighted and is called a "dip". The peak adhesion point is indicated and beyond that point the velocity increases rapidly, often to infinity. This is because the nanoindenter is no longer recording the data correctly during this deformed unload segment. As can be seen from the graph v increases very slowly from the initiation of the unload until well into the tensile region. The vertical dotted line on the graph shows were the test transitions from the compressive to tensile regions. As the peak adhesion is approached v increases rapidly and the data is reliable until after the peak adhesion point.

As discussed in Chapter 2 the energy release rate for a spherical contact with elastomers can be found from the JKR formulation. The equation used is [63]

Equation 34

$$G = \frac{(P' - P)^2}{6\pi K a^3}$$

where P' is the Hertz force found from $P' = \frac{Ka^3}{R}$ where K is an elastic constant and R is the indenting sphere radius. An additional finite size correction factor is necessary to account for the fact that the PDMS is a thin layer coating the sphere [59]

Equation 35

$$fG_P\left(\frac{a}{h}\right) = \left(\frac{0.56 + 1.5\left(\frac{a}{h}\right) + 3\left(\frac{a}{h}\right)^3}{\left(0.75 + \left(\frac{a}{h}\right) + \left(\frac{a}{h}\right)^3\right)^2}\right)$$

where h is the thickness of the PDMS sphere. The final version of the JKR energy release rate is then given by

Equation 36

$$G = \frac{(P' - P)^2}{6\pi K a^3} fG_P\left(\frac{a}{h}\right)$$

For the inking test being analysed here $h \approx 20$ um. This thickness can be found by indenting the tip after testing with a cube corner and measuring the distance over which the phase angle changes during the tip. Alternatively it can be measured optically using a microscope.

Figure 52 shows the energy release rate G calculated from Equation 36. It is plotted against time. Also shown is what values G would have had the finite size correction not been included. What is immediately apparent is that without the correction G would be an order of magnitude larger during the test. What is also striking is the distribution of the values of G. In the compressive region where the test has been loaded to its peak load the G values are much larger than elsewhere in the test, including at the peak adhesion where v has become larger than anywhere else. It is apparent that the finite-size correction is very important for the analysis of these tests using the JKR.

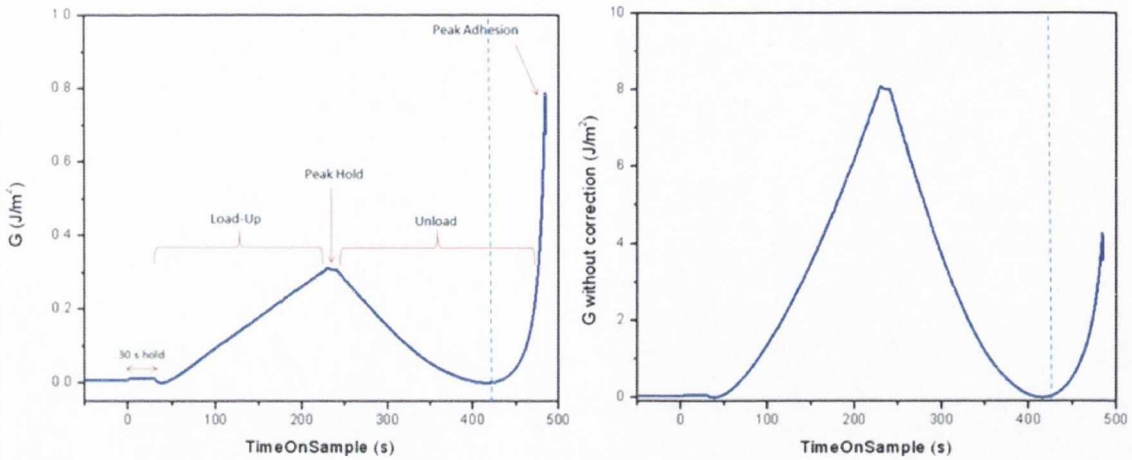

Figure 52. The energy release rate G with the finite-size correction factor (a) and without (b). Also shown are the test segments in (a). The vertical dotted line indicates that point where the test passes from compressive to tensile.

The vertical dotted line show where the tests pass from the compressive to the tensile regions. As can be seen the value of G drops to zero at this point and then starts to increase rapidly. The vast majority of inking events discussed in this thesis occur in the tensile region and being able to analyse G and v in this portion of the test is the most relevant. This is also where the largest deformation of the PDMS begins to occur and therefore the most significant viscoelastic effects. As was discussed in Chapter 2 for a viscoelastic material the energy release rate can be related to the crack velocity by the equation [38]

Equation 37

$$G = G_0(1 + \left(\frac{v}{v^*}\right))^n$$

It should therefore possible to find out values for G_0 and v^* by fitting the G vs. v to this equation. This will be discussed in more detail in the results chapters.

Displacement Data

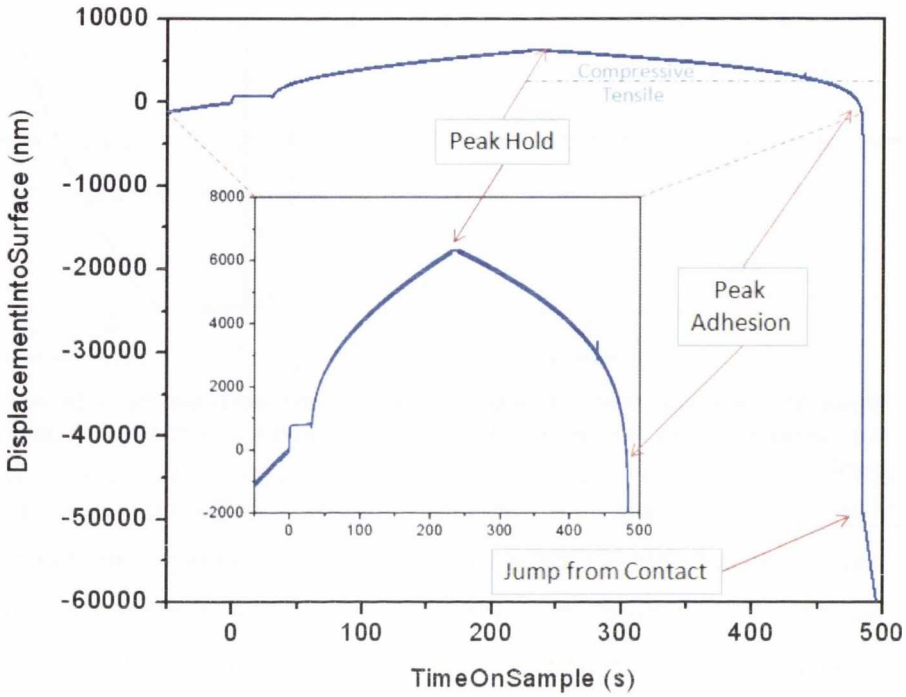

Figure 54. Displacement vs. Time for a 20 mN load test on alumina. The inset shows the data without the deformation region. The compression and tensile regions are separated by the blue dotted line.

It can also be useful to examine data based on the displacement into surface channel. Examining the displacement can provide information about how much the PDMS deforms during the test, either by being compressed on the load segment or "stretched" out in the tensile region. The load-displacement curve has been described previously. Figure 54 shows the Displacement-Time curve for a test done on alumina whereby the peak load had a value of 20 mN. The inset shows the same data but without the rapid deformation segment. An important consideration regards the transition from the compressive to the tensile regions. These regions concern the change of sign of the *load* data, **not** the displacement data. Therefore the transition will not be at D = 0 but is as in this case at D = 3 um as is shown by the dotted blue line. This demonstrates the inherent hysteresis in the system and should always be considered when analysing the displacement data.

3.5 Experimental Materials Preparation

Tip Preparation Method

Tips were prepared by using crystal bond to attach 1 mm diameter silicon spheres to nanoindenter mounts. PDMS was then spin coated onto the tips using a spin coater and the thickness of the PDMS was controlled by the maximum spin speed. For 20 um thick PDMS layers a spin speed of 2000 rpm was used. A schematic cross-section of the tip configuration is shown in Figure 55. The Si spheres have a near lithographic grade polish (~2 nm roughness) and were bought from the Silicon Ball Corp. TX, USA.

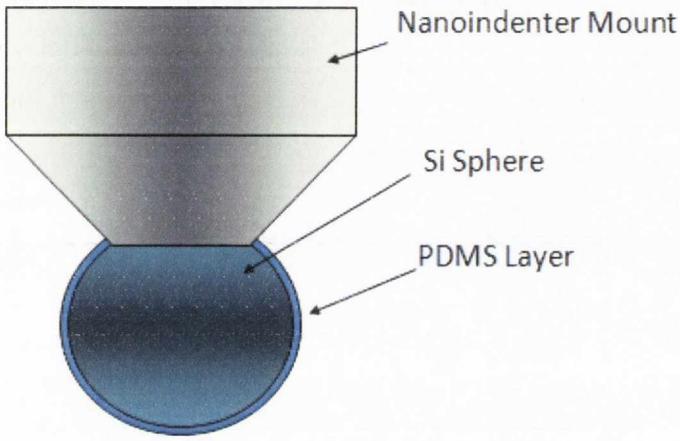

Figure 55. Schematic showing a cross-section of a PDMS tip used in the nanoindenter.

PDMS Preparation

The polydimethoylsiloxane (PDMS) used in this work is Sylgard 184 from Dow Corning. It consists of a silicone based elastomer and a cross-linker curing agent (Sylgard 184b) which is a photosensitive silicone resin solution containing dimethyl and methylhydrogen siloxanes as described by the manufacturers. Mixing the two components cross-links the material which can then be cured to a solid form using heat or time.

The manufacturer's recommendation of mixing 10 parts elastomer to 1 part curing agent was used in this work. The proportions can be measured either by weighing or by using disposable pipettes. Glassware is not recommended for use as the elastomer can be difficult to remove being resistant to normal solvents. Chloroform is the best way to remove the elastomer from surfaces. Once the cross-linker has been added the substances are mixed thoroughly. This step cannot be emphasised enough. Insufficient mixing means that the elastomer will not cure properly and will always remain in a semi-liquid state instead of turning into a rubber. The mixture should be mixed by hand for at least 5 minutes until the mixture is white and foamy. The mixture is then placed in a vacuum oven and degassed for 30 mins to remove air bubbles and to enhance mixing further. After degassing the PDMS is ready for spin coating.

A small drop of the PDMS mixture is dropped onto the Si sphere and spinning commences. For a PDMS layer thickness of 20 um the tips are spun at 2000 rpm. Further in this thesis we describe experiments done with different tip thicknesses which are varied by changing the rpm. Once the spin cycle has ended the tips are placed in an oven at 100°C for 45 minutes to cure the PDMS.

Once the tips are cured they are ready for use in the indenter. Generally we make up a set of several tips at the same time which we term a *fabrication family* of tips. There can be large variations between families based on the mixing, inconsistencies in the exact amount of curing agent added as well as environmental factors which are not accounted for such as ambient temperature and humidity. Generally it is found that a family of tips will display very similar characteristics in the mechanical tests and show good consistency between them. Tips have been found to be useful for inking experiments for up to a month after curing. They do appear to become less adhesive as time passes however and certainly become noticeably harder and less compliant as well as feeling less "sticky" to the touch.

3.6 Mounting Samples

The usual method for mounting samples for use in nanoindentation experiments is to use crystal bond, a heat-based wafer mounting adhesive. The advantage of this material is that when cooled, there is no elastic "give" with the material, and therefore any elastic response seen in the experiments is due to the sample. Crystal bond takes the form of a resinous, hard stick which when heated melts into a liquid. It is applied to a heated nanoindenter stub (at about 70°C) and the material to be tested is placed on top of it and pressed into place. The stub is then cooled and the crystal bond solidifies. The crystal bond used in this thesis work is purchased from Electron Microscopy Science®.

Using crystal bond with alumina is somewhat challenging as alumina is a porous material. This means the crystal bond can flow through the pores then covering the top side of the sample. This is undesirable as it changes the alumina interface and will also destroy any nanomaterials on top of the alumina. Experimentation with various different ways of mounting the sample had limited success. One method was to use crystal bond only on the outside edges of the alumina and try to adhere the alumina tightly to it like a drum. However when the crystal bond cools there appears to be some shifting of the material and the tautness of the alumina cannot be maintained. This introduces give in the material, like a drum that has not been stretched tightly enough. Experiments done of alumina samples which appeared to be well adhered in this way were found

to be useless because as higher loads were reached it could be seen very clearly in the mechanical signature that the alumina was not rigidly attached to the stub.

The solution to this problem has been to heat crystal bond on a glass slide at a much lower temperature (around 30 degrees) until is just starting to feel tacky to the touch. At this point, it is sticky but does not flow as a liquid. Once it is slightly tacky, it is possible to mount the alumina to it without the crystal bond being viscous enough to flow through the pores. This has worked out to be a very satisfactory solution for mounting the alumina samples.

3.7 Preparation of Nano-network Films

As previously explained in Chapter 2 on the theory of the nanomaterials silver nanowires and carbon nanotubes have a tendency to aggregate which means they must be dispersed in a solvent before the nano network films can be created. The procedure for doing this is similar for both materials and so the silver nanowire dispersion is discussed first followed by an explanation of the slight differences for the carbon nanotubes.

Ag Nanowire Film Creation

Silver nanowires (AgNW) were bought in an isopropanol (IPA) solution from Seashell Technology Inc. Although the solution is IPA-based the exact components have not been specified by the manufacturer. The nanowires range in length from 4.1 to 17.2 um and have diameters of 55 to 105 nm according to the manufacturer. They have a tendency to bundle due to van der Waals interactions but are easily dispersed using sonication in water and surfactants.

A summary of the sample creation is as follows:

a. Dispersion in a solvent
b. Filtration onto alumina membranes

The NWs are further diluted in Millipore water using an initial solution of 10 mg/ml diluted to 0.001 mg/ml. Once mixed, this solution is sonicated using a Branson MT 1510 sonic bath for up to 20 minutes to reduce bundling. Further details of this method can be found in Coleman *et al* [104] Estimating the thickness of completed films can be challenging as they are quite rough, making profilometry measurements difficult. The way in which the thickness of the film can be chosen is based on the volume of dispersion used in the filtration. For example 0.1 mg of nanowires creates a film of roughly 100 nm, therefore the volume of dispersion used is based on this relation. Once the films have been filtered and transferred onto transparent substrates such as PET, transmission

measurements can be done on them to get a more accurate estimation of the thickness. This can be done using a transmittance spectrometer and applying the formula for transmittance

Equation 38

$$T = {}^{I}/_{I_0} = e^{-\alpha z}$$

where I is the intensity of the transmitted light, I_0 is the intensity of the incident light, α is the absorption coefficient of the material which has been found from experiment [96] and z is the distance the light travels through the medium.

Once the sonication step is complete the dispersion is ready for filtration onto porous alumina membranes. The reason for using the alumina membranes rather than Teflon or cellulose is that the nanomaterial films have low adhesion to the alumina [2] thus allowing them to be removed relatively easily from the membranes. One can quite easily remove them by rubbing them with a finger.

Filtration of Nanomaterial Films

The AgNW films are filtered onto 20 nm pore-size alumina (Whatman ®, Anodisc™) membranes using a Buchner Funnel as schematically conveyed in Figure 56. Although this figure shows CNTs in NMP as the dispersion, it is exactly the same technique as for the nanowires.

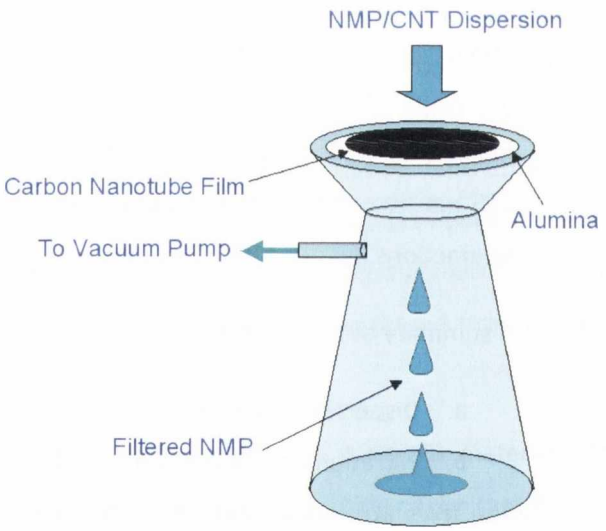

Figure 56. Buchnar funnel filtration set-up of nanomaterial films

Alumina membranes are brittle when dry and so it is important to wet them adequately in solvent before trying to filter onto them so that the pressure of the Buchner funnel doesn't fracture them. Once the vacuum pump is on, the solution is poured on top of the membrane and the solvent is drawn through the membrane leaving a nanowire or nanotube network resting on the alumina. Although rinsing with acetone and water is recommended in the literature to remove excess solvent, this is not recommended for the CNT films on alumina as they tend to break up and float up off the alumina. We therefore place them in a heated vacuum oven for 24 hours to try and evaporate as much excess solvent as possible.

Once the films are ready they are carefully broken into fragments for mounting in the indenter.

Creation of CNT films

Carbon nanotubes (CNTs) also have a tendency to aggregate limiting their exceptional tensile and electric properties. It is not possible to disperse them in water only however they can be dispersed in a surfactant-water combination or in organic solvents. The solvent used in our work is *N*-Methyl-2-pyrrolidone (NMP). This is a polar solvent which binds to the nanotubes overcoming their van der Waals attractions to one another. The purity of the NMP is very important as the introduction of any water into the solution causes the CNTs to fall out of the solvent. Starting with a concentration of 0.5mg/ml of CNT/NMP and sonicating using a high powered ultrasonic tip processor (GEX600) disperses the nanotubes. This is followed by sonication in a bath and then centrifugation to remove the larger bundles. A spectrum is taken of the supernatant using a Cary 1600 series UV-Vis spectrometer. The concentration of the solution can be found using the equation [96]

Equation 39

$$C_{fin} = C_{\text{int}} \frac{A_f / l}{A_i / l}.$$

Typically the concentration is found to be between 0.1 and 0.2 mg/ml. Previous tests on thicker films have shown that 0.6 mg of CNTs corresponds to a 1 μm thick film. Using this information and the definition of the concentration as $C = m/V$, where m is the mass of CNTs used and V is the volume of the solution, we can estimate the thickness of the filtered film we wish to create. Thickness measurements of CNT films are challenging and although AFM step-height measurements seem to agree with this simple calculation, transmission measurements of the films on PET using spectroscopy seem to suggest that the films are a little thinner than estimated using the volume.

The CNT dispersion is filtered in exactly the same way as the silver nanowires. Once the films are dry they are ready for mounting with crystal bond.

3.8 Conclusion

The aim of this chapter was to introduce the reader to nanoindentation techniques and interpretation of the data. There is a wealth of information which can be gleaned from examining

the mechanical channels such as the load, the displacement and the stiffness and how they relate to other mechanical channels. In doing so it is possible to build a picture of the interactions of the tip and the surface in a regime where optical measurements maybe not be possible, either because of the materials involved for because the scale on which the interaction is occurring. Nanoindentation techniques provide a powerful method for understanding the physical and chemical effects of material interactions and the reorganisation of surfaces under conditions of stress and strain. The work done for this thesis provide a novel format for use in the nanoindenter and often pushes the limits of what the machine can do. The nanoindenter has provided copious amount of information on the materials during contact, inking and printing which will be discussed in the next few chapters. Finally an overview of the materials preparation and processing was provided in the discussion.

Chapter 4 Contact Mechanics and Adhesion Studies on Alumina

4.1 Introduction

The transfer problem discussed in this thesis involves a porous nanomaterial residing on a rough ceramic substrate. In order to fully understand and appreciate the mechanics behind transfer we examine the fundamental contact of our PDMS transfer stamp with the substrate in the absence of any third-body for transfer. It supplies insight into the underlying mechanical mechanisms of stamp operation which are necessary to understand the more complicated transfer interactions. By applying the methods and interpretations described in Chapter 3 to specific materials an understanding can be developed as to how the PDMS stamps interact when different experimental conditions are imposed upon the interface.

The main surface studied in this chapter is porous alumina which comes as a thin filter membrane. This form is of great importance as it is the substrate the nanowire and carbon nanotube networks are prepared on. The membranes are rigid ceramic materials with randomly distributed pores of 20 to 200 nm diameter, making them rough surfaces. Silicon (with a native oxide) is also briefly examined which provides a contrasting smooth and continuous surface, allowing for a topologically distinct comparison of contact interaction with PDMS. As well as examining varying experimental conditions on the different materials, the tip geometry itself was also modified by varying the thickness of the PDMS layer and is discussed in this chapter.

4.2 Measuring the Contact Radius

Contact Impression

In order to understand the contact mechanics and the dynamics of the tip-material interface, knowledge of the contact radius throughout the test is needed. Knowing how the contact area is changing with respect to time, load and displacement provides information on the tip crack propagation speed, the deformation of the PDMS during testing and allows us to apply models such as the JKR theory to our test results. Most contact mechanics experiments have the ability to measure the contact radius optically throughout the test using a camera. Many of the tests use transparent materials with a camera underneath the sample allowing for a very accurate

measurement of the contact area. For various logistical reasons this approach has not yet been possible using our set-up at this time.

Therefore we have had to devise an alternative way of measuring the contact radius throughout the test. One way of doing this is to use the *contact impression* due to excess-crosslinker from the PDMS tip as outlined in Chapter 3. The contact impression is particularly useful for analysis of tests on alumina because a high resolution image of it always appears on the alumina.

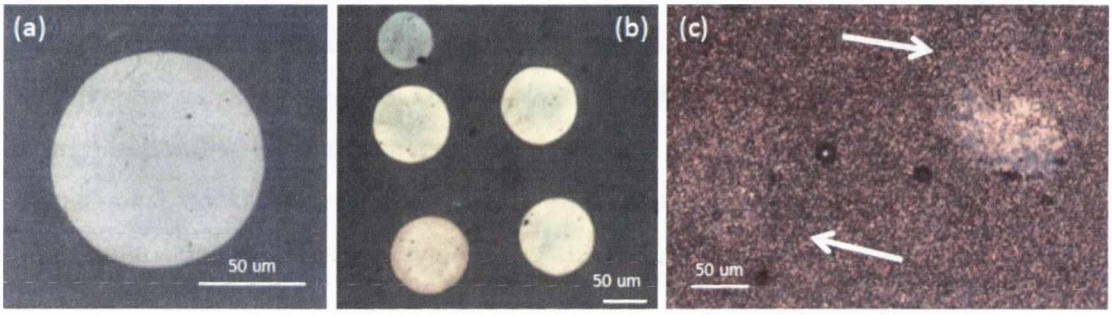

Figure 57. Images showing residual cross-linker (contact impression) left by the spherical PDMS stamp on (a) porous alumina (b) CNT network film and (c) AgNW film. Notice how distinct the impression is for (a) and (b) in contrast with (c). The white arrows indicate the contact impression on the AgNW film.

Figure 57 (a) shows an example of the contact impression on alumina. This excess crosslinker is not visible on other materials however and generally is only visible on alumina, carbon nanotube films and sometimes on silver nanowire films. It has very occasionally been visible on glass and SiO_2 but these instances are rare. Figure 57(b) shows the contact impression on carbon nanotube film and (c) shows it on a silver nanowire film. Whereas the contact impressions on alumina and carbon nanotubes are very distinct with sharp edges, the image on the silver nanowires is fuzzy and more difficult to see. As has been discussed in previous chapters the contact impression gives an absolute value of the contact radius at peak load of a test and can be correlated to the stiffness data to provide the contact radius throughout the test using Sneddon's equation [75].

An important observation regarding the contact impression is that it is larger for tests with higher peak loads. Figure 58 shows a series of tests done on alumina with the same tip on the same day. As the peak load is increased so too does the visible contact impression. The mechanical data demonstrates how the peak stiffness increases with peak load which can be correlated to the contact impression in each image. Also notable is the increase in the peak adhesion force for each increase in peak load.

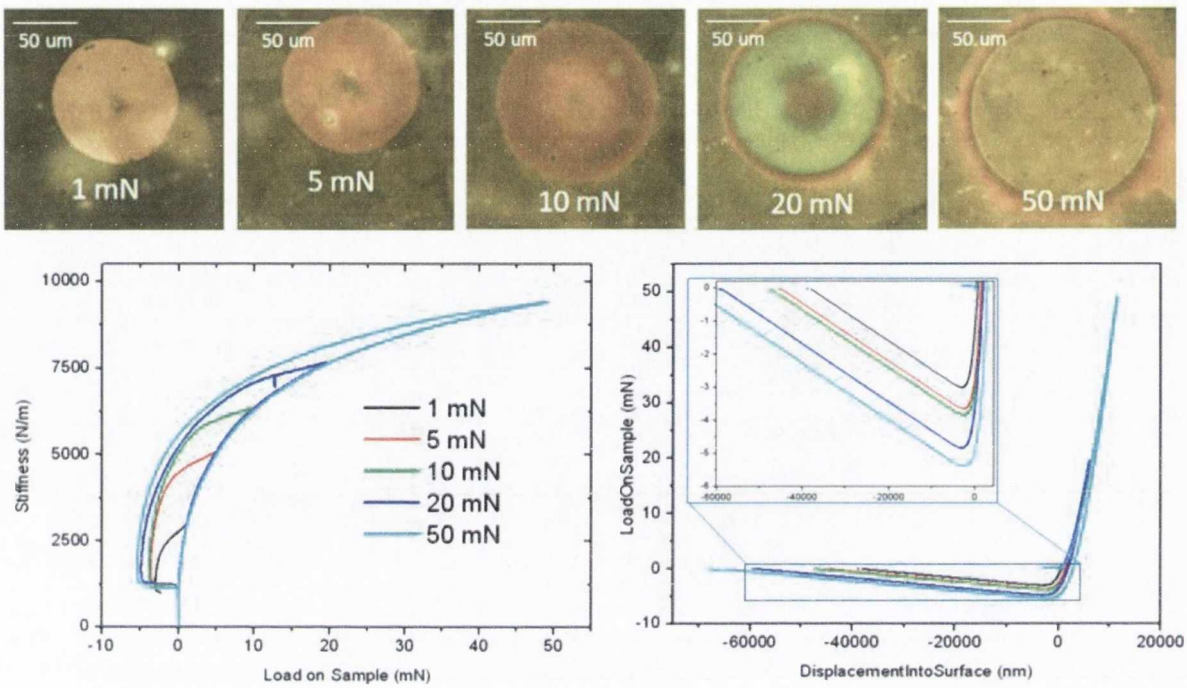

Figure 58. Contact impressions and mechanical data for tests done to higher peak loads. The contact impressions increase in size for each subsequently higher load test. The mechanical data demonstrates that the peak stiffness also increases for each peak load test. The peak adhesion force also increases with peak load.

"Halo Effect" in Contact Impression

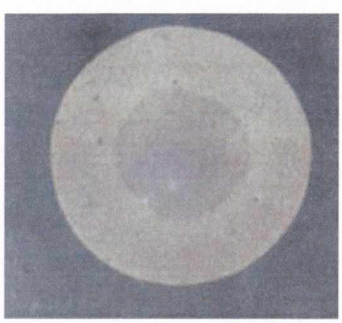

Figure 59. Contact impression on alumina showing an inner region and an outer "halo".

Before describing in detail how the contact impression on alumina is used for finding the contact radius, an important observation needs to be discussed. It is common when testing on alumina to observe a contact impression that has the configuration of that shown in Figure 59. There are two distinct regions in this image: A darker *inner region* and an outer, lighter region which we refer to as the "halo". This type of contrast can be observed for at least 50% of all contacts on alumina and the inner region will always have the same contact radius length for a particular tip. Figure 60 illustrates this by showing tests done on alumina with the same tip for two different peak loads, 1 mN and 10 mN. Although the "halo" is larger in the 10 mN test, the darker inner region is still exactly the same size as indicated by the dotted line circle.

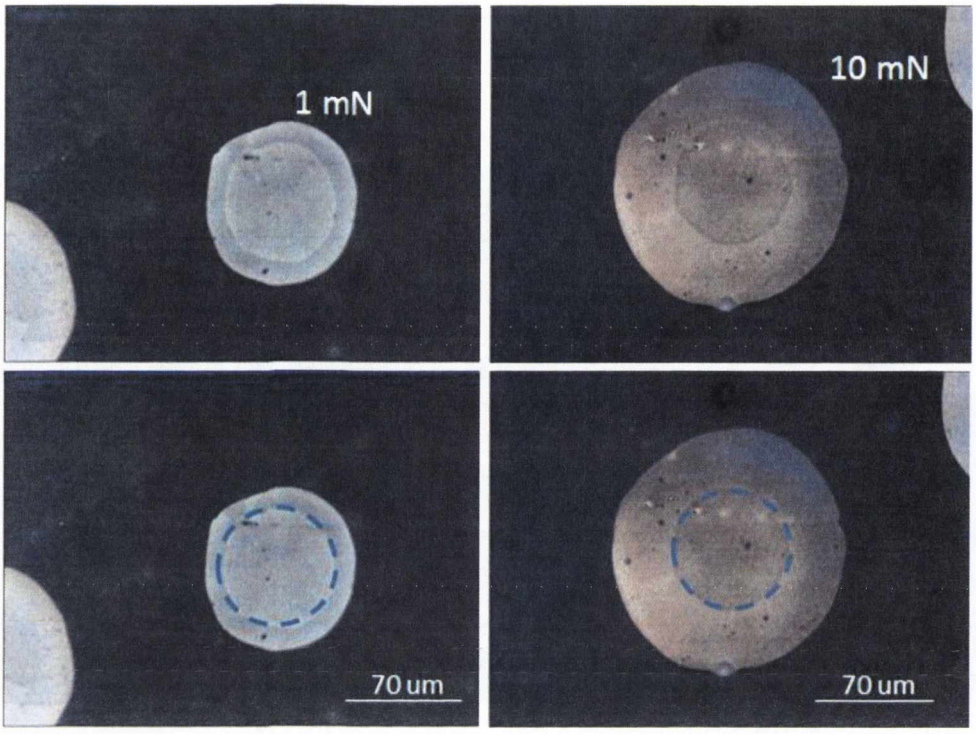

Figure 60. Contact impressions for two different peak loads illustrating that while the inner region remains the same size, the outer halo increases with load. The left hand figures show a 1 mN peak load test and the right hand figure shows a 10 mN peak load test. The bottom figures show the inner region highlighted by a broken blue line. Both contact impressions were made with the same tip.

The size of the inner region is found to vary only with PDMS thickness, h which will be discussed in Section 4.5. Ideally one would be able to do AFM on this contact impression to try and understand if the contrast is due to more cross-linker being deposited in one region relative to the other but the roughness of the alumina makes this very difficult. The halo effect has not been optically observed on smooth materials but perhaps careful AFM studies could provide an additional clue as to its nature. The halo will be discussed again presently.

Defining the Contact Radius Stiffness Correlation

The contact impression provides a measure of the maximum contact area of the PDMS tip in contact with the alumina membrane at the *maximum stiffness* S_{max} value of the test. The method is designed to load the tip up against the alumina to a peak load value set by the user. At this peak load there is a corresponding peak stiffness value which measures the stiffness of the PDMS contact on the alumina at this peak load. Knowing the size of the maximum contact radius a_{max} and the maximum stiffness allows us to correlate the contact radius throughout the test to the measured stiffness channel using Sneddon's equation [75] as described in Chapter 3. Generally Sneddon's equation relates the stiffness of an elastic material to the contact radius as $S \sim a$. If this equation holds true throughout the test is provides a means from which the contact radii during testing can be calculated from the stiffness channel using a *calibration factor*

Contact Radius = Calibration Factor x Stiffness

For example the following test was loaded to a 10 mN peak load and the contact impression was measured with a Carl Zeiss Axio Imager Microscope with measuring feature. Using the microscope meant that there was an error of no more than 1 um in the measured radius though a larger source of error can be due to establishing the exact boundary of the contact impression. Therefore we assume an error of no more than 4 um in measuring the contact radius.

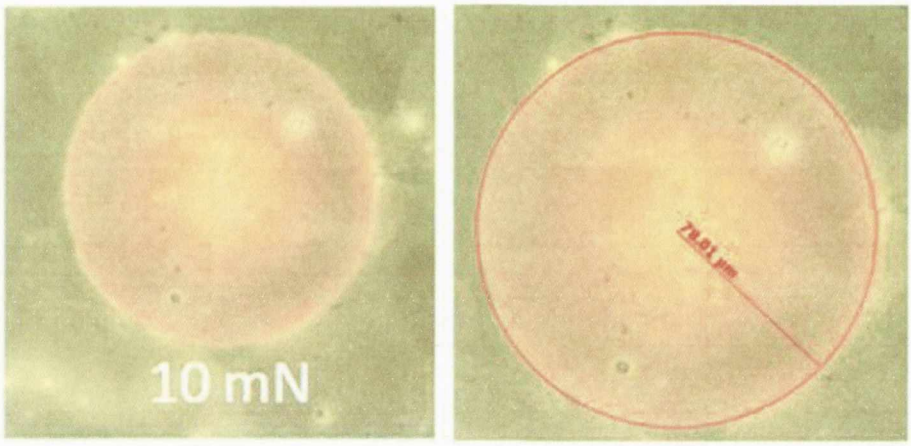

Figure 61. The contact impression of a 10 mN test using a Carl Zeiss Axio Imager Microscope. The measurement can be made very accurately with the microscope and the largest source of error is due to the establishing the exact position of the contact impression boundary with the alumina.

Figure 62 shows the stiffness vs. load curve (S-L curve) for the test shown in Figure 61. The maximum stiffness is measured to be 6460 N/m which for an a_{max} = 78 um gives a calibration factor of 0.01.The S-L curve featured shows considerable hysteresis between the load and unload segments of the test. The direction of load and unload are indicated by the arrows and were there no hysteresis in the system the load and unload curves would lie on top of one another. There are two sources of hysteresis in this test. Firstly the adhesion of the PDMS on the alumina means that the during the unload a tensile force will be experienced between the tip and the alumina that is not apparent during the load up. In this test this tensile force or peak adhesive force reaches a peak value of -4 mN, the minus sign indicating it is a tensile rather than compressive force. The other source of hysteresis is due to the viscoelastic nature of the PDMS. Viscoelastic materials by their definition experience hysteresis because of the additional time-based component expressed in their behaviour. This viscoelastic aspect presents us with an important considering. The use of Sneddon's equation [75] in calculating the contact radius from the stiffness channel assumes that the PDMS is an *elastic* material. Although PDMS is treated as an elastic material in much of the

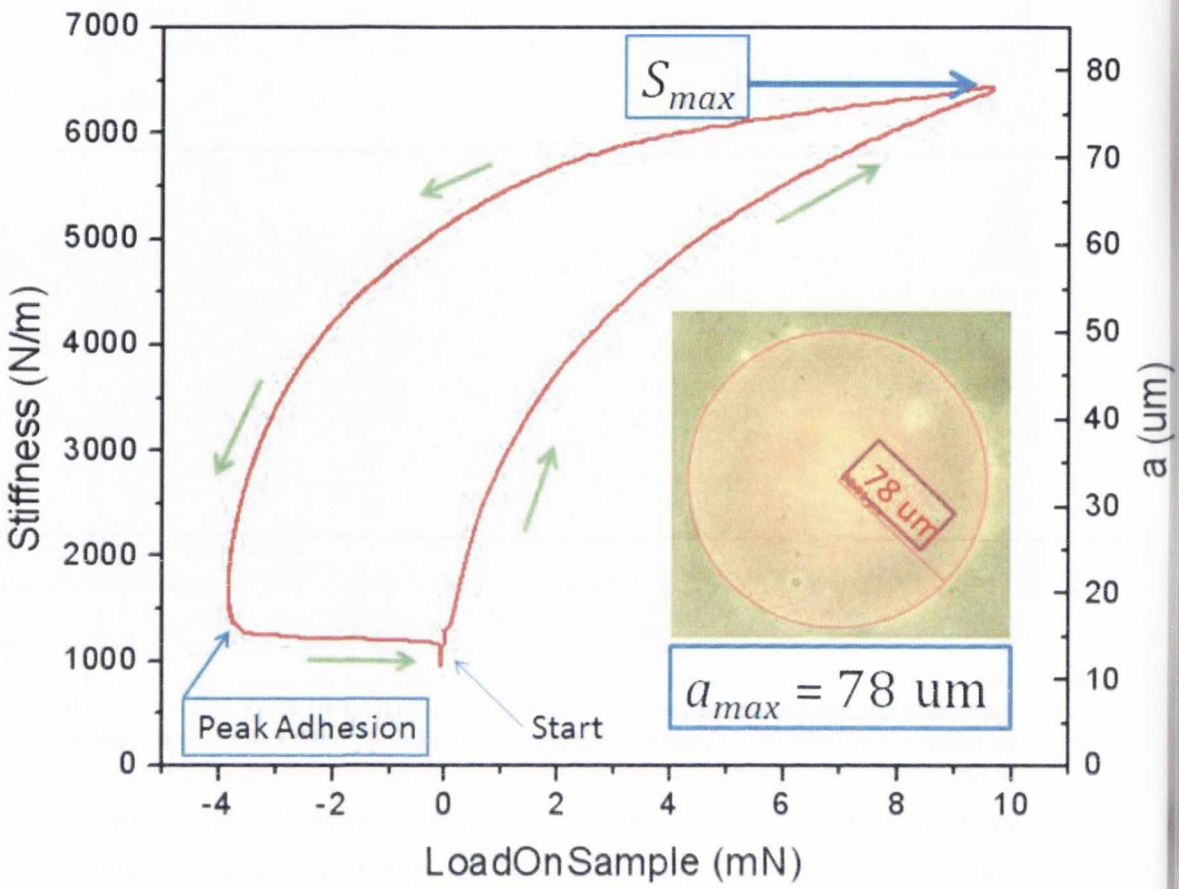

Figure 62. Stiffness vs. Load curve for a PDMS tip on alumina. The direction of load and unload are indicated as well as the maximum stiffness and the peak adhesion. Knowing the maximum stiffness and the maximum measured contact radius allows the contact radius to be found throughout the test.

literature [8] its viscoelastic behaviour can manifest itself at the crack edge when it is strongly deformed [14]. Therefore a check is needed to ensure the calibration factor we use is valid in our system. Although it is not possible to measure the contact radius optically from below the contact it is possible to view the test side on and make very approximate measurements of the contact radius during the unload portion of the test using a video camera in conjunction with a microscope. The details the experimental set-up for this are given detail in Chapter 3. We now discuss the use of the video camera in verifying the contact radius/stiffness correlation.

Measuring the Contact Radius Directly

In Chapter 3 the video data set-up was described and how it could be used to verify that Sneddon's relation holds for PDMS. We now describe this in more detail for tests done on alumina at two different peak loads, 0.3 mN and 10 mN. A set of images will also be shown of the test done on SiO_2.

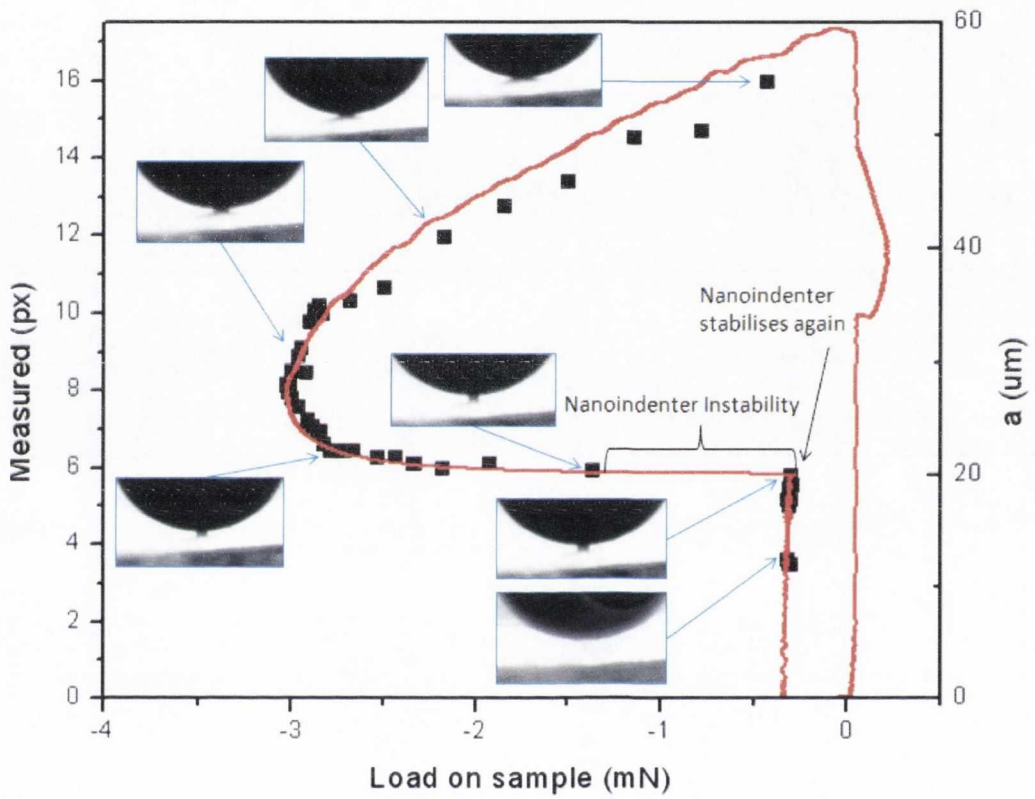

Figure 63. S-L curve on alumina for a test with a peak load of 0.3 mN. The test was recorded with a video camera from a side-on view which shows the PDMS neck forming between the tip and the alumina during the unload segment of the test. Please note the dark line in the foreground of the video stills. This is the edge of the alumina side-on. The surface of the alumina is at the end of the neck where a slight shadow can be observed. This is shown by an arrow in the left-hand most video still.

frame rate of 30 frames/second. The red curve shows the data measured by the nanoindenter during the test. The black squares indicate the video frames which were individually viewed and measured using Inkscape ™ graphical software. A distinct neck is visible for tests throughout the unload segment. The neck diameter was measured using the pixel length of the image. The video images are of relatively low resolution and there is an error of 1-2 pixels for each image. This error is larger for the points at the initial part of the unload as the images are more obscured than later in the tests. The spread of the measured points is compared with the contact radii extrapolated from the stiffness data for comparison. The data shows a good match between the data measured from the video and the data measured by the nanoindenter. There is a maximum error of

approximately 5 um for the initial part of the unload which decreases significantly for the latter part.

The figure also shows a short period of instability in the nanoindenter data due to the indenter springs being unable to keep up with the rapidity of the unload during this time. However the data stabilises again before contact between the PDMS and the substrate is broken and the inset shows the video stills from that region. This demonstrates distinct necking behaviour and is shown in greater detail in Figure 64 sets (a) and (b) Set (a) shows the original video images taken. Set (b) shows the same images an additional neck outline added for clarity. The neck starts off

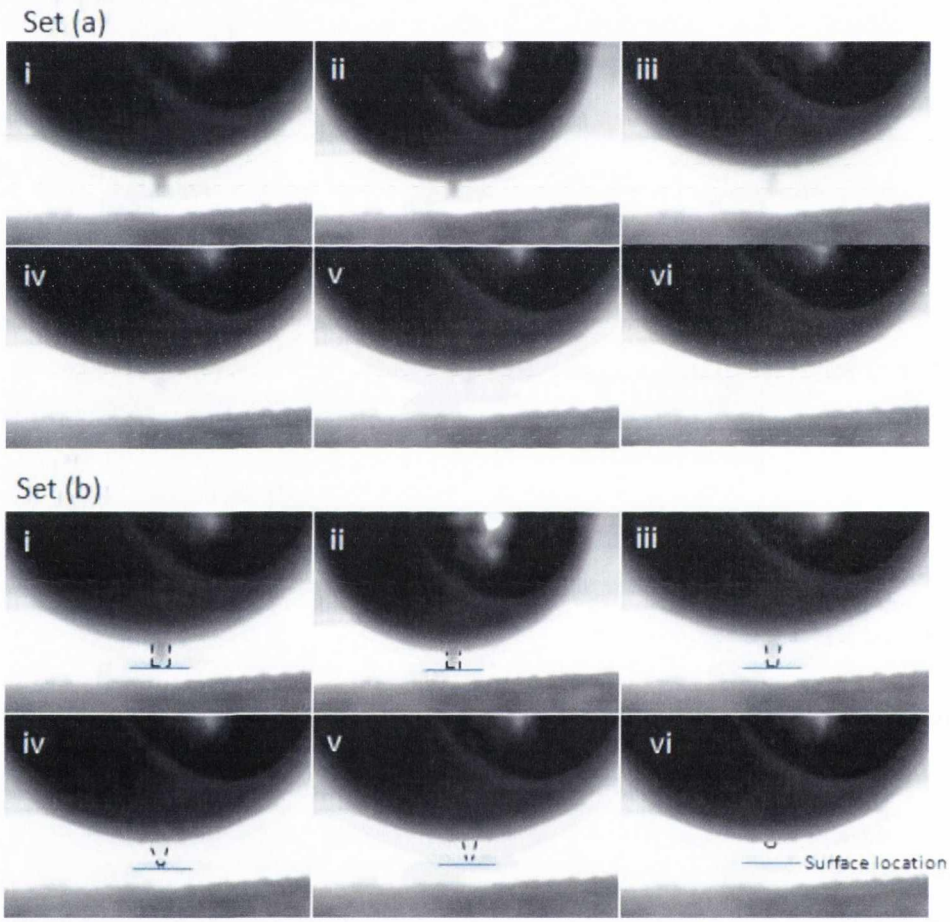

Figure 64. Video stills showing the neck formation of the PDMS during the unload segment. Set (a) shows the original images. Set (b) shows an additional neck outline for greater clarity. The neck starts as a flat punch until the very end when it becomes more cone-shaped with a flat apex. There appears to be a finite contact radius as it retracts from the alumina membrane. Again the dark line in the foreground indicates the edge of the alumina sample. The surface of the alumina is shown by the horizontal line in set (b).

with a perfect flat punch configuration. Figure 63 shows that it maintains its flat punch configuration for the duration of the unload load through the peak adhesion point and through the rapid unload segment as the load is returning to zero. The data also shows that even when the

load has returned to zero the neck still exists though bottom of the neck in contact with the alumina begins to shrink faster than the top of the neck. This creates a flattened cone configuration. The final image shows the neck as it is retracting from the alumina and at appears to return to a flat punch configuration. Figure 65 illustrates this schematically.

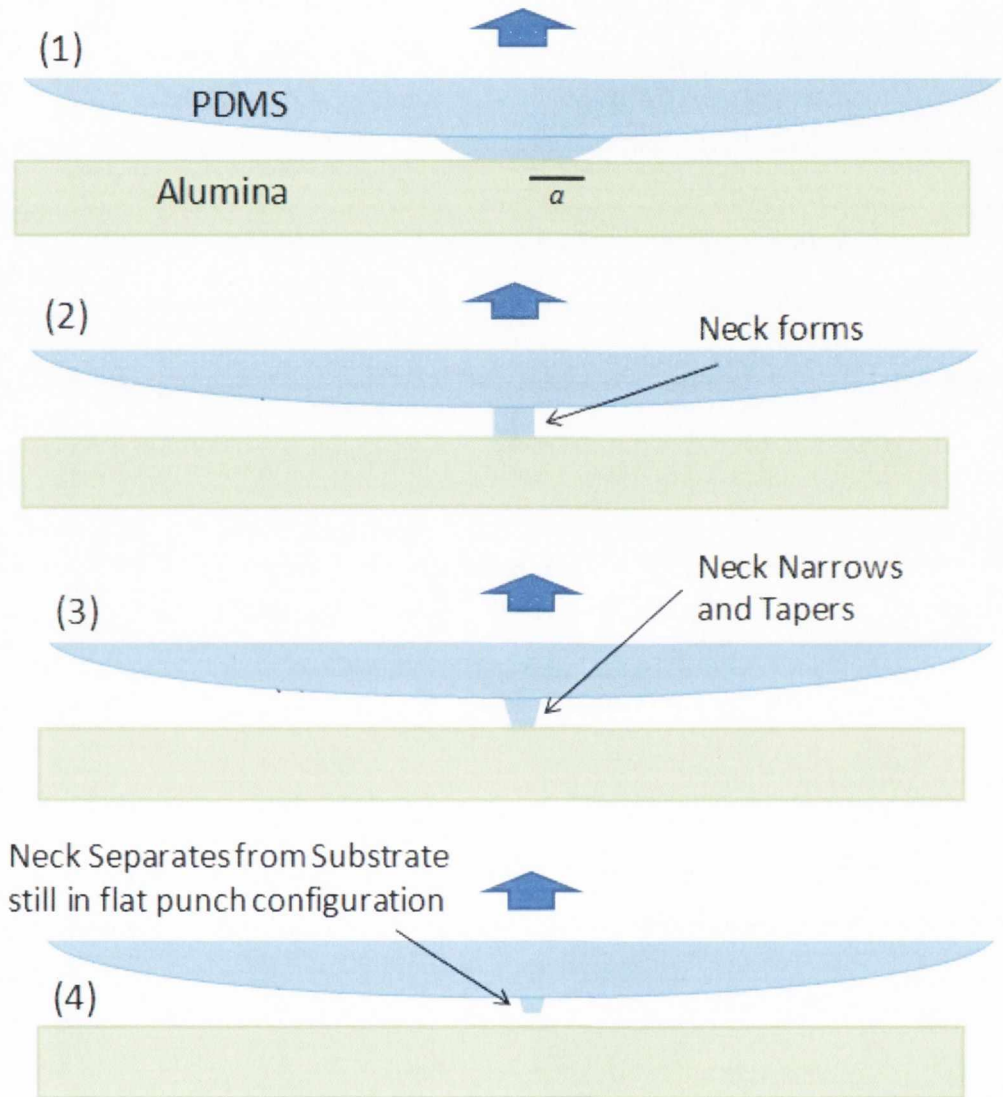

Figure 65. Schematic illustrating how the neck evolves during the unload segment of the test.

Figure 66 shows a comparison of the load on sample and the raw load channels for a test on alumina. The load on sample is calculated from the raw load, the raw displacement and a correction for the springs in the indenter:

Load on Sample = Raw Load – (Spring Correction x Raw Displacement)

The load on sample and the raw load are very similar throughout the test, the major exception being at the period of instability after the peak adhesion where the necking is forming. At this point the load on sample is modified by a significant drop in displacement of 40 um and the load on sample returns quickly to the zero value. It is possible that at this point there is an almost instantaneous relaxation of the spring formed by the neck which occurs so quickly the nanoindenter data becomes unstable at this point. For the 0.3 mN test however the data re-stabilises itself once the indenter has returned to the zero load position.

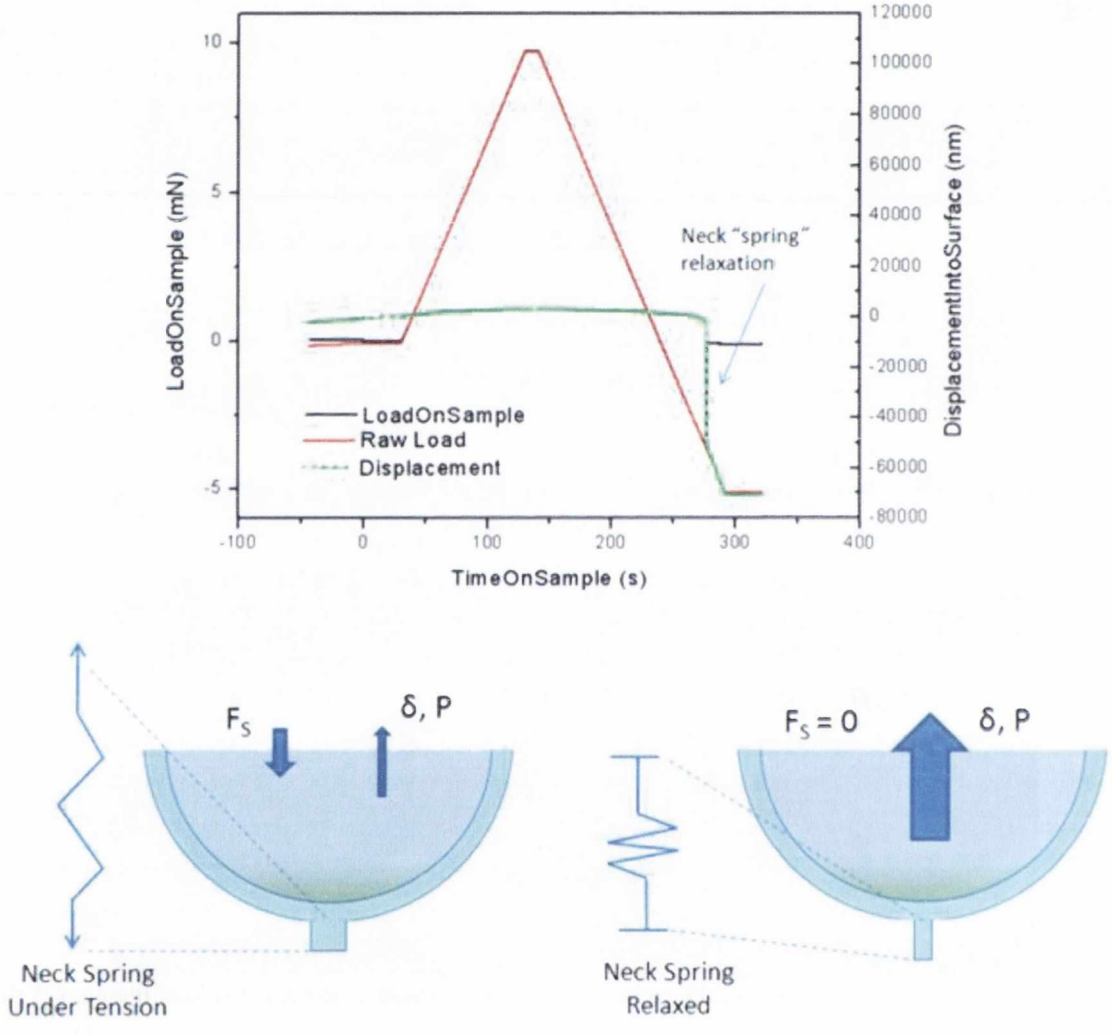

Figure 66. Raw Load, Load on Sample and Displacement vs. Time curves are compared to shown mechanically how the neck behaves like a spring after the peak adhesion point. During the rapid unload segment the neck relaxes like a relaxing spring. This spring-like behaviour is illustrated schematically.

A 10 mN test was also conducted and recorded by video for comparison. It has been noted previously that the maximum contact area and peak adhesion force increase as the peak load of the test has been increased. Figure 67 (a) and (b) shows video stills taken towards the end of the

10 mN test. Figure (b) is the last image taken before the tip disconnected from the alumina. Note the thickness and length of the neck compared to that from the 0.3 mN test shown in Figure (c).

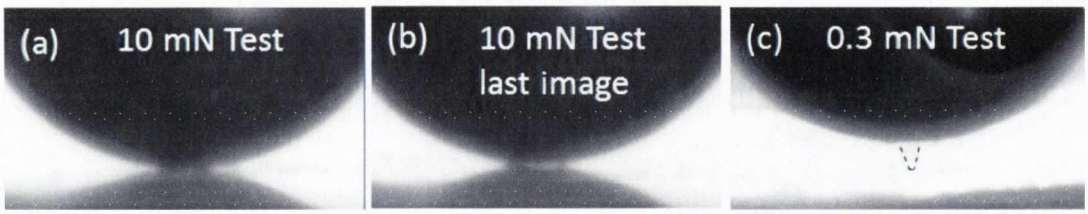

Figure 67. Selection of images from the 10 mN test including the last image taken just before the neck lost contact with the alumina (b). Also for comparison is an image from the 0.3 mN just before the tip lost contact (c). Note the relative difference in neck size.

Contact and Surface Forces During Approach

As the tip approaches the material and reaches a certain minimum distance it can suddenly engage in contact with the material. This is called the *jump to contact* event and most likely involves deformation of the PDMS tip under the influence of surface forces. Figure 68 shows the L-D curve for a test on alumina. The jump to contact is highlighted in the inset and shows a 0.06 mN change in load and a 750 nm jump in displacement. This indicates that the range of surface forces involved is less than or equal to 750 nm. The deformability of PDMS suggests that deformation of the tip should occur around the contact position however we do not have high

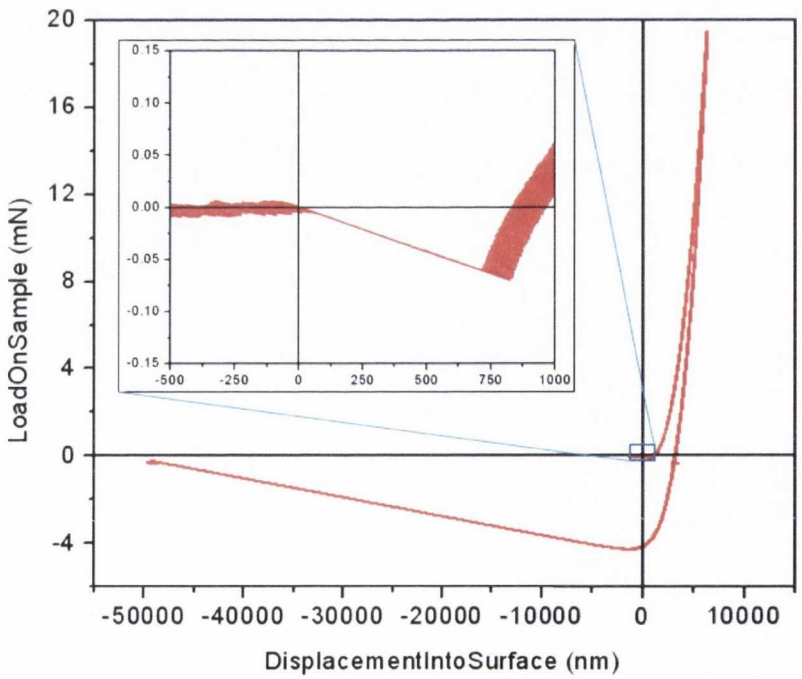

Figure 68. L-D curve of PDMS on alumina. The inset features the jump to contact event measured by the nanoindenter. The PDMS is a deformable material and it would be expected to deform due to surface forces somewhere during the jump to contact segment i.e. within 750 nanometres of the surface. However without high resolution optics and a very fast camera this is impossible to observe optically.

enough resolution optics to observe such an event. The nanoindenter has the sensitivity to detect even a minimal amount of contact between a deformed tip and the surface and what follows is a discussion on verifying this sensitivity.

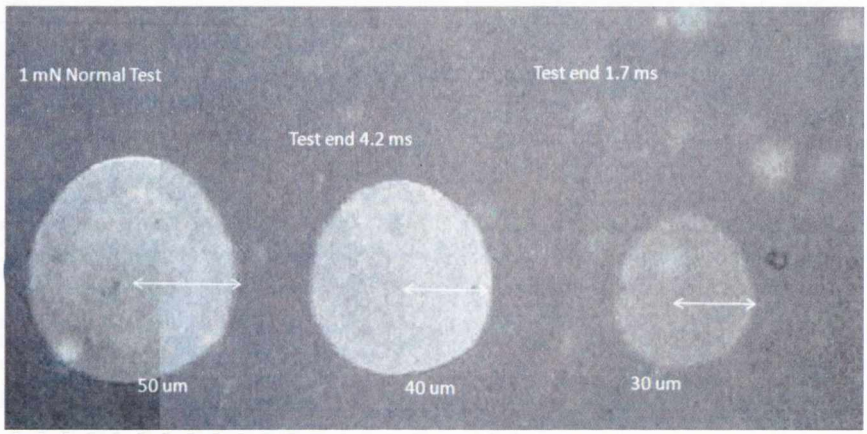

Figure 69. Test showing differing contact radii. The first test was loaded to 1 mN before unloading and shows a_{max} = 50 um. The second test was ended 4.2 ms after the surface was found giving an a_{max} of 40 um. The final test was ended 1.7 ms after the surface was found giving an a_{max} of 30 um.

Experiments were done whereby the test was stopped just as the tip was coming into contact. This was in order to see if a visible contact impression was left just before or during the jump to contact event measured by the nanoindenter. By manually controlling the test so that the tip is almost at the surface or has *just* come into contact it could be possible to find the contact radius exactly at the jump to contact. Three tests were conducted for comparison and the first test was allowed to execute normally resulting in a load up to 1 mN. The second and third tests had standard surface find segments and once the surface was detected the tests were aborted.

Test 2 was ended 4.2 ms after the change in phase angle indicated the surface had been reached and test 3 at 1.7 ms after the change in phase angle indicated the surface had been reached. The contact impressions for all three tests are shown in Figure 69. The 1 mN test yielded a maximum contact radius of 50 um. Test 2 yielded a maximum contact radius of 40 um Test 3 shows a contact radius of 30 um.

Tests 2 and 3 were ended very soon after the tip came into contact. This means that the CSM will not have had time to settle and so there is no reliable stiffness data for those tests. A measured channel which does provide reliable information in this region is the displacement channel. Figure 70 shows the displacement versus time for the three tests showing the distances at which the tests end. Bear in mind that the tip is deformable whereas the alumina is not. Therefore the displacement is the amount the PDMS has been compressed from its shape at the initial contact. Just before contact the tip could have deformed from its spherical shape by bulging near the

surface due to surface forces. It is likely that this compression is into the deformation rather than the PDMS sphere itself.

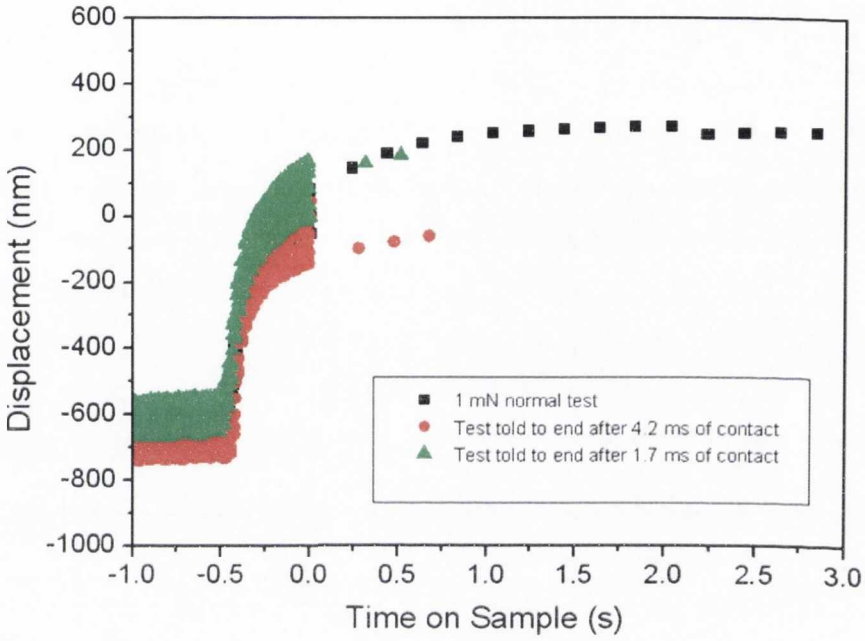

Figure 70. Displacement vs. time for the three tests.

Possible Origin of the Contact "Halo" during Initial Contact

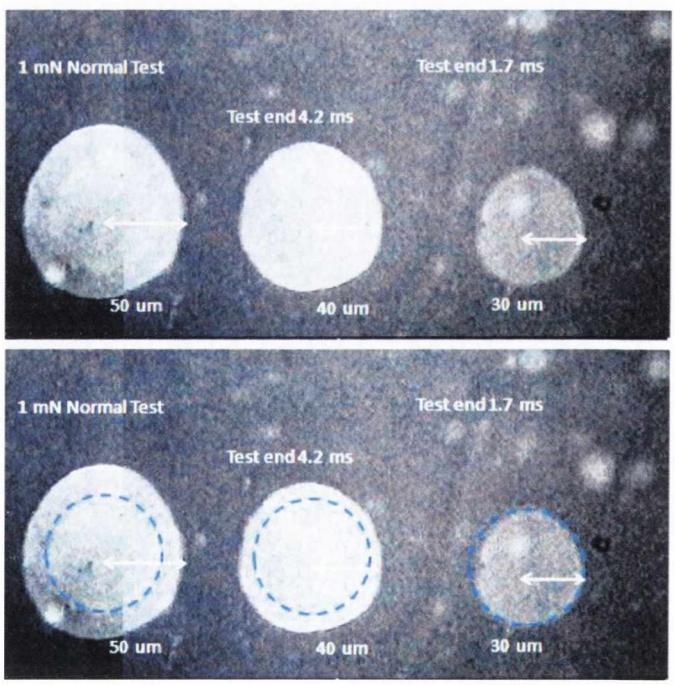

Figure 71. Comparison of the 50 um, 40 um and 30 um a_{max} tests. The 50 um and 40 um exhibit the "halo" mentioned in Figure 54. The lower picture features an outline indicating the border between the inner region and the halo. The inner region is the same size for each test and is measured as 30 um.

Figure 71 shows the same series of contact impressions from Figure 69 again. The halo which was described in Figure 60 is apparent for the 50 um and 40 um tests, though it is difficult to see in the 40 um test. The lower image shows an outline which indicates the location of the border between the inner brighter region and the halo. The inner, brighter region has a 30 um contact radius which is the same size as the 3rd test in the series. The third test also does not have a halo. It is possible that the inner, brighter region indicates the *initial* contact area of the tip as it comes into contact with the alumina. The initial contact area during the jump to contact may deposit a more significant amount of excess crosslinker than occurs during the rest of the test. As the tip spreads across the alumina during the test less crosslinker could be deposited than during the jump to contact. The larger deposit of crosslinker could create an optical contrast which is observable in the microscope and indicates the initial contact area between the tip and alumina.

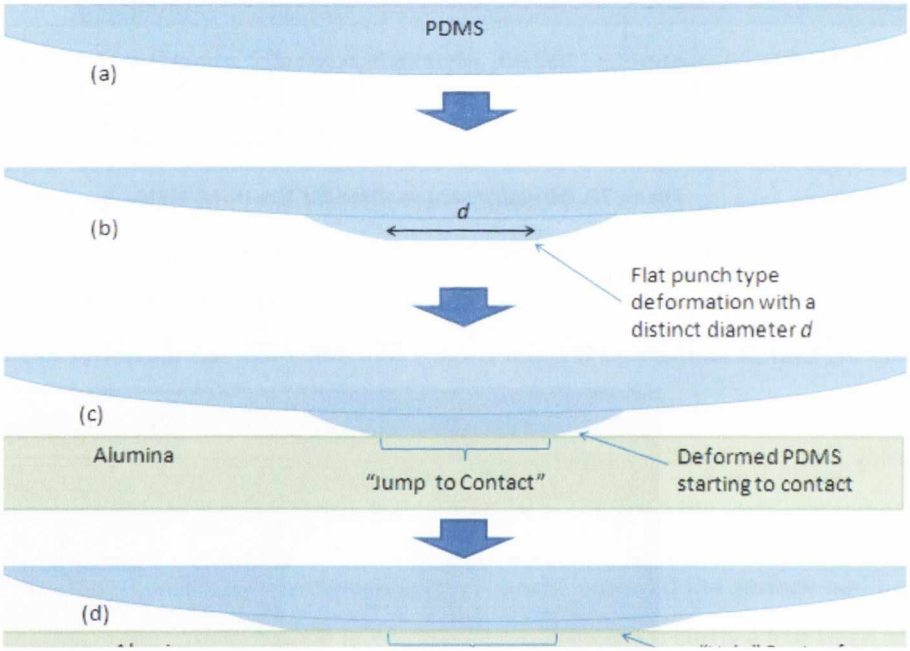

Figure 72. Schematic showing the PDMS coming into contact with the Alumina membrane. The origin of a "jump (or snap) to contact" region provides a possible explanation for the inner region and the outer halo visible in the contact impressions.

Figure 72 shows a schematic of the possible origin of the inner region and outer halo. Figure (a) shows the undeformed PDMS coming into contact with the alumina membrane. (b) shows how van der Waals forces between PDMS and the alumina surface could cause an outward bulging of the PDMS. This would occur very close to contact, with a range of 10 – 100 nm. If this bulging was similar in shape to a flat punch it would already have a distinct diameter d even before contact was made. The formation of a flat punch would depend on two parameters: the geometry of the PDMS itself and the gradient of its curvature near the contact which defines the range of attractive forces over the surface. The deformability of the PDMS dictates how easy it is for the surface forces between the two materials to change the surfaces thus stabilising the surface

forces distribution. For a flat, deformed punch the distribution of attractive forces across the two materials would be even with some variation at the edge of punch.

If as shown in (c) this punch made initial contact with that alumina, this would be the *minimum contact area* at the initial contact with a distinct contact diameter. The contact event would involve the flat punch "snapping" into contact with the alumina and is called the *jump to contact*. It is reasonable to imagine that a distinct amount of excess crosslinker would be deposited during this sudden event which might correspond to the boundary of the inner region. Figure (d) shows as the contact continues to grow as a result of creep and applied load the rate of deposition of the excess crosslinker could be different resulting in a contrasting region known as the "halo".

One could argue that perhaps the increased contrast is due to the neck disengaging from the alumina during the unload segment. If for example the fracture of the neck from the alumina was a *cohesive* rather than an *adhesive* process as has been assumed, the increased contrast could be due to a thin layer of cohesively fractured PDMS on surface. However we have shown in the video data that for tests with low loads the PDMS forms a long thin neck which has a diameter of only a few microns. Therefore this is an unlikely explanation. An interesting observation which will be discussed later in the chapter regards the thickness of the PDMS film. It was found that although the inner region is always the same size for different peak load tests on the same tip, it varied in size between tips with different thicknesses of PDMS. This suggests that the ability of the tip to deform upon contact is a critical factor in its size.

This theory explaining the contact impression halo will need further experimental work before it can be verified but it suggests a way in which the minimum contact of the PDMS with alumina can be pictured. It is clear that there is a lower limit on the minimum contact size that can be formed between the PDMS and surface, which will depend on the PDMS geometry and surfaces forces between the two materials.

Measurement of Jump to Contact

We now explore the mechanical data measured during the jump-to-contact event. The mechanical data for all three tests are compared in Figure 73. Figures (b), (c) and (d) show the

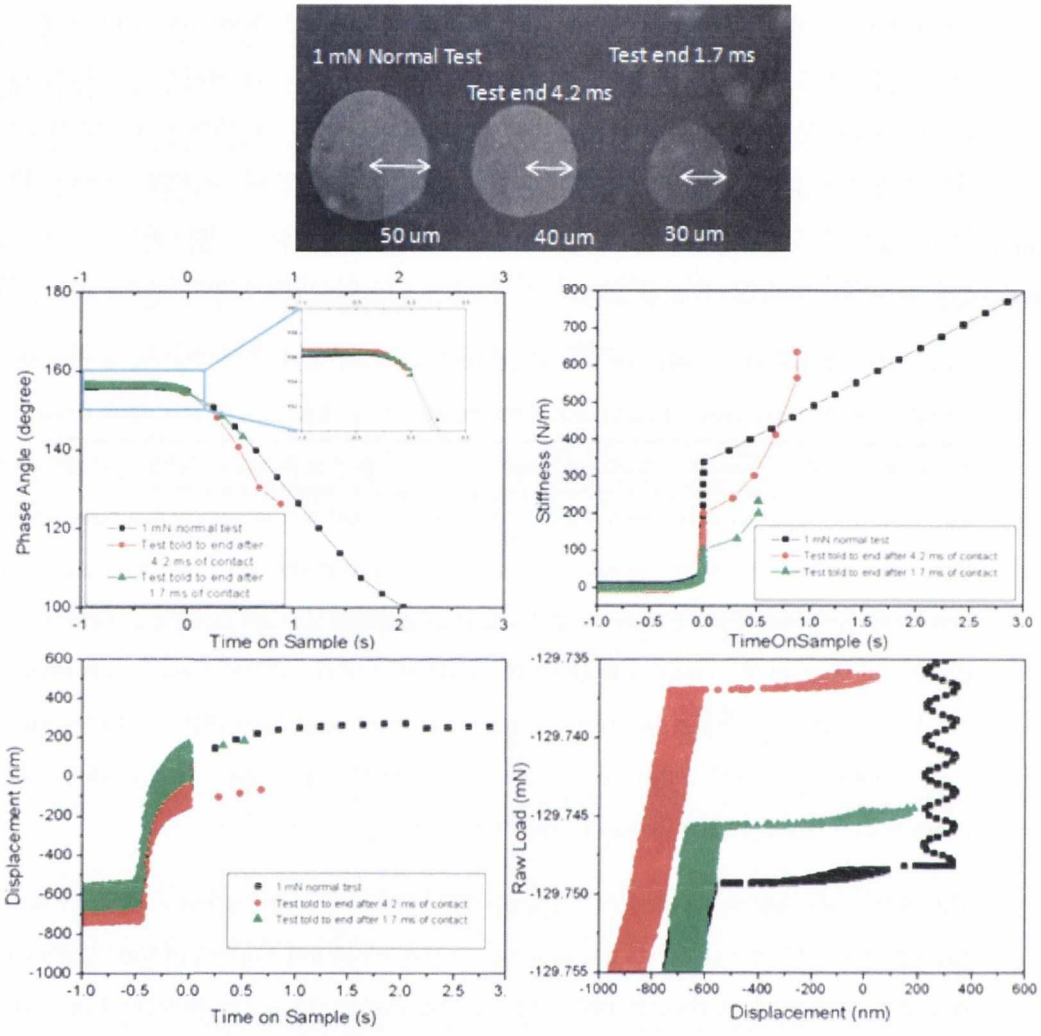

Figure 73. Series of impressions from tests at low loads. The left hand side is the 1 mN test for comparison. Note how less distinct the 30 nm impression appears compared with the others. The right hand test was taken just as the tip was jumping into contact. Anything earlier yielded no impression and presumably is not in contact.

stiffness, phase angle and displacement as a function of time. Both the phase angle and the stiffness signals start to change at around 0.25 s before the determined contact position. This corresponds to a displacement of 200 nm above the surface. In this pre-contact region, the stiffness increases by 26 N/m. Figure (d) shows the raw-load displacement data for the tests since load on sample cannot be calculated for tests that have been ended prematurely. This data shows that there is a 1.2 uN increase in raw load in the 200 nm before the surface position.

For tests where a contact has been confirmed (due to the contact impressions) it is seen that there is an increase in stiffness and in load at a distance of 200 ± 100 nm from the determined

surface point. Further tests were conducted whereby the tests were ended just before the measured surface point to see if there was any change in phase, stiffness or load recorded. A change in these channels could indicate that although the materials were not in contact it was possible to register an attraction between them.

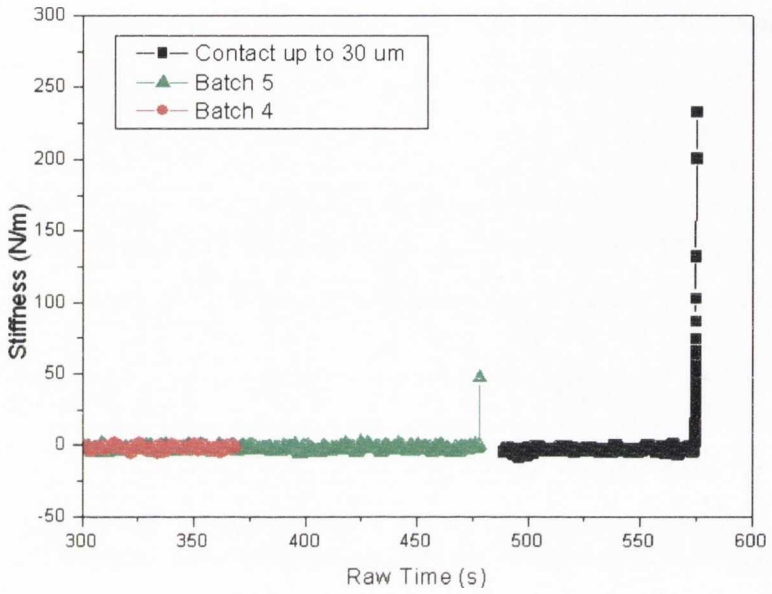

Figure 74. Stiffness of tests on approach to the jump to contact point. Batches 4 and 5 were ended within 1 um of the surface and no contact impression was observed on the alumina. The stiffness began to increase for batch 5 suggesting that the nanoindenter was detecting the surface attraction between the PDMS and the alumina.

This argument is further supported by the data in Figure 74 which shows the three attempts at stopping the test just before or at the jump to contact point. The black curve shows the test with a maximum contact radius of 30 um which was ended after the jump to contact. The other two tests were attempts to make contact before the nanoindenter registered that contact had been made. In both cases the indenter did not register contact. As can be seen the red curve shows no increase in stiffness, however the green one shows the stiffness just starting to increase. Careful examination of the alumina after this test showed that there was *no trace of PDMS* on the surface suggesting that this increase in stiffness was purely due to surface forces between the tip and surface.

4.3 Adhesion and Contact Mechanics Studies

In Chapter 3 we defined *applied channels* such as load, *measured channels* such as displacement and stiffness and *calculated channels* such as contact radius, crack velocity and energy release rate. The observation of a contact impression allows us to use the measured and applied channels to calculate the information in the calculated channels. Varying nanoindenter parameters such as peak load, test location and unload rate allows for comparison and analysis of the PDMS/material interface under different conditions.

Adhesion Studies on Alumina

As has been previously discussed in Chapters 2 and 3, we divide the unload segment into two regions: The compressive region where the load is positive and the tensile (adhesive) region where the load is negative. It must be borne in mind that these regions describe the force very generally. Throughout the unload segment, the measured load is a combination of tensile and compressive forces, with the middle the contact in compressive contact and the outer, peeling edge in tensile contact. As the test enters the tensile region the contact becomes progressively tensile in character until reaching a peak adhesion load at which point the PDMS is pulling on the contact material and is in full tensile contact. For simplicity's sake we will continue to refer to the regions while bearing in mind we are using approximate definitions of compressive and tensile regions.

Mechanical Tests for Different Peak Loads

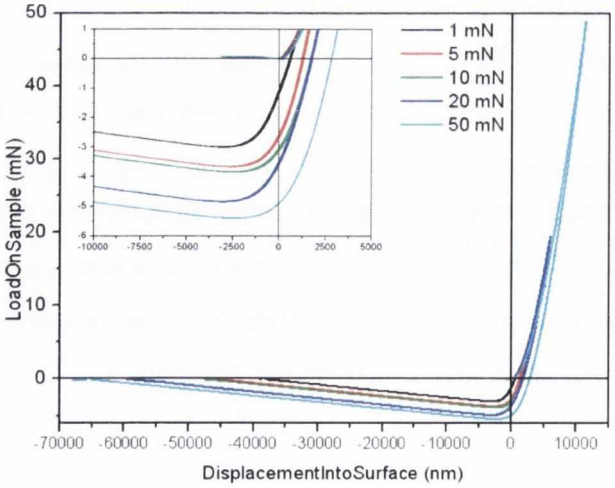

Figure 75. L-D curves for a series of peak loads on alumina. The inset shows clearly that the peak adhesion force increases for tests with a greater peak load

Figure 75 shows a series of L-h curves on alumina for ascending peak loads with a single tip at new sample locations. The data is highly reproducible in the load up segment, while in unloading adhesion hysteresis becomes increasingly pronounced for each higher peak load. The inset shows

that the peak adhesion values increase as peak load increases. This is to be expected because the higher peak loads create larger surface areas as was illustrated in Figure 58. This increases the amount of chemical and dispersive debonding that can occur as well as exposing more the surface to van der Waals attractions. Additionally, loading the tests to a higher peak load means that the PDMS is in contact with the alumina for a longer time which allows for more relaxation of the elastomer in contact with the rough surface of the alumina. PDMS takes several hours to relax completely [26] and the more time that passes, the greater the level of conformal contact that may be expected. We operate on much shorter time scales than several hours but the time it took to conduct the 50 mN test was 15 times that to conduct the 1 mN test.

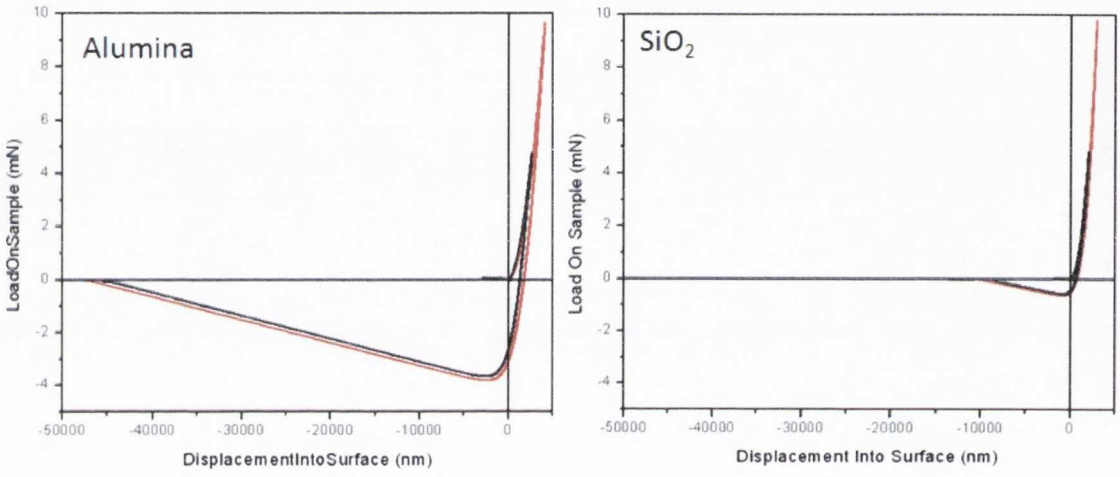

Figure 76. L-D data for 5 mN and 10 mN for alumina and SiO_2. The difference in the peak adhesion value is significant indicating that the alumina is far more adhesive to PDMS than the SiO_2.

Figure 76 shows the load-displacement data for tests on Alumina and on SiO_2. Two tests in each are shown where the tip was loaded to 5mN and to 10mN. The difference in adhesion is considerable between the two materials. The SiO_2 also shows a correlation between the peak load and the value of the peak adhesion. Doubling the peak load yielded an increase in the peak adhesion of 18 % for the SiO_2 compared with 5.5% for the alumina. This indicates that the smoother material has a greater adhesion dependency on peak load than the rougher material. The overall adhesion of SiO_2 is lower than for alumina which is to be expected as it has a smaller "true surface area" as defined in Chapter 3. The fact that is has a larger adhesion dependence on peak load than the rougher material suggests that the contact size between different peak loads is proportionally higher than for alumina. Being a smooth material the growing PDMS contact would be less likely to get "pinned" than on alumina which may facilitate the contact covering a larger optical surface area (i.e. that which can be measured optically without having to take roughness asperities into account which increase the "true area"). If this were the case then the contact would be proportionally larger than for the alumina and therefore the adhesion is proportionally

larger. Without being able to measure the contact area directly however it is difficult to verify this idea.

Figure 77 shows a comparison of the video data for latter part of the unload segment for a tip on alumina and on SiO_2. While a neck is very clearly visible for the alumina no such feature is visible on the SiO_2. If there is such a feature the resolution and speed of the video is too low to be able to capture it. This shows that there is a significant deformation on the unload from alumina that is not apparent for smoother materials.

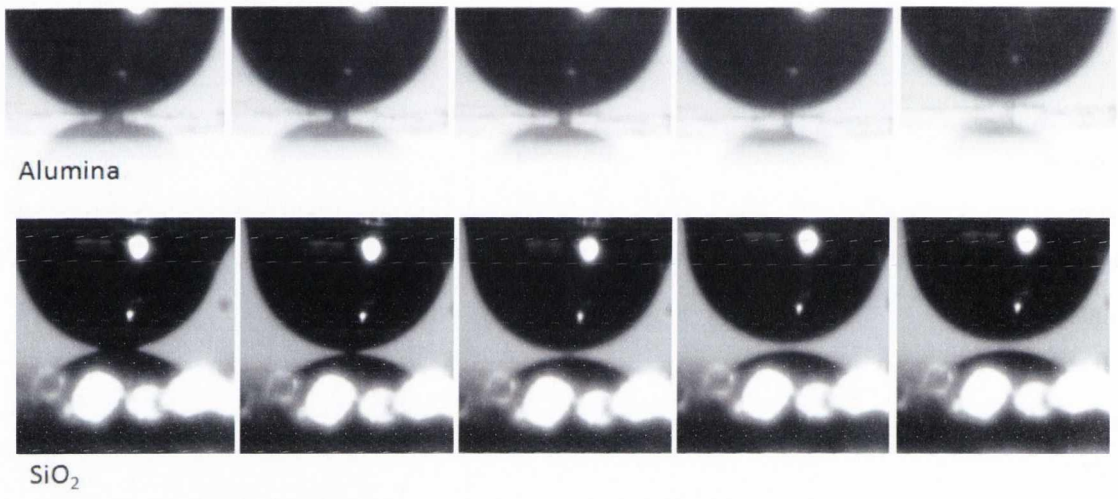

Figure 77. Video images of PDMS tip on alumina and SiO_2 showing later stages of the unload segment. Notice the formation of a neck on the alumina while no such feature is visible on the SiO_2. What might appear to the reader to be a neck on the alumina is only a shadow of the reflection of the PDMS in SiO_2.

Peak Adhesion and Work of Adhesion

Figure 78 shows the how the peak adhesion force and the maximum contact radius increase as a function of peak load for the alumina test. This relationship is observable for all tips regardless of tip thickness and demonstrates how the adhesion can be very simply manipulated by changing the peak load. For transfer problems it is far more useful to consider *work of adhesion* rather than peak adhesion force. The work of adhesion is calculated from the area of the load displacement curve where $L < 0$. However in Chapter 3 we saw that the rapid disengagement of the PDMS contact is not always recorded by the nanoindenter. Any data provided may not be reliable especially for higher load tests. This means that we do not know the exact shape of the L-D curve throughout the test. Even low load tests such as 0.3 mN peak loads have periods of instability on the unload and it was not possible to integrate the curves. It is hoped in the future that this problem can be resolved but at this point in time the work of adhesion cannot be measured and only the peak adhesion force can be used for comparison between tests.

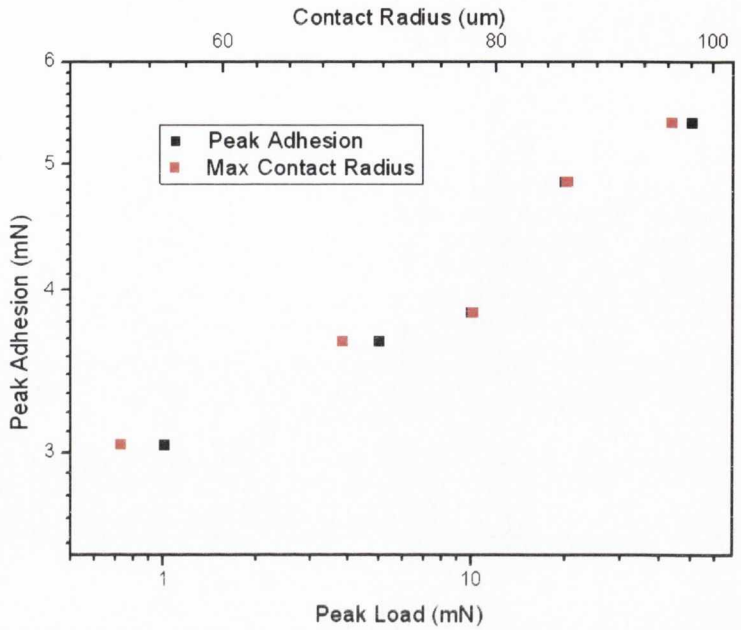

Figure 78. Log-log plot showing how peak adhesion and maximum contact radius scale with peak load.

Location Testing & Adhesion

When inking attempts are done it is not unusual to test the same location over and over during tests. For this reason it is important to know how previous contact might affect the adhesion in future contact due to transfer of material or other. Figure 79 shows the Load-Displacement curves for a series of tests on alumina membranes. These tests were conducted at the same location

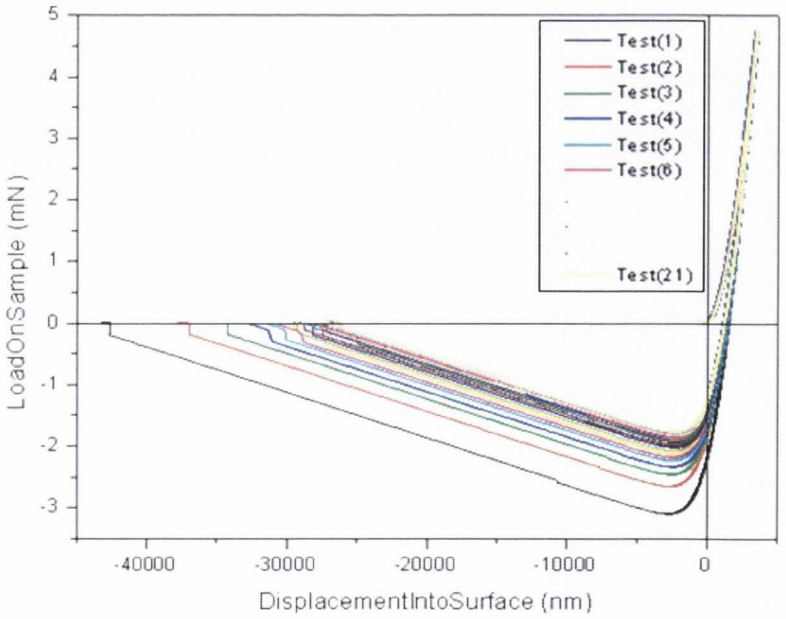

Figure 79. Load Displacement Curve for series of 21 tests in the same location on alumina. The tests are listed in the legend as Test(1), Test(2) etc. until the last test, Test(21). Note how Test(1), the black curve has the largest adhesion and the adhesion of each tests reduces sequentially. This decrease in adhesion is further examined in Figure 75.

with the same experimental parameters including peak load, unload rate and load up rate.

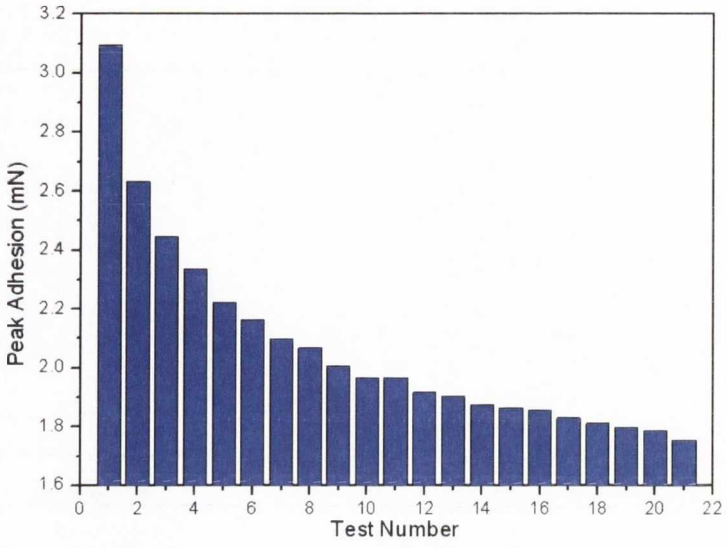

Figure 80. Peak Adhesion Force for each subsequent test in the same location.

As can be seen, the peak adhesion force between the tip and the alumina decreases for each test. The decrease is not linear though the rate of decay decreases as testing continues. It is possible that after a certain number of tests the decay saturates and there is no more change in the peak adhesion force. Figure 80 shows the peak adhesion force decrease for each test. The decrease in adhesion could be due to a build-up of excess crosslinker on the surface. As this layer becomes thicker it could decrease the ability of the PDMS to adhere to the alumina. However further studies will be needed to confirm this.

Figure 81 shows the Stiffness-Load data for the same series of tests. It nicely illustrates how the mechanical curves diverge at around the zero displacement region i.e. where the load transitions from being compressive to tensile in general character. This suggests that the divergence is due to the adhesive regime of the tests. In the compressive region the bulk of the contact is experiencing a compressive force. However there is a contribution from the contact edge which is tensile during unloading. The inner compression is repeatable and reversible. As the net force becomes tensile the crack opening at the periphery of the contact becomes more sensitive to the changing surface conditions due to material transfer (probably deposition of excess crosslinker remaining in the PDMS). With each subsequent indent the amount of material accumulates until such point that there is not a significant change to the surface between tests and the effective change in the adhesion becomes less significant.

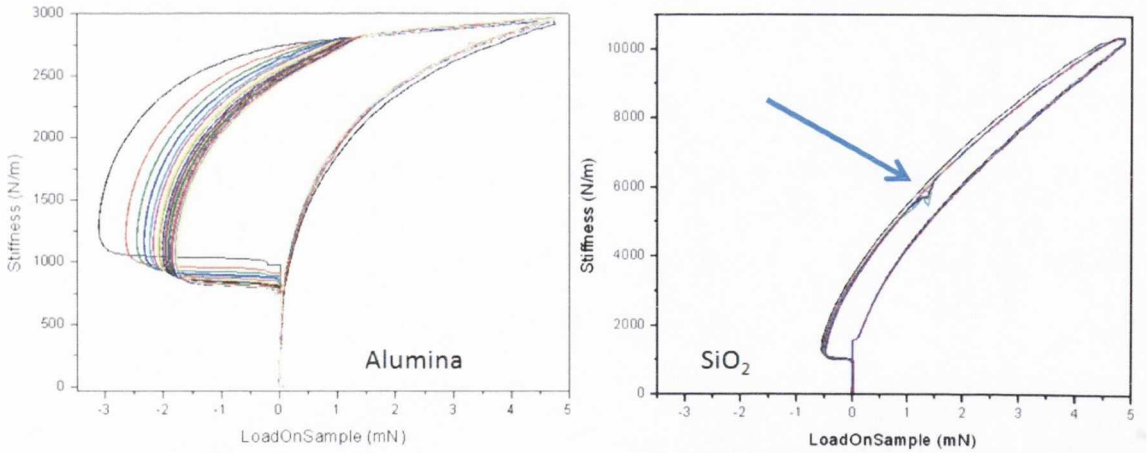

Figure 81. Stiffness-Load Curves for series of tests on alumina and on SiO_2 on the same spot. Notice the sequential decrease in adhesion for the alumina test. The SiO_2 tests also show a sequential decrease in adhesion but it is by very small amounts. The arrow indicates a characteristic kink on the stiffness curve which is often apparent at around 6400 N/m but whose exact cause is unknown.

The SiO_2 test also shows a sequential decrease in the adhesion but it is by such a small amount as to be barely detectable. There is very little adhesion hysteresis for the SiO_2 test although there is some, probably due to hydrogen bonding of the PDMS with the silicon surface [30]. The crossover point between the tensile and adhesive regions in the SiO_2 is much less distinct than for the alumina. In the compressive region, the stiffness at a given load is much higher for the SiO_2 than for the alumina suggesting that the contact area is larger. However a contact impression is not visible on smooth materials such as SiO_2 and so a direct comparison cannot be made. The lower adhesion of the PDMS to SiO_2 could mean that the elastomer can propagate more easily across the sample surface allowing for a larger contact area at a given load. We also note the brief kink in the load during unloading indicated by the arrow. The possible origins of this kink have been discussed in Chapter 3 but are most likely due to a mechanical discontinuity elsewhere in the nanoindenter itself as opposed to a physical effect in the contact dynamics.

The same tests were also repeated at distinct, pristine locations on the two surfaces. In this case, it was found that there was little or no change in mean adhesion, although there is some random variance between locations. The implication is that important changes to the contacting surfaces only occur for the substrate. Figure 82 shows a comparison of tests done on the same spot and different spots on SiO_2. These tests were repeated for various materials and the same behaviour was found in all of them.

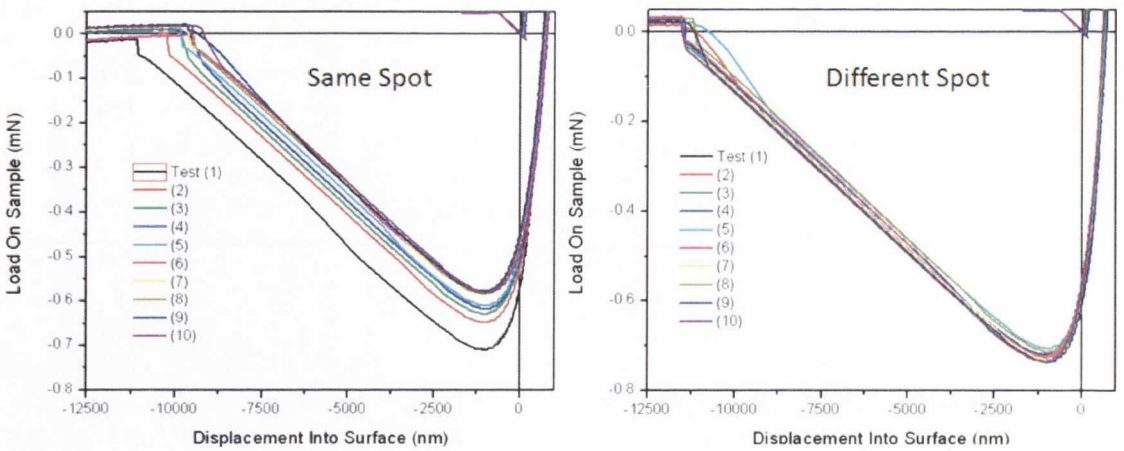

Figure 82. Comparison of tests done on the same spot and on different spots on SiO_2. The sequential decrease in the same spot tests is very clear while the different spots show little, if any variation. This indicates that it is not the tip that is changing with each test, but the contacting material. The values for Load do not return exactly to zero after testing as would be expected and it is unknown exactly why that is so. It is possible there is a calibration issue with the nanoindenter or that the recalculation of the Load after testing is not quite adequate. At this time most of the analysis is done on the curves up to the peak adhesion point and so this is a problem which can be examined in more detail at a later time.

Unload Rate and Adhesion

The unload rate which is measured in mN/s is a value set by the user and for many of the inking experiments which are described in Chapters 5 and 6, the unload rate can be the deciding factor between an inking and non-inking event. However for the theory of transfer the important parameter is the crack velocity v and this set of experiments will illustrate the dependency of v on the unload rate.

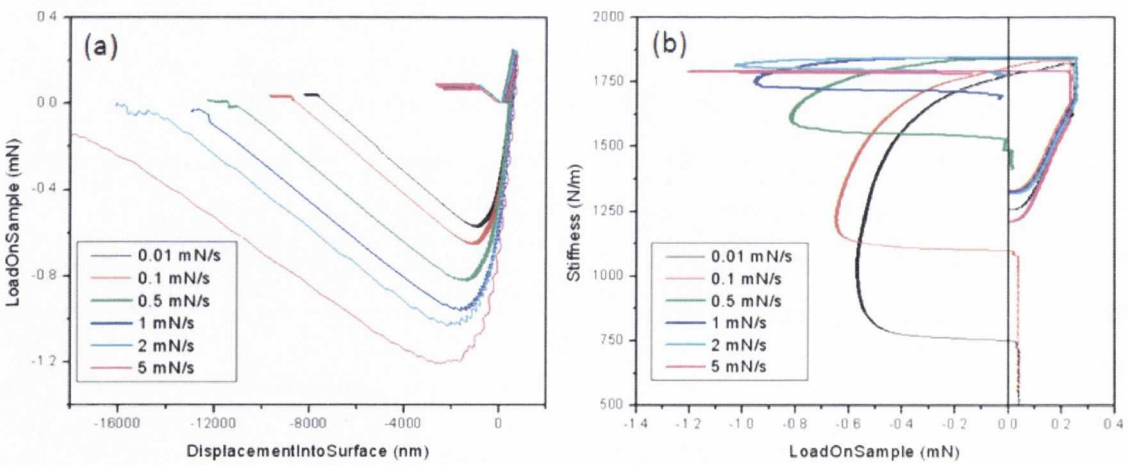

Figure 83. Load-Displacement and Stiffness-Load data for a series of tests for different unload rates. The adhesion values increase incrementally with each increase in the unload rate which is predicted from transfer theory.

Figure 83 shows a selection from a series of tests which were done on a carbon nanotube film where no inking event occurred. In this set of experiments only the unload rate was changed. This particular set is used because it shows a good spread of unload rates from 0.01 mN/s to 5 mN/s. Figure 83 (a) shows the load-displacement data and there is a very clear correlation between the increased unload rate and increased adhesion on the system. Viscoelastic theory suggests that as the crack edge is propagated at faster rates, a viscoelastic resistance to the moving crack edge develops at the periphery which leads to pinning of the crack and deformation of the PDMS [14]. This would contribute to a higher adhesive energy for the faster unload rates since the viscoelastic effects are by definition time dependent. The stiffness-load data shown in (b) shows how the contact during the unload changes for the different unload rates. As the unload rate becomes faster the adhesion increases but the PDMS does not have a chance to relax back to its original value before it leaves the surface. Correleating the stiffness and contact area shows that for the fastest tests the contact radius is almost at its maximum value before entering the rapid deformation unload segment as defined in Chapter 3 (the segment whereby the indenter can no longer record accurate data but where the video camera indicates a large amount of necking and deformation).The question still remains so to the effect the unload rate has on the crack velocity. Figure 84 shows the crack velocity as a function of unload for various unload rates.

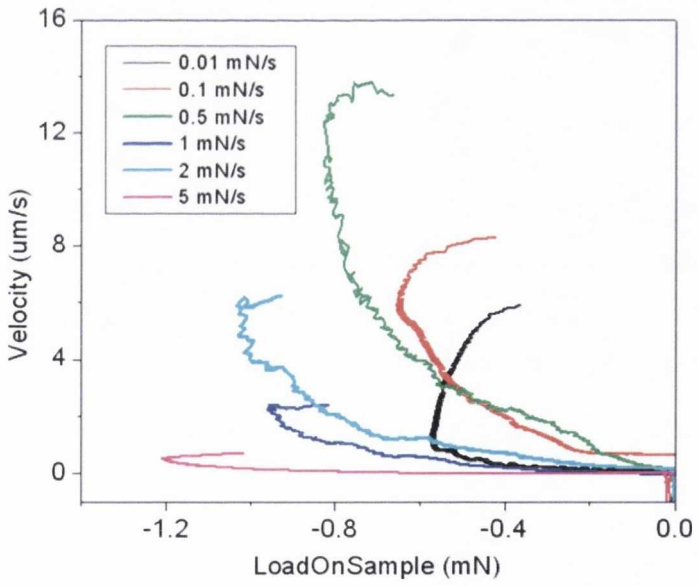

Figure 84.Velocity vs. load and for various unload rates. Data after the peak adhesion force has been removed for clarity. There is no clear correlation between the unload rate and the crack velocity gained by the tip on sample interaction. Therefore increasing the unload rate *does not guarantee a faster crack velocity*.

Interestingly although the crack velocity has a dependency on the unload rate, higher unload rates do not necessarily yield faster crack velocities as illustrated in Figure 84. The 0.01 mN/s test

has the lowest adhesion but it has a higher velocity than the 5 mN/s test. The 0.1 and 0.5 mN/s have almost the same crack velocity which is higher than the crack velocities for the 1 mN/s and the 2 mN/s. This seems counter-intuitive as one would imagine that a faster crack velocity would pull the tip off the surface more quickly, therefore yielding a faster opening crack. However if one considers again the contribution of viscoelasticity at the crack edge it can be surmised that these effects cause more pinning of the contact as the PDMS is deformed more quickly, thus slowing the crack edge down.

4.4 Contact Mechanics of the Interface

The adhesive properties of an interface can be further quantified by a relation between the energy release rate and the crack velocity during contact. In Chapter 1 it was shown how this relation could be used to define regions where transfer would or would not occur [46 52]

We saw in Chapter 2 that this relation can take on the form of

Equation 40

$$G = G_0(1 + \left(\frac{v}{v^*}\right))^n$$

where G_0 is the critical energy release rate above which a crack can form, v* is a characteristic crack velocity for the materials describing dissipation at the crack front and interfacial effects and n is a scaling parameter.

The experimental crack velocity v can be measured from the time derivative of the contact radius measured throughout the tests. Figure 85 shows an example of a G vs. V curve measured by Rogers et al which demonstrates the relationship described in Equation 40 for a scaling parameter of 0.65. This experiment was conducted for a thin continuous film of gold being peeled by PDMS where the velocity was kept constant. The experiment featured a rectangular geometry which allowed for a straightforward, direct measurement of G based only on the peel force and the width of the crack front. More details on this can be found in Chapter 1.

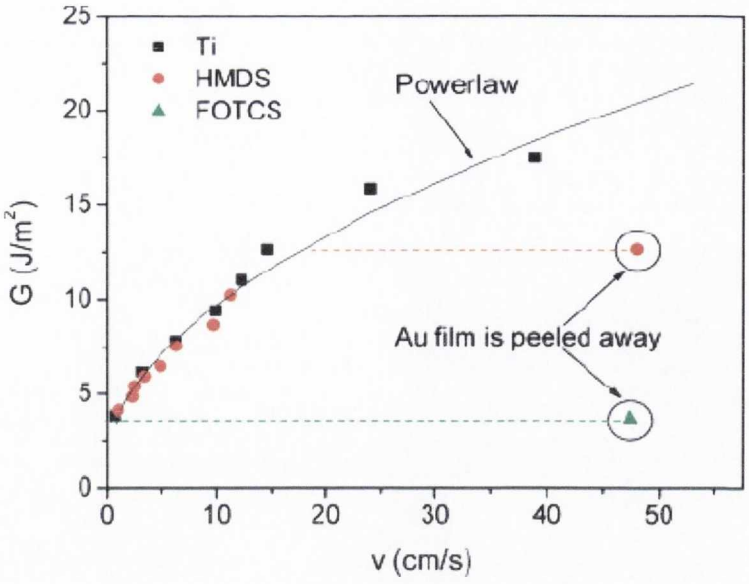

Figure 85. Figure from Rogers *et al* [42] showing measured *G* vs. *v* values for the peeling of a thin gold film which fits equation 40. The *Au* was adhered to a glass substrate with three varying degrees of adhesion. The adhesion of the Au to the glass was mediated by three different surface treatments for the glass, a tricholorosilane (FOTCS) vapour treatment, a hexamethyldisilazane (HDMS) vapour treatment and thirdly an adhesive layer of titanium (Ti).

G can be measured for a spherical contact on a flat material using the JKR formulation as used by Shull *et al* from

Equation 41

$$G = \frac{(P' - P)^2}{6\pi K a^3} f G_P\left(\frac{a}{h}\right)$$

where P' is the Hertzian load given by $P' = 16E_S a^3/9$, E is the elastic modulus of the material and a is the contact radius at any given point in the test. $f G_P\left(\frac{a}{h}\right)$ is the finite size correction factor [59,60] which is included in the case where the elastomer layer is confined between two hard surfaces. The JKR theory and the finite size correction are described in detail in Chapter 2. The theory assumes that the elastomer is a purely elastic material and that the interface is between smooth materials. Assuming an elastic modulus for PDMS of 1.7MPa [63] and using Sneddon's equation [75] to calculate a throughout the test allows for the calculation of the G values based on the measured stiffness values during testing.

Figure 86 shows the G vs. v curve measured for a tip on alumina. The figure on the right shows a close up of the lower G valued curves. The PDMS on the tip was 20 um thick and the tip was loaded to peak loads ranging from 1 mN to 50 mN. All tests were done on the same day with the same load up and unload rates. The peak adhesion force for each test is indicated by a coloured arrow. The G vs. v relation illustrated in this figure is not similar in shape to that in Figure 85. The

shape of the unload curve to the peak adhesion force is concave instead of convex as predicated by Equation 40. The data taken after the peak adhesion force cannot be fully trusted due to instabilities in the nanoindenter from the rapid movement of the tip on the material, either by necking or by disengaging with the alumina as shown in the video data. Without visual measurement of the contact radius in this portion it is difficult to draw any reliable conclusions though the data does appear to be following the model.

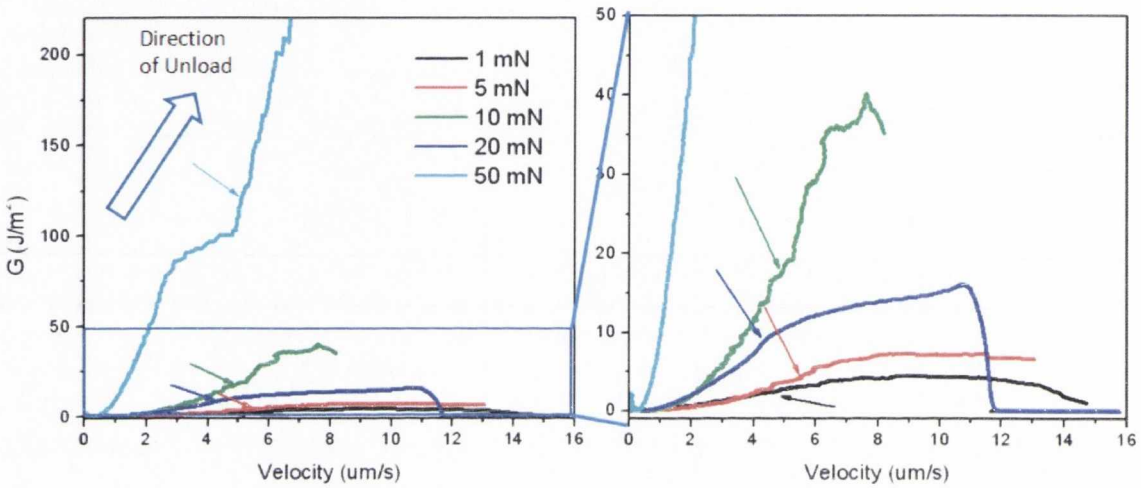

Figure 86. G vs. v data for different peak loads on alumina. Only the unload portion of the test is indicated. The coloured arrows indicate the location of the peak adhesion force on the test. To the right of these arrows the data may or may not become unstable, depending on whether the tip is still in contact or not. There is no way of knowing this without observing it with a camera. The data before the peak adhesion point does not follow fit to Equation 40 as shown by Rogers *et al* in Figure 80.

Assuming the model is correct then the shape of the curve is most likely incorrect values for G being calculated. The video data strongly supports the calculation method of the contact radius which means that the velocity data is reliable. There are several reasons however as to why the calculation of G using the JKR theory could be incorrect for our system.

1) Whereas the measured values such as load are very accurately measured by the nanoindenter, assumed or calculated parameters such as E or a could be incorrect.
2) The JKR theory assumes the interaction is between smooth materials whereas alumina is a very rough material.
3) The JKR theory assumes that the elastomers is fully elastic and in bulk form. Our set-up uses a thin film of the elastomer and it is possible that the finite sized correction is inadequate for our system.

We shall address each of these possibilities in turn.

1) The video data has verified that how we measure a is quite accurate. Even accounting for an error of 5 um in the measurement of a makes only a minor change to the G vs. v curve.

Also increasing or reducing E changes only the values of G it does not change the shape of the G vs. v relation.

2) Tests were conducted on SiO_2 using the same load up and unload rate as the alumina test. The test was loaded to a peak load of 10 mN. Unfortunately smooth materials such as glass or SiO_2 do not leave an optically visible contact impression. This means that the peak contact radius a_{max} cannot be measured. To overcome this we assumed a range of values from 40 um to 120 um for a_{max}. The G vs. v graphs for each a_{max} is shown in Figure 87. Although the G and v values vary considerably for each different a_{max} the shape of the G vs. v relation stays the same. The arrows indicate the location of the peak adhesion and the unload curves are the same shape as those for alumina. This suggests that whereas smoothness may be a significant factor in using the JKR theory to calculate the G values, it is not the reason for the model predicted in Equation 40 breaks down for our system.

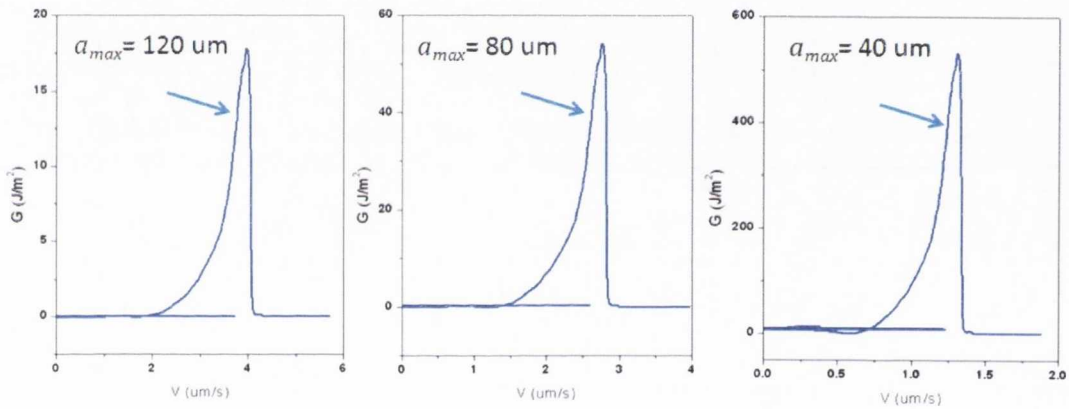

Figure 87. G vs. v values for a 10 mN test on SiO_2. There is no visible contact impression for this material so the data is shown for three possible maximum contact radii, 40 um, 80 um and 120 um. Although both the G and v values are different for each a_{max} the shape of the curve remains the same. This shape matches the alumina data rather than that predicted by equation 40 suggesting that the relative smoothness of the materials is not the main factor why the model breaks down for our system.

3) Another possibility regards the finite sized correction of the tip film. The tests discussed so far in this chapter have all been done with tips which have a PDMS layer of 20 um. Another tip was created for comparison that had a 50 um layer of PDMS on it. Figure 88 shows a comparison of a 1 mN test done with the thicker tip compared with the standard thickness tip. The tips were loaded to 1 mN peak load as they were less likely to experience the effects of the PDMS film compression less than at the higher loads. The arrows indicate the location of the peak adhesive force on the curve. Although the standard tip still deviates in shape from the model predicted by Equation 2 the thick tip data exhibits a much more reasonable match to the model. The data is at no point convex in shape and assuming the tip remains in contact with the alumina after the peak adhesion point has been passed, shows a reasonable match to the shape of the G vs. v

data in Figure 85. The data in both graphs have been scaled to have the same aspect ratio. An attempt was made to fit the data to Equation 40 as shown in Figure 89.

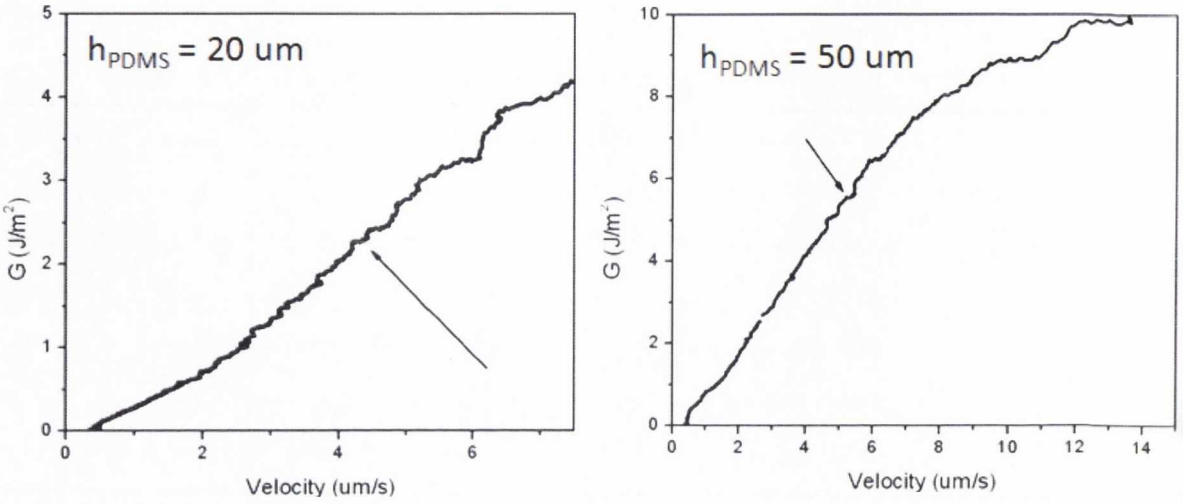

Figure 88. *G* vs. *v* for tips on alumina with different thicknesses of PDMS layer. Again the arrows indicated the peak adhesion force on the curves. The standard thickness tip which is used in the vast majority of work in this thesis has a layer of PDMS which is 20 um thick. This is compared with a tip which has a 50 um layer of PDMS. These test are both conducted at low loads of 1 mN where the effect of confinement of the layer is at its lowest. The thicker tip clearly shows a shape much closer to that predicted by the model from Equation 40.

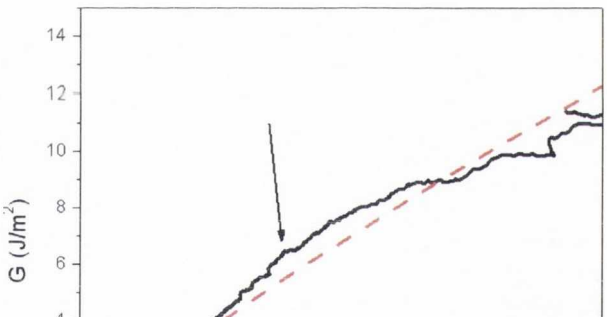

Figure 89. Attempt at fitting the data for the thick tip (h = 50 um) to Equation 40. The red dashed line indicates the fit line and the black arrow shows the location of the peak adhesion force.

This fit yielded values as follows: G_0 was measured to be 0.01 J/m^2, v^* = 3 nm/s and the scaling parameter n = 0.85. Table 1 shows a comparison of the fitting parameters measured for glass on PDMS by Shull *et al* [63] and gold peeling from glass by Rogers *et al* [46].

G_0 is a measure of the critical energy release rate which needs to be overcome to initiate debonding. The values for the gold on glass and the glass on PDMS are much higher than what we predict in our fit. In the case of the gold film however G is only measured in the regime where the

gold is peeling from the glass, which started at a minimum value of 3.5 J/m^2. G_0 is sensitive to the surfaces involved and one would expect the critical debonding energy to be higher for materials that are better adhered to one another. In the case of the literature featured here, all the surfaces involved were treated to increase the adhesion at the interface which could explain the higher values. The v^* value is the characteristic crack velocity for the materials. It is a measure of the dissipation occurring at the crack tip through bulk dissipation and interfacial effects such as contact charging [60]. The value we measure is similar for the experimental work done by Shull indicating that the dissipation in the PDMS with alumina is of a similar level as PDMS and glass. The scaling parameter for our work is somewhat larger than predicted by Maugis [38] who predicts values of 0.5 – 0.6 for elastomers.

Table 1. The fitting parameters from fitting equation 3 to Figure 16 for different peak loads.

Peak Load	G_0 [J/m^2]	v^*	n
PDMS from Glass (Shull *et al* [63])	0.1	2.5 [nm/s]	0.5
Au film peeled from glass (Rogers *et al* [46])	2.16	1.55 [cm/s]	0.65
PDMS from Alumina	0.01	3 [nm/s]	0.85

Although Equation 40 is predicted to be valid for low velocities it is possible that the relatively weak adhesion between the PDMS and the alumina in our experiments means the test ends before a high enough velocity is reached to verify the model. Experimentally this could be tested by treating the PDMS and/or alumina to increase the adhesion between the interfaces so that higher velocities could be measured between them.

That aside the most likely cause of the break down in the model is due to *the confinement of the PDMS layer between the silicon sphere and the contacting material.* The correction used is based on a flat confined layer rather than one following the contours of the sphere and it is possible that there are additional geometry effects which need to be taken into account. Although PDMS is often described as being an elastic material in the bulk, with its viscoelastic properties only becoming apparent at the crack tip [14 4], it is possible that confining the film reduces its ability to behave as an elastic material. In this case the viscoelastic properties may become more apparent requiring modifications to the JKR theory.

The experimental transfer work done in this thesis has all been conducted with tips that have a PDMS layer of 20 um. Therefore Equation 41 may not be applicable to our transfer events using a thin PDMS film rather than a bulk stamp. Ideally however our calculation of G needs to be improved, either by additional corrections to the JKR theory, or by developing a new theory to describe this system. The next section will describe an attempt to correct for viscoelastic effects in the JKR theory using the analysis done by Doi *et al* as described in Chapter 2.

Correcting for Viscoelasticity in the JKR Theory

We will now revisit some of the ideas introduced in Chapter 2 based on the work of Doi *et al.* In that experiment the author contacted pure PDMS spheres to glass and measured the contact angle and contact radius directly. They applied this data to a modified JKR theory which had an *apparent surface energy* w_{app} to account for the viscoelasticity in the system. What follows is an application of the same analysis to the alumina and SiO_2 tests already introduced in this chapter.

In using the JKR theory, thermodynamic equilibrium of the material in contact is assumed. Schapery [79,110,111] and Maugis and Barquins [38] suggest using an *apparent surface energy* w_{app} which is the work needed to separate a unit adhesion area of the adhering surface. For time dependant materials, this value is not constant and depends on the crack velocity v. The apparent surface energy can be calculated from the JKR theory by

Equation 42

$$w_{app} = \frac{3K}{8\pi a}\left(\frac{a^2}{R} - d\right)^2$$

where K is an elastic constant which depends on the elastic modulus, a is the contact radius, R is the curvature of the spherical indenter and d is the displacement.

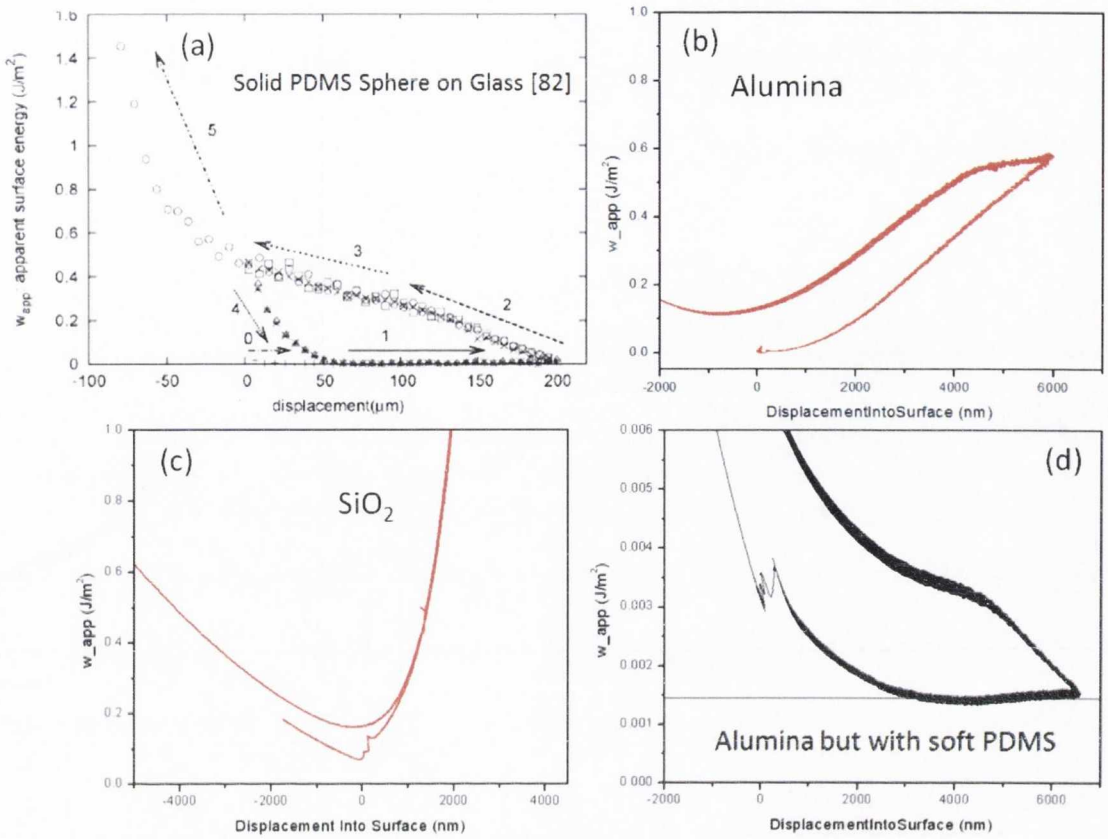

Figure 90 shows the calculated apparent surface energy for various materials. (a) is the data generated by Doi *et al* for their solid PDMS sphere on a glass slide. The authors state that their PDMS is very soft with an elastic modulus of $9x10^{-2}$ MPa. The load-up data indicated by arrow 1 is completely flat with a slope almost equal to zero which indicates that only surfaces forces are at play with no contribution from adhesion. It is also constant on the load-up and can therefore be considered a value for the surface energy between the PDMS and the glass. The unload data is completely different however and differs widely with displacement which indicates that there is a variable adhesion contribution to the data.

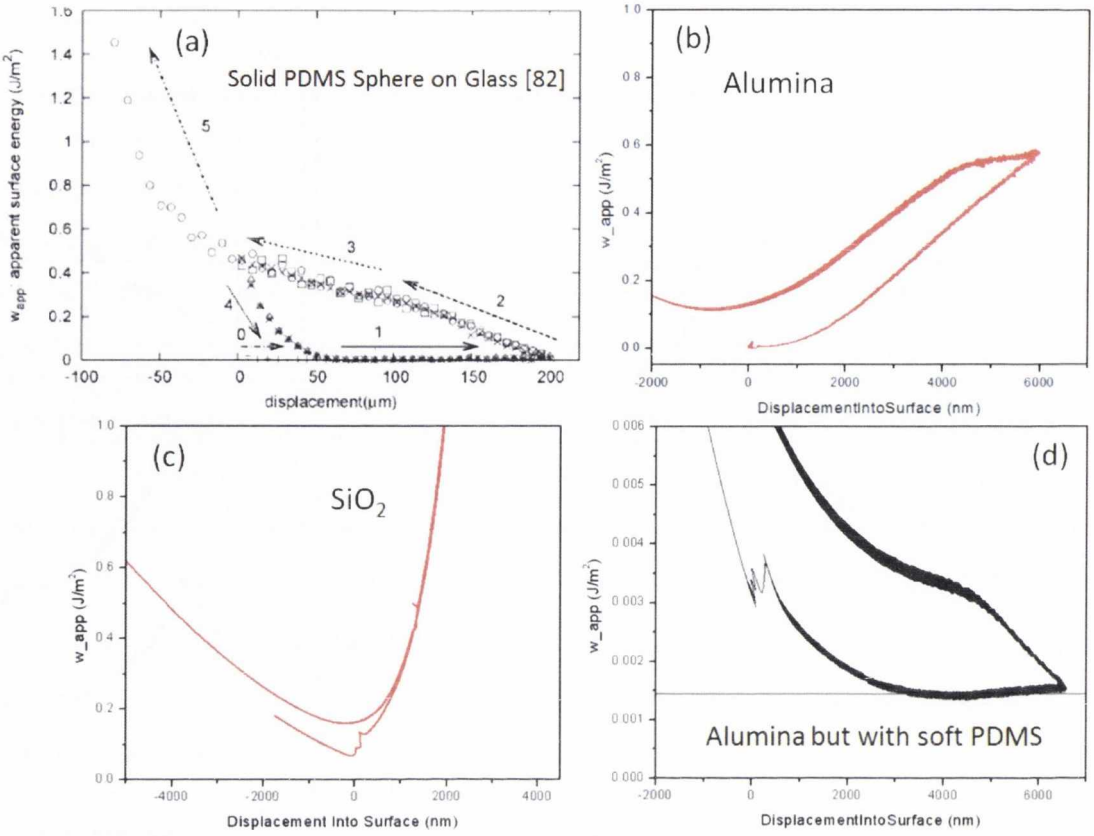

Figure 90. Apparent surface energy calculated from equation 42 vs. displacement. (a) is the data done by Doi *et al* [82] with soft PDMS on glass. (b) and (c) were done with our tips on alumina and SiO_2 respectively. (d) was done with one of our tips whereby reducing the cross-linker ratio the PDMS was made very soft. The load-up indicated by arrow 1 in (a) gives an indication of the surface energy of the contact without any adhesive contributions.

Repeating this analysis on alumina and SiO_2 for our custom tips we found that whereas the hysteresis is quite evident the apparent surface energy for the load segment is not constant suggesting that adhesion is present on the load up segment. This means this data cannot be used exclusively to estimate the true surface energy of the contact. This is the case both for the alumina and the SiO_2 which suggests that roughness is not the mitigating factor. It is possible that the geometric confinement of the PDMS due to its thin film status combined with the higher elastic modulus could be a factor. To test this, a test was done on alumina with one of our custom tips where the level of cross-linker was reduced to 1/3 of the normal level. Assumptions were made as to the elastic modulus and conversion factor but as can be seen this data exhibits the same constant w_{app} on the load up, which is indicated by the black line. It is likely that we made an incorrect assumption for the conversion factor which is why the data is not closer to zero. However it is the shape that we are interested in here. We found that using a lower elastic modulus for the data in

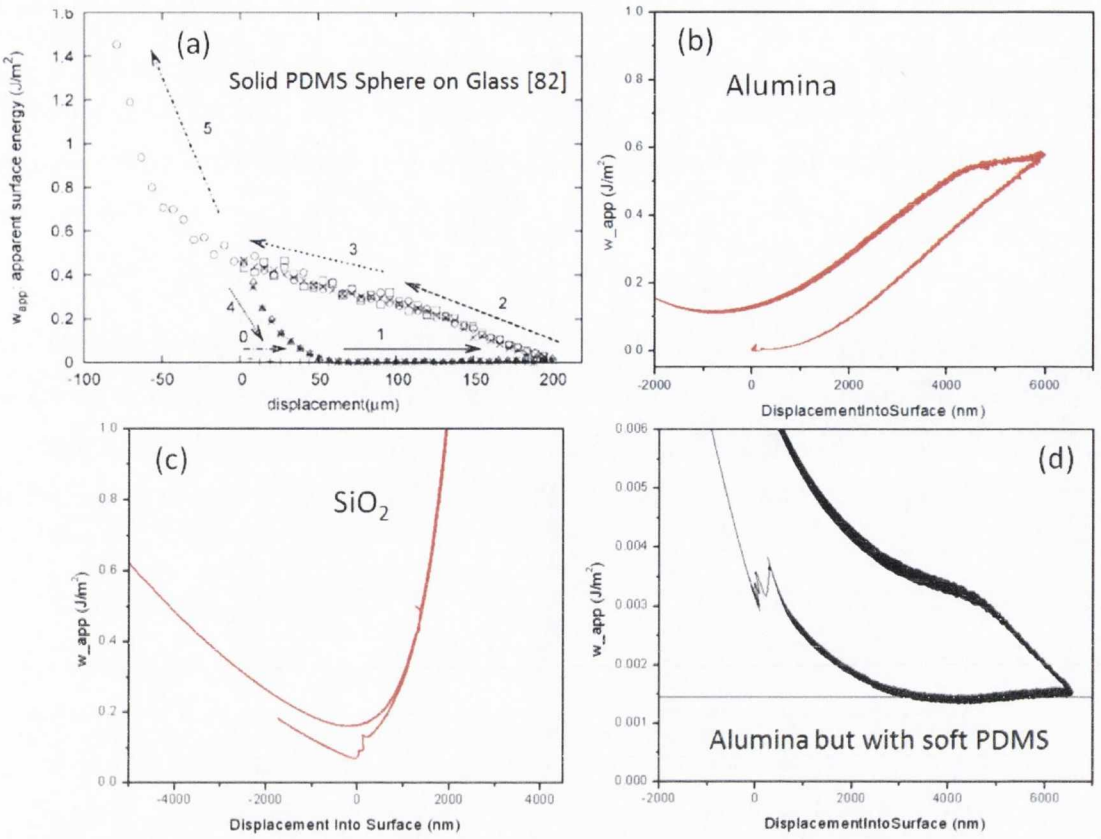

Figure 90 did not yield a constant value for w_{app} on the load up but just shifted the data relative to its present position. This shows very clearly that the softness of the PDMS is a factor as to whether using the apparent surface energy in the JKR theory will yield true surface energy values. The "softness" of PDMS in our case can be considered a combination of the confinement of the PDMS film on the silicon sphere and/or the value of the elastic modulus.

We have discussed the dependence of adhesion on the peak load and the unload rate. We have also discussed how the crack velocity and changes for those parameters and for different materials. The last topic to consider in this chapter is that of the tip geometry which is discussed in the next section.

4.5 PDMS Layer Thickness

The overall aim of studies on alumina is to understand how the experimental system may be optimised to facilitate transfer. A story is emerging of a delicate balance between the inherent adhesion in an interface and the dynamics occurring as that interface is modified due to removing one material from another. So far in this chapter we have examined the different parameters which may affect the adhesion and the crack interaction of PDMS with a material. We have investigated the role of smooth versus rough materials, peak load, contact location and rate of unload. Tip geometry is one more parameter which can be investigated and a simple way of

adjusting the geometry is to change the PDMS thickness h_{PDMS} by varying the spin speed parameters when creating the tip. The tip thickness can be measured after testing by indenting the tip itself with a cube corner indenter tip as described in Chapter 3. The tip thickness can also be measured optically by tearing off a small section of the PDMS and measuring it under the microscope. For the majority of the tips used in this thesis, and for all those used in inking experiments the thickness of the PDMS was found to be approximately 20 um.

The following discussion examines aspects of tip thickness on the contact area, the peak adhesion force and the crack velocity dynamics during the unload segment. In Section 4.4 we saw that thicker tips (with h_{PDMS} = 50 um) began to obey the model relating the energy release rate and the crack velocity. Because we see this only for the lowest peak load for the thickest tip, only the crack velocity will be considered here.

Experimental Results for PDMS of Different Thickness

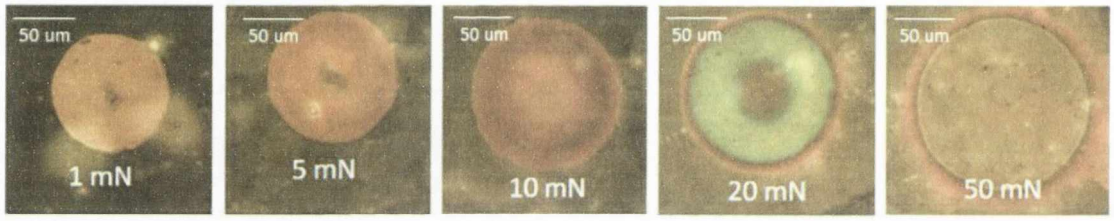

Figure 91. Images on alumina of contacts made with a standard thickness tip for different peak loads.

Three tips were prepared with thicknesses of h_{PDMS} = 8 um, h_{PDMS} = 20um and h_{PDMS} = 50 um. They are classified as *thin*, *standard* and *thick* in this discussion. Each tip was contacted to alumina for a variety of peak loads ranging from 1 to 50 mN. After testing the alumina contacts were measured carefully for maximum contact radius. **Error! Reference source not found.** shows images on alumina of contacts made for the standard thickness tips for peak loads ranging from 1 to 50 mN. Similar images were taken of the contacts for the thin and thick tips.

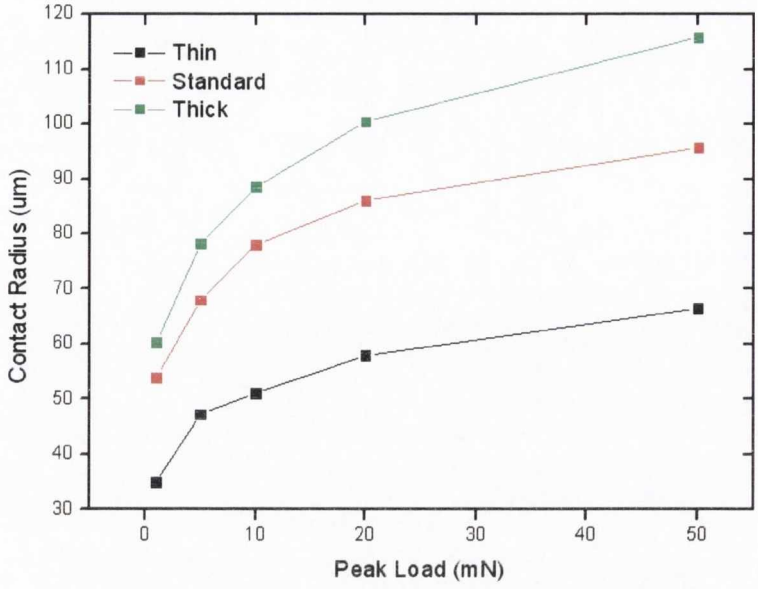

Figure 92. The measured maximum contact radius against the peak load for tips of three different thicknesses.

After testing the maximum radius of the contacts were carefully measured. Figure 92 shows the measured contact radius a_{max} as a function of peak load for the tips. For a given peak load a_{max} increases with h_{PDMS}. As h_{PDMS} increases the PDMS layer experiences less confinement between the silicon sphere and the target substrate allowing it to behave more like a bulk elastomer rather than a thin film. Therefore the stiffness experienced by the PDMS for a given load is lower than for a thin film which leads to a larger a_{max}. As the peak load is increased the stiffness also increases as the PDMS experiences more confinement between the silicon and the substrate. This is shown by the flattening of the data for all the tips at the higher loads.

In conventional nanoindentation tests the Displacement into Surface channel is an indication of how far a tip is indenting into the surface. However the tips we use are soft and do not indent into

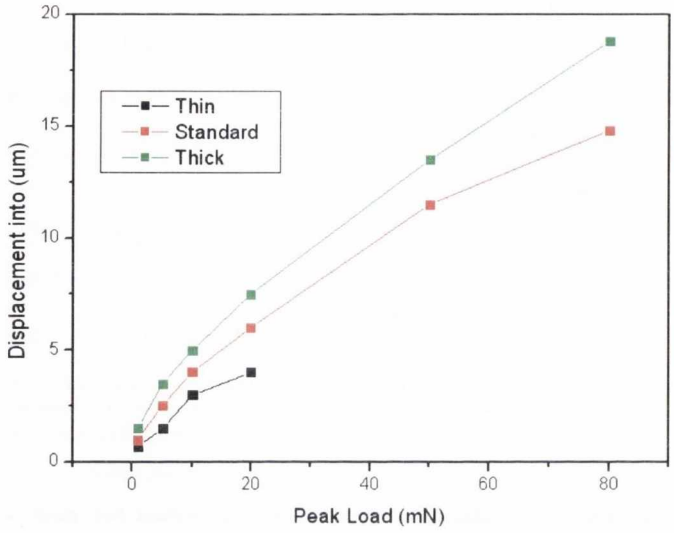

Figure 93. Comparison of the displacement of the PDMS layer as a function of peak load for each of the three tip thicknesses. The flattening of the data for higher peak loads indicates the confinement of the PDMS layer becomes more significant. The divergence in the curves between the three tip thicknesses shows the degree of significance confinement causes to the Displacement channel.

our samples at all. In this case, the Displacement into Surface channel must be considered as how far the tip is *compressed* by the surface it is in contact with. This provides a clue as to how thick the PDMS layer is. If the PDMS layer were infinitely thick, a plot of the Displacement versus Peak Load would be a linear plot through the origin and all the compression would be due only to the flat sample. Figure 93 shows the Displacement channel versus Peak Load as measured by the indenter for each tip. Examining the higher loads it is apparent that the thicker PDMS tip has a more linear relationship than either the standard or thin tips. This would suggest that for the loads being tested (up to 80 mN) the thick tip behaves more as though it had an infinitely thick layer of PDMS. The standard tip also follows this behaviour up to 50 mN after which is begins to

flatten, suggesting that the PDMS is being squeezed more at 80 mN than at 50 mN. This effect is even more pronounced for the thin tip. A sharp difference can be seen in the data between 10 mN and 20 mN indicating that the squeezing effect is being felt much more significantly by the thin tip.

Error! Reference source not found. shows the peak adhesion for each tip for each peak load. There is a significant difference in adhesion between the thin tip and the other two. The PDMS thin films have two components, a bulk elastic component which dissipates mechanical energy easily and a short range viscoelastic and surface force component. If the bulk component behaviour is repressed due to the high confinement of the thin film, then the adhesion will be dominated by the surface forces for a static contact as illustrated in the Figure. Therefore the adhesion is significantly lower for the thin tip.

Figure 94. Peak adhesion force vs. peak load for the three tip thicknesses. The peak adhesion force is significantly suppressed for the thinner tip. The PDMS layer may be too confined for energy dissipation to occur easily thus reducing the adhesion. Any adhesion which is measured for such a confined film will be dominated by the surface forces between the PDMS and the alumina.

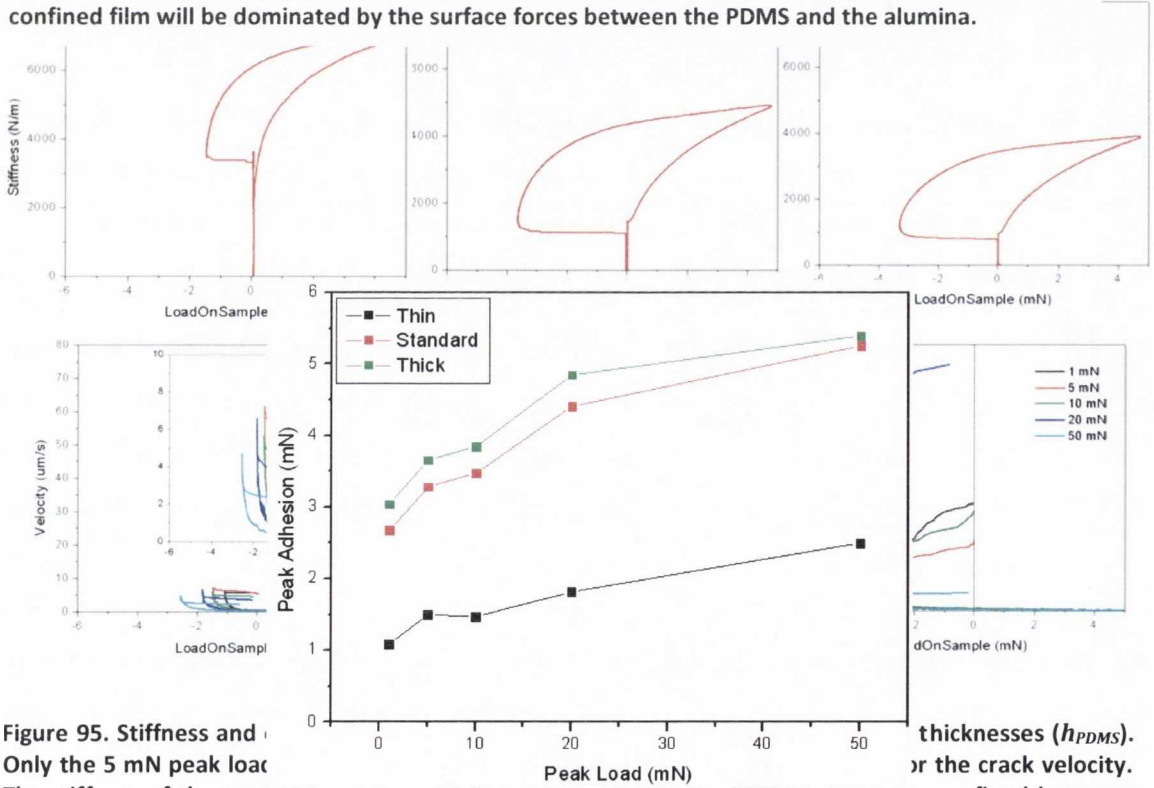

Figure 95. Stiffness and thicknesses (h_{PDMS}). Only the 5 mN peak load or the crack velocity. The stiffness of the contact increases with lower h_{PDMS} due to the PDMS being more confined between the silicon sphere and the substrate. This effect increases for the thicker tips. The range of magnitude of the crack velocities between the thinnest tip (h_{PDMS} = 8 um) and the thickest (h_{PDMS} = 50 um) exhibits a full order of magnitude difference.

An important consideration for transfer is the crack velocity between the PDMS and the target material. A critical energy release rate is needed to initiate transfer. Although calculating G remains a challenge, its value depends on the crack velocity v. Therefore it may be possible to define a critical crack velocity v_{ink} which will initiate transfer. Although all the transfers in this thesis used a tip with a PDMS layer h_{PDMS} = 20 um, it is important to understand how h_{PDMS} can effect crack velocity. Figure 95 shows the stiffness and velocity vs. load data for tips with h_{PDMS} = 8 um, h_{PDMS} = 20 um and h_{PDMS} = 50 um respectively. Only stiffness curves for 5 mN have been shown but the v data for a range of peak loads from 1 to 50 mN are shown. The stiffness increases with load for the thinner tips as would be expected. This is because the PDMS is more confined between the silicon sphere and the substrate.

Before discussing the different crack velocities between different tips is it important to note that for a single tip, the crack velocities for each peak load test remain the same for the *compressive* part of the unload at a value close to zero. This is true for all the tips even the thinnest one indicating that the crack is opening at a steady state for this region of the unload. This behaviour continues until the tips begin to experience the peak adhesive force. The peak adhesive force is different for each peak load but the *rate of change of the crack velocity* remains the same up until this point for all the tips. After this point the rates of velocity for each peak load test diverge which could be due to instability in the data, and/or different necking rates of the PDMS at this point. A proper understand of this region can only be gained with direct measurements of the contact radius throughout this portion as opposed to relying on the stiffness data.

For a single tip of a particular thickness the implications of this analysis are that the peak load of the test *does not influence the crack velocity* during the test up until the peak adhesion point. However examining the velocities between tips of *different thickness* it can be seen that the range of crack velocities of the thin tip are a full order of magnitude less than for the thick tips. This is to be expected as the PDMS has less freedom of movement across the interface. As before its confinement means the bulk component of the PDMS is suppressed. This means that it is more difficult to dissipate energy and the viscoelastic component at the crack front dominates. Viscoelasticity resists mechanical movement on a short time scale thus impeding the material propagation at the crack front. Therefore adhesion effects at the crack front likely to be due to surface energy and viscoelastic effects rather than energy dissipation in the PDMS.

The implications of this analysis are that for greater adhesion and greater crack velocity one needs to use thicker tips that can easily dissipate energy during the unload. However the confinement of the film may provide potential for using surface effects to control the interface. In

this system there may be totally different contact mechanics at play where we move from a JKR type system to perhaps a DMT system. It is possible that only surface effects influence transfer which allows for greater tunability in the transfer system. Removing the dissipative element of the bulk elastic PDMS might allow for an intensive study based only on surface energies and viscoelastic effects shedding new light on the processes that occur at the crack tip between interfaces.

4.6 Chapter Summary

This chapter showed how PDMS behaves on different solid materials in order to understand the effect of changing materials and mechanical parameters. Several aspects of this problem were examined and a summary of the results is as follows:

1. Relating the *measured* stiffness channel to the *calculated* contact radius channel

   We showed that although we cannot measure the contact radius directly throughout the test, Sneddon's Equation can be used to relate the contact radius to the stiffness channel as $a \sim S$ once we have a visible contact impression. The video data analysis verifies that this relation is accurate for our system.

2. Observation of the PDMS neck formed as the tip unloads from the surface

   The video data provided evidence of a distinct neck forming in the PDMS as it unloaded from the rough alumina. This necking behaviour was not observed for smooth materials such as SiO_2. It was found that the diameter of the neck as the PDMS disengaged from the surface was related to the peak load of the test. A low peak load test yields a thin, narrow neck which lasts throughout the test, even after the load on sample channel has returned to a zero value. The higher load test creates a shorter, thicker neck and the tip disengages from the alumina almost immediately after the peak adhesion force point has been

reached. This variation in neck size at uncontact, due to the loading parameters is of great importance when discussing transfer of CNTs in Chapter 6.

3. Adhesion response to a change in mechanical parameters or materials

   The adhesion between the PDMS and the target sample was investigated by changing samples between rough and smooth, or by changing the mechanical parameters in the testing method. Parameters such as peak load, testing location and unload rate were all investigated for their effects on adhesion. The crack velocity between the unloading PDMS crack and alumina was also investigated. It was shown that the crack velocity was unaffected by the peak load or peak adhesion in the test and it was shown that increasing the unload rate of the test did not necessarily mean an increase in the crack velocity as shown in Figure 84. This observation is very important for understanding the optimum parameters needed to initiate transfer in Chapters 5 and 6. The main influence on the crack velocity came from the thickness of the PDMS tip used whereby the thicker tips experienced greater crack velocity.

4. Calculating the energy release rate for our experimental set-up

   We found the using the JKR theory to calculate G was inadequate for our tests. The main problem was due to applying the JKR theory to a thin film configuration such as PDMS as opposed to a bulk PDMS stamp. Confinement of the thin PDMS film between the silicon sphere and the solid contact sample changed the energy dissipation within the stamp and valid values for G could not be measured. The effect lessens for thicker tips at low loads but reliable G values were unattainable. Therefore the discussion of transfer in the next two chapters will revolve around the crack velocity more so than the energy release rate.

4.7 Conclusions

Although a model describing the energy dissipation and full adhesion between thin film PDMS tips and solid surfaces remains elusive at this time, experimental techniques were developed and analysed that allows for transfer to be studied in a detailed manner. We have shown the effect that changing mechanical parameters has on the PDMS/material interaction and how we many measure the contact size throughout testing. The next two chapters will extend this knowledge to transfer problems involving networks of silver nanowires and carbon nanotubes. Parameters facilitating the transfer of these materials will be discussed and compared. Although both

materials consist of networks of cylindrical nanomaterials their transfer behaviour is vastly different. The AgNWs behave as discrete objects loosely bound together and their transfer is facilitated by one set of parameters. The CNT films however behave as cohesive thin films which need to be fractured before transfer can occur.

Chapter 5 Transfer of Silver Nanowires

5.1 Introduction

Nanowire films have great potential in plastic electronic applications due to their superior electrical and tensile properties as outlined in Chapters 2 and 7. Generally nanowires are processed in one location and then have to be transferred to another for use in devices. Techniques for doing so include spraying [112], inkjet printing [113] and printing using an elastomer stamp as is introduced in this thesis. We have successfully inked and printed circular sections of silver nanowires using custom PDMS nanoindenter tips. We can control the size of the inked nanowire sections and can accurately pick and place them with an error of only a few microns.

Initially, attempts were made at transferring AgNW films using a bulk PDMS stamp by hand. The nanowires in dispersion had been filtered onto a porous alumina membrane and a bulk stamp was brought into conformal contact with the film and peeled off. Films of two thicknesses were created using the method outlined in Chapter 3. The film thicknesses were approximately 150 nm and 400 nm thick respectively. Inking the PDMS stamp was accomplished on the first attempt in both cases and the 400 nm thick film was successfully printed onto the PET destination substrate using a hot plate as outlined in Chapter 7. Having achieved a smooth and successful transfer event the next step was to use the nanoindenter to facilitate the inking process.

As with previous materials, the analysis of inking events was performed considering the applied and measured channels of load, displacement and stiffness and calculated channels such as contact radius a and crack velocity v. The events were observed using a side-on video camera which provided information about how the tip behaves in the AgNW inking events compared with how they behave on pure alumina. The properties and preparation of these films for transfer experiments are described in detail in Chapter 3.

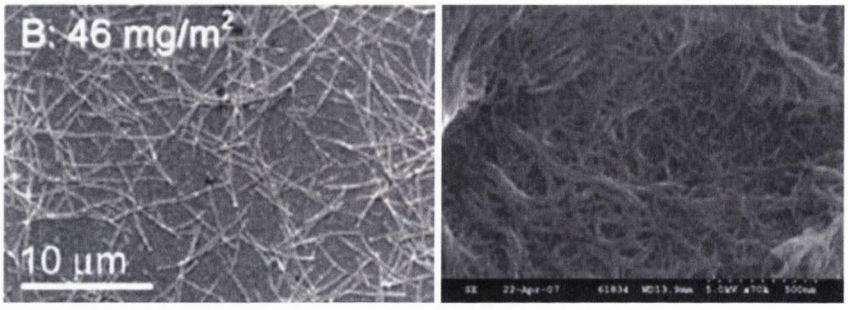

Figure 96. SEM images of AgNW films (left) and Iljin CNT films (right) showing the different in morphology between the nanowires and the carbon nanotubes.

Figure 96 shows SEM images of an AgNW film and a CNT film. Nanowire films consist of randomly dispersed rigid rods which are often compared to the configuration of dry spaghetti of different lengths which has been tossed together, creating a loosely bound network. In contrast, the carbon nanotubes resemble a picture of wet spaghetti which has conformed and entangled with itself creating a cohesive membrane type film.

We observe that AgNWs will always ink the tip for crack velocities of greater than or equal to 0.25 um/s. This is in contrast to the less straight-forward behaviour of the carbon nanotube films which will be discussed in Chapter 6.

5.2 Nanowire Inking Test

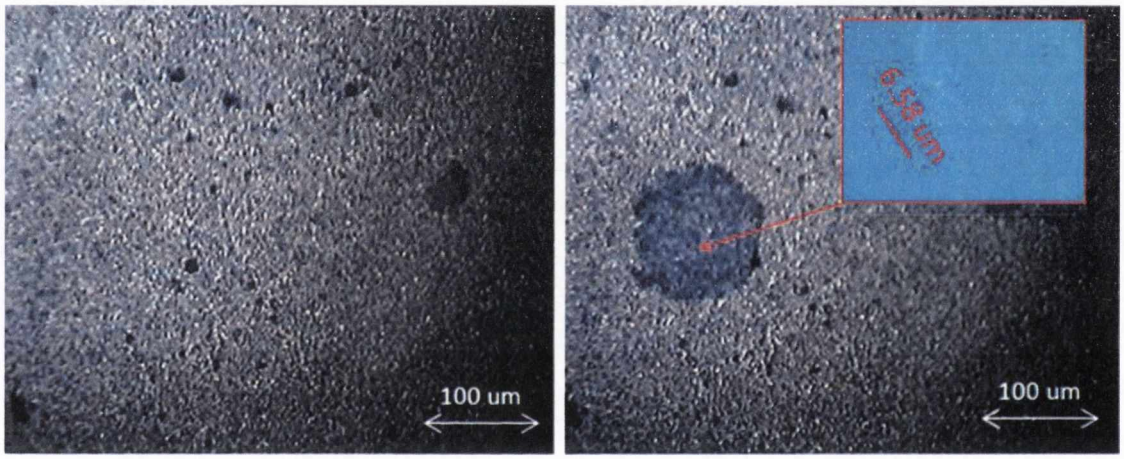

Figure 97. AgNW film before and after inking event. A circular section of nanowires with a radius of 60 um was removed from the film. The inset in the right hand image shows some nanowires left behind on the surface of the alumina after that transfer had occurred. These are scattered, individual wires and no longer form a network.

Tips with a "standard" PDMS layer of 20 um thick were created as described in Chapter 3. Testing of the tip was initially conducted on pristine alumina to find the sample height. Once this testing was completed, the tip was tested on a filtered AgNW network on alumina using the same method and surface find described in Chapters 3 and 4. This used a phase angle surface-find with the harmonic displacement set at 50 nm and the frequency of the dynamic mode set at 45 Hz.

For the test shown in Figure 97 the tip was loaded to a peak load of 20 mN and held for 10 seconds before unloading at a rate of 0.1 mN/s. A circular section of AgNWs inked the PDMS tip and had a radius a_{ink} = 60 um. Figure 97 (b) shows the film after the test has completed. A circular region is visible where a section of nanowire film with a radius of 60 um was removed. This radius is termed the *ink radius* a_{ink}.

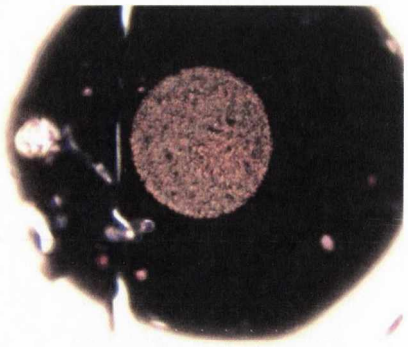

Figure 98. AgNW section on a PDMS tip. As can be seen in this dark field image the nanowire film appears quite opaque and relatively even.

Before considering the transfer mechanism in detail one must consider the nature of the network itself. Does it behave like a cohesive film which undergoes fracture and peeling as is the case of inking a viscoelastic polymer film as seen in the work of Shull's group [63]? Or does it behave like an array of rods which have little or no interaction with one another, demonstrating an inking process more akin to picking up scattered needles with a piece of sticky tape? This would then follow the kind of behaviour described by the Rogers group [46,52] where individual objects are inked to the tip. As explained previously, nanowires have a tendency to bundle due to van der Waals interactions. At the same time, they are rigid rods which lack the flexibility to entangle with one another in the manner that carbon nanotubes do. The nature of how the nanowires interact with each and hence the film itself is an important consideration when analysing transfer.

Another aspect to note is the mottled appearance of the underlying alumina after the section of nanowire network has been removed. Investigations done in Section 5.4 will identify this as PDMS cross-linker passing through the porous network. Figure 98 shows a dark field image of an inked nanowire region on a PDMS tip. As can be seen the layer on the tip appears opaque, indicating that a significant amount of the nanowires within the ink contact area were picked up.

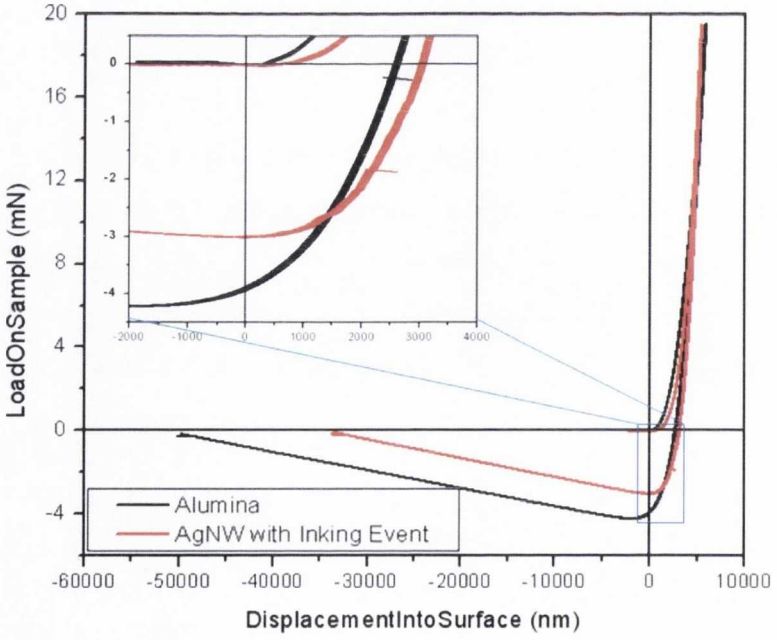

Figure 99. Load-displacement curves for alumina and the AgNW inking event with a peak load of 20 mN. Both tests were done with the same tip. The alumina test was conducted first.

Figure 99 shows a comparison of the load-displacement (L-D) curves for alumina and for the AgNW inking test, *both of which were conducted using the same tip*. The convention with data from the nanoindenter is to designate the compressive part of the test with positive load and displacement values and the tensile (or adhesive) part with negative load and displacement values. Although we generally describe the regions above the *x*-axis as "compressive", it is important to remember that the PDMS stamp may be experiencing both compressive and tensile forces. The inner part of the stamp is under compressive load however the outer periphery experiences tensile forces which allow the crack to open at the interface between the stamp and the substrate. It has been shown in Chapter 4 that the nanoindenter may have a segment of instability during the unload portion following the peak adhesion point. The video data shows that tests on alumina loaded to a low peak load value such as 0.3 mN create a long narrow neck during the unload segment which reaches an approximate value of 2 um radius before disengaging from the substrate after the load on sample has returned to zero. However for tests loaded to a higher peak load such as 10 mN or 20 mN as shown in Figure 67 the contact radius at disengagement is closer to 40 um and occurs very soon after the peak adhesion point has been reached. An arrow on the figure indicates the point beyond which the unload data for 10 mN tests is not reliable.

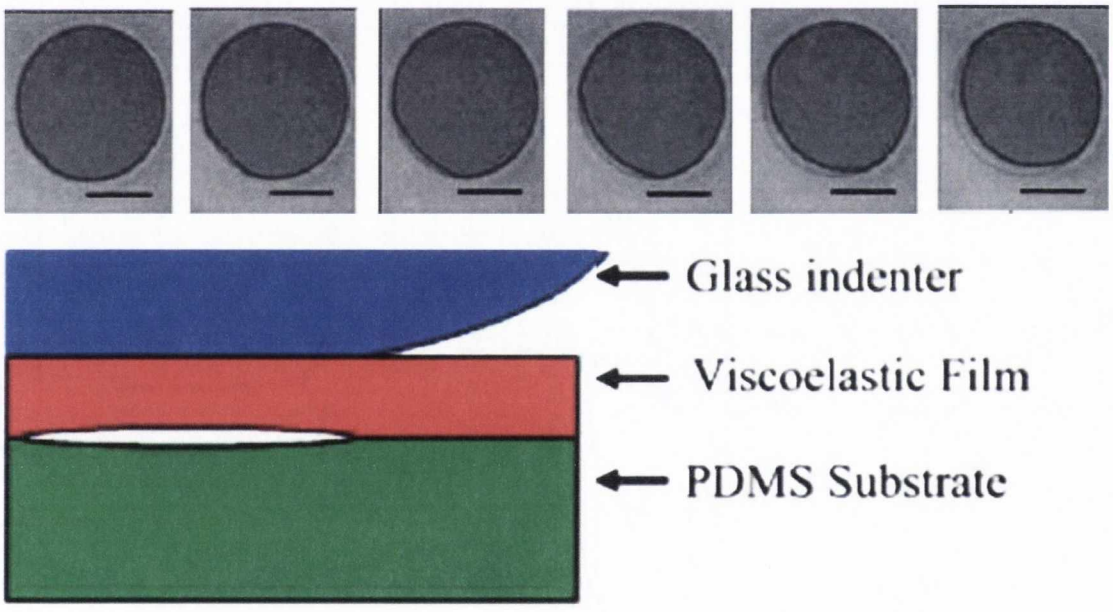

Figure 100. Images from Shuli *et al* [62] showing the change in contact area during the inking of a polymer film with a glass indenter sphere. The top images show photographs of the contact as the indenter tip is unloaded from the sample. Note the asymmetric decrease in the contact, whereby the lower left-hand side peels during the unload. The lower image is a schematic illustrating the formation of a cavity between the polymer film and its PDMS substrate, as the glass indenter sphere is unloaded.

What is initially striking about the adhesion data is the difference in the peak adhesion force for both tests. In this case the alumina has a peak adhesion of -4 mN whereas the AgNW test has only -3 mN. The second thing to note is the shape of the unload curve as it approaches the peak

adhesion. This is illustrated in the inset. Whereas the alumina has a typically smooth unload curve, the nanowire curve exhibits quite a jagged looking behaviour. The calculation of the contact radius during the test which is to be discussed presently shows that the inking event took place soon after the unload segment began. The jagged appearance of the curve begins after this point. It is most pronounced in the peak adhesion force regions and is compared with the work done by Shull *et al* [62] in **Error! Reference source not found.**. As was discussed in Chapter 1 and Chapter 2, Shull *et al* inked a glass spherical indenting tip with a thin polymer film that was coating a slab of PDMS. In this case, the tip was retracted creating a cavity between the PDMS and the polymer film as illustrated in Figure 100.

Also visible in this figure is a series of images showing how the contact area of the polymer changed during the test. A camera was placed below the transparent PDMS substrate to image the contact. The dark outline in each of the series of micrographs is the contact boundary between the glass indenter and the polymer and the lighter outline shows the contact boundary between the polymer film and the PDMS substrate.

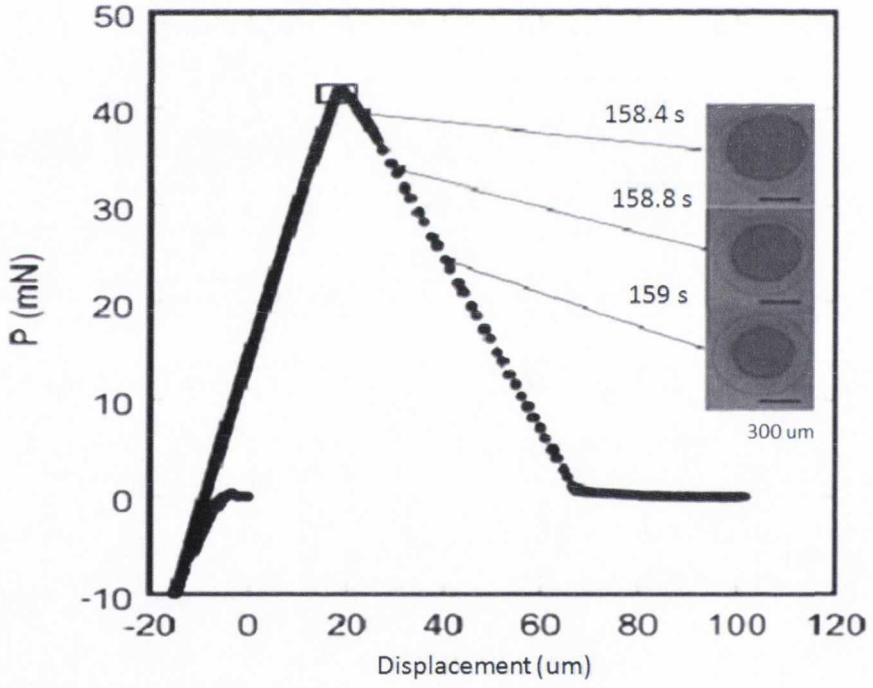

Figure 101. Load-displacement curve for the test described in Figure 5 [62]. Also shown is how the contact area changes during the test. Note that in this case the authors express the adhesive load and displacement with a positive sign, in contrast to our tests where we use the convention of negative load and displacement in the adhesive regime.

Error! Reference source not found. shows the load-displacement curve corresponding to this experiment with photos of the contact at various points along the curve in the adhesion region. Note that in contrast to the convention used with the nanoindenter the authors express the adhesive load and displacement with a *positive* sign. Although we are unable to photograph the contact area during the test as done by Shull *et al*, comparisons can still be made between the mechanical curves measured by the authors and in our work.

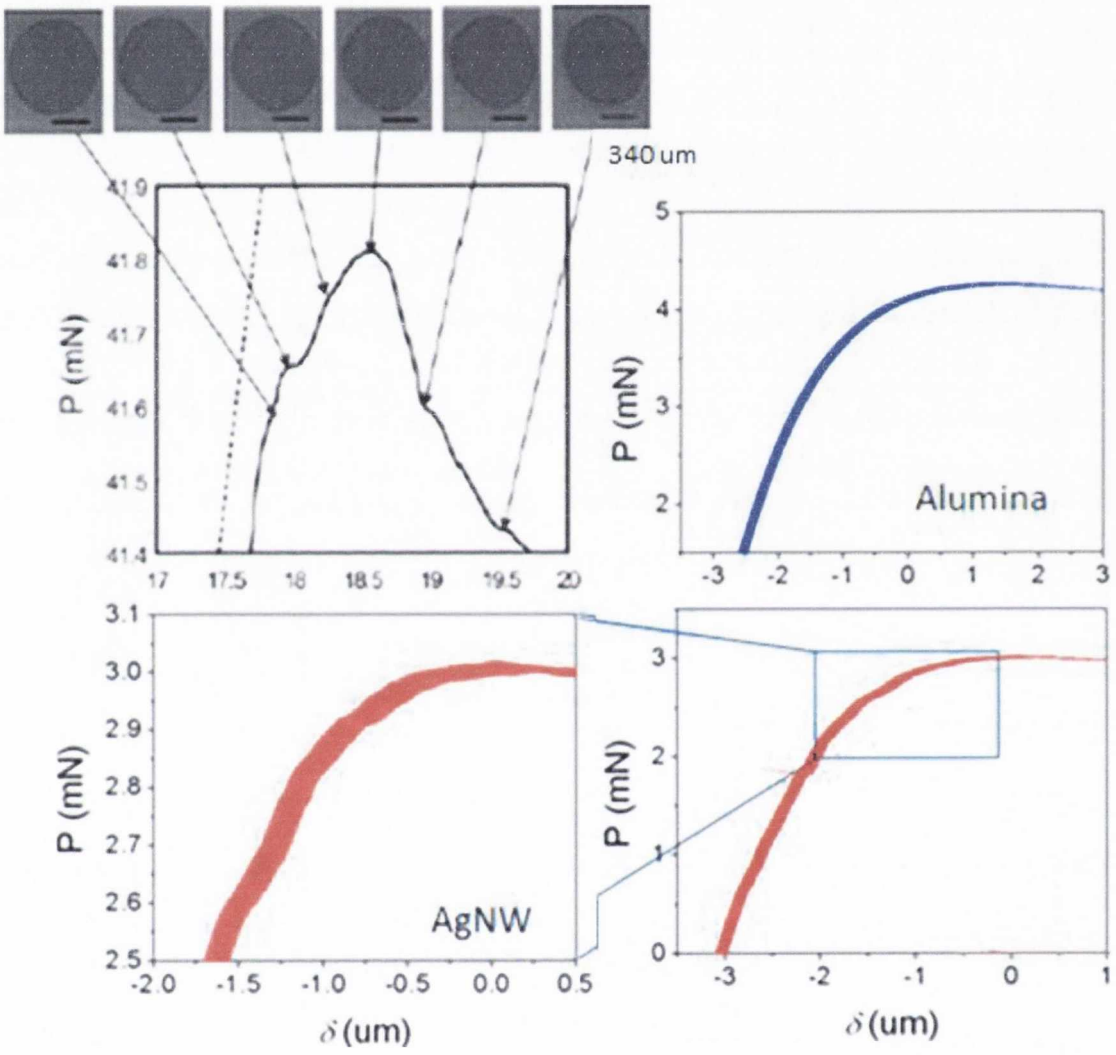

Figure 102. Comparison between work done by Shull *et al* [62], one of our alumina tests and the AgNW test showing a comparison of the behaviour of the load-displacement curves in the adhesive regime. In the Shull test on the top left hand corner, images are shown of the contact as the tip approaches and passes the peak adhesion force i.e. where the adhesive load is a maximum. The Shull test shows significant jagged peaks as the polymer film peels from the PDMS substrate.

AgNW tests. Although both

Error! Reference source not found. compares the behaviour of the load-displacement curves for the tests done by Shull *et al*, one of our alumina tests and the AgNW test. Shull's test exhibits a strongly jagged curve near the peak adhesion force with deviations from a smooth path corresponding to the peeling of the polymer film from the underlying PDMS substrate. Our alumina test in contrast exhibits a completely smooth L-D curve in the same region whereas the AgNW film also displays a certain amount of jaggedness. The AgNW film and the alumina membrane have similar surface roughness. Comparing the smoothness of the alumina test with the AgNW test shows that the roughness of the substrate is not the cause of this jaggedness. As with the polymer film the source of this jaggedness in the L-D curve is likely to be due to changes in the interface between the AgNW film and the underlying alumina membrane as the PDMS tip creates a tensile force on the AgNW film. These changes could manifest themselves in the removal of individual nanowires or in the loosening of the nanowire film from the alumina membrane. Nanowires can be entangled in the alumina pores as a result of filtration and the application of the tensile force could change their mechanical interaction with the substrate.

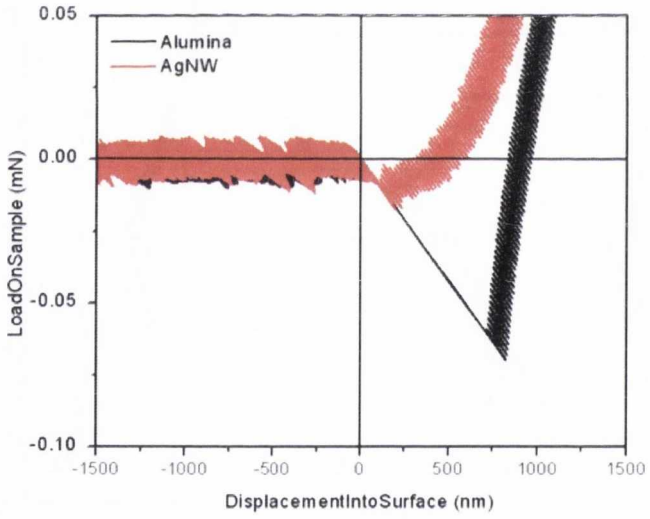

Figure 103. Jump to contact for alumina and AgNW. There is a considerable difference between the two materials with a large jump for the alumina and a supressed one for the AgNWs

Figure 103 shows the jump to contact for the alumina and the nanowire tests. As can be seen there is a significant difference. The jump to contact for the alumina occurs over a displacement of about 0.5 um, while that for the nanowires was less than 100 nm. There is also a striking difference in the loads involved with alumina jumping more than 0.05 mN whereas the nanowire load change is at least 5 times lower. This behaviour was observed for all nanowire tests compared with alumina over a range of time, tip age, and small environmental lab changes.

The jump to contact in the alumina is too long range to be explained solely by van der Waals interactions. A high Hamaker constant for a material implies a high surface energy. For alumina it is valued at for alumina at 36.9 x 10^{-21} J [114]. However silver nanoparticles have a value of 147 x 10^{-21} J [115] suggesting the surface energy of nanowires should be higher. This is only a rough assumption however as other factors involved with the nanowires may include state of oxidation, the crystalline facet of the wires and their geometry and curvature. These considerations are not studied in this work. Contact angle measurements were also conducted on the materials. Both alumina and AgNWs were highly hydrophilic which again suggests a high surface energy. Carbon nanotube films in contrast were more hydrophobic suggesting they have lower surface energy. However as will be seen in Chapter 6 the jump to contact for CNTs is similar to alumina. Therefore the jump to contact does not seem to be a factor of surface energy alone.

Another consideration is that it is unknown what exactly the AgNWs have been dispersed in as this information has not been disclosed by the manufacturer. It is possible that the surface energy of the nanowires has been reduced by whatever additive was in the dispersion. More experimental work is needed to try and understand exactly what causes the jump to contact and how the materials interact on a surface energy level.

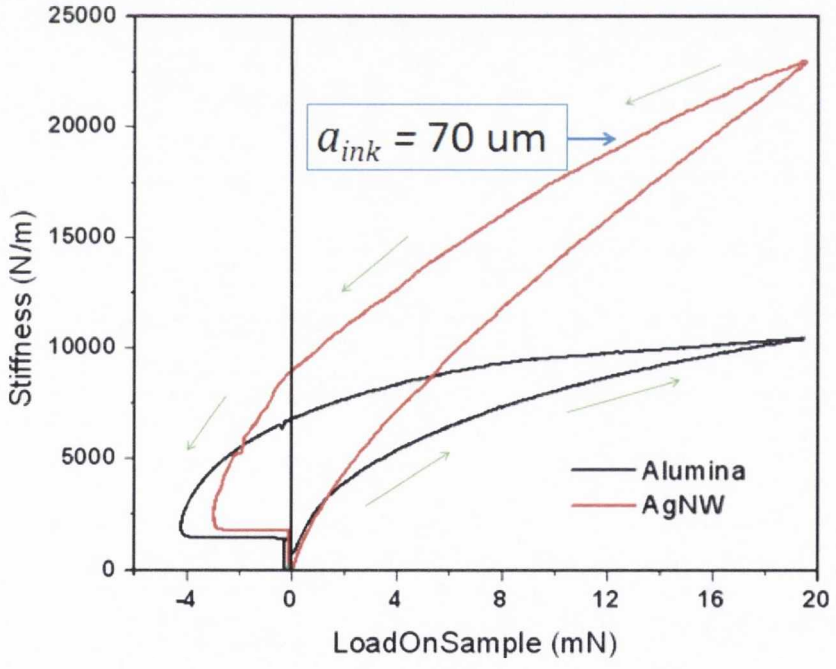

Figure 104. Stiffness-Load curves for the alumina and AgNW inking events. The green arrows indicate the direction of the load and unload. a_{ink} indicates where the AgNW began to peel during the test.

Figure 104 shows the stiffness-load curves for the alumina and the AgNW tests. Although both tests were done with the same tip, the stiffness curves are significantly different. Whereas the peak stiffness for the pristine alumina reaches only 10,500 N/m, the stiffness for the nanowire film is more than double this amount at 23,000 N/m. This indicates that the tip propagation across the two materials is different.

The stiffness data can be used to calculate the contact radius throughout the test using Sneddon's equation [75]. The maximum measured contact radius a_{max} left by the contact impression is used in combination with the maximum stiffness S_{max} to create a *calibration factor*:

$$\text{calibration factor} = (a_{max})/(S_{max})$$

Figure 105 shows the stiffness data graphed with the contact radii calculated from the calibration factor. Also indicated is the contact radius of the inked portion of the film at a_{ink} = 60 um which was measured on the film in Figure 97. The simplest mechanism for which the AgNW film could be transferred to the PDMS tip is if the film is *peeled* from the alumina substrate.

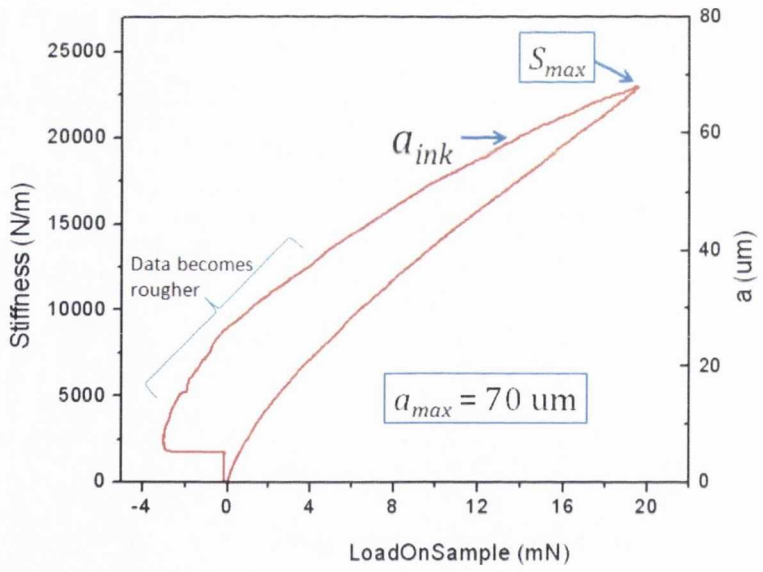

Figure 105. Graph showing the contact radius calculated with the calibration factor described in the text against the measured stiffness data for an AgNW test. The maximum contact stiffness, S_{max} is indicated. The contact radius at which inking of the tip begins during the unload is indicated by a_{max} and in this case has a value of 60 um.

If peeling has been the transfer mechanism then the irregularity in the stiffness-load curve could be due to the AgNW film being peeled back from the alumina substrate. Although the AgNW film is loosely bound to the alumina (which can be demonstrated by the ease with which one can rub the film off the alumina with a finger) surface forces and the bond created by individual wires and bundles embedded in the alumina pores have to be overcome to transfer the film. The wires

themselves could also be loosely bound to their neighbours additionally providing some additional resistance to transfer.

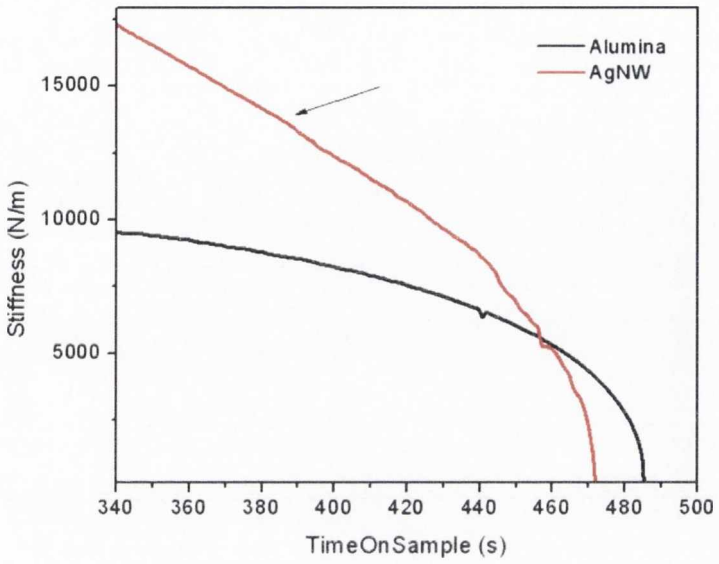

Figure 106. Comparison of alumina and AgNW unload curves for the S-L data featuring the roughness of the AgNW film compared with the alumina membrane. The arrow indicates the point during the unload after which the AgNW data becomes rough compared with that data on alumina.

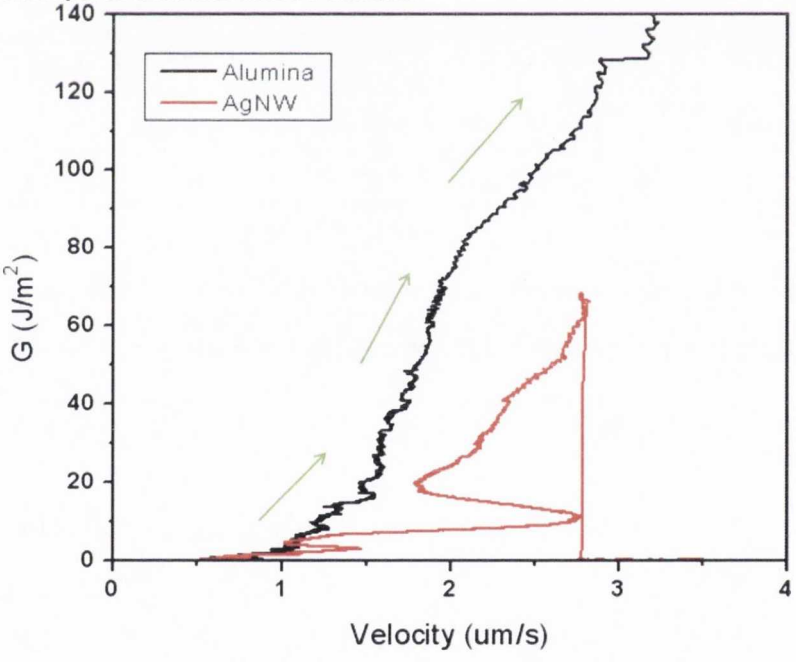

Figure 107. *G* vs. *v* curves shown for alumina and AgNW where *G* was calculated using the JKR. As was the case with alumina the curve does not follow the model described by Equation 39 in Chapter 4.

Error! Reference source not found. shows the G vs. v data calculated using the JKR theory[33]. As was the case in Chapter 4 the figure does not fit the shape predicted by

Equation 43

$$G = G_0(1 + \left(\frac{v}{v^*}\right))^n$$

indicating that our calculation of G is inadequate. The reasons for this have been discussed in detail in Chapter 4 showing the model needs to be modified for our tip configuration. We are unable to accurately estimate G, however we can still calculate v.

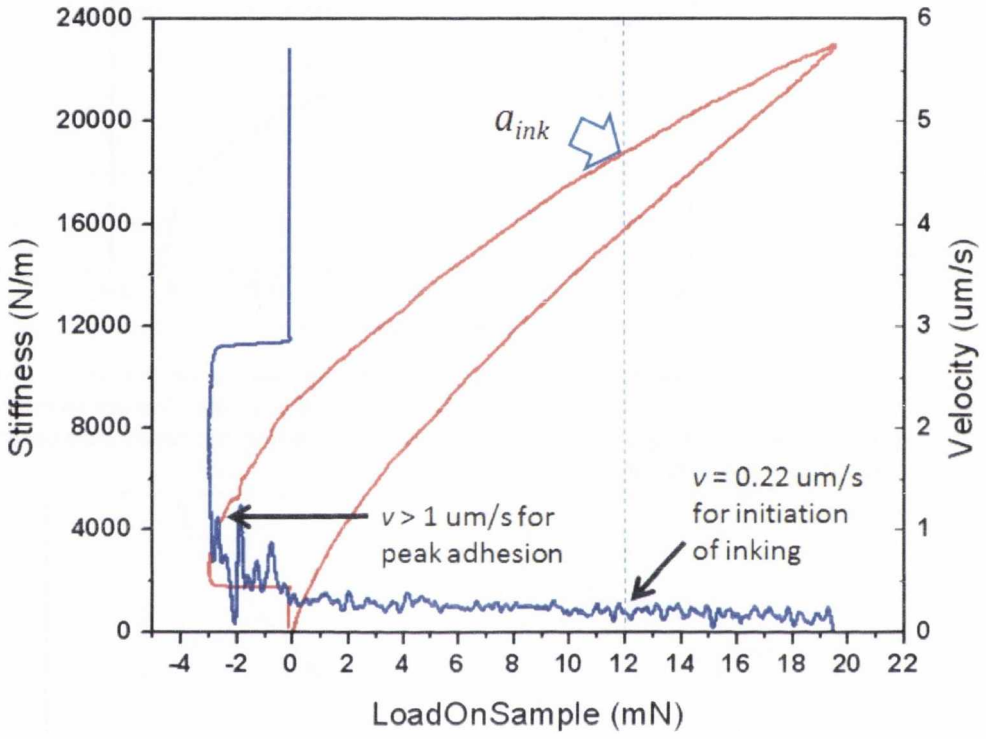

Figure 108. Stiffness curve for AgNW inking event overlain with the crack velocity data. The ink location is indicated by a_{ink} and corresponding crack velocity is v = 0.22 um/s. Also shown is how crack velocity has increased to ≥ 1 um/s around the peak adhesion force for the test.

Figure 108 shows the stiffness curve overlain with the crack velocity for given load values. Only the unload is shown for the velocity. The location of the initiation of peeling, a_{ink} is indicated and the corresponding velocity is v = 0.22 um/s. The crack velocities for inkings performed by Rogers *et al* were in the order of cm/s for silicon structures, pollen and mica structures which were sized in microns. An interesting study for the future would to investigate if the low crack velocity needed to pick up AgNWs is related to their physical size.

5.3 Kinetic Control of AgNW Inking

Work done by John Rogers *et al* [46,52] demonstrates how transfer processes can be kinetically controlled. The analysis of PDMS tests on alumina described in Chapter 4 demonstrates that the tensile nature of contact can be dynamically controlled with higher unload rates leading to higher work of adhesion mainly as a result of the viscoelastic nature of the elastomer. We now address if this dynamic control can be usefully applied to inking a silver nanowire film.

We present four tests on an AgNW film performed with different unload rates. The same compressive loading rate and peak load were used for all the tests. A peak load of 10 mN was used to ensure a large contact area was established (a_{max} = approx. 80 um). For each test, a new pristine PDMS tip from the same fabrication family was used. Unload rates of 0.1, 0.01, 0.005 and 0.0001 mN/s were employed, however the 0.005 mN/s was the lowest unload rate practically realizable by the nanoindenter control software. The software was unable to process the data for the 0.0001 mN/s test despite several attempts. In each of the 0.0001 mN/s tests no inking occurred at all.

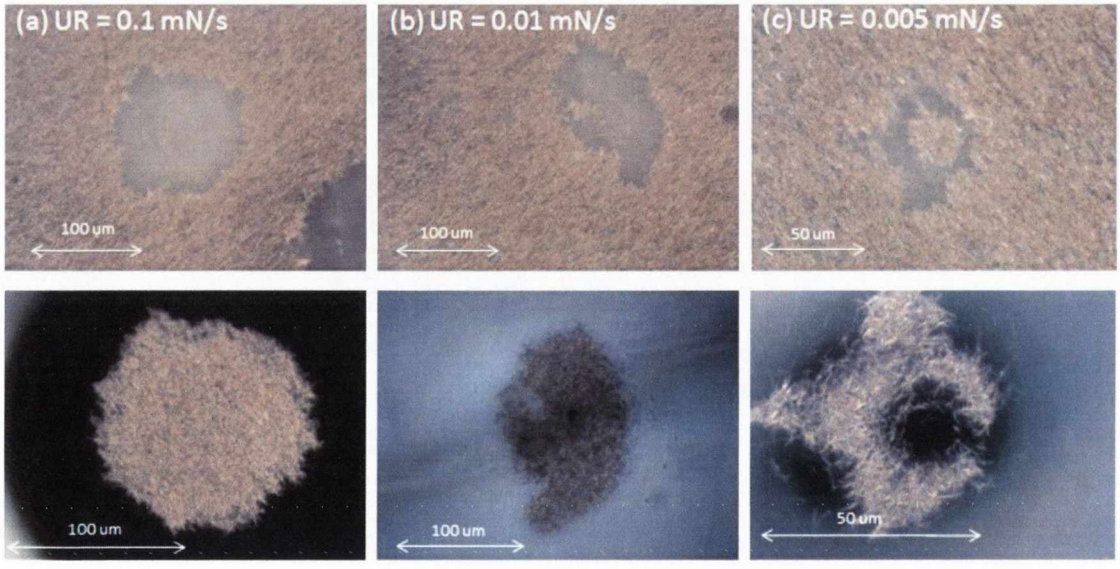

Figure 109. Images of NW film and nanowires on the PDMS tips after different unload rates. All the tests were loaded to a 10 mN peak load and only the unload varied. Each test was done with a different tip from the same fabrication family. Image (a) shows the nanowire film following a 0.1 mN/s unload rate. (b) shows the inking after 0.01 mN/s and (c) shows the film after the 0.005 mN/s. The images of the nanowires on the tips are not shown to scale.

Figure 109 shows images of the AgNW surface and tip surface post-test for each of the executed unload rates, each exhibiting quite different results. Note that the transferred segments are the same size as the gaps left in the film. As with the test presented in Section 5.2, the test in Figure (a) demonstrates that a highly circular section of nanowires was removed. In contrast, the 0.0001 mN/s unload test (not shown) had an unload rate 2 orders of magnitude slower than (a) and had no inking event at all. Image (b) shows only half of the nanowires were removed from what might have been expected from the shape of contact. What is interesting is the shape of the removed section. The fact that one side of the circle was removed and not the other suggests that for a particular unload rate on the test the crack propagation rate is not uniform all the way around the contact. Similar observations have been made by Shull [63] where it was observed that the peeling rate of a circular viscoelastic film was not uniform throughout the circumference.

Only a small, doughnut shaped amount of material was removed for the 0.005 mN/s unload rate test indicated in (c). The size of the outer section had a contact radius of approximately 30 um. The radius of the inner portion of nanowires which were not removed was measured at 16 um. Although it is difficult to see in the figure, a contact impression indicates that the maximum contact radius was 77 um.

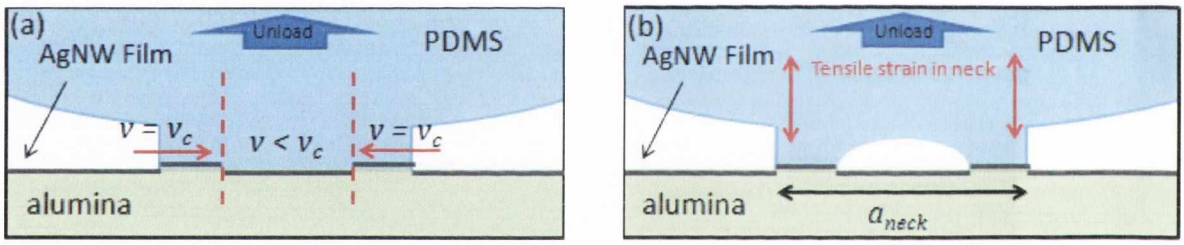

Figure 110. Schematics showing how the doughnut shaped transfer in the 0.005 um/s unload rate test may have occurred. Figure (a) suggests the possibility due the crack velocity varying during the unload of the tip. Figure (b) explores the possibility of a cavity or penny-shaped crack occurring between the PDMS neck and the target material.

There are two possible explanations for the doughnut shaped transfer which are schematically illustrated in Figure 110. One concerns uneven crack propagation across the interface and is illustrated in Figure (a). In this scenario the crack propagation changes speed as the tip unloads from the surface. In the regions where the crack velocity reaches a critical value, $v = v_c$ inking occurs. However if there was a region where for some reason the crack propagation slows down to $v < v_c$ then inking stops. Because the nanowire film is loosely bound together the sections in the $v = v_c$ region and the $v < v_c$ region are relatively independent of one another. This effect may only be applicable to slower unload rates since the crack velocity throughout the test might only occasionally reach v_c whereas for the faster test, v_c might be reached sooner during the unload. Figure 111 shows the velocity data for all the unload rates with the green data indicating the 0.005 mN/s unload rate. The green arrows show the location in which inking took place. From the

data the crack velocity increased from 0.077 – 0.18 um/s in this region. However even though the velocity increased further still inking stopped. This seems to contradict the story predicted by Figure 110 (a). It is important to remember that the velocity data is based on the stiffness data and does not give the velocity throughout the periphery of contact which might not be uniform. Therefore the velocity could be much faster on one side than the other, as seems to be the case with the 0.01 mN/s unload rate test. For this unload rate a semi-circular inking occurred at 0.07 um/s but only half the contact inked, suggesting an uneven velocity distribution across the contact. Both these tests experienced inking at very low crack velocities of less than 100 nm/s which suggests that crack velocity is not the only critical parameter needed for inking to occur. The other possibility regards the stress distribution in the tip itself, which is investigated in Figure 110 (b).

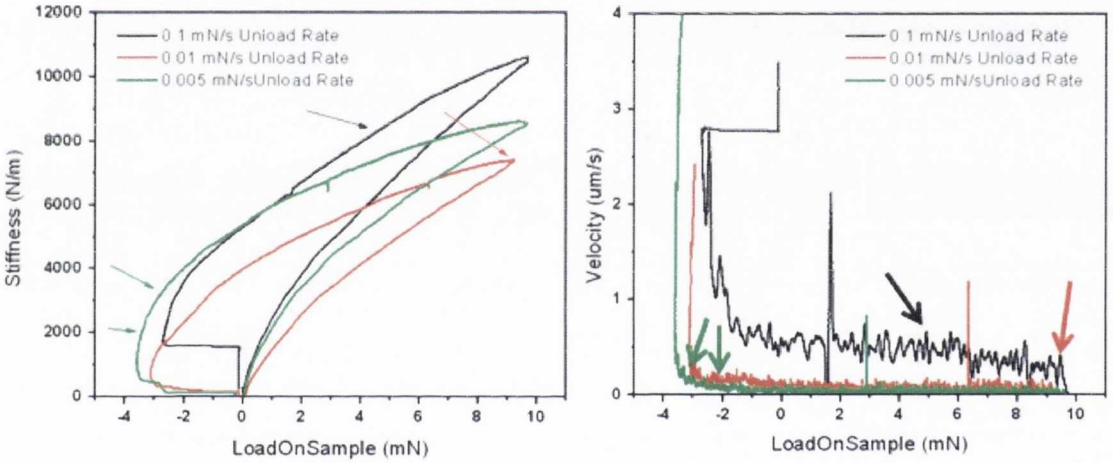

Figure 111. Comparison of the crack velocity for each of the unload rates (a) 0.1 mN/s (b) 0.01 mN/s and (c) 0.005 mN/s. The stiffness-load curves are also shown and the arrows indicate where peeling commenced during the unload segment. Each of the tests were done on different tips which explains the scatter in the load up curves. The arrows indicate the location on the test where peeling initiate, with the colours of arrows matching the curve they are associated with. In the case of the two green arrows, the top one shows where peeling began and the bottom one where peeling ended, creating a "doughnut" shaped inked region.

Figure (b) shows how a cavity might form in the PDMS contact as described in Chapter 2. The size of the neck for a PDMS stamp on alumina for a 10 mN peak load test is approximately 30 – 40 um. The size of the outer region of the doughnut is 30 um. Therefore it is possible that the doughnut shaped inking occurs during the disengagement of the neck from the material. If this were the case the crack velocity on the outer periphery of the contact is essentially zero and the PDMS *neck* is undergoing tensile strain due to the pinning of the contact. This could cause an unequal hydrostatic pressure in the neck which leads to a penny shaped crack in the contact or even a cavity in the PDMS itself. Therefore when the PDMS tip disengages from the surface at high speed

the inner portion is no longer in contact with the AgNWs and they get left behind. We shall see in Chapter 6 that the transfer of CNT films is mediated not by a peel velocity as the PDMS propagates across the surface, but by the tip disengaging from the sample at the end of a necking event. Figure 112 shows a series of video images of the PDMS neck on AgNWs showing that a neck does form with this material.

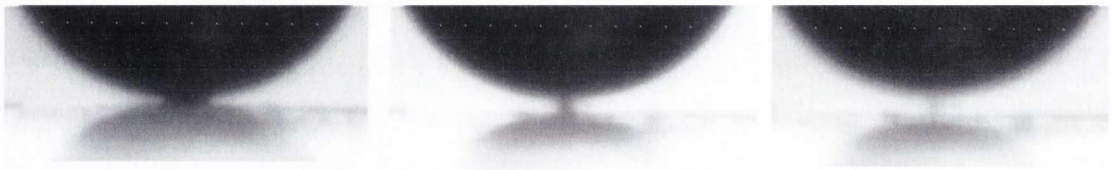

Figure 112. Video data showing that a neck forms on AgNWs as it does on alumina membranes. Chapter 6 will show that the necks also form on CNT films. They do not form on smooth materials such as SiO_2 as shown in Chapter 4.

For these tests two conclusions seem evident. There is a difference in crack velocity v between test of different unload rates such as 0.1 mN/s and 0.01 mN/s. However this effect seems to break down for lower unload rates whereby there is very little difference between 0.005 um/s and 0.01 um/s. This means that if we wish to initiate *a full transfer event* of nanowires using kinetic effects, the unload rate needs to be higher than 0.01 mN/s. For the lower unload rates a different type of process seems to be mediating transfer. Transfer at these unload rates is only partial and the crack velocity appears not to be uniform around the periphery of the contact. Transfer at the lowest unload rate of 0.005 um/s is quite possibly mediated not by the crack velocity (and thus G) but by the strain in the neck as it disengages from the surface. This neck may also form a cavity which contributes to only a partial transfer. As we will see in Chapter 6, this appears to be the way that transfer is initiated for CNT films also, even with faster crack velocities.

5.4 Comparing Adhesion between Interfaces

The next series of tests to be examined are done with the same tip and with the same load-up, peak load and unload parameters. For this set of experiments the peak load was 10 mN and the unload rate was 0.1 mN/s. The precise sequence of tests and overview of the outcomes is listed as follows:

1. Pristine PDMS tip on Alumina
2. Pristine PDMS tip on NW film – inking of NW occurred
3. NW loaded PDMS tip on Alumina

4. NW loaded PDMS tip on NW film again – second inking occurred
5. NW loaded PDMS tip on Alumina
6. NW loaded PDMS on NW film – no further inking of tip.

Figure 113 shows images of the alumina and NW films after each test was conducted. The maximum contact radius for the tests is termed a_{max}. Where an inking event occurs, the radius of the inked region is termed a_{ink}. All tests were conducted within one day with the same tip. Some residual nanowires are apparent on the alumina surface where the nanowire film had been removed using a bulk stamp which gives a less clean visual impression of the alumina compared with pristine alumina. As is often the case with the AgNW films, the contact impression due to excess cross-linker is difficult to detect and requires a more powerful microscope than that in the indenter.

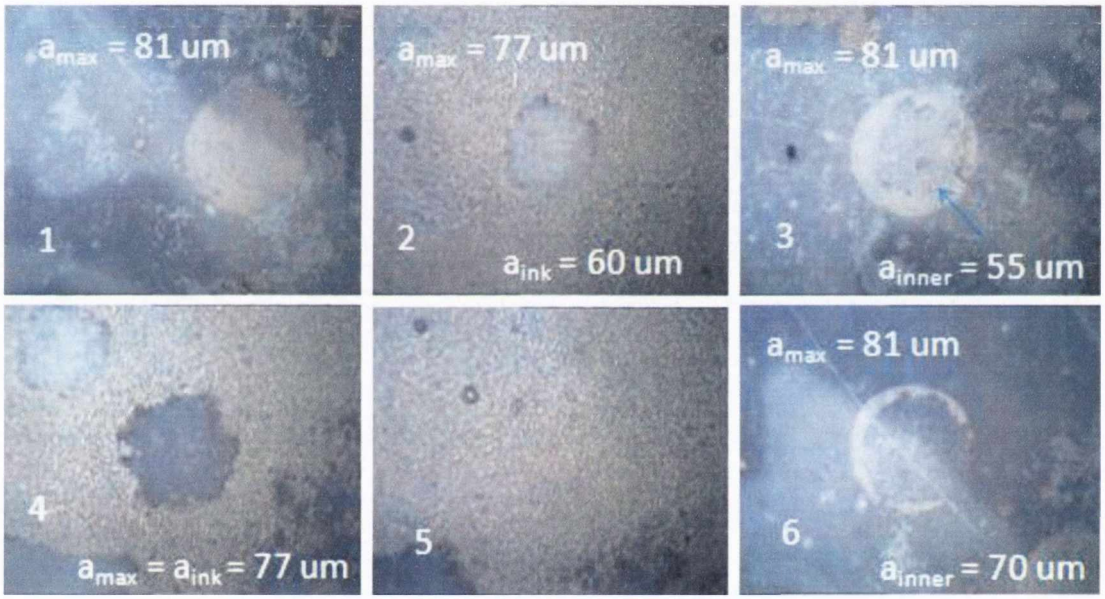

Figure 113: Series of 6 tests on Alumina and AgNW. a_{max} corresponds to the maximum contact radius. a_{ink} corresponds to the radius of the area inked.

For the tests in this series it was found that the maximum contact radius was 81 um on alumina and only 77 on AgNW despite the stiffness values being similar.

Mechanical Data from the AgNW Tests

Figure 114 shows the Stiffness-Load curves for all of the tests done in this study and Figure 115 shows the sequence of data for each test.

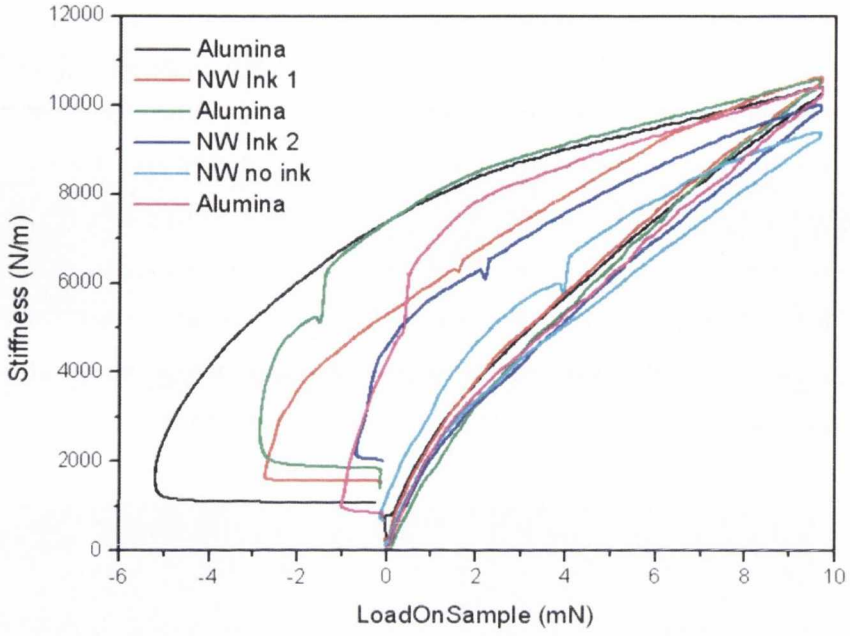

Figure 114. Stiffness-Load curves for each of the tests done in this study with the same loading and unloading parameters.

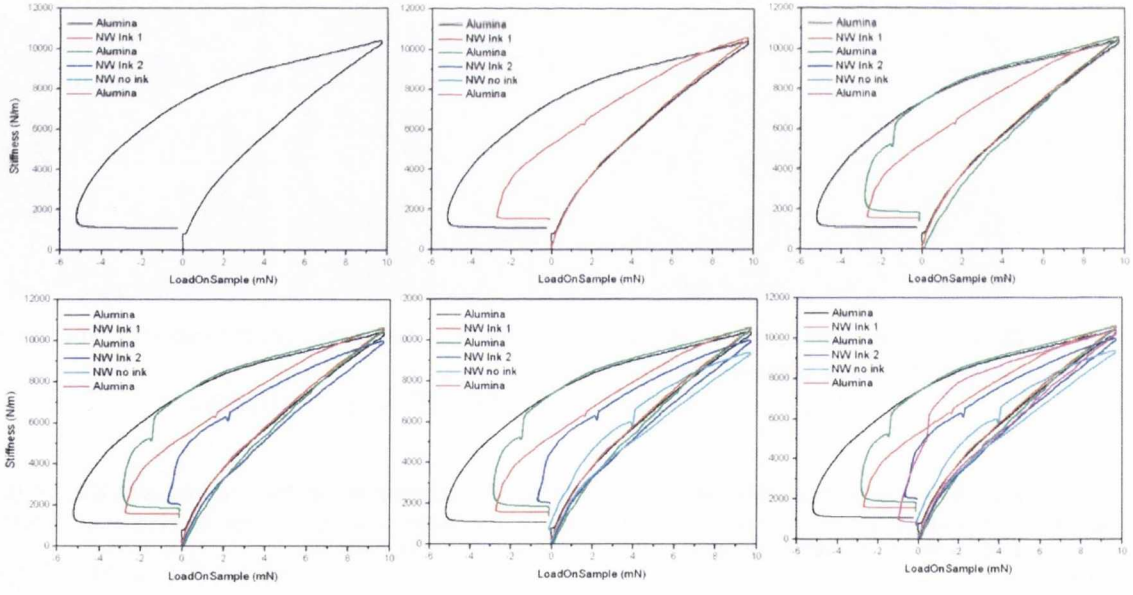

Figure 115. Stiffness-Load data for each test in sequence. Details of the data can be found in the text.

Initially a comparison will be conducted between the first test on alumina and the first inking event of the AgNW, which is similar to Section 5.2. This will be followed by discussion of the second inking event with the already inked tip and the implications that has for the tip surface interactions. Evidence will be presented that the interaction of the PDMS with the AgNW has a

strong component due to the PDMS-Alumina interaction from the substrate beneath the nanowires.

After Test 1:

In this test, a clean, pristine PDMS tip was brought into contact with the exposed alumina membrane. As can be seen from Figure 113, the excess crosslinker indicates that the maximum contact area a_{max} = 81 um corresonding to a peak stiffness of 10444 N/m. The peak adhesion force of -5.2 mN is the highest adhesive force for the series. This is a typical value for a 10 mN peak load when contacting a clean PDMS stamp onto alumina, and the overall shape of the stiffness vs. load curve is also typical for this contact.

After Test 2:

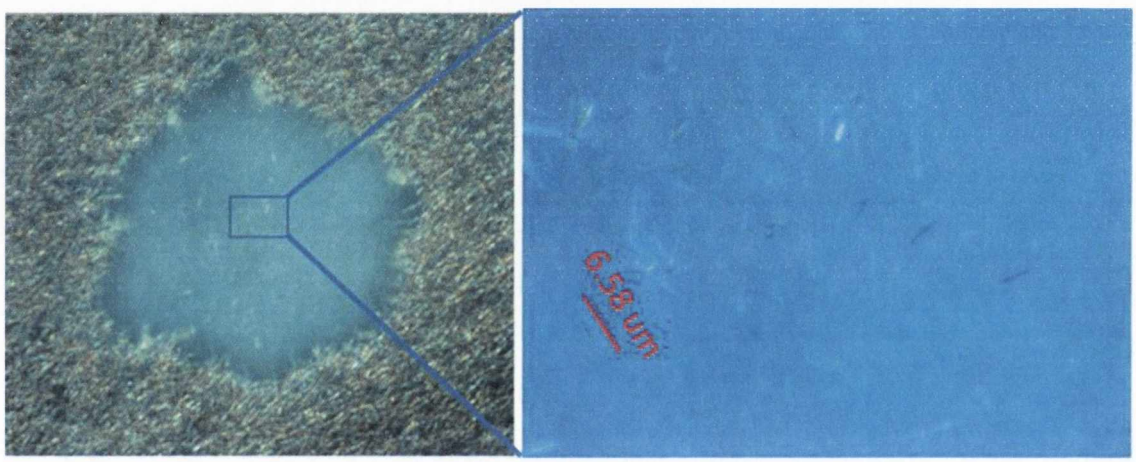

Figure 116. Images of the inked region after Test 2. The image on the left shows the AgNW network after inking. The image on the right is a higher magnification of the alumina after inking. As can be clearly seen there are still individual nanowires in this region and one is measured to be 6.6 um long.

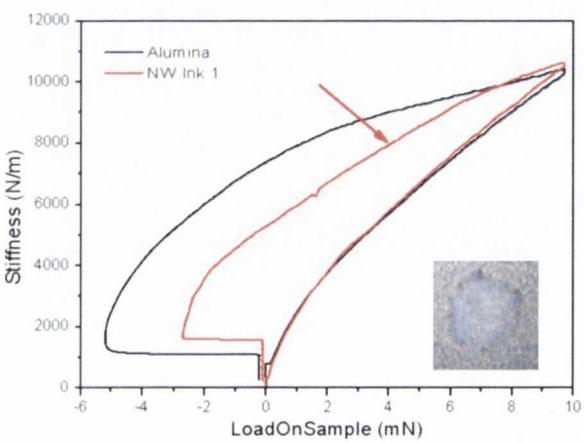

Test 1 was repeated on the nanowire film and as can be seen from Figure 116 a successful inking occured with an ink radius of 60 um. The contact impression was measured to be 77 um. Figure 117 shows the subsequent Stiffness-Load curve as well as that from Test 1 for comparison. Both tests are almost identical on the load up segment

Figure 117. After Test 2 with first AgNW inking event. The red arrow indicates the point during the test where peeling begins.

but the unload data is quite different with a markedly reduced adhesion on the AgNWs. Since we can calibrate the peak stiffness to a 77 um contact radius for the AgNW, this means that peeling of the AgNW began at the point on the curve indicated by the arrow. Unlike the tests discussed previously for this particular unload rate, the peeling begins in the compressive region instead of the tensile region. (Note: This test has been discussed previously as the 0.1 mN/s unload rate test described in Section 5.3.)

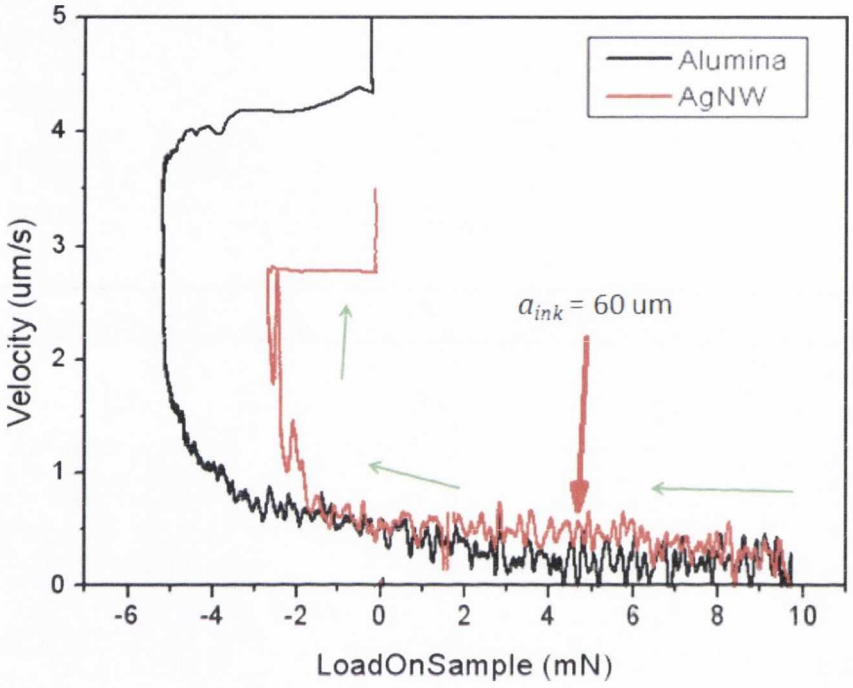

Figure 119. Crack velocity for the first alumina and AgNW tests in the series. Only the data for the unload is shown and the red arrow indicates where the inking event began. The green arrows show the direction of the tests. The velocity for the nanowires is only slightly faster than for the alumina.

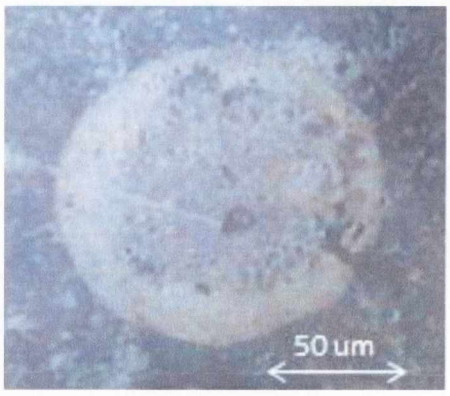

Figure 118. After Test 3 on alumina. The contact imprint is shown with a lighter inner region and a more solid outer region. The inner region shows the position of the AgNWs inking the tip. A crack in the microscope lens caused the shadow through the centre of the image.

Figure 117 shows the crack velocity as a function of load for Tests 1 and 2. The velocity for the AgNW test is slightly higher than the alumina during much of the unload. This is the case at the initiation of peel location indicated by the red arrow. At this point v = 0.5 um/s compared to 0.25 um/s on alumina. The crack velocity on AgNWs increases much more rapidly than for alumina as the peak adhesion force is approached. At this point the tip will already be peeling nanowires from the alumina and the question is if the velocity represents the propagation of the crack between the AgNW film and the alumina only, or if the PDMS is still interacting with the alumina substrate. In that case *v*

would describe the propagation of the PDMS layered with porous nanowires interacting with the alumina substrate. This question is considered in more detail for the subsequent tests.

After Test 3:

After the successful inking of the tip with nanowires the tip was tested again on alumina. Figure 118 shows an image of the alumina after the test. Examination of this image shows an inner and outer region. The inner region has the exact shape and size as the inked segment from the AgNW film. It is lighter in colour than the outer region and has a mottled appearance. The outer region is solid and the same colour as the contact impression from Test 1. This indicates that the inked nanowires were still present on the tip when contact with the alumina was made. The mottled appearance of the inner region suggests that some cross-linker is seeping through the inked nanowires and leaving an imprint on the alumina. Therefore the interaction in this contact is between the nanowires present on the tip and the PDMS on the tip with the alumina membrane. This also suggests that despite the presence of nanowires, the tip could potentially be used to print again.

After Test 4:

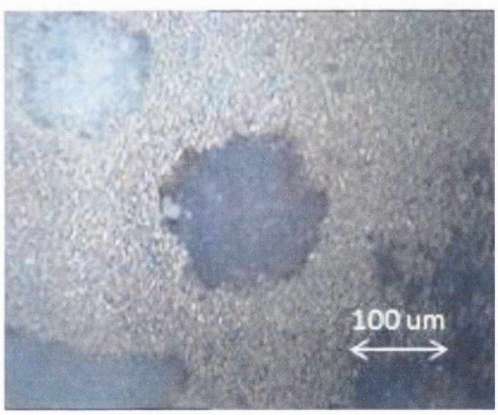

Figure 120. AgNW film after the second inking, test 4 was conducted. Notice the contrast in colour between it and test 2 which is visible in the upper right hand corner.

A second inking attempt was carried out in Test 4 where the same tip was tested on a new, untouched region of nanowires and the results are shown in Figure 120 The first inking is visible in the top left hand corner for comparison. As can be seen, despite the presence of nanowires on the tip, another circular segment of nanowires was removed. This segment is slightly larger with a_{ink} = 70 um compared with 60 um for Inking 1.

Another noticeable feature is the contrast in the colour of the underlying alumina in the inked regions. It is much darker after Inking 2. This is further evidence that excess crosslinker was able to seep through the nanowire film while Inking 1 was taking place. However when the second inking occurred, the thicker layer of nanowires on the tip prevented the contact impression from further occurring on the alumina. A schematic illustrating how this might work is shown in Figure 121.

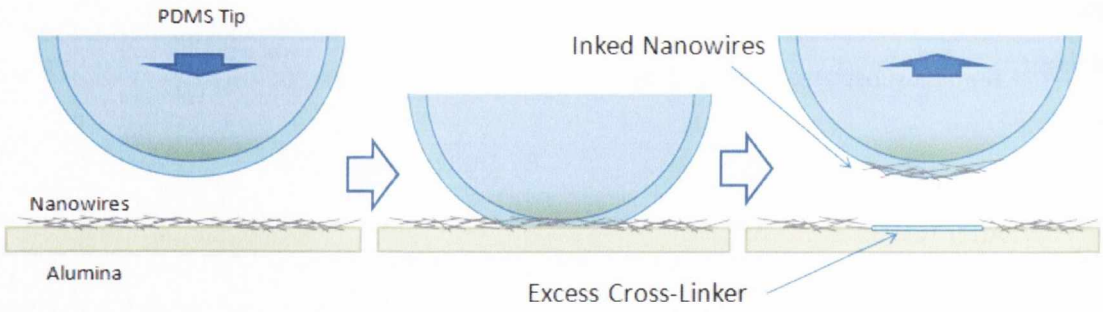

Figure 121. Schematic illustrating how the PDMS can make contact with the underlying alumina through the nanowire film while inking the tip.

One possibility for the difference in colour of the alumina could be due to the underlying crystal bond which is used to adhere the alumina membrane to the nanoindenter sample stage. Observation of Test 6 in Figure 113 shows contrast in the colour of alumina depending on how much crystal bond is beneath the alumina. However checking carefully with the microscope showed that the crystal bond level was the same in the region where both inkings occurred and so the contrast is not due to that. Therefore it seems safe to say that it is due to contact of the tip with the underlying alumina substrate during testing.

After Test 5:

The tip was then tested on the AgNW film again to see if a further inking event would occur. Figure 122 shows the AgNW film before and after the third inking attempt. As can be seen they are almost identical except for a tiny feature shown by the arrow. Analysis under the microscope did not indicate what this feature was, and apart from that no transfer event took place. There was also no visible evidence of excess crosslinker however it is very difficult to see that on AgNWs unlike on CNTs and alumina.

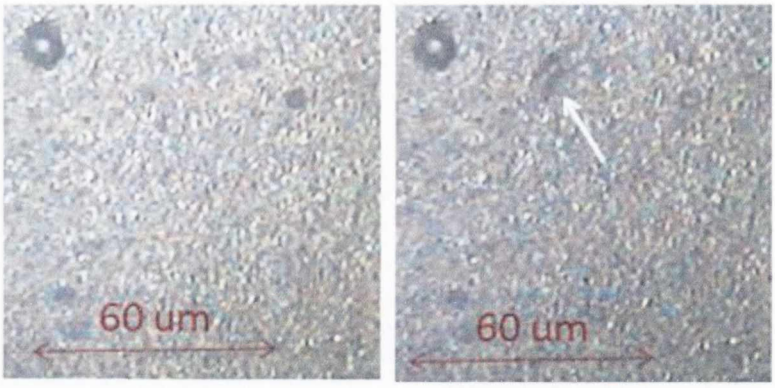

Figure 122. AgNW film before and after ink attempt 3. The white arrow indicates a feature that appears after the inking attempt. It is not known what this feature is and aside from it, not transfer appears to have occurred.

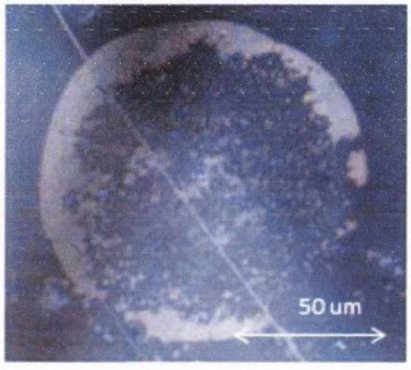

Figure 123. Alumina after contact with a tip which had been inked twice with AgNWs.

After Test 6:

The final test conducted was to contact the tip to a clean piece of alumina. An image of the contact impression is shown in Figure 123. As can be seen in this image the presence of the nanowires on the tip are again visible. Although some excess crosslinker still managed to deposit on the alumina, it is sparse and patchy compared with previous tests suggesting that the tip was not making much contact with the alumina substrate through the nanowire film.

Before examining the mechanical data in detail for the test sequence a summary of the observations during tests is outlined below.

1. A pristine PDMS tip was contacted to alumina and a clear imprint of the contact was visible. This was a straightforward PDMS/Alumina interface contact.
2. An inking event of the AgNW took place which removed most of the nanowire layer at the point of contact. There is strong evidence that the PDMS tip was able to make contact with the underlying substrate during the inking process. Therefore the interface was of PDMS with both AgNWs and alumina at the same time.
3. When the tip was contacted to alumina again the shape of the inked nanowires was clearly visible in the contact impression and again there was strong evidence of the PDMS tip making contact with the alumina membrane despite the presence of the nanowire layer. In this case, it was an interface between PDMS and nanowires, with alumina.

4. A second inking event occurred with same tip which had a layer of nanowires on it from the previous test. In this case a slightly larger circle of nanowires was removed and the colour of the underlying alumina after testing suggested that this time the tip did not make contact with it during inking.
5. The tip was then brought into contact with another section of nanowire film where there was no further inking of the tip. In this case the interface was that of nanowires on nanowires or PDMS/nanowires on nanowires.
6. In the last test the nanowire loaded tip was contacted to alumina and again the shape of the nanowire layer was clearly visible in the imprint. There was no evidence of any interaction of the PDMS with the alumina through the nanowires and therefore the interface was that of nanowires on alumina. (Note there was some interaction on the edge of contact of the PDMS with the alumina but not through the inked nanowires).

The materials which interface with one another for each test are summarised in Table 2.

Test Number	Material 1	Material 2
1	PDMS	Alumina
2	PDMS	AgNW + Alumina
3	PDMS + AgNW	Alumina
4	PDMS + AgNW	AgNW + Alumina
5	PDMS + AgNW(doubled)	AgNW
6	PDMS + AgNW(doubled)	Alumina

Table 2. Table showing what materials are involved in the interfaces between tip and target for each nanowire test in the sequence. The "doubled" nanowires refers to the fact there are two layers of nanowires on the tip.

Figure 124 (a) shows the stiffness curves for the nanowire tests. Tests 2 and 4 are almost identical for most of the region where $L > 0$. This then changes in the adhesive region ($L < 0$) where the adhesive force is seen to drop substantially between the two tests. It appears that the presence of the nanowires does not change the unload behaviour substantially during the compressive unload but makes a large difference to the adhesion of the tip when undergoing tensile strains. Test 5 shows similar behaviour to the other two tests in the initial unload but the stiffness quickly drops off indicating that the contact is shrinking faster than in the other two tests. This is supported by the crack velocity data in **Error! Reference source not found.** (b) where v is increasing faster than the other two as the tensile region is approached. The crack front is moving more easily at this point than in the other two tests. The test ends almost immediately after passing into the tensile region indicating that there is no adhesion between the nanowire-loaded tip and the nanowire film.

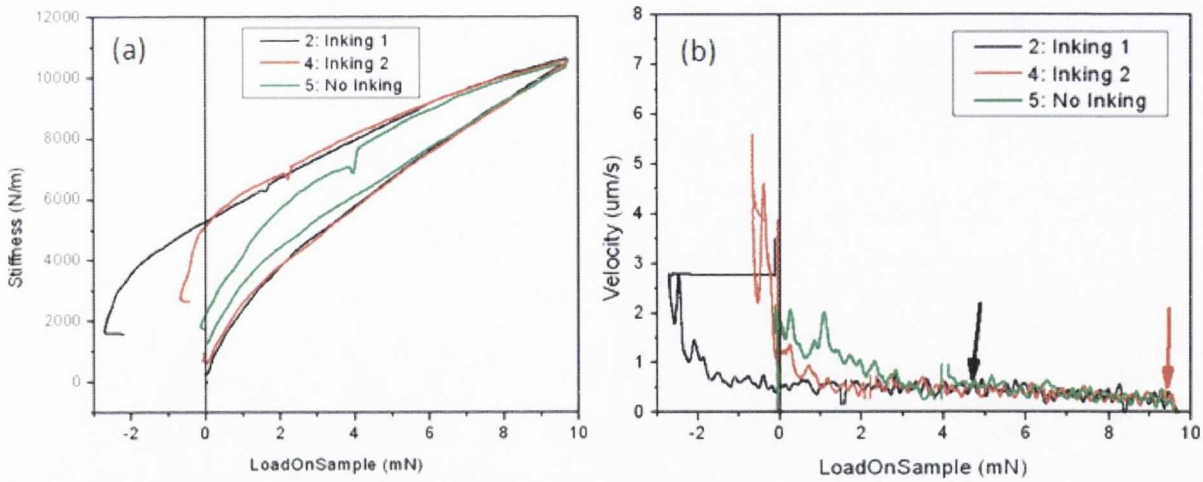

Figure 124. Stiffness, crack velocity and energy release rate are plotted against the Load for the three nanowire tests in the series. (b) shows the stiffness data lined up to illustrate the absolute difference in hysteresis between the three tests. The black vertical line indicates the transition from compressive to tensile regions and the arrows indicate where peeling began for the test 2: black arrow and test 4: red arrow.

Correlation of Peak Load and Ink Size

A significant challenge in analysing the inking experiments on AgNWs has been measuring the contact size. The contact impression is often not visible on the films and so we do not know the maximum contact area after testing. Therefore we have only been able to present a full mechanical analysis on tests where a contact impression was visible.

Experiments were conducted to relate the peak load to the size of contact. We wanted to see if using specific peak loads could determine the size of the inked segment for AgNWs. Figure 125 shows the results for three different tips for different peak loads. For a given tip, say T230112_6 the size of the inked region does increase for greater peak load. However this is not a linear relationship. The relationships also holds for T230112_7 though the spread is different from the first tip. It is probably that peak loads will give larger inked sections for any given *tip* but the size of the segment cannot be predicted beforehand. The variation in values between the tips could relate to the quality of the tip, its age, its exact thickness or ambient environmental factors. The film quality could also be a factor as the films can display limited uniformity over areas larger than a few microns. Statistically a great deal more data needs to be measured to find a conclusive relationship between peak load and inking radius.

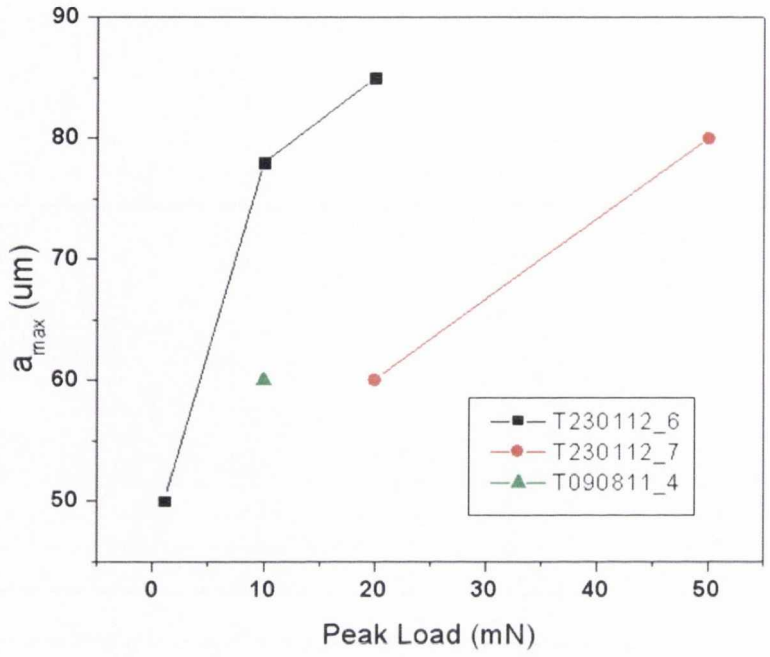

Figure 125. Correlation of the size of the inked segments of AgNWs with peak load for three different tips. Although the spread varies from tip to tip, the peak load does yield larger inked segments of AgNWs.

5.5 Chapter Summary

Inking a PDMS tip with AgNWs

In this chapter we demonstrated inking of AgNW films onto a PDMS tip using the nanoindenter to facilitate transfer. We were able to measure mechanical data from the transfer which provided us with information regarding the inking method. It was found that the AgNW films peel relatively easily from the bulk film without seeming to require fracture from the film. Where a contact impression was visible the calibration factor could be used to define the location where peeling begins, a_{ink}. A minimum peeling velocity was measured at 0.22 um/s which we consider a critical inking velocity v_c. All tests exhibiting full transfer had inking velocities above this critical value. We also found a correlation between the peak load and the size of the inked region for a given tip, however contact impressions were not visible for most tests, which means velocity data was not available.

Kinetic effects of Inking AgNWs

Attempts were made to influence the crack velocity by varying the unload rate. Although it had been demonstrated in Chapter 4 that faster unload rates do not necessarily translate into faster crack velocities, we found that using unload rates of less than 0.1 mN/s did decrease the crack velocity throughout the tests. We also found that there was a lower limit on this effect with almost no variation in crack velocity between tests done at 0.01 mN/s and 0.005 mN/s. The slower unload rates mean that either no transfer occurred or only a partial transfer occurred. The 0.005 mN/s was especially interesting in that it cut out a "doughnut" shaped section of AgNWs whose outer radius seemed to correspond to the size of the PDMS neck as the tip disengaged from the surface. The inner portion was most likely left behind due to cavitation between the PDMS and the substrate during the neck segment. In the absence of the critical crack velocity, the high stress field generated by the neck at this juncture seems to allow the tip to be inked.

Multiple Inkings

We demonstrated that a single tip can conduct at least two inkings, one on top of the other due to the porous nature of the film. This showed that even during inking events the PDMS tip is still interacting with the underlying alumina membrane. This makes analysis of the interface rather more complicated than that described by Prof. John Rogers [46] in that we have materials interacting at one interface. We also found that, as in Chapter 4, the power law model relating the energy release rate with crack velocity breaks down, most likely due to insufficient calculation of G. Our experiments open up the possibilities for exciting new analysis based these novel materials, further enhancing our understanding and potential control of the transfer process.

Effect of Excess Crosslinker in Transfer

We saw in Figure 113 (2) that after transfer, excess crosslinker is visible on the underlying alumina. This begs the question about what effect crosslinker has, if any on the transfer process. Figure 121 shows schematically how the crosslinker can pass through the porous material and be deposited on the underlying alumina during a transfer event. An interesting possible outcome of this is that the crosslinker in some way facilitates or *lubricates* the AgNWs during transfer, thus easing their de-adherence from the alumina membrane. If the surface energies of the materials involved were such that the crosslinker favoured adherence to the alumina but repelled the nanomaterials, this could provide another clue as to how these materials can be manipulated during transfer. This is an important consideration and needs to be examined in more detail. It is possible that a lubrication effect could enhance the transfer process but that the excess crosslinker could inhibit the electrical properties of the materials as it is itself non-conductive.

Careful experiments where the crosslinker can be rinsed out or removed is required for this further investigation.

Chapter 6 Transferring Carbon Nanotube Films

6.1 Introduction

The second nanomaterial studied in this thesis work consists of networks of Single Walled Carbon Nanotubes (CNTs). The nanotubes are dispersed in an organic solvent and filtered onto alumina membranes for transfer as described in Chapter 3. Nanotube films exhibit different transfer behaviour from silver nanowire films. Although the AgNWs can be considered as a loosely bound network whereby each individual nanotube is relatively independent of its neighbour, carbon nanotubes form a more cohesive network of intertwining, flexible tubes. An analogy which is often used to describe their morphology is that of wet spaghetti which has been mixed up together. Even this analogy falls short in describing the transfer behaviour which we observe in our experiments. The nanotube film is similar to a continuous thin film in many ways however it does have a strong porous component which is not visible optically but creates for some interesting dynamics.

The transfer mechanics for the AgNW films and the CNT films differ due to the nature in which they ink the tip. The AgNW films behave like a collection of rods which ink the tip based on a critical crack velocity as described by Rogers *et al* when discussing the inking of nano-objects [52]. The cohesive nature of the CNT films implies a transfer that is similar to that of a solid thin film. Rogers *et al* briefly discuss the transfer of thin gold films [46] but only in so far as *peeling* the film from a substrate. In this thesis work the CNT film is being peeled but also *fracture* during inking as the cohesive inked segment is torn from the rest of the film. Therefore additional considerations during the inking process need to be considered. Work done by Shull *et al* [1] analysis the inking of a polymer film which also needs to be fractured when inking. Both these approaches have been described in detail on Chapters 1 and 2.

The discussion in this chapter will initially begin with describing one CNT transfer event. This will be followed by a description and discussion of some the more unusual transfer behaviour of this fascinating material.

6.2 Inking of CNT films

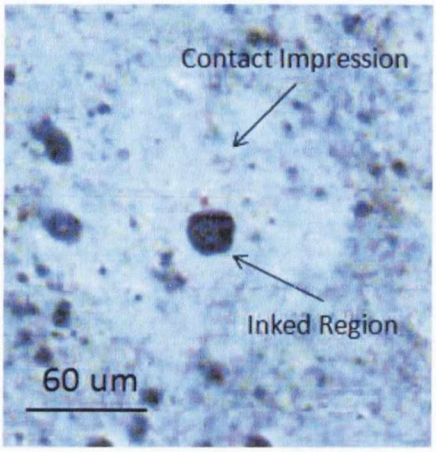

Figure 126. CNT film after a successful inking event. The tip was loaded to 5 mN for this test.

Figure 126 shows a CNT film after a successful inking event. The method and control parameters used were exactly the same as had been used for the AgNW inking tests and for the contact mechanics studies on alumina and other materials. The tip was loaded to a peak load of 5mN in this test. There is a visible contact impression and a roughly circular section of CNTs has been removed from the centre of the contact. The radius of this inked region is approximately a_{ink} = 10 um. In Chapter 4 we discussed how the contact radius of the PDMS stamps is approximately 30 um before the tip is loaded up on the sample. This indicates that the inking event here occurred during the *narrow necking phase* of the unload. For an AgNW inking event however the size of the inked region was never smaller than 35 um, even for tests with peak loads as low as 1 mN. There are two possible reasons for this. The first is that the critical ink velocity for inking has been reached long before a narrow neck can form between the PDMS and the AgNW/alumina interface. The other is that a neck smaller than 35 um never forms on the AgNW material. The jump to contact of the PDMS with AgNWs is significantly supressed suggesting that the PDMS does not adhere strongly to the nanowire film. Therefore a narrow neck is unlikely to form during the unload and it has never been observed in the video imaging of the AgNW tests.

Figure 127 shows the load-displacement data for the CNT test described above. The same tip was first used to test alumina and both materials are compared. The peak adhesion force for the CNT test is half that of the alumina. The inset shows the jump to contact for both materials and shows that there is not a significant difference in the jump to contact behaviour. This is substantially different than the AgNW tests. A large jump to contact usually results in a large initial contact area as was examined in Chapter 4 on alumina. In those tests the minimum contact radius we could measure during the jump to contact was 30 um. Because CNTs have a similar surface energy and jump to contact size as alumina it is reasonable to assume that the initial contact area will also be large. However the necking of the PDMS on alumina during the unload allows for much smaller contact areas with a contact radius as small as 6 um as measured by the video camera. If this behaviour is the same on CNTs then inking of objects as small as only a few microns is possible.

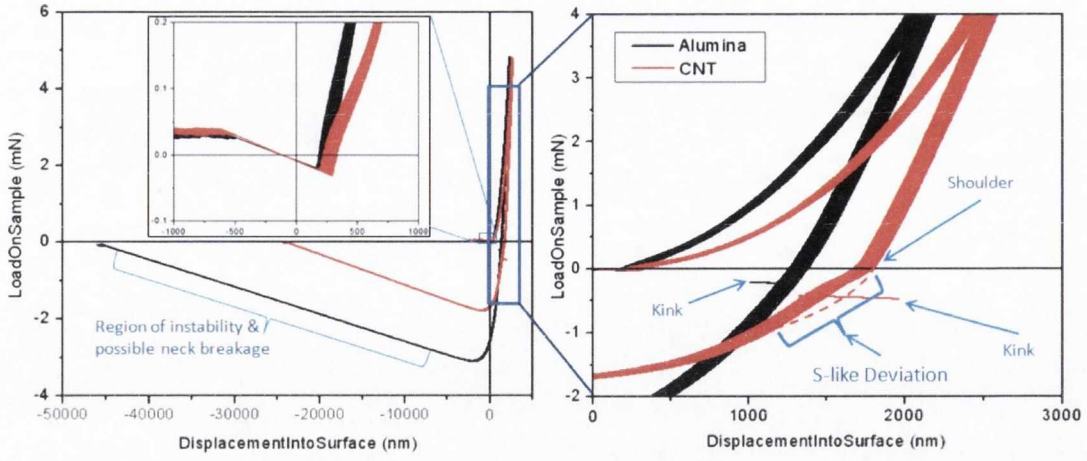

Figure 127. Load-Displacement data for tests done on alumina and on CNTs. The same tip was used for both tests. The inset shows the jump to contact for the materials and the right hand figure highlights the shoulder on the unload data for the CNTs.

The load-up and unload behaviour of the CNTs deviates from the alumina. Whereas the very initial jump to contact is the same there is an apparent shoulder in the CNT data at the zero load value on the unload segment. The shoulder on the unload load is very significant, indicating a major change in the contact mechanics at the point where the test enters the tensile region. The shoulder has a sharp corner at L = 0 but then follows a flattened out S-shape to where it conforms to the usual L-D curve shape. The shoulder and S-shape are indicated by the bracket and the dotted line indicates how the curve might have looked without this feature. The sharpness of the shoulder followed by the softness of the change in the L-D curve suggests a sudden event followed by a relaxation phase before returning to the normal L-D curve and is discussed in more detail with the next figure. Arrows indicate the characteristic "nanoindenter kink" in both the alumina and CNT tests. This feature has been discussed in detail in Chapter 4 and is visible for load, displacement and stiffness channels always at a stiffness of approximately 6000 N/m. It is most likely this kink is a feature of the nanoindenter mechanics as opposed to special physics in the contact.

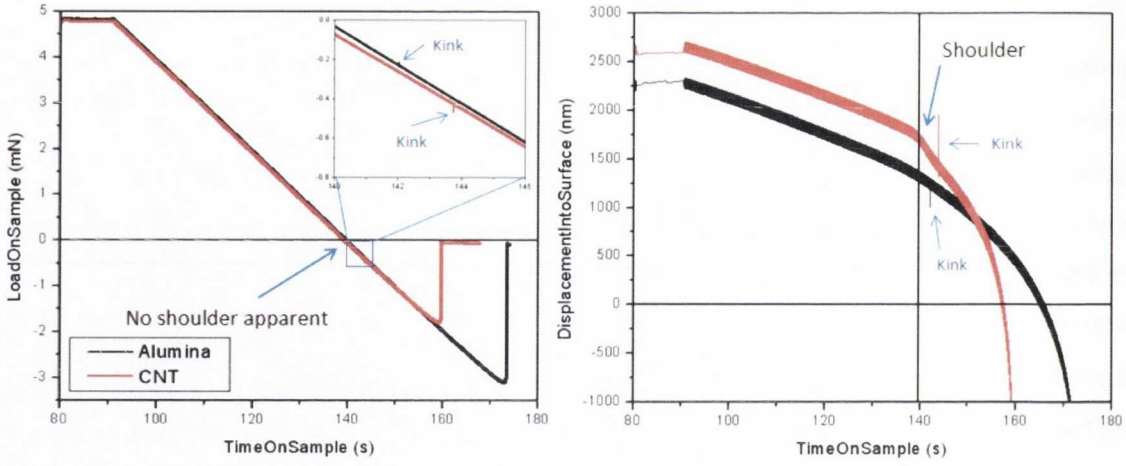

Figure 128. Load vs. Time and Displacement vs. Time for the alumina and CNT tests showing that the shoulder of Fig. 122 is not evident in the load data but is in the displacement channel.

Figure 128 shows that the shoulder is not apparent in the load data but *is* apparent in the displacement channel. Bear in mind that the nanoindenter uses *load control* which means the load is an *applied* channel, not a measured one. The load (on sample) channel is a combination of the raw load and the support spring correction in the nanoindenter which is based on the displacement channel which is a *measured* channel. Were the indenter a *displacement controlled* machine the load would be measured while the displacement is applied. In a load controlled machine the contact physics is not apparent in the applied load channel but will be detected in the measured displacement channel. Since the shoulder is not apparent in the load on sample data but is apparent in the displacement data it is due to a change in the contact mechanics of the test*.

One possible clue as to the origin of the shoulder lies in the fact that it occurs at the point where the PDMS contact switches from being mainly compressive with a tensile periphery to entering a mainly tensile regime with a compressive component in the centre. It is possible that this shoulder represents a vertical shift in the CNT film position itself. As will be seen in later discussions the cohesive nature of the CNT film means that it is possible to cause it to blister from the alumina membrane. This phenomenon is called *tenting*. Note how the displacement data at peak load for the CNTs is approximately 0.5 um greater for the CNT films. This suggests that the PDMS is slightly more compressed for the CNT films due to the way in which the PDMS propagates across the CNT film. There appears to be greater friction between the PDMS and the alumina membrane whereas the CNTs seem to lubricate the contact allowing the PDMS to slide more easily across the surface.

*A sudden event such as the jump to contact event could cause a signal in the load on sample data because of an inductive spike being introduced by the magnet due to the sudden movement of the magnet.

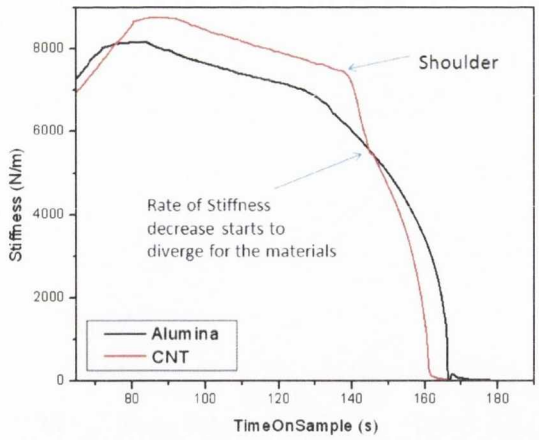

Figure 129. Stiffness vs. Time for the alumina and CNT data. In this case the alumina data has been translated in the negative x-direction to illustrate the different rates at which the stiffness drops for both materials. This difference becomes apparent at 150 s.

After the shoulder the displacement channel decreases very rapidly, much more so than for the alumina. Figure 129 shows the stiffness vs. time for the unload segment. In this case the alumina data was shifted to the left to illustrate the difference in the decrease in stiffness rates for the two materials. Since the contact radius is a function of stiffness this shows that the PDMS is decreasing faster on the CNT film than on the alumina. Again this indicates that the PDMS slides more easily over the CNTs than the alumina. This in combination with possible tenting of the CNT film shows a very different mechanical behaviour between the CNT film and the alumina. One might be tempted to relate the shoulder to the kink at 6000 N/m as they are coincidently very close together. Figure 130 shows the stiffness-load curves for the test as well as an additional test which was done on CNTs with a peak load of 10 mN. The 10 mN test also shows the shoulder on the unload, but in a very different location than the kink near 6000 N/m. This suggests that the location of the shoulder on the 5 mN has nothing to do with the kink.

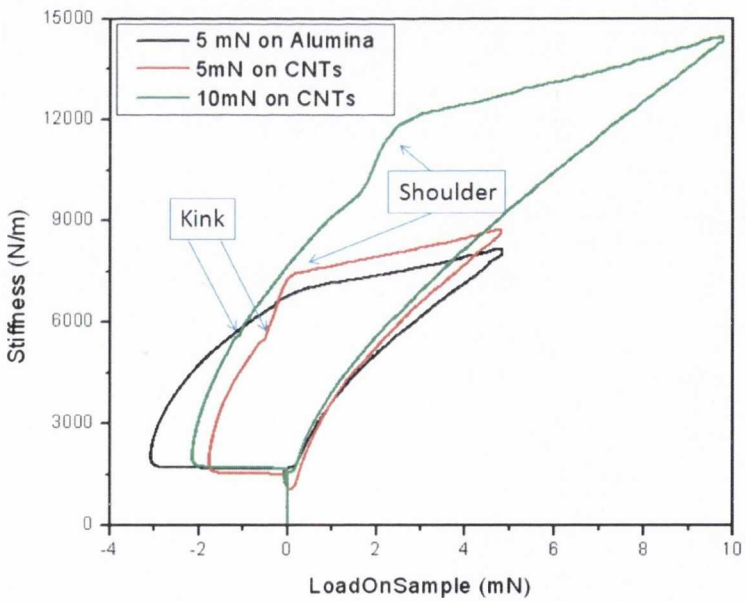

Figure 130. Stiffness-Load data for the alumina and CNT tests at 5 mN compare with one on CNTs at 10 mN. The shoulder is very obvious as is the characteristic kink at 6000 N/m. The location of the shoulder on the 10mN test shows that this tip is not related to the shoulder.

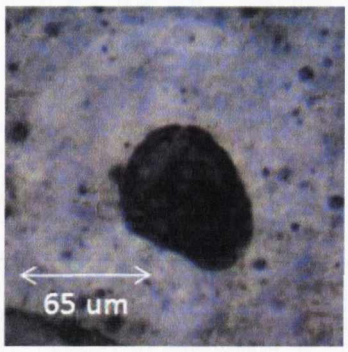

Figure 131. CNT film after a 10 mN inking event.

An image of the CNT film after the 10 mN inking test is shown in Figure 131. The contact impression yields an a_{max} = 73 um and the size of the inked portion is a_{ink} = 27 um. The inked portion does not appear to be completely circularly symmetric when the film is viewed under the microscope. As with the AgNW films this could be due to a variation in the crack velocity across the periphery of the PDMS/CNT crack front. There are two aspects to be considered when analysing the inking of the CNT films. The first is as to the nature of transfer. We have seen already that a nanowire film is *peeled* from the alumina membrane during the unloading segment when a critical velocity has been reached. The nanowire films are loosely bound together meaning that fracturing them at a_{ink} in order to initiate peeling is relatively straightforward. CNT films however behave much more like a cohesive, possibly even rubbery film. Therefore the mechanism of fracturing them at a_{ink} could be more complicated. This will be examined in further detail later and for the moment a simple peeling event like that with the AgNWs is assumed.

Figure 132. Comparisons of the aink measured from the CNT film and on the PDMS tip after the 10 mN test. There is a difference of almost 10 um between them. The image on the left hand side has an outer radius of 27.07 um and the right hand figure has an outer radius of 18.22 um.

The second consideration regards how we measure a_{ink}. It seems relatively straightforward to image the missing CNT portion in the film with the microscope. However it has been found that when the *inked* portion is measured on the tip, the contact radius is often smaller. Figure 132 shows images of the missing portion of the CNTs from the film and the corresponding portion which is inking the PDMS tip. The shape of the portions matches up well including their asymmetry but there is a difference of approximately 30% in the measured contact radius a_{ink}. There are two possible explanations and both are due to the imaging of a three dimensional object as a two dimensional one. Firstly the real size of the image on the tip may be larger than what is measured due to the radius of the tip itself. This is because the PDMS tip is a curved surface with a radius of curvature which is not corrected for by the microscope. However the

radius of curvature of the tip is 0.5 mm which is 17 times larger than the radius of the inked object. Therefore the correction would most likely be negligible.

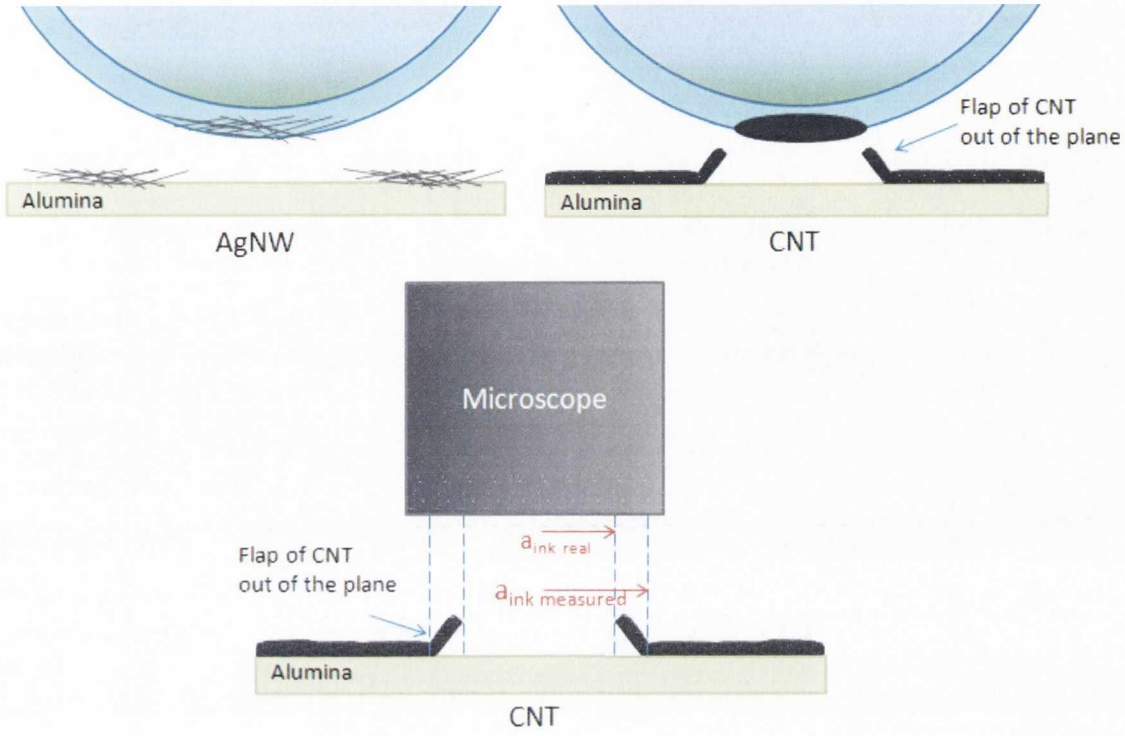

Figure 133. Schematic illustrating the difference in how AgNWs and CNT inked portions are removed from the surrounding film. The tearing of the CNT films can cause deformation which can obscure an accurate measurement of a_{ink}.

The other explanation involves the way in which the CNT film itself fractures and "deforms" near a_{ink}. AgNW films fracture easily due to the loose bond the wires have with their neighbours and the inking is similar to the nanowires being simply "picked-up" when the crack velocity reaches a critical velocity. The CNT films are cohesive and so more resistance to inking by the surrounding film would be expected. In this case the inked portion needs to be *torn* from the rest of the film causing deformation of the film at the crack edge. Figure 133 shows a schematic illustrating how the removal of a portion of film is different for AgNW films and CNT films. Tearing of the CNT film can cause distortions in the film that obscure the image when viewed with a microscope thus causing incorrect measurements of a_{ink}. For example flaps of loose CNT material can stick up out of the plane which obscures the true radius of inking. Alternatively the original radius no longer exists due to distortion of the film. It is therefore better to use the inked portion on the tip itself to find a_{ink}.

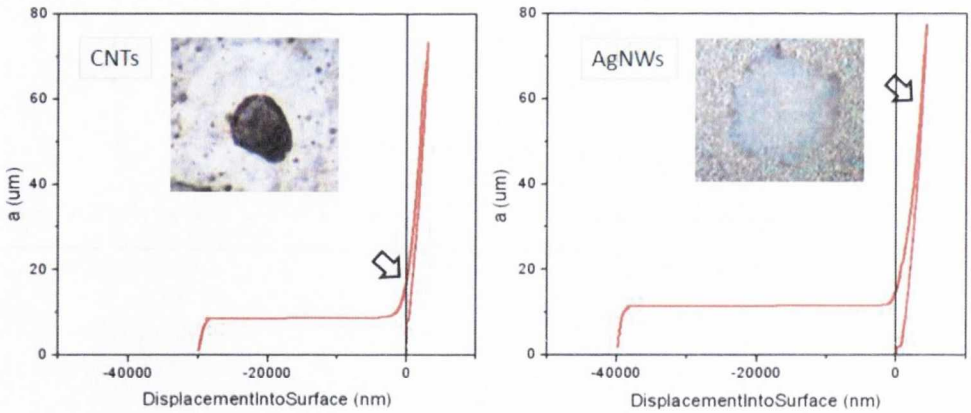

Figure 134. Contact radius a vs. displacement for 10 mN peak load tests done on CNTs and AgNWs respectively. The black arrows indicate the location of "peeling" initiation for the inked portions of the films.

In Figure 134 a comparison is made between the contact radii for inking tests done on CNTs and AgNWs. Both tests had the same method parameters including a 10 mN peak load and a 0.1 mN/s unload rate. The arrows indicate the location a_{ink} the radius of the inked portion in each test. The transfer mechanism of the AgNWs has already been discussed as a peeling event of the nanowire film from the alumina when a critical velocity has been reached. Let us assume for the moment that the mechanism of inking CNTs is the same as AgNWs, and that fracture occurs in the film during the unload followed by peeling from the alumina membrane by the tip.

Figure 135 compares the crack velocity v for tests done on CNTs and silver nanowires. The red arrows indicate the location on the stiffness curve where $a = a_{ink}$ for both CNTs and AgNWs. For the 10 mN tests shown in Figures (a) and (b) the value of v for the initiation of peeling of the CNTs was 3 um/s. For the nanowires it was 0.5 um/s, half the value of the CNT film. The location of the initiation of the peel is also significant. For the AgNWs the peeling began very soon after the unload commenced. The CNTs did not experience peeling until the unload had reached the peak adhesion force, at which point the crack velocity was double that of the AgNWs at peeling. The 5 mN test illustrated in Figure (c) shows that transfer did not occur until the necking portion of the test with a velocity of 5 um/s, higher than either the AgNWs or the 10 mN CNT test. This point will be returned to presently.

If the relation between v and G follows

Equation 44

$$G = G_0(1 + \left(\frac{v}{v^*}\right))^n$$

then the value of G for initiating peeling of the CNTs is also higher than for the CNTs. The CNT films behave as a cohesive film which requires *fracture* before peeling can be initiated. If the

loosely bound nanowire film does not require fracture before peeling then the energy to initiate transfer is lower.

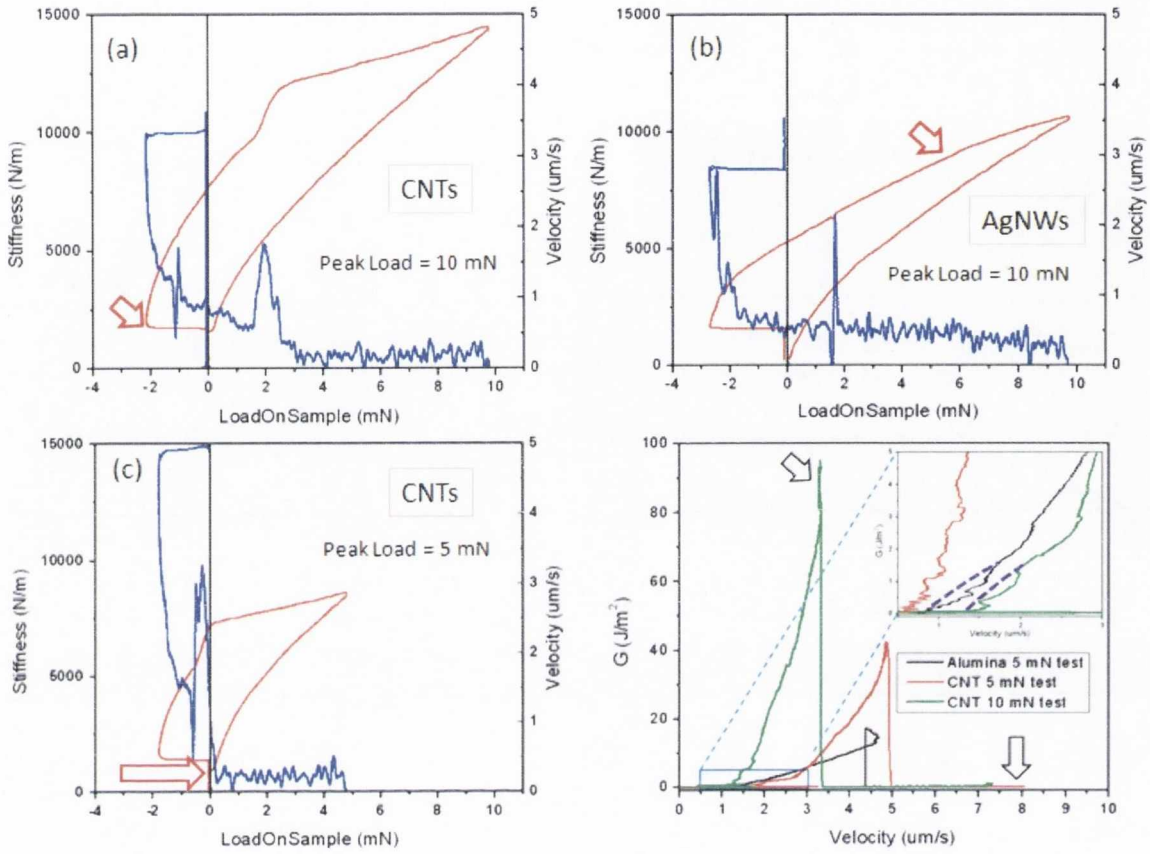

Figure 135. Comparison of the S, G and v for 10 mN peak load tests on AgNWs and CNTs and the 5 mN CNT test. The red arrows indicate the location of a_{ink} for inking events on each material. Figure (d) shows the G vs. v data with G calculated using the JKR theory. As is the case for alumina and AgNW the values of G do not fit the relation described by Equation 1. The dotted lines in the inset illustrate the shape of the relation for correct values of G. The locations of the CNT inking are shown by the black arrows.

However the relation described in Equation 44 cannot be evaluated for our system as was described in Chapter 4. This is because of difficulties calculating G for a thin film of PDMS coating a solid sphere which is then compressed against a solid flat substrate. Figure (d) illustrates how the G values do not follow Equation 44. The dotted lines in the inset indicate the shape which the curve should follow were the G values correct. Even without the correct G values, the figure is still useful for determining the position of transfer as a function of the crack velocity, which are indicated by the arrows.

Returning to the difference in v for the 5 mN and 10 mN test it is apparent that a_{ink} for the 5 mN test occurs *after the measured load on sample has dropped back to zero*. Recall the discussion of tests on alumina using the video data from Chapter 4. In that chapter it was shown that a neck forms for PDMS during the unload segment of the test which is maintained even after the peak load as returned to a zero value.

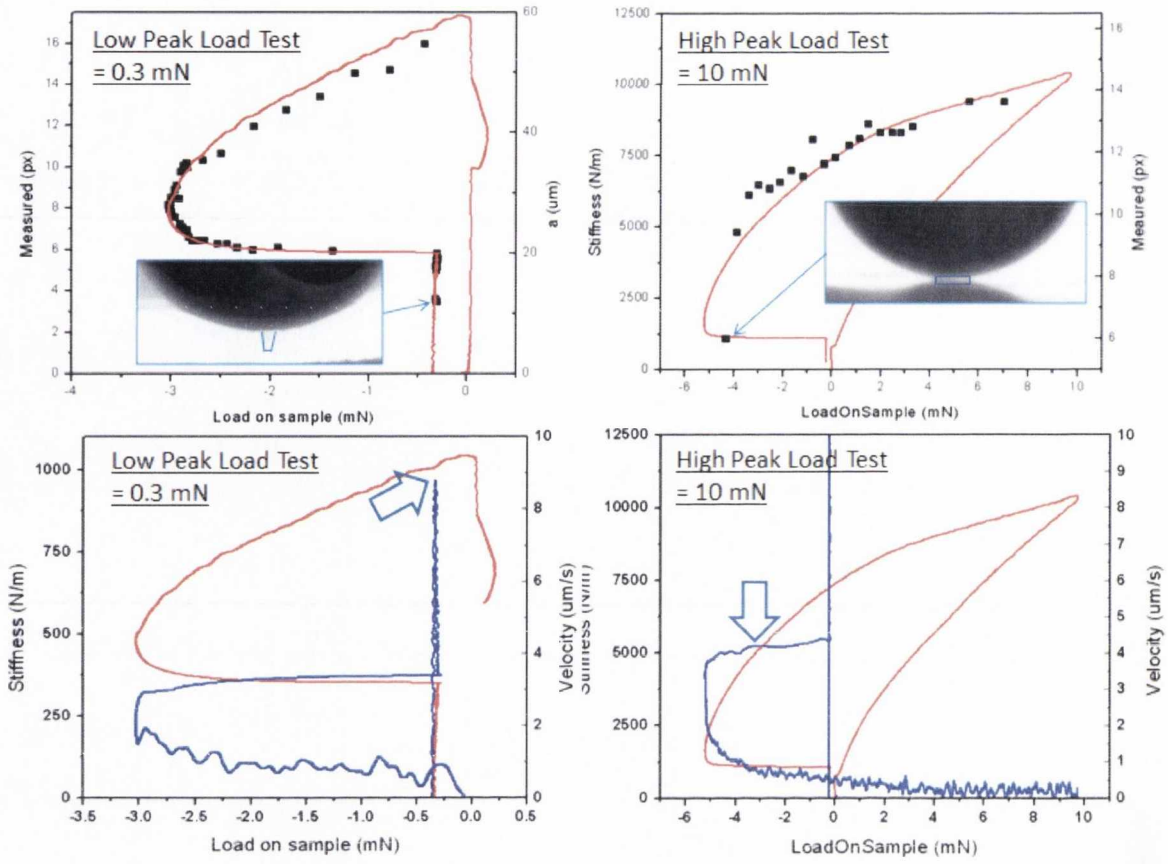

Figure 136. *S* vs. *L* curves for a low peak load (0.3 mN) and a higher peak load (10 mN) demonstrating the size of the PDMS neck as the tip disengages from the underlying substrate. Also shown are the *G* vs. *v* curves for both tests with the blue arrows indicating the location of the neck on the curve, just before it disengages from the surface.

Figure 136 shows the Stiffness-Load curves for those tests loaded to two different peak loads. The location of the neck and an image of it just before the tip disengages from the surface is shown. The neck is highlighted with a blue outline for clarity. For tests which had a *low peak load* such as 0.3 mN the neck survives throughout the whole of the unload segment, even to the point where the load on sample has returned to zero. When the neck finally disengages from the alumina it can have a very small contact radius of only a few microns.

The lower figure shows the velocity data for the same test with a blue arrow indicating the crack velocity as the neck disengages from the alumina. The velocity at this disengagement point is between 6 and 9 um/s for the 0.3 mN test compared with only 4 um/s for the 10 mN test. This suggests that inking of the CNT film occurs when the neck disengages from the sample and is not dominated solely by the crack velocity value as is the case with AgNWs. Therefore an additional factor such as the stress distribution of the tip as it disengages may fracture the film. In order to fully study this effect knowledge regarding the failure modes of the adhesive contact between the PDMS neck and the sample is required. Aside from the edge crack propagation velocity we

measure with from the stiffness, we also saw in Chapter 2 that failure modes can include cavitation formation and/or internal crack propagation. Direct study of these effects will require far superior optics than our present set-up provides. Further discussion of the failure modes of the PDMS tip and the CNT film with alumina is discussed in the next section.

The conclusion is that that *the inking event on CNT films occurs as the PDMS neck is disengaging from the substrate*. **Despite the challenges imaging the inking events for these tests we have found a reliable way to describe the events that take place during inking using the measurements done by the nanoindenter.**

6.3 Stacking of Carbon Nanotubes

It was shown in Chapter 5 that a tip could ink a portion of nanowires and then another portion of nanowires on top of the first inked portion. This was shown to be due to the porosity of the nanowire film and the ability of the PDMS tip to pass through the nanowires and interact with the material beneath, be it alumina or more nanowires. The evidence of the PDMS interaction with the underlying material was shown by a measureable contact impression of excess cross-linker from the PDMS tip.

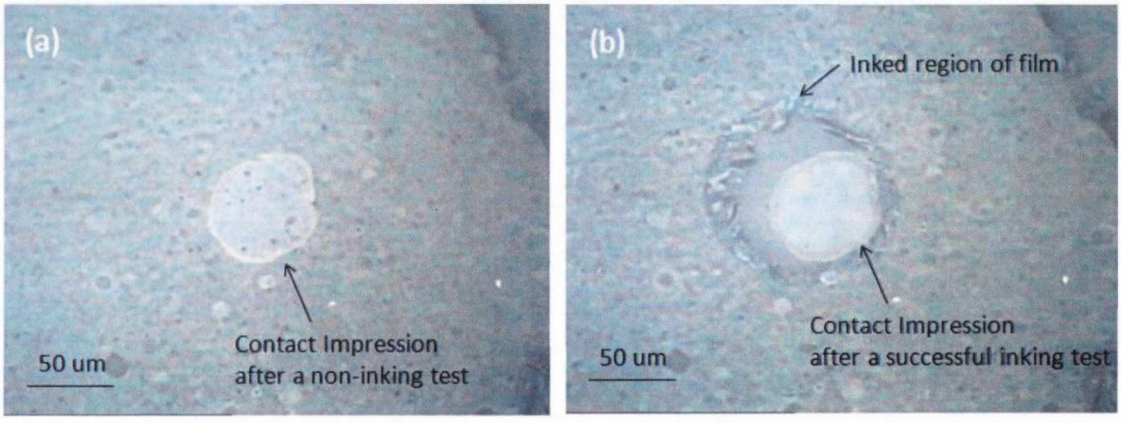

Figure 137. Tests on CNT showing (a) a contact made where no inking occurred and (b) a test after inking occurred. Notice the contact impression on the underlying alumina substrate.

CNT films are also porous in nature suggesting that multiple inkings with them are also possible. The porous nature of the CNT film is illustrated in Figure 137 by showing a CNT film after two tests. (a) shows the CNT film after a test was conducted where no inking event occurred. There is a contact impression after this test as is usual. (b) shows the same section of CNT film after an inking event occurred. Again a contact impression is visible but this time on the underlying alumina substrate, indicating that the PDMS or excess crosslinker was able to pass through the porous CNT film to make contact with the alumina below. The contact impression has the same

shape and size as the original from test (a). Note how the inked region is larger than the contact impression. The reasons for this will be discussed later in this section when the tenting phenomenon is described.

An outstanding question with regards to this is if only the cross-linker is passing through the pores or if the crosslinked PDMS network is also able to penetrate the pores to interact with the substrate below. Figure 138 shows a schematic of inking through a CNT network whereby a tip which has already been inked with CNTs makes contact with a fresh section of CNT film. If only excess cross-linker passed through the film, we would expect to see its contact impression on the CNT film but no inking will have occurred as the crosslinker will have separated from the PDMS bulk as illustrated in Figure 138 (a). If however the PDMS is also passing through and interacting with the CNTs then it would be expected that the CNTs could ink to the tip as shown in Figure 138 (b). This action of inking an already inked tip is referred to as "double-inking". However the inking event may also depend on parameters such as crack velocity, energy release rate and possibly stress in the deformed PDMS. As has been observed many times, even a totally fresh clean PDMS stamp will not always ink a CNT film it comes into contact with. A comparison of tests where an attempted and successful inking of the same film with the same tip is shown later in this chapter.

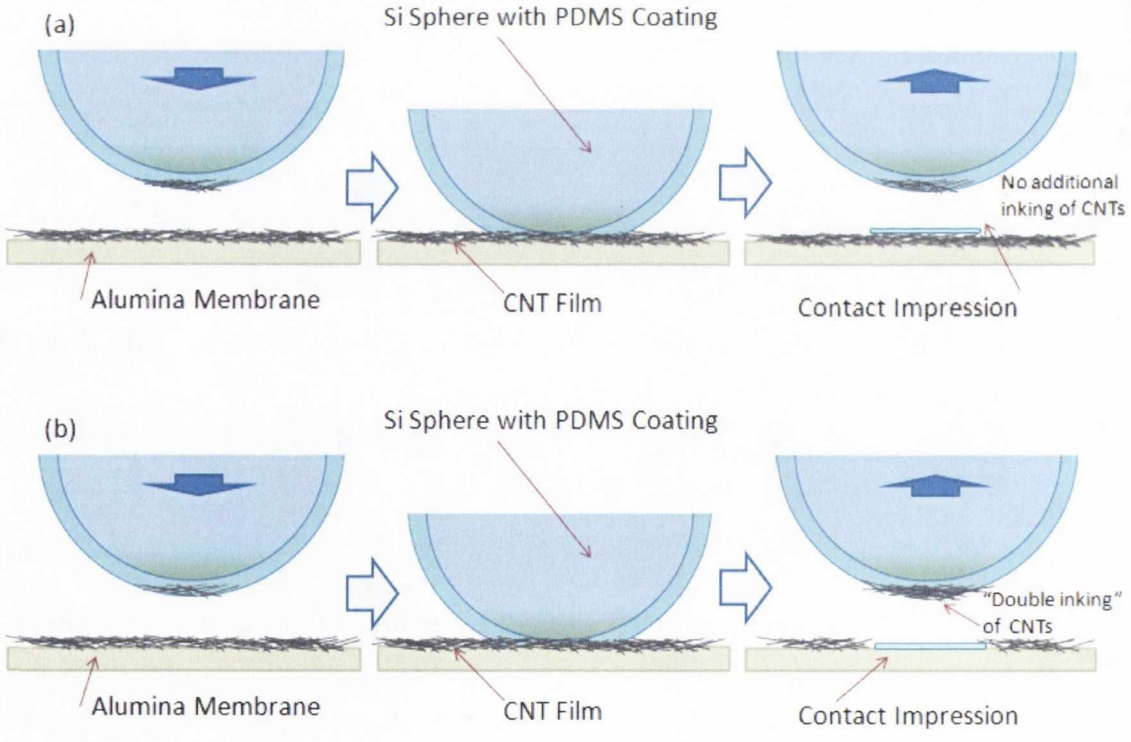

Figure 138. (a) Inking attempt demonstrating how excess cross-linker passes through the CNT film to the substrate below. If only crosslinker makes contact with the film no inking occurs. (b) same test again but if the PDMS makes contact with the CNTs inking can occur.

In the following discussion we demonstrate multiple-layer inking using one test. The 5 mN and 10 mN tests have already been introduced in this chapter and yielded inked regions of a_{ink} = 10 um and a_{ink} = 20 um respectively. An additional test was conducted with the same tip which had the CNTs from the previous tests adhered to it. This had a peak load of only 1 mN and surprisingly a much larger area was inked with a_{ink} = 53 um. Figure 140 shows the differences in the CNT film after each test was conducted. Note the difference in size between the three tests. The 5 mN and 10 mN have already been discussed but the 1 mN test is completely different. Before discussing the 1 mN test in detail we shall first return to our discussion of the 10 mN test.

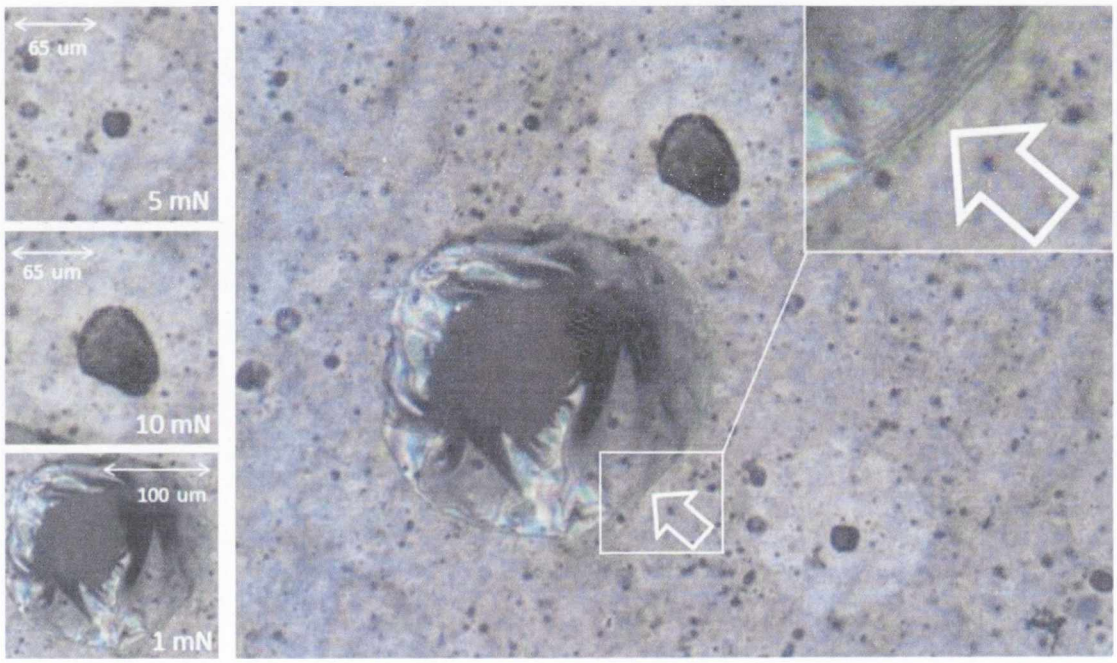

Figure 140. Series of images showing the inking events for CNT tests with different peak loads. The size comparison is shown on the right hand size. Note the interference fringes in the 1 mN test, which are zoomed in on in the insert This is will be discussed in detail presently. The white arrow indicates the boundary of the tented CNT film.

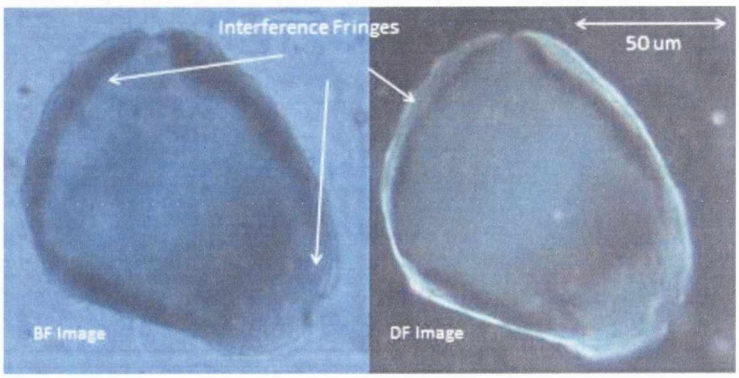

Figure 139. Bright and dark field images of the inked region of the CNT film after the 10 mN test. A shadow is visible in both images due to the material being raised at the edges as illustrated in Figure 10. Notice also the interference fringes at the edge of contact indicating that the film was stressed in this region.

Refer again to Figure 133 which showed cross-section schematic of the effect inking has on the bulk AgNW film and the CNT film. Whereas the AgNWs still lie in the plane afterwards, the fracture boundary of the CNT film can rise out of the plane. The post-tearing remnants of such a structure are observable optically for most CNT inking events. An interesting feature of the contact is the appearance of interference fringes around the fracture border as illustrated in Figure 139. A Carl Zeiss Axio Imager Microscope with a halogen lamp was used to image the inked section of the CNT film in both bright field and dark field modes. The interference fringes are clearly visible at the edge of the contact.

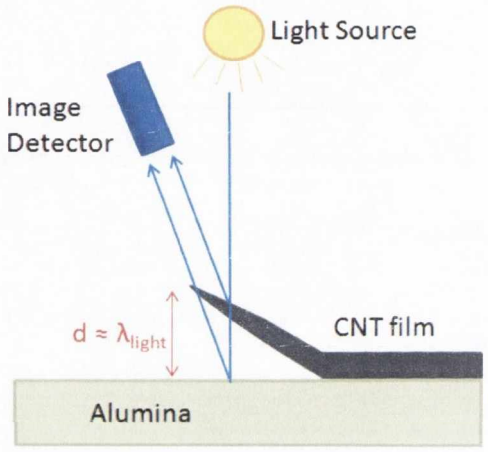

Figure 141. Schematic showing how a small height differential in the CNT film could cause interference fringes to be visible in the optics of the microscope.

The most likely source of the fringes is due to light being phase shifted by the difference in height between the CNT film lifted of the substrate and the substrate itself. The CNT films are optically transparent (at a thickness of 50 nm). This means some light could be transmitted through the CNT film and then reflected from the alumina below. If this reflected light is phase-shifted (by an amount equal to the wavelength of the incident light) relative to the light reflected by the CNT film interference fringes can be observed. Figure 141 shows a schematic illustrating how this works.

For CNT films which experience a height differential above the alumina that is greater or less than the wavelength of the incident light, no fringes will be observed. This is why they are not observed for flat CNT films in the plane, or for films which have been lifted more than approximately 500 nm above the alumina. Interference fringes were never observed with the AgNW films, possibly because they do not behave like a cohesive film which can be distorted out of the plane. Another possibility is that they can be lifted but only by a distance smaller than the wavelength of light.

Before discussing the interference fringes in the 1 mN test let us return to the topic of tenting of the CNT film. The visual blistering of the CNT material around the inked region is very evident in Figure 140. It is like someone created a tent, the apex of which is formed by the PDMS tip contact pulling on the network. Where the film is still firmly bound to the alumina membrane is indicated by the white arrow.

Figure 142 shows schematically how tenting can work. Figure (a) shows the scenario with the 10 mN test where flaps of material stick up out of the plane. Figure (b) shows the situation where

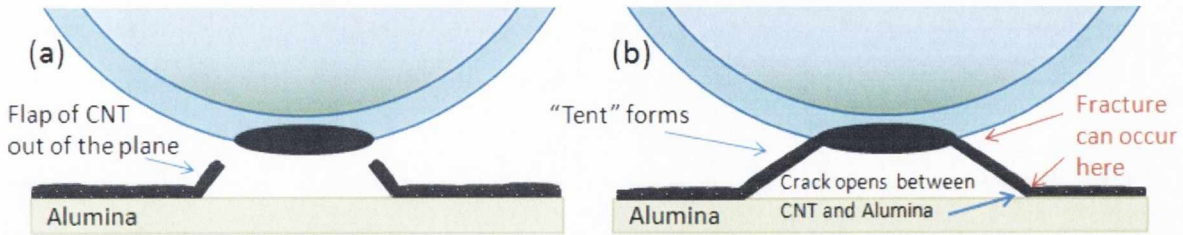

Figure 142. Schematic comparing two CNT fracture situations. In (a) tenting did not occur and fracture occurred in the plane of the bulk CNT network. The test in (b) shows how tenting can occur opening a crack between the CNT and alumina.

tenting occurs, before the film fracture occurs. It has been observed that fracture of the film may take place at the boundary of the contact on the tip, or at boundary between the tent edge and the substrate as shown in the figure by the red arrows.

Referring again to Figure 140 the 1 mN test shows that a larger sized section inked the tip and is a beautiful example of tenting behaviour. The CNT film has been distorted and wrinkled around the inked area and stands up out of the plane with the rest of the CNT film. There is a distinct boundary indicated by the arrow between where the CNT film is still well adhered to the alumina. This boundary has a radius of 120 um. Although both the inked and tented regions of the film are symmetric the inked region, which corresponds to the contact area of the PDMS/CNT contact is not in the centre of the tented region. This suggests that from one side to the other there is different crack propagation behaviour between the CNT film and underlying alumina. The tenting behaviour further supports the idea of treating the CNT films as a single membrane just like the inked films outlined in the literature [63]. Unfortunately a contact impression is not visible in this image but that could also *suggest that fracture occurred at the maximum contact area, where* $a_{ink} = a_{max} = 53$ *um*. This seems like a reasonable assumption based on the maximum contact radii measured by alumina tests for various peak loads. In those tests, which are described in Chapter 4 the 1 mN, 5 mN and 10 mN test had a_{max} values of 54 um, 63 um and 78 um. The a_{max} values of the tests on CNT have values of 66 um for the 5 mN test and 73 um for the 10 mN test.

Figure 143 shows a larger image of the 1 mN inked region of CNTs where interference fringes are clearly visible. From the distribution of the interference fringes it seems likely that the film was pulled out of the plane by a few hundred nanometres around the periphery of the tented region. The absence of interference fringes on the right hand side suggest that this portion of the tented material is either still in the plane or is high up above the plane. The left hand side however shows strong interference effects suggesting that this portion of the film is approximately 500 nm above the plane also. This portion of the CNT network appears loose and distorted which also indicates that this section is no longer in contact with the alumina substrate.

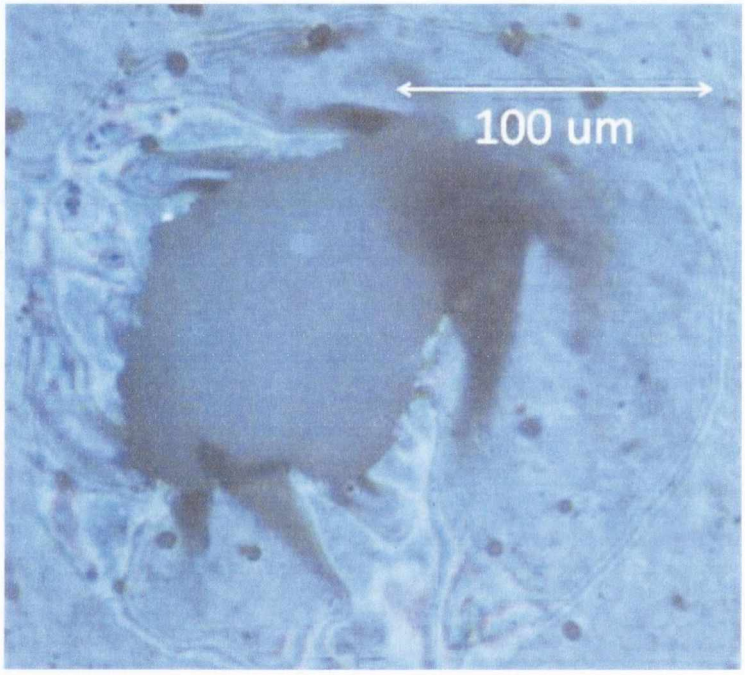

Figure 143. CNT film after inking from the 1 mN test. Interference fringes are clearly available at the edge of the "tent" shown by the arrow and in the "tented" material where the film appears loose and distorted.

Both the 5 mN and 10 mN tests had inking events occur at the point where the neck disengaged from the substrate. The size of the neck determined the size of the inked CNT film. However the situation with the 1 mN test is much more complicated. It appears that inking occurred for a contact size equal to the maximum contact size a_{max} for the PDMS on the CNT film. Is it possible that the PDMS neck radius never decreased from its maximum value? Figure 144 illustrates schematically how this might occur.

In (a) the tip is in contact with the CNT film at its maximum contact value a_{max}. As the tip begins to unload a_{max} does not decrease or does so very slowly. To begin with the tip has not been loaded to a very high value which means a_{max} is close to its value directly after the jump to contact

(approximately 30 um). Additionally the tenting of the CNT membrane could create a tensile force on the PDMS tip which causes it to maintain its present contact area. As the tip unloaded the PDMS remains static but the CNT film begins to change with a crack front opening between the film and the alumina membrane as shown in (b). At some critical point whereby the force on the CNT film is not enough to hold the PDMS tip in place the CNT film fractures, either at the tip interface in (c) or at the alumina interface (d).

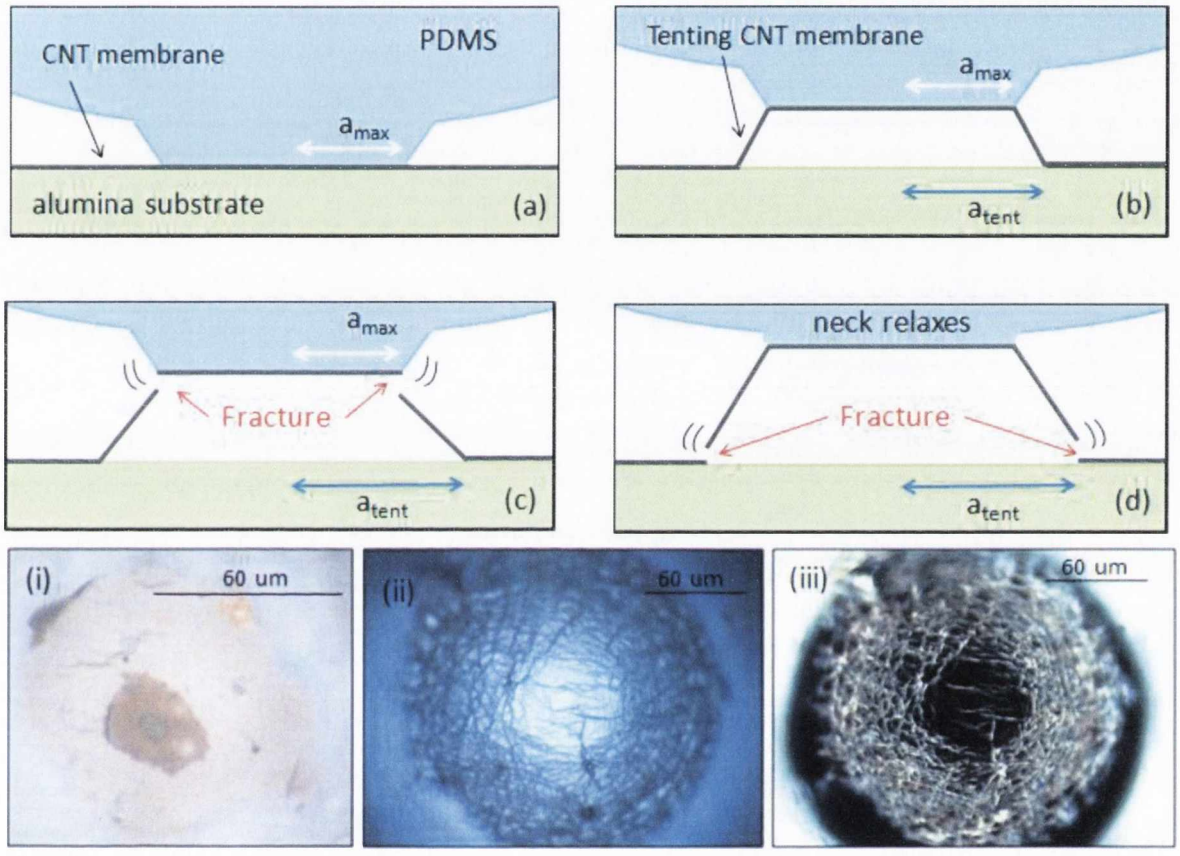

Figure 144. Figures showing the simplest way in which tenting followed by fracture can occur for CNT films. In (a) the tip is in contact with the CNT at the maximum peak load. (b) shows the tip after unloading whereby the neck stays the same shape and size. There is a competition between the restoring force on the neck which wants to change the shape and size of the neck and the CNT tent which causes the neck to maintain its shape and size. (c) and (d) show the two fracture locations of the CNT film after tenting has occurred.

Figure (i) shows the CNT film on a tip which fractured at the neck boundary as in (c). Figures (ii) and (iii) show the same CNT film on a tip in both bright field and dark field view where fracture occurred at the tent boundary as in (d). Note how the film in (i) is completely smooth. However the film shown in (ii) and (iii) has an inner smooth part surrounded by a rather wrinkled film. More discussion is to be found in the text.

conducted for a peak load of only 0.3 mN. A maximum contact radius of approximately 40 um is very typical for this type of test, which correlates the smooth area to the contact of the PDMS on the CNT film. The wrinkled material around it is tented CNT film which was never in contact with the CNT film before fracture occurred. Therefore it is very possible it became distorted as it settled on the PDMS tip after fracture.

This proposed model for the tenting and inking of the CNT film is somewhat simplistic however. It does not take into account if the PDMS neck is still interacting with the underlying alumina for example. It is also unknown if the tautness of the CNT tent would be strong enough to cause the neck to maintain its maximum radius as the unload occurs. It seems compelling however that this effect only seems to occur for tests done with low peak loads whereby the initial contact radius has a similar value of the maximum contact radius. To really investigate this effect properly tests Experiments would need to be done with better optics that might be able to observe the tenting behaviour and the PDMS is necking and deforming throughout the test. This set-up is not available at this time but the picture outlined in Figure 145 provides an excellent starting point for a more in depth and complex analysis of the tenting and transfer phenomenon.

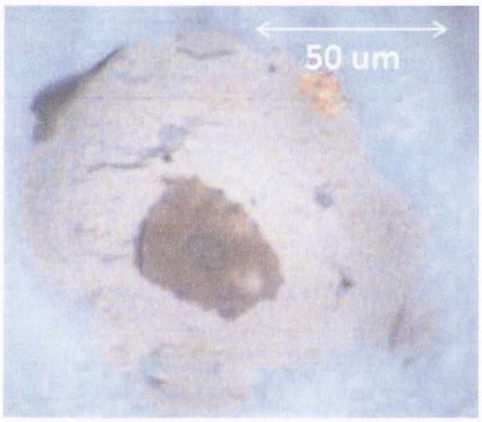

Figure 145. "Stacked" layers of CNT films on one tip. Each layer is approximately 50 nm in thickness.

Figure 145 shows each of the inked CNT sections stacked on top of another on the PDMS tip. Note the change in colour contrast with each stacked layer. Where the stacking is thickest the contrast is darkest. Each stacked section was measured for radius as shown in Figure 146 and shows that the dimensions of the CNT regions on the tip are consistently smaller than the missing CNT piece in the film bulk.

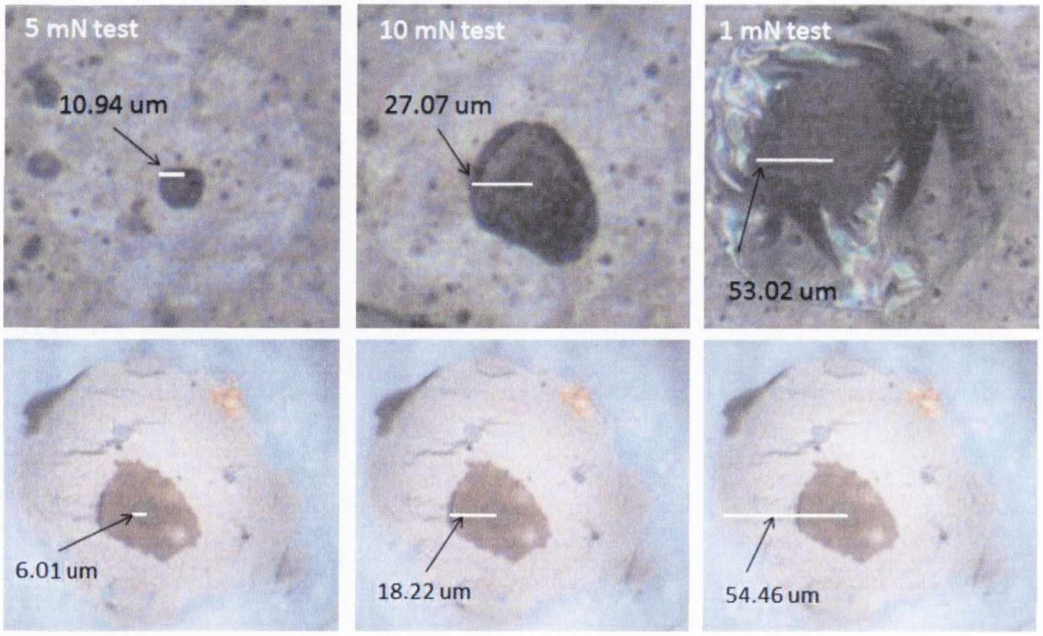

Figure 146. The radius of each inked region and the corresponding nanotubes on the tip are shown. Table 3 shows a comparison of the values measured for each test.

Test	Missing CNT section from film (um)	Inked CNT section on tip (um)
5 mN	10.94	6.01
10 mN	27.07	18.23
1 mN	53.02	54.46

Table 3

In Section 6.1 we discussed how this could be due to the radius of curvature of the tip and/or because of the tearing distortion of the CNT film. If the fracture occurs at the tent boundary with the alumina membrane it is possible that the CNT film could experience some shrinkage in size due to the release of tension as it fractures. Its wrinkled aspect on the tip would have a smaller diameter and circumference than when it was smoothly bound to the alumina membrane.

This brings us to an interesting question regarding the tension in the CNT film during tenting. Is the CNT film a stretchy rubbery material when it experiences a tensile force or not? In Chapter 7 we will discuss electromechanical tests of the CNT films where it has been shown that they can undergo tensile strain without losing their ability to conduct electricity [116]. These nanotube films are adhered to a flexible substrate however which could enhance their mechanical ability to remain in contact with one another when undergoing strain. If they are well adhered to the substrate they are simply carried along with it without losing contact with their neighbours. Although carbon nanotubes individually are noted for their tensile strength there is much work to be done to see if the same holds for the CNT films.

One way of examining their tensile strength is to use a simple geometry argument using the tenting phenomenon. Figure 147 shows the inked CNT film corresponding to the bright field and dark field images in Figure 144. The maximum contact radius of a test done previously on CNTs

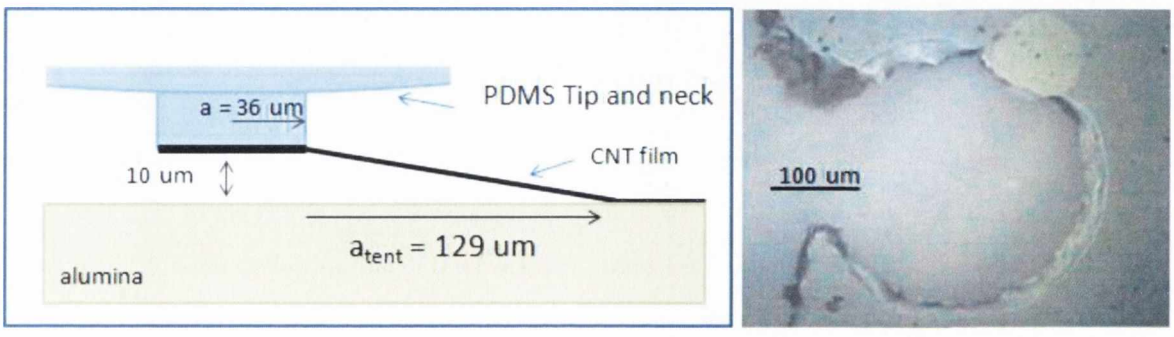

Figure 147. Schematic showing the geometry of tenting. The right hand figures shows the actual test being analysed. Using a simple geometry argument it can be shown that the CNT film extends by only 0.3% before fracture occurs in the test.

showed a_{max} = 50 um. However the smooth region on the tip is only 36 um. Let us assume that the contact decreased slightly at the point of fracture of the CNT film to a value of 36 um. A schematic showing a cross sectional view of the geometry can then be formed as in the figure. This test was loaded to a peak load of 0.3 mN. The maximum displacement above the surface point is less than or equal to 10 um for such tests. This provides a maximum displacement in the z-direction for the tented material. The radius of the removed portion of the film was found to be 165 um. By a simple geometry argument this provides a value for the length of the tented material as 129.4 um which shows little or no extension of the CNT film when tented. This suggests that the CNT film is not elastic and will fracture when a tensile force is applied to it.

CNT Film Extension and Failure

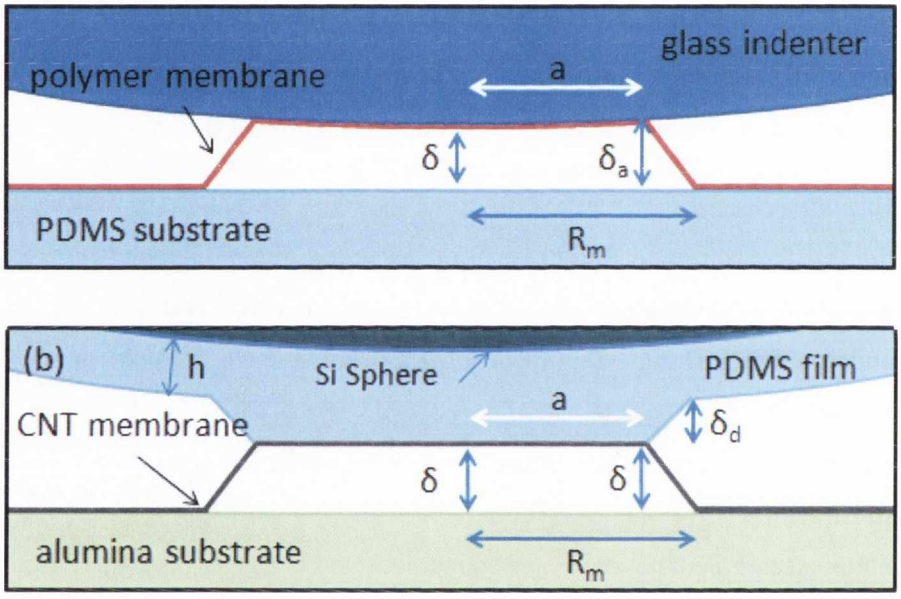

Figure 148. Schematics showing how films extend during inking. (a) shows the schematic described in (REF Shull) and (b) shows the corresponding schematic for our set-up.

Another way of analysing this effect is to use the work done by Shull *et al* [58] on viscoelastic polymer films. Figure 148 (a) shows the schematic used in their paper whereby they are indenting a solid glass sphere into a membrane which is coating a thick layer of PDMS. As can be seen the membrane is being extended and there are two contact radii. The contact radius of the membrane adhered to the glass sphere is designated a and the contact radius of the membrane de-bonded from the PDMS substrate is designated R_m. The glass sphere is rigid and so retains its curvature during testing. The height of the sphere above the substrate which is measured by the experimental set-up is designated δ while the height at the edge of the contact is δ_a.

The deformation of the inked membrane can be described by an extension ratio

$$\lambda = \sqrt{1 + \Delta^2}$$

which has $\Delta = \frac{\delta_a}{R_m - a}$ and $\delta_a = \delta + R - \sqrt{R^2 - a^2}$ where R = radius of curvature of the glass indenter. In Shull's work an extension ratio of 3 was found which when applied to a large strain theory for this geometry gives $G \approx 0.3$ J/m^2 for the energy release rate needed for crack propagation between the polymer film and the PDMS substrate.

Figure 144 (b) shows a schematic of our configuration. In this case the indenting sphere consists of a rigid silicon sphere with a finite layer of deformable PDMS. The thickness of this layer for most of our work is h = 20 um and so exhibits deformation as the CNT film is pulled off the substrate. This deformation forms a cylindrical flat punch geometry as described in the literature [14] and demonstrated by the video data in Chapter 4. Therefore the height of the de-bonded CNT film from the substrate will be the same everywhere i.e. $\delta_a = \delta$. The total displacement measured by the indenter will consist of the height of the tented CNT film δ *and* the height of the deformation in the PDMS δ_d. So the displacement channel during tenting will be $D = \delta + \delta_d$.

Video data taken of low load tests on alumina indicate that the neck δ_d height can be as much as 20 um in length. Figure 149 shows the L-D curves for the CNT tests. The distance between the displacement channel at peak load and the where the load has returned to zero is measured as approximately 38 um. Assuming that the neck was able to extend to a length of 20 um this implies that δ = 18 um. As previously observed the inked region is not in the centre of the de-bonded CNT film but for simplicity Rm is taken to be 123 um. Therefore $\Delta = \frac{\delta}{R_m - a}$ = 0.25 which when filled into $\lambda = \sqrt{1 + \Delta^2}$ yields an extension ratio of 2.2. The problem with this analysis is that it assumes that although the neck does not narrow during the test, the height of it still extends by as much as 20 um. It also predicts that the CNT film is very elastic which is contrary to our previous geometry argument.

Examining Figure 149 again there is unusual behaviour apparent near the peak adhesion point for the 1 mN test. There is sharp corner apparent in the data which is in contrast to the smooth peak adhesion region for the 5 mN and 10 mN tests. Let us assume that the PDMS neck neither narrows nor lengthens during the unload past this point but that this is the location of the fracture of the tented CNT film. Let us also assume that the neck does not lengthen during the unload so that $D = \delta$ = 0.6 um approximately. We then get Δ = 0.009 which yields λ = 1. This value is what we expect for a non-elastic material. Combined with our geometry argument from before

it seems likely that the sharp corner is in fact the location of the fracture of the CNT film whereby

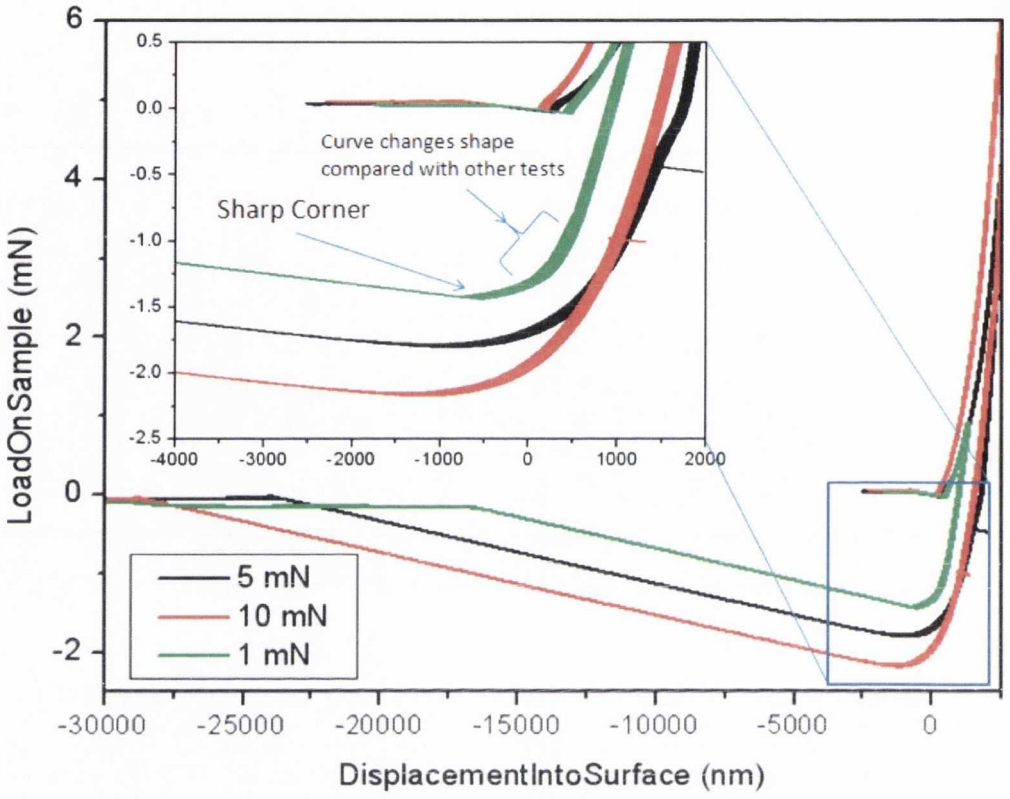

Figure 149. *L-D* curves for the CNT tests showing the location of the sharp corner in the 1 mN test. Also shown is how the curve shape deviates from the other two tests as the peak adhesion point is being reached.

the neck did not decrease in size in the lateral direction.

Closer examination of Figure 149 shows that the curve before the peak adhesion force is different in shape from the 5 mN and 10 mN tests. It is possible that this is due to the neck being constrained by the CNT tent pulling on it and that the CNT film delamination from the alumina is slowing down or stopping at this point. When the CNT film no longer delaminates from the alumina the force of the PDMS tip fractures the film and inking occurs.

Shull's analysis extends to calculating G from the extension ratio information. Adapting the work by Williams [117] on large strain theory an expression for G relating to λ was found

Equation 45

$$G = \frac{Eh}{6}\left(\lambda^2 + \frac{3}{\lambda^2} + \frac{2}{\lambda^4}\right)$$

For $\lambda = 1$ this simply reduces to $G = Eh$. If the CNT film had a Young's modulus similar to a metal like gold for example this means that for a 50 nm film the value of G is approximately 4 J/m^2. Using this knowledge could allow us to tests models calculating the G values for our tests. Figure

150 shows the G vs. v data for the 1 mN test where the G values were calculated from the JKR theory. It can be seen that the maximum value of G at the peak adhesion point, where we think fracture occurs is approximately 3 J/m^2 matching well with the large strain theory. This suggests that the model is at least yielding reasonable values for G at the peak adhesion point. However it must be emphasised that this is a very rough calculation and a much more rigorous approach will be needed to use it for calculating G. However it does provide another clue as to how the contact mechanics for our system could be fully described.

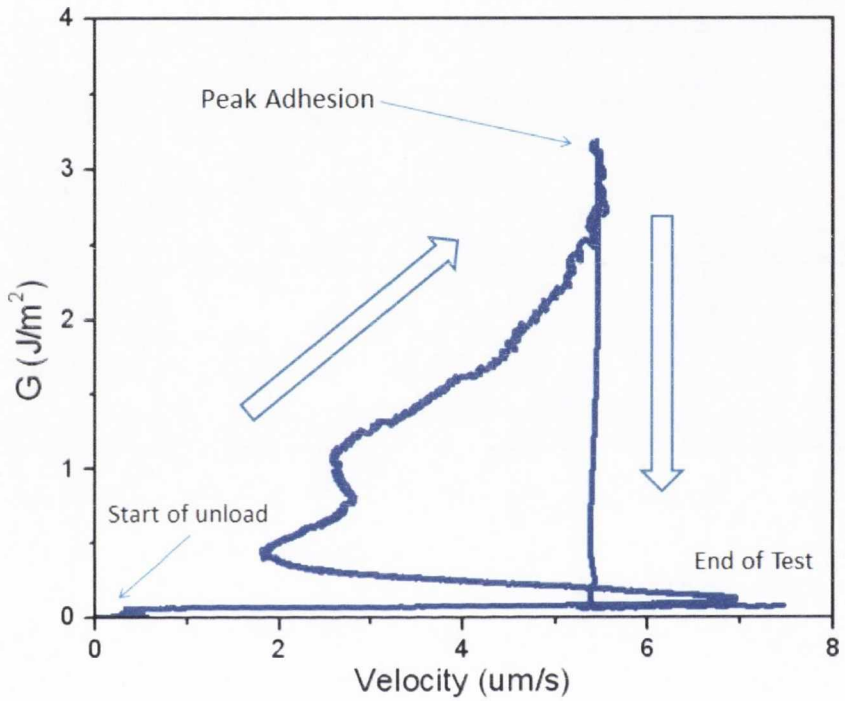

Figure 150. G vs. v data for the 1 mN test on CNTs showing a peak G value of 3 J/m^2 at the peak adhesion point. This matches well with the large strain theory calculation predicting G = 4 J/m^2. The test direction is indicated by the large arrows and the start of the unload and the end of the test are also shown.

6.4 CNT "Seeding" Events

In conducting experiments on inking of the CNT films an interesting and highly reproducible phenomenon was encountered. It was discovered that when a tip is contacted to a CNT at the same location several times at a *low load* a tiny segment of CNTs can ink the tip. As the tests are continued in the same location, this tiny removed segment can grow larger and larger with each subsequent test. The initial inked CNT film is known as a CNT tip "seed".

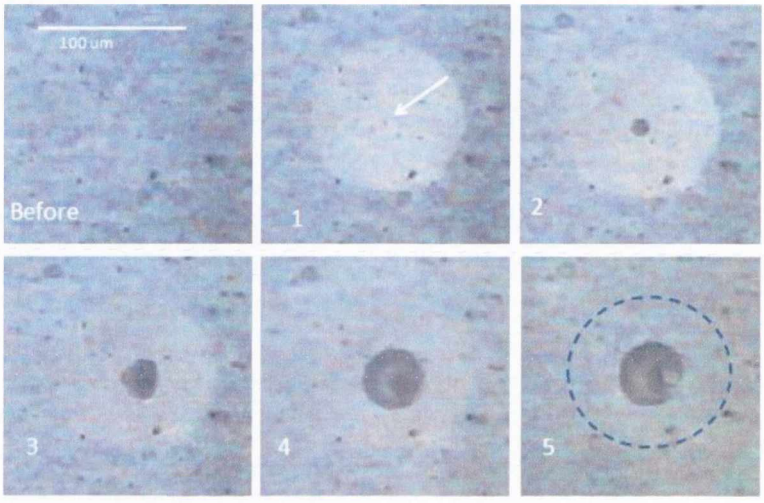

Figure 151. Figure showing a "seeding" of the PDMS tip followed by an incremental increase in the size of inked segments.

Figure 151 shows a series of tests done on the same location on a 50 nm thick network of CNTs. The tests in panels (1) – (3) were loaded to a peak load of 0.3 mN. Panels (4) and (5) were loaded to 0.1 mN. The peak contact radius for the tests was approximately 48 um though. Careful examination of (1) shows a tiny removed circle which is estimated to be 1-2 um radius. A white arrow indicates its location. Figure 152 shows a magnified view of the contact and the removed portion of the CNT film. For each subsequent test the transferred segment increases in size. This increase in inked regions starting with a small circular transfer is known as "seeding transfers". For many tests the last transfer exhibits tenting followed by a larger area transfer as seen in the previous section.

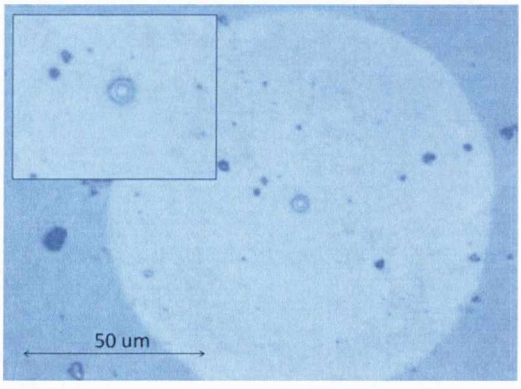

Figure 152. Close up of a seeded CNT film. The inset shows a magnified view of the removed portion of the CNT film.

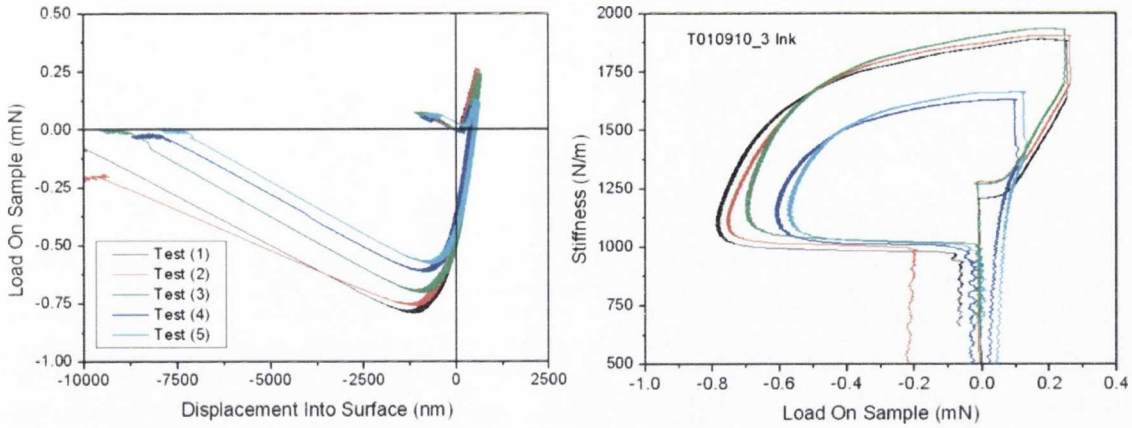

Figure 153. L-D and S-L curves for the series of tests illustrated in Figure 27.

Figure 153 shows the mechanical data for the tests. As with alumina, tests conducted in the same location exhibit a decrease in the peak adhesion for each test. The ink radius of each test is less than 20 um or less indicating again that the inking event took place during the necking segment of the unload in each test. Because the peak load was so small at 0.3 mN there is very little if any instability in the data on the unload. In the case of Figure 151 we demonstrate a sequence of successful inkings for the PDMS tip on CNTs with the same peak load and unload rate. However this was not the first inking attempt with this tip on the CNT film.

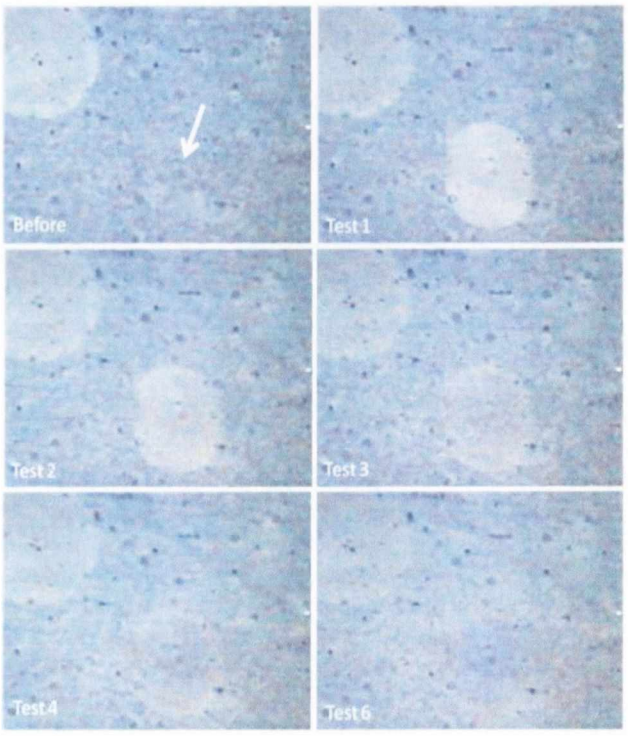

Figure 154. Series of tests on CNT film where the unload rate was increased with a range of values from 0.01 mN/s to 5 mN/s.

The same tip had previously been used in another location close by where no inking event took place. In this situation the unload rate had been varied for each test and the contact impressions are shown in Figure 154. The white arrow indicates a feature that was present in the CNT film before testing which could be mistaken as a seed after test 1. As can be seen no inking of the tip took place. The only difference between this test and the successful inking test is the varying unload rate and the location. Many previous attempts to ink the tip by changing the unload rate have never been successful.

However using the unload rate of 0.1 mN/s with a peak load of 0.3 mN has a very high success rate.

Figure 155 shows the Load-Displacement curves and the v vs. L curves for the series where transfer occurred and the series where it did not. The end of each test is indicated on the L-D curves. The method was not optimised for these tests causing some of the L-D curves to be skewed slightly however it is apparent that tests with higher unload rates such as 1, 2 and 5 mN/s end on or before the zero load on sample point during the unload. Those tests never achieve crack velocities about 6 um/s as a result of ending so quickly. The slower unload rate tests however all continue even after that load has returned to its zero value. This means that when the tip disengages from the sample the crack velocity is greater than 10 um/s. The successful

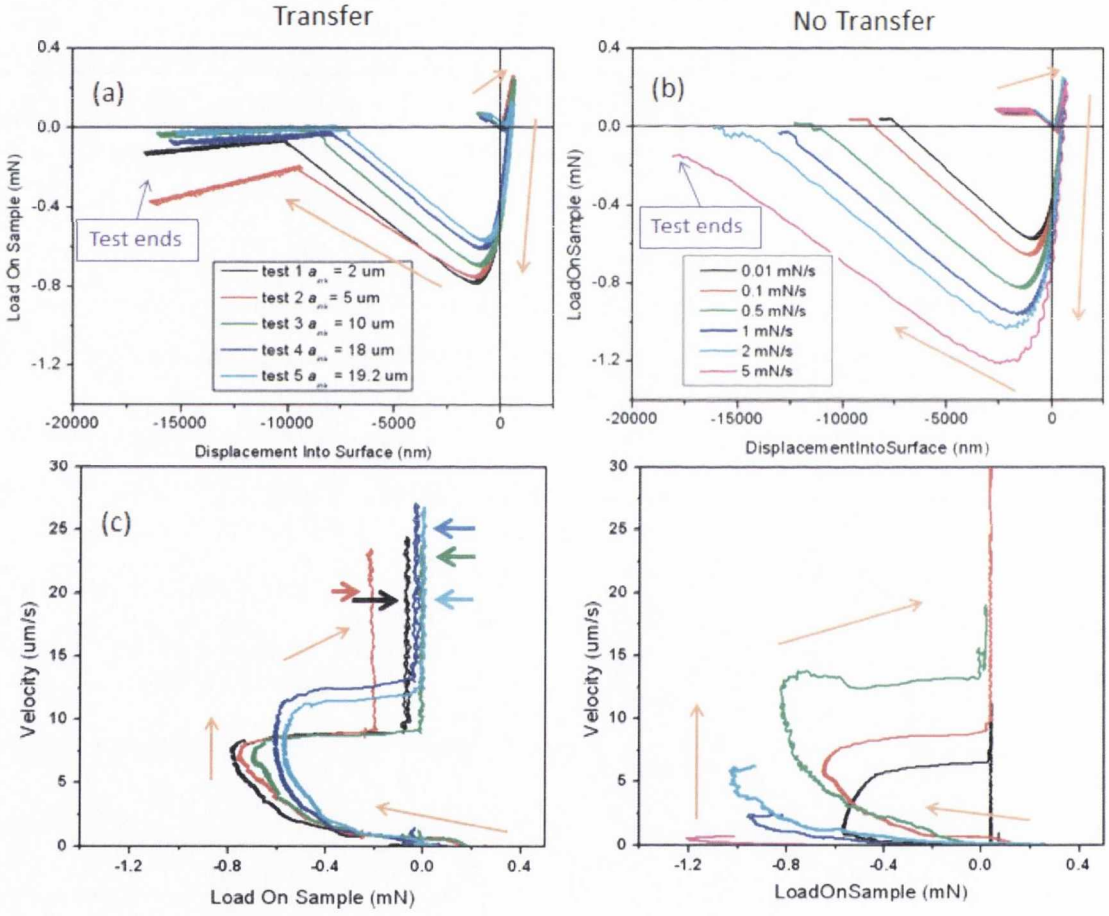

Figure 155. *L-D* and *v-L* curves for the successful and non-successful CNT inking events where a 0.3 mN peak load was used. The successful transfer tests shown in Figures (a) and (c) used the same unload rate of 0.1 mN/s for each test. The end of the tests in Figures (a) and (b) are indicated. The arrows in Figure (c) indicate the location of each inking event. All the inkings occurred at crack velocities of approximately 20 um/s. For the non-transfer series shown in Figures (b) and (d) the unload rate was increased with each test. For unload rates ≥ 1 mN/s the test ends before the load channel returns to zero. The *v- L* curves show with the exception of the 0.1 mN/s test the crack never reaches a velocity greater than 20. Therefore using faster unload rates does not translate into faster crack velocities which suggests that inking of the CNTs is a combination of the disengagement of the tip from the sample mediated by a critical crack velocity. The orange arrows show the direction of the tests.

inking tests (with the exception of the 0.1 mN/s test) all had crack velocities greater than 20 um/s. The unsuccessful tests generally had crack velocities lower than 20 um, presumably due to a neck interaction dependency mediated by the nanoindenter unload rate. This indicates that *there is an optimisation between the neck diameter and the crack velocity mediated by the nanoindenter unload rate*. One may wonder why the 0.1 mN/s test did not ink however it is not unusual to need two or three tests on same location to initiate a seed.

There is a further aspect to the story with regards to the critical crack velocity needed for fracture and transfer to occur.

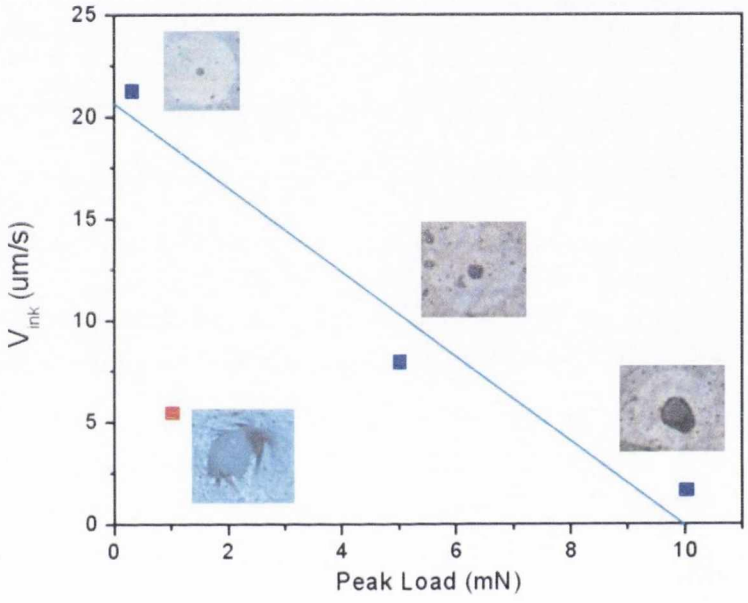

Figure 156. The crack velocity at each inking event, v_{ink} is shown against the peak load for each test highlighted in this chapter. The 1 mN test is an exception because of the way it tented before fracture. The other tests however show that for tests loaded to higher peak loads the crack velocity needed for inking is lower.

Figure 156 shows the crack velocity for all the inking events described in this chapter. This crack velocity is termed v_{ink}. The average v_{ink} of the 0.3 mN test series is found to be 21.3 um/s and is used in this analysis. The 1 mN test is highlighted red and disregarded in this discussion because of its strong tenting behaviour.

There is an obvious trend between the 0.3 mN, 5 mN and 10 mN test whereby the larger the peak load in the test the lower the v_{ink} required to ink the tip. There is also a correlation between the size of the initial transferred region and the peak load of test as discussed previously.

6.5 Summary

Inking of CNT films with PDMS tip

We demonstrated inking of a CNT film with a PDMS tip showing the mechanical data as well as images of the CNT film and the tip after inking. The mechanical data was compared with that for tests on alumina showing lower adhesion on the CNT films. It was demonstrated that tests with a higher peak load yield larger transferred regions due to the size of the neck as the tip disengages from the sample. We also showed how a blister can be created in the CNT film which we call "tenting" and how a crack front can open and propagate between the CNT films and the alumina substrate. Analysing this behaviour may provide information about the elasticity of the film and its tensile strength.

Comparison of CNT and AgNW inking tests

We compared the mechanical data and optical measurements for AgNW tests and CNT inking events. Whereas the AgNWs begin peeling during the unload segment the CNT films do not ink until the tip disengages from the sample. This is because CNT films behave like a cohesive film which needs to be fractured before transferring. Fracturing appears to require conditions of high critical stress and/or cavitation to start the process

Stacking and Seeding of CNT films

It is possible to stack sections of CNT film on one tip due to the porous nature of the films. This is because the PDMS can pass through CNTs on the tip to reach a new film. It is possible that in this way stacked layers of different porous materials could be loaded onto one tip for transfer elsewhere. We demonstrated how a tip could transfer a small region of CNTs and then subsequently larger portions with the same tip using the same parameters. The presence of CNTs on the tip possibly change the neck formation dynamics resulting in a larger diameter neck during the unload. This could explain why larger sections can be transferred for subsequent tests.

This chapter has shown the difference in inking CNTs compared with AgNWs. Whereas the AgNWs behave mostly like individual rods scattered together, which are relatively independent of their neighbours the CNT films behave like cohesive, stretchy membranes from which inked regions need to be torn and which separate cohesively from the alumina membrane. This fundamental

difference in the behaviour between AgNW films and CNT films effect the crack velocities needed to initiate peeling of the film and finally fracture of the films. Whereas a critical crack velocity is often enough to transfer an AgNW film the CNT films require a high critical stress or cavitation process to fracture and finally ink the PDMS stamp.

Chapter 7 Printing and Applications

The vast majority of this thesis work has been concerned with removing a nanomaterial from a surface using a stamp. The next step in the process is to be able to place the nanomaterial somewhere useful, perhaps onto a chip or a device for use in electronics applications. This chapter will describe the processes for doing so as well as the experimental work we have done in this regard. The first part of the chapter describes the printing process itself and the second part describes the applications of printing including published electromechanical testing of the materials.

Section I –Printing

Printing Using a Bulk PDMS Stamp

Work published by Grüner *et al* [2] describes a method for printing carbon nanotube films. Initially the CNT film is on a bulk PDMS stamp and the receiving substrates include plastic such as PET, glass or passivated SiO_2. The method for printing their CNT film involves a thermodynamic process as outlined by Rogers *et al* [46,52] described in Chapter 1.

Initially the authors ink a bulk PDMS stamp as described in Chapter 1. They then heat the receiving substrate (usually glass or plastic) on a hot plate to approximately 80°C for about 10 mins. Then they contact that CNT loaded PDMS stamp to the receiving substrate and peel the stamp away leaving behind a complete CNT film. This works both for patterned and un-patterned films as shown in Figure 157. The authors also claim that they can print on SiO_2 which has been hydrogen passivated, although there are no images of the resulting film.

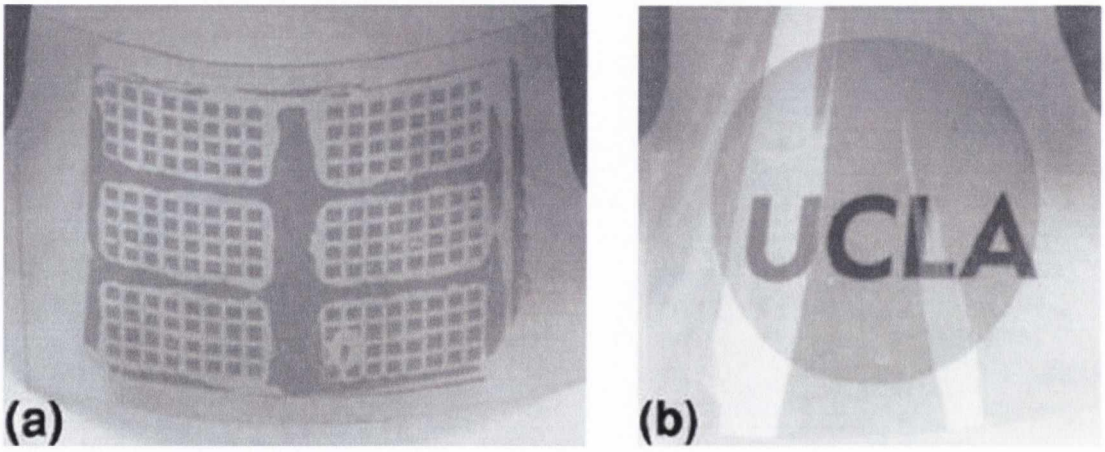

Figure 157. Patterned and un-patterned CNT films on PET substrates as described by Grüner *et al* [1].

This method appears relatively straightforward and simple and there is no discussion of any additional mechanical modifications, such as peel rate or chemical modifications to the method. Nor is there a discussion of why heat might facilitate printing. This topic is discussed in work done by Rogers *et al* [46] and described in Chapter 1, which relates the rate dependence of the crack velocity with the temperature of the system, using the temperature shift parameter a_T where

Equation 46

$$\log_{10} a_T = -17.6 \frac{T - T_g}{52 + T - T_g}$$

and T_g is the glass transition temperature of the PDMS. This can be related to the power-law relation for G and v using

Equation 47

$$G = G_0(1 + (a_T v^* v)^n)$$

Although they demonstrate the validity of this system we have not been able to adequately measure G as described in Chapters 4, 5 and 6. Conducting printing experiments using the nanoindenter is still in its initial stages and this chapter will be providing only a brief overview of printing done so far in our group. In the future a much more rigorous experimental and analytical approach will be taken to the printing methods but it is hoped that the reader will appreciate some of the possibilities and applications that printing of the materials will provide. The first portion of the chapter will describe printing methods done by hand, using temperature and pressure. Printing on this scale (in the order of centimetres) has shown that the printing system can be scaled up from micron sized segments of material and the last section in the chapter discusses the applications of these films in the Electromechanical Testing section.

Printing Using Heat in the Nanoindenter

Aside from the normal sample stage described in Chapter 3 the nanoindenter also has a heat stage which allows the sample to be tested under different temperature conditions. The heat stage consists of a heating element onto which a metal puck holding the sample can be placed. It is controlled by a heating supply unit onto which the target temperature can be set. Figure 158 shows a schematic of the heat stage setup in the nanoindenter.

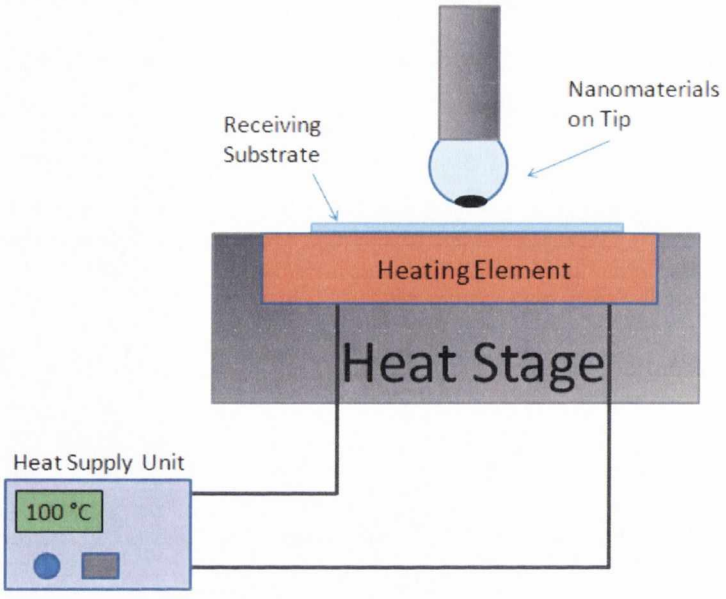

Figure 158. Schematic illustrating the use of the heat stage for a transfer event in the nanoindenter.

One problem to be overcome regards attaching the sample to the sample holder without using crystal bond. Crystal bond cannot be used because it melts when heated no longer forming a solid, unmoveable interface. Therefore we used silver paint to attach the samples. The samples were placed in a vacuum oven to remove excess solvents from the paint and the result was a firm attachment of the sample to the sample holder.

The tests and the method were exactly the same as for the AgNWs and the CNT films described in chapters 5 and 6. A rough surface find was done initially on the receiving substrate while *cold* and then an extra 40 um pull-back was added before testing to account for changes in the substrate height due to heating. The substrates were set to be heated to 100°C and a thermistor was used to check the surface temperature of the receiving substrate before testing commenced. Once the test was complete the test area was imaged with the microscope to find any printed nanomaterials.

Although the printing experiments were attempted for both AgNWs and for CNTs on PET and glass, success was only found with the CNT films. There was no evidence of printing transfer of the AgNWs despite several attempts at various temperatures.

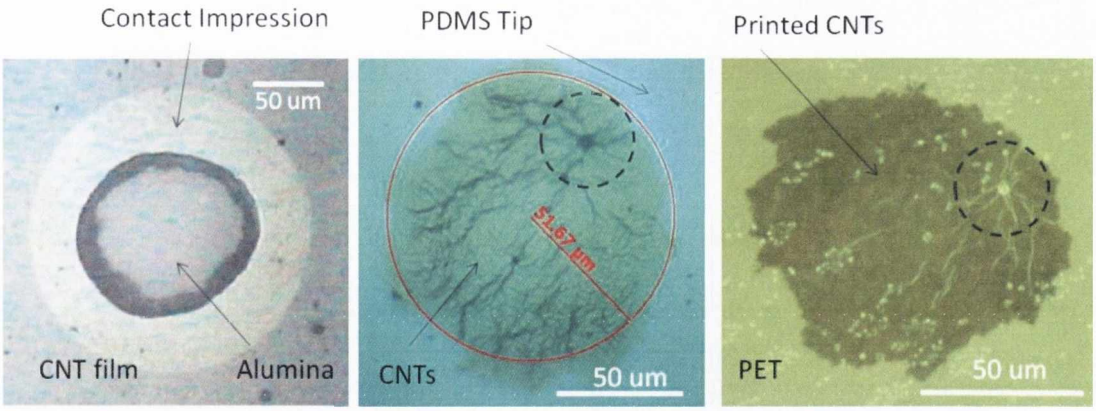

Figure 159. Series showing the stages of transfer of a CNT film from inking the tip to printing on PET. Notice the distortions in the CNT film on the tip and how they are perfectly preserved in the printed version.

Figure 159 shows the stages of a CNT transfer event, from inking to printing. The first image shows a CNT film after an inking event has taken place. The contact impression is clearly visible as is the underlying alumina. The CNTs inking the tip show some distortions and wrinkling of the CNT film indicating that it is not completely smooth. A discussion on the smoothness of the inking CNTs was made in Chapter 6. Finally the printed CNTs are shown on PET. As can be seen the shape the CNTs was preserved perfectly as were the wrinkles and distortions, including an "eye-like" feature indicated by the black dotted circle.

Although we had hoped to measure careful data for the printing experiments as was the case for the inking experiments, there were some difficulties in obtaining good data sets relating to the software and the nanoindenter itself. It is hoped these issues will be resolved in the future.

The next section shows some very recent work where we were able to print CNT films and AgNW films onto silicon oxide at room temperature. This was a very surprising result as even at temperature it had not been possible to ink on silicon with a native oxide. The silicon oxide described in the next section had been treated by oxygen etching, photolithograpy with SU8, development with acetone followed by sputtering and removal with acetone. Perhaps one of these processes, or the defined oxygen layer of the SiO_2 somehow contributed to the adhesion and printing of the materials.

Section II Applications

Printing for Electrical Devices

A long-term aim for this research is to be able to ink and print novel materials such as AgNWs and CNTs using a PDMS stamp for use in devices. The nanomaterials need to be processed in a particular way, including being dispersed. Therefore it would be of great use to be able to pick them up post processing, perhaps cut out shapes and sizes and then place them for use in devices. To this end in collaboration with Prof. Georg Duesberg's research group attempts were made at printing AgNW and CNT films onto circuits.

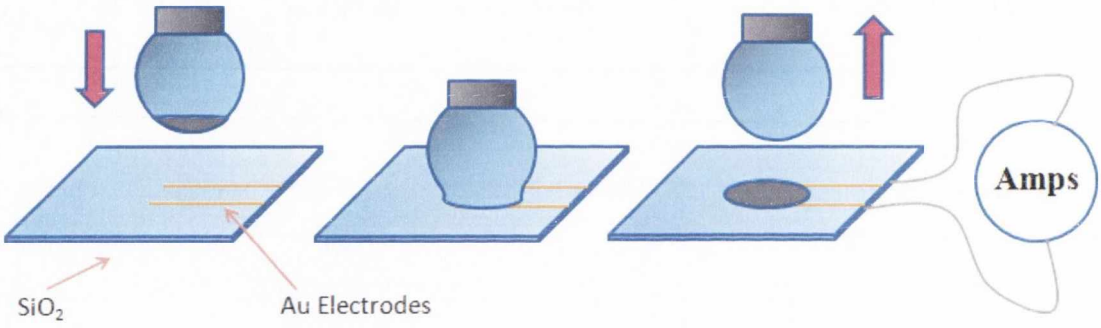

Figure 160. Schematic illustrating printing of nanomaterials onto gold electrodes for use in a circuit.

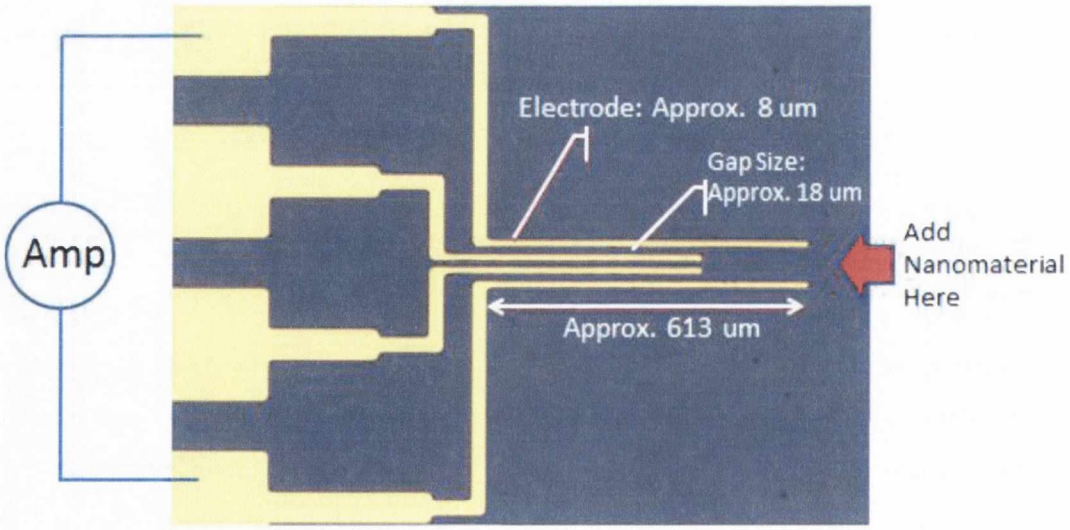

Figure 161. Photograph of a four point probe circuit device created with gold on an SiO_2 substrate. Image courtesy of Dr. Kangho Lee from Prof. Duesberg's group, CRANN, Trinity College Dublin.

Figure 160 shows a schematic of how such a material could be printed into a circuit. By passing a current through the circuit it could be seen if the nanomaterial is 1) still conductive after processing, inking and printing and 2) can be placed accurately on the device to close the circuit. Figure 161 shows a photograph of a circuit device which will have the printed nanomaterials

added to it. This device is made from evaporating a 100 nm layer of Au onto a silicon chip using a photolithography mask. The Au has an 20 nm thick adhesive layer of nickel.

Initially we simply attempted to contact the nanomaterial loaded tip to the circuit in order to measure the change in electrical response. What we discovered to our surprise is that the nanomaterial adhered to the circuit. This occurred for both the AgNWs and the CNTs and is shown in Figure 162. Another interesting observation is that in some cases a contact impression was visible on the SiO_2. This is the first time that has been observed and will allow for a mechanical analysis of the process.

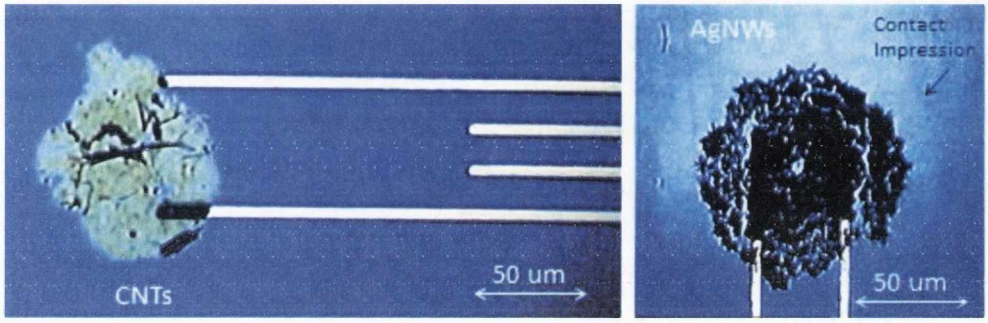

Figure 162. Images of CNTs and AgNWs which have been printed onto circuit devices. Notice that the PDMS left a visible contact impression for the AgNW test. This is the first time it has been observed on silicon.

A presence of the CNTs and AgNWs closed the circuit of the two point probe device pictured showing that using a nanoindenter to ink and print these materials can create useable electrical devices. Our future work includes optimising the nanoindenter so that we can measure the electrical data as a separate channel alongside the mechanical channels. We also want to contact the materials to a four point probe system to better measure the electrical properties of the materials and to be able to monitor any degradation that may occur during transfer. It will be important to measure the effect the excess crosslinker has on the materials. The crosslinker is not electrically conductive and so may inhibit the conductivity of the nanomaterials. This could present quite a serious problem if the crosslinker proves difficult to remove and will require careful experimental investigation.

Possibilities for this Technology

A major goal of current research in materials is the discovery and manipulation of materials with superior electrical and mechanical properties for use in a new generation of electronic circuits. One can see the emphasis moving away from silicon based devices to ones which provide more flexibility, greater power and smaller size. Using our printing technique we have demonstrated how such novel materials such as CNTs and AgNWs could be processed in one place and then very precisely picked up and deposited into a circuit or device and become part of that structure.

Although the main emphasis of this thesis has been on simple circular sections of nanomaterial, patterning of the PDMS stamp could provide possibilities regarding the size and shape of the nanomaterials being transferred. They could be printed on devices which might have proved awkward to access using standard lithography techniques and there are potentially no additional chemicals or processes required. This could be scaled up to create a cheap, fast and easy transfer tool for industrial applications. A logical next step in this research would be to try and transfer materials of different shapes and sizes, arrays and patterns and this work is ongoing at this time.

Another aspect to consider is the application of this technique to other materials. Potentially this technique could be applied to any nano or micromaterial that was desired. In fact transfer of discrete objects such as nanospheres could be easier than the transfer of continuous thin films which was demonstrated in Chapter 6. This is because no tearing of the material would be required first, it would be just be a simple pick up and hopefully put down. One can speculate that there could be limitations, most notably as a result of contamination by the excess crosslinker or from a lack of adhesion between the target material and the PDMS stamp but these limitations could perhaps be overcome by trying a range of polymers for the stamps and testing how each corresponds to a particular material.

There is a wealth of possibilities and investigating materials with different geometries, surface energies and chemistries could provide information on modifying the mechanical parameters such as load and unload rate in order to manipulate and facilitate the transfer of any material. This is a very exciting prospect and the possible uses in industry and research are very many.

Electromechanical Testing of AgNW and CNT films

The use of nanomaterials with superior conducting and tensile properties opens the door to many novel electronics opportunities as well as solving existing limitations of materials currently in use such as ITO. Aside from small scale use of the materials in electronic circuits as discussed in Chapter 7, the materials can be scaled-up for use over larger areas. An example of this would be for transparent conducting electrodes for use in computer screens or electronic paper (e-paper). The current technology material in use for these applications is indium-tin-oxide (ITO). There are several disadvantages to using ITO. Firstly indium supplies are dwindling from continued mining leading to a massive increase in the price of the material. Another limitation involves the nature of the material itself in that is it very brittle. This means that its use in touchscreens for example is limited. The ITO eventually fractures leading to no electricity being conducted in that area. The

other issue with ITO is that it has a yellowish tint which contributes to difficulties seeing images in sunlight. This is of great inconvenience as advances in technology makes the use of smartphones ever more prevalent.

In contrast novel nanomaterials such as carbon nanotubes and silver nanowires have every potential for replacing ITO in larger conducting interfaces. Their superior electrical and conductive properties make them potentially ideal candidates. They are also extremely flexible and do not appear to break down easily due to mechanical stress and strain. Films can be created which are as transparent as ITO and lack any yellow tint and they can be created in a laboratory. Carbon is a common element and silver supplies plentiful. Using these novel materials opens to the door to opportunities in *flexible electronics*. Imagine a tablet or e-paper that can be rolled up like a sheet of plastic.

In order to test the feasibility of these novel materials tests were done to study the electronic properties of the materials as a function of stress and strain. There were two approaches taken. One tested the behaviour of the materials while undergoing tensile or compressive strain, either by pulling apart the materials or bending them. The other approach was to conduct cyclic testing of the films whereby they were bent several thousand times and the change in their electronic properties was tested. The next section describes the experimental set-up used for these tests.

Experimental Set-up

In order to test the electronic behaviour of the nanomaterials under stress and strain, tests were done on the nanomaterials printed onto PET and their electrical resistance was measured as a function of the strain and/or cycle number. A simple two point probe system was used to measure the resistance across the samples. Although a four-point probe system would have allowed for the contact resistance to be eliminated it would have created significant experimental challenges. Therefore in this work we considered the *relative change* in resistance of the materials, rather than the absolute values measured.

A commercial tensile tester (Zwick Z0.5 ProLine Tensile Tester) was used to conduct the mechanical testing of the samples. During testing a current was passed through the samples using a Keithly KE2601 sourcemeter. A custom LabView® program was developed which allowed the user to correlate the mechanical data measured by the tensile tester with the electrical signals applied by and measured by the sourcemeter. This LabView® interface was developed by our industrial partners, Hewlett Packard ®.

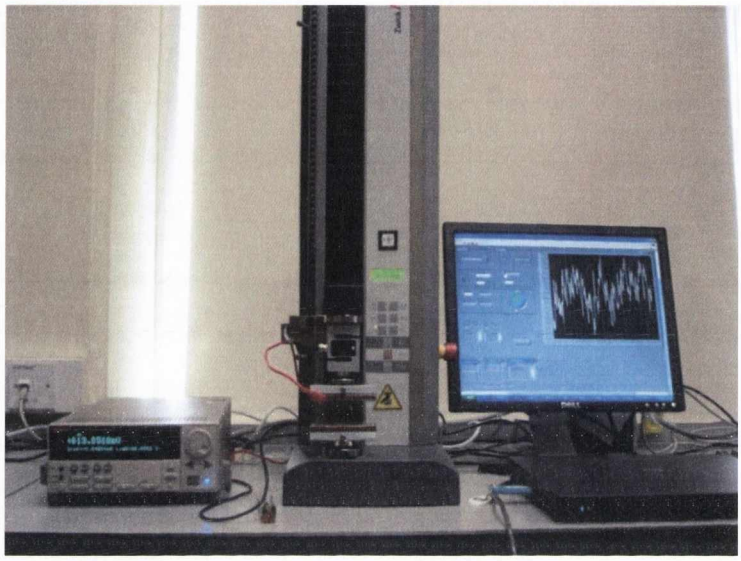

Figure 163. Experimental set-up showing a commercial Zwick tensile tester and a current supply used for in situ electromechanical testing of nanomaterials on PET.

Custom clamps were created for the tensile tester which allowed for a two point probe measurement of the sample using the sourcemeter. A current is fed into the sample via these probes and the resistance across the sample is measured using the LabView® software. The LabView® program also "spies" on the tensile tester software for information about its channels such as the force on the sample, the cycle number, the grip to grip separation etc. An image of the experimental set-up and a diagram of the clamps are pictured in Figure 164.

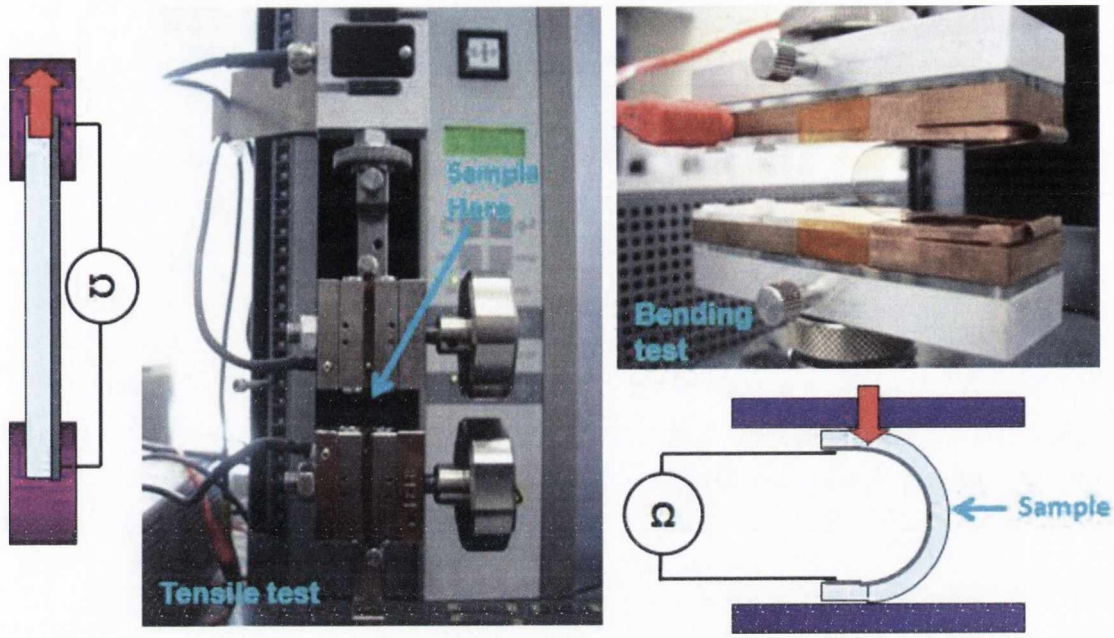

Figure 164. Custom clamps for conducting tensile and bending tests on the materials. A schematic illustrating the 2-point probe system is also shown. The initial distance between the clamps is 15 mm. The final distance, at the maximum bend of the sample is 5 mm. This means that the samples have an initial bend radius of 7.5 mm and a final bend radius of 2.5 mm. The samples all have lengths of 35 mm.

After the nanomaterials had been printed onto the PET, gold conducting pads were evaporated on either end. The samples were carefully placed in the custom clamps, using silver paint if necessary to improve the contact between the copper electrodes of the clamp and the gold pads. Once the sample was in place the LabView® software was used to set a current across the sample and the resulting resistance was measured. Typically samples underwent either tensile tests, where the films were slowly stretched in the z-direction or bending tests with the film either on the inside or the outside of the PET. In this way, the bending tests could be considered either tensile or compressive. Figure 165 shows an example of the LabView® interface where the force and resistance can be compared.

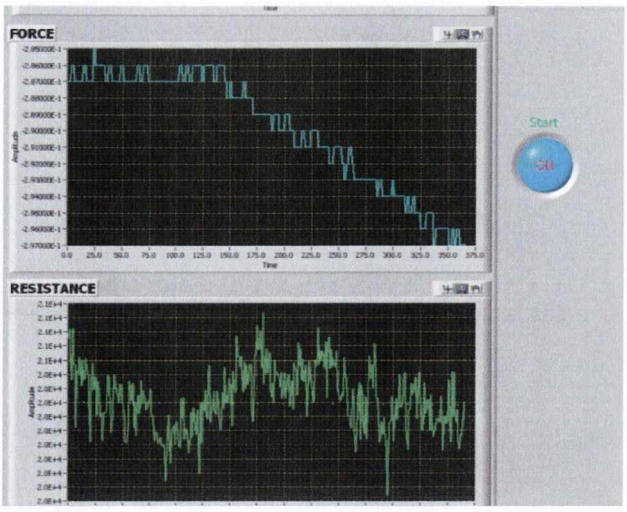

Figure 165. LabView interface showing the force and resistance changing across the sample during testing.

Using work by Bouten *et al* [118], the bending test can be analysed as follows, where pure elastic deformation of the substrate is assumed. The relationship of the critical strain of the substrate to the minimum radius of the bend is given by

Equation 48

$$\varepsilon_{\max} = h / 2r_{\min}$$

where r_{min} is the minimum radius. Here, h is half the total thickness of the film and substrate together. The critical strain is defined in the theory as being where the relative resistance increase, $\Delta R/R_0$ = 10 % where R_o is the initial resistance of the film defined by $R_o = R_s l/w$, R_s being the surface resistance of the film and l and w referring to the length and width of the conductive sample respectively.

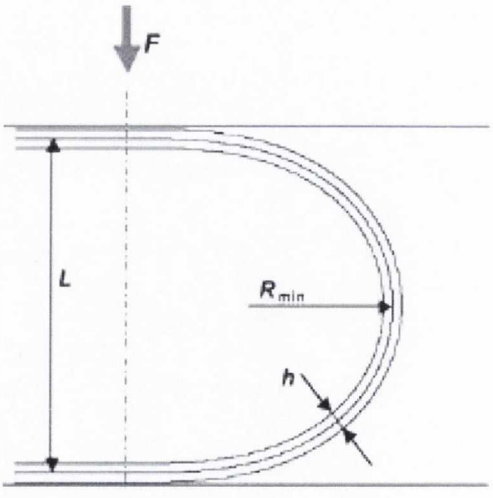

Figure 166. Schematic illustrating the geometry of bending used in Equation 48. From Bouten *et al* [101]

The LabView® software measures the resistance of the sample during the tests. Because it "spies" on the tensile tester software, and because both programs had to be activated manually, there is a small time delay between the two which we were aware of but which didn't significantly affect our results. Once the resistance is measured, it is applied to the following formula in order to calculate the sheet resistance of the film in Ohms per square (Ω/□):

Equation 49

$$R_S = \frac{Rw}{L}$$

where w is the width of the silver contacts and L is the distance between the two inner contacts. The units of Ω/□ are dimensionally equivalent to resistance and the square is there to indicate this is *sheet resistance* rather than bulk resistance. The conductivity of the films is then found from the following relation:

Equation 50

$$\sigma = \frac{1}{R_S t}$$

where t is the thickness of the film.

Results

The first range of tests to be discussed were conducted on Iljin Nanotech tubes which had been dispersed in water and surfactant. The electromechanical testing was part of a larger study comparing the optical, conductive and electromechanical properties of films dispersed in two different types of surfactant, sodium dodecylbenesulfonate (SDBS) and sodium dodecylsulphate (SDS) [116]. As explained in Chapter 3 dispersing carbon nanotubes in surfactants or polar solvents overcomes the bundling tendencies of the nanotubes. In the case of surfactants this is done by overcoming the hydrophobicity of the nanotubes thus allowing water to intersperse between the tubes.

Different thicknesses of films were printed onto PET for electromechanical testing. In the case of this first set of results the films underwent *bending tests* where the film was bent from an initial bend radius of 7.5 mm to a minimum bend radius of 2.5 mm. This is called the *bending* phase of the cycle. The film was held at the lower bend radius for 5 seconds before being relaxed back to the 7.5 mm radius. This is called the *relaxing phase* of the cycle. Again the film was held for 5 seconds before commencing with the next bend. The films were bent in this way for at least 1000 cycles. The tests were conducted for the film on the inner side of the bend radius (compression tests) and the outside bend radius (tension) as shown schematically in Figure 167.

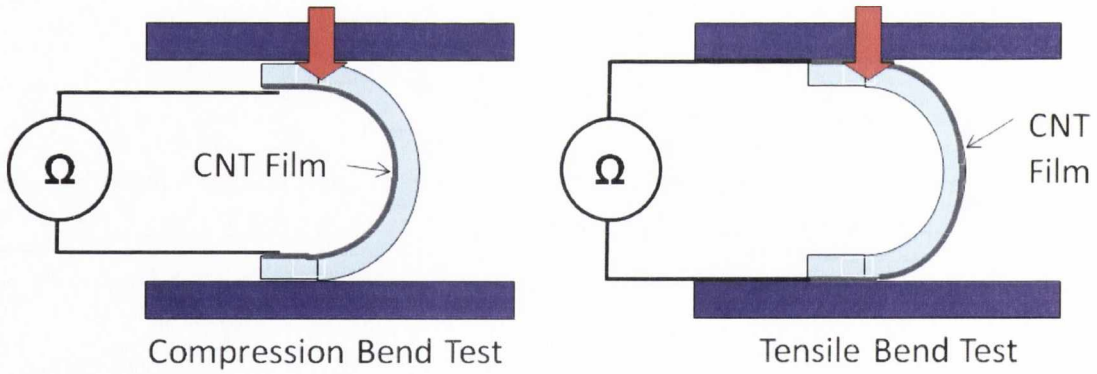

Figure 167. Schematic of compression and tensile configurations of the bend tests.

Analysis was conducted on the first bend cycle for the change in sheet resistance as a function of bend radius. Subsequently the sheet resistance as a function of the cycle number was examined.

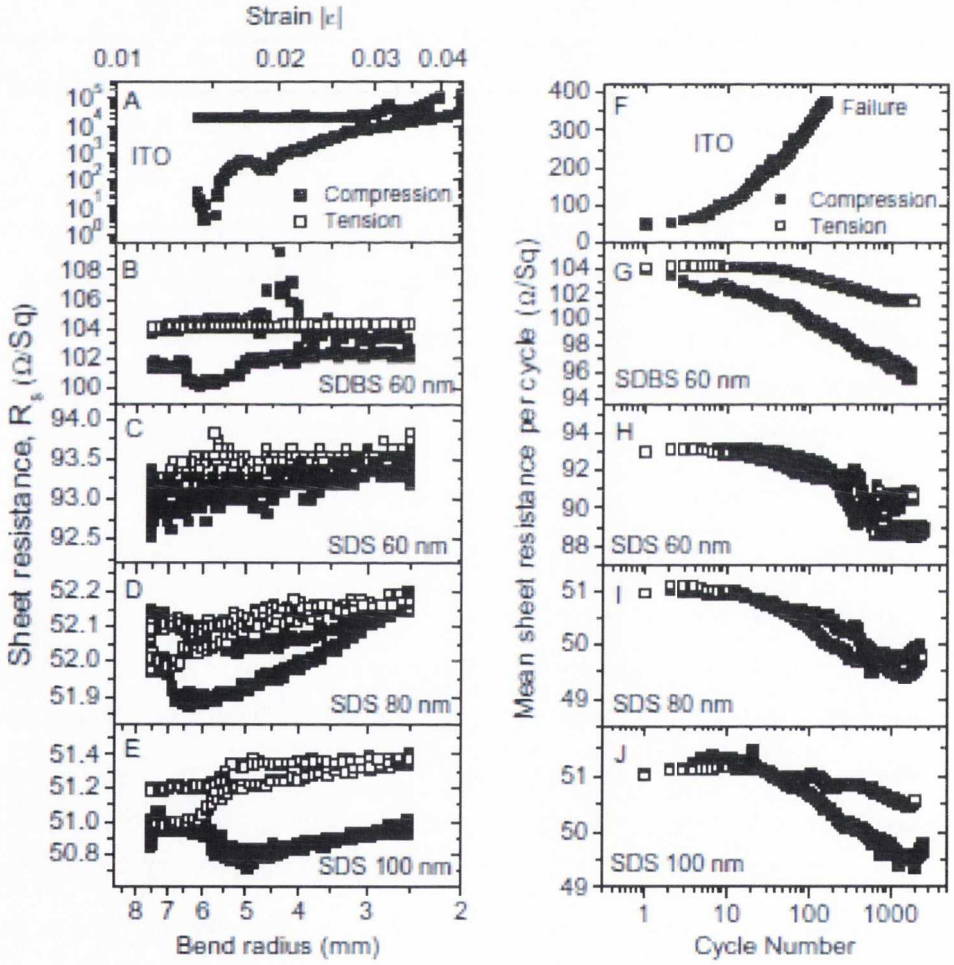

Figure 168. Data showing a comparison of electromechanical tests for CNT films dispersed in SDS and SDBS. Different thicknesses for the SDS films are shown. Tests on ITO are also shown for comparison where only compression tests were done. As can be seen the ITO films failed completely after approximately 100 cycles whereas the CNT films exhibited no more than an 8% change in resistance over 100 cycles. For many of the films in tension, only 2 % was observed. From Doherty *et al* [99].

Figure 168 shows the results from the electromechanical testing of films on PET for one and many cycles for the films. An ITO film is shown for comparison. To avoid complete failure on the first test the ITO was only bent to a minimum of 20 mm in each cycle. The left-hand column documents the change in the sheet resistance for one cycle as a function of bend radius and the subsequent strain calculated by Equation 48. Only the compression data is shown for ITO but as can be seen from the data, the sheet resistance increases steadily by four orders of magnitude during the bending cycle but does not recover at all during the relaxing phase. The cycling data on the right-hand column shows that the ITO sheet resistance increased fourfold over 100 cycles before experiencing complete failure.

In contrast the CNT films had a sheet resistance change of less than 5% for the first cycle and overall the resistance changed by only 8% over 1000 cycles. Failure never occurred for any of the films and time constraints were the only reason for ending the tests. The PET exhibited some plastic deformation after the electromechanical tests and it would be an interesting study to examine whether the PET or the CNT films would fail first. Additionally the reasons for the change in sheet resistance may have less to do with the CNT films themselves than with their lamination to the PET substrate. The printing methods in this thesis yield a good adhesive contact between the CNT films and the PET in that they cannot be easily removed by rubbing them off the adhesion has never been rigorously tested. It is possible that as the PET plastically deforms defects in the adhesive contact between the CNT film and the PET film may appear and grow with cycle number, leading to microscopic partial delamination of the film from the PET and a subsequent break down with the gold contact pads at either end. In Chapter 6 we demonstrated complete fracture of "freestanding" CNT films at high strains and a non-uniform strain across the PET sample might induced domains where local fracture of the films can occur, again causing a breakdown in the conductivity of the bulk film. In order to investigate this hypothesis more testing would be needed on the films such as *in situ* bending or tensile tests in an SEM where the nanotube film itself can be viewed during the experiments. This is perhaps a future possibility.

Figure 169 [104] shows the cycling tests done on a set of silver nanowire films on PET. Each film has a different thickness of t = 90 nm, t = 182 nm and t = 271 nm respectively. All the films experienced compressive bending tests and the 182 nm film also experience a tensile bending test. As with the CNT films the maximum bend radius was 7.5 mm and the minimum was 2.5 mm.

The thinnest film began to fail after 200 cycles with an increase in the sheet resistance of approximately 2 orders of magnitude. However the film then stabilised at that level and did not fail completely by 1000 cycles. The thicker films showed a sheet resistance variance of < 2% over

1000 cycles. A bulk silver film was also shown for comparison and exhibited a similar variance of sheet resistance after 1000 cycles.

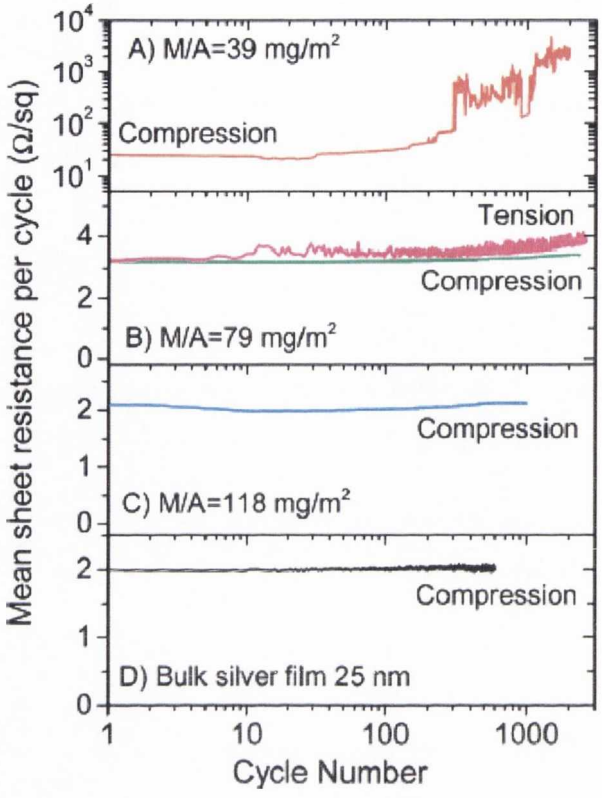

Figure 169. Cycle number tests for silver nanowires films of different thicknesses on ITO. A) has a thickness of 90 nm, B) 182 nm and C) 271. All are shown for compressive bends and the 182 nm is also shown for the bend tests in tension. A bulk silver film is also shown for comparison. From De *et al* [91].

A major difference between the silver nanowire films and the CNT films however lies in their adhesion to PET. It is relatively easy to remove the nanowire films from the PET just by rubbing them off. This means that additional mechanical or chemical processes could be required to increase the adhesion to the PET. It should be emphasised however that this adhesion problem only occurs when one *tries* to remove the film using a shear force. Conducting the electromechanical tests cause hardly any change to the sheet resistance of the AgNW films. As we have discussed in Chapter 5 the AgNWs do not behave like a cohesive film but the nanowires are loosely bound to their neighbours. Therefore each nanowire adheres independently to the PET substrate. Were they to delaminate from the PET it is likely that large conductive gaps would appear in the bulk nanowire film which would result in increased sheet resistance. Since this is not the case it can be assumed that the AgNW films do not delaminate from the PET as a result of the electromechanical tests.

Conclusions

Chapter 7 has shown some of the methods and applications of printing of novel materials such as carbon nanotubes and silver nanowires. We have shown how they can be printed on a small scale for use in microcircuits and on a large scale for applications such as flexible transparent displays We have demonstrated how they perform electromechanically under tensile and compressive bending conditions. The inking and printing methods used in this thesis have allowed the use of materials processed in one area to be picked up and placed for use in a more desirable location. It is possible to choose the size and possibly even the shape of the nanomaterial sections to be used and it has been demonstrated that the materials maintain their unique electrical and mechanical properties post transfer creating infinite opportunities for their use in the electronics of the future.

Chapter 8 Conclusions and Future Work

Experimental Repeatability and Accuracy

Before discussing the conclusions and future work in this chapter, a word needs to be said about the repeatability of the experiments in this thesis. Extensive testing of the tips and materials was done and repeated throughout this PhD work. In the case of non-transferrable materials such as alumina or silicon, the tests were repeated several times. This is apparent in the discussion of testing on alumina in Chapter 4. In the case of transferred materials such as AgNWs and CNTs, the tests could often be conducted only once with a tip before it was unusable for further tests due to the presence of nanomaterials on it. However all the transfer attempts were repeated with fresh tips for both the CNTs and the AgNWs. Only the most significant results have been presented in this thesis. What follows is a general overview of the repeatability and accuracy of the testing parameters during experimentation.

Calibration of the Nanoindenter Testing Set-up

The nanoindenter is well calibrated by the manufacturers as outlined in Chapter 3. For the majority of the experiments the indenter was well calibrated. However there were a couple of small issues, most likely due to bugs in the method used for testing.

1. As was noted in Chapter 3 the load often did not return to zero at the end of testing but would have an offset value of less than 1 mN. The load is calculated from a number of raw channels measured by the nanoindenter which are then corrected for with the perceived location of the surface. As was described in detail in Chapter 3 the finding of the surface with the soft PDMS tip does have in itself some error up to a displacement of about 1 um. This could be considered a rather large error for the types of experiments that a nanoindenter normally conducts but because we were using micron scale materials (the sphere is 1000 um in diameter and a typical minimum contact has a diameter of 80 um) this error is acceptable. It is possible that it introduces inconsistency in the recalculation of the load that occurs at the end of the test. Further testing and experimentation, and perhaps a reworking of the recalculation of the load could be needed to eliminate this error. As it stands this error manifests itself at the very end of the test which is not well analysed at this time and may need to be dealt with in the future.
2. The rapid jump from the peak adhesion point to the end of test provides some difficulty for the electronics in the nanoindenter. This could be another cause of the load not returning to zero. In some cases the nanoindenter seems to be able to keep up with the rapidity of the unload of the tip at this point but it is pushing the limits of what the

nanoindenter can do. It has been observed optically that in some tests, the tip will have detached from the surface after the peak adhesion point was reached but that the nanoindenter will not have recorded this and will assume the tip is still in contact. For that reason we generally have disregarded most of the data after the peak adhesion point for our analysis.

3. As was noted in Chapter 3 there is a characteristic "kink" that occurs at a stiffness of approximately 6000 N/m in many of the tests. This kink occurs for positive or negative load but is always at around that stiffness value. At this time we do not know what this is but we assume it is a feature of the nanoindenter since it always occurs at the same stiffness value. The curve always returns to the same shape it had before the kink and so for that reason we disregard it at this point. It is possible there is some sort of resonance in the electronics which is causing this to happen for our particular harmonic frequency (of 45 Hz) during the experiments. Further investigation on this is required.
4. We have experimentally verified a degree of accuracy with regards to placement of the tip on the surface of a material to being accurate within 1-2 um. For the sizes of materials we are testing (> than 80 um diameter) this is very accurate and in testing smaller-scaled materials we expect to find an even greater accuracy during testing.

Variation between Tips and Testing

All of the tips are created by spin coating the PDMS layer onto the silicon sphere. There seems to be a certain amount of variability using this method as the tip is placed on the spin coater by hand and the PDMS is dropped using a glass tube which does not provide a standard drop size. The repeatability in creating the tips could be improved by creating a custom holder for holding the indenter tip in the same position each time. Also a more accurate method of dropping PDMS could be used such as a micropipette. The viscous PDMS is quite difficult to handle when in its liquid state however which creates its own limitations. We predict an error of ±10 um in thickness during the tip-creation stage but further work and analysis is needed to really pin down an accurate error in creating the tips this way.

Once the tips are created however they can be tested for variation during testing. In this way we can see if a tip is reliable or if a testing material is introducing variation. Figure 170 shows a comparison of a tip on two different materials. The same tip was used in each case and the same experimental parameters (peak load, load up rate, unload rate etc.) were used. Both materials were tested on the same day. It can be seen that there is very little variation in the five tests done on the silicon with the curves being almost identical.

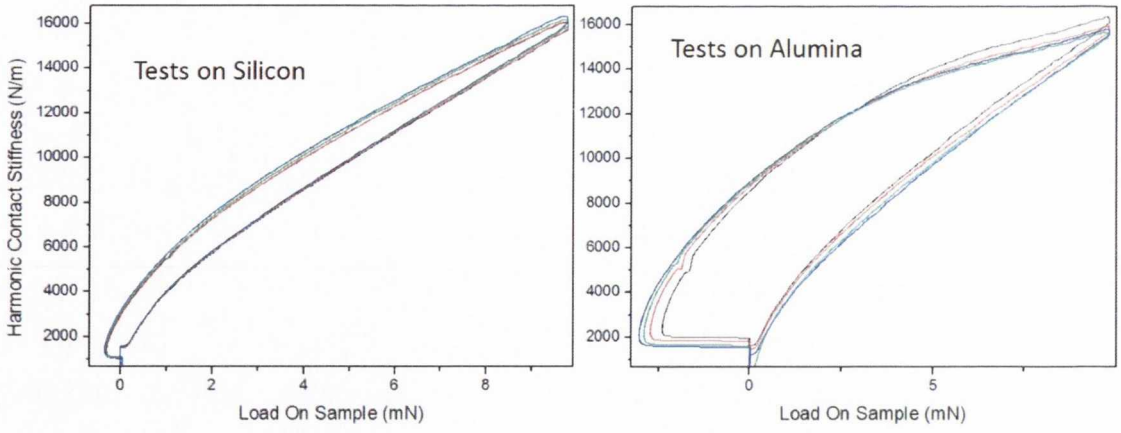

Figure 170. Comparison of the same tip, with the same testing parameters (peak load, unload rate etc) on silicon and on alumina. Note the consistency on the silicon. There is greater variation on the alumina however.

For the alumina however there is quite a bit more scatter both on the load up and the unload. This is to be expected as the alumina membranes are rough and porous with the surface is not uniform. In this way we can test a tip for repeatability though the material used might introduce variation. This is even more pronounced for rough, uneven films made from carbon nanotubes and silver nanowires, there the materials themselves vary in thickness and length and are randomly interspersed with one another.

In this way it can be seen that there is a certain amount of variation between tests. Every attempt was made to keep things as consistent as possible and the variation and repeatability was within acceptable limits. The main way of minimising variation would be in a more rigorous and consistent way of making tips and in keeping everything as clean as possible. For the experimental work in this thesis we were able to show that even without that degree of rigour, excellent experimental results were possible in the transfer process.

It is likely that the extreme limit in precision afforded by this nanoindenter method will be dictated by the limitations of the nanoindenter itself and with creating the materials for testing. All of these parameters lie within the nanoscale or lower end of the micron scale providing hope for a fast, inexpensive and precise technique for transferring materials.

Conclusions

The goal of this thesis was to investigate the manipulation of exotic nanomaterials such as silver nanowires and carbon nanotubes for use in electronics applications. A major difficulty in using these materials is in their processing requirements and their deposition for use in devices. We have investigated the transfer of these materials from their processing location to more desirable materials, where their electrical and mechanical properties can be tested. This investigation involved measurement and control of the transfer process using a custom PDMS stamp in a nanoindenter. We drew on contact mechanics theories to formalise our experimental work and found in some cases excellent agreement with the theory, and in other cases additional corrections were required.

Stiffness to Contact Area Correlation

Our work involved using spherical silicon spheres coated with a PDMS elastomer to transfer nanomaterial networks. These tips left an impression on rough materials which could be used to correlate the stiffness data measured by the nanoindenter with the size of the contact area throughout the test. The stiffness was measured using the continuous stiffness measurements (CSM) which is a small amplitude dynamic mode used by the nanoindenter. Using a video camera to image the contact between the PDMS and the target material we were able to verify that Sneddon's Equation [75]

$$S = \frac{2E^*\sqrt{A}}{\sqrt{\pi}}$$

for elastic materials is valid for PDMS stamps throughout most of the test, where E^* is the Young's Modulus of the PDMS, S is the stiffness measured by the nanoindenter and A is the contact area. PDMS displays viscoelastic properties when being strongly deformed but for the majority of the test the elastic bulk properties dominate. Where a contact impression is present, this provides a powerful way of measuring the contact area during testing without the need for additional optics. This is advantageous in situations where there is difficulty applying optics to an experimental system, for example with very small contacts and/or non-transparent materials.

We discovered that in the latter part of the test when the tip is unloading from a rough material, the PDMS becomes deformed and exhibits a pinned contact edge. This causes the formation of a neck, the diameter of which depends on the peak load of the test as set by the user. This has implications for transferring films with a high cohesive strength, such as CNT films, in that the fracture and transfer of the films occur when the neck disengages from the underlying substrate creating great speed and stress in the CNT film. Different peak loads dictate the diameter of the neck at this point of the test and hence the size of the inked region.

Transfer of AgNW films

We facilitated transfer of silver nanowire films using the PDMS stamp in the nanoindenter. Although considered to be network, we discovered that the nanowires are very loosely bound to one another, creating a low cohesive film which is easily fractured and peeled. The mitigating factor for transfer to occur is a critical crack speed, v_{crit}, above which peeling is initiated. We also investigated kinetic control of the transfer process whereby lower crack speeds did not facilitate transfer or only a partial transfer occurred. We found that below the critical crack speed, transfer occurs only when the tip is disengaging from the substrate at the end of the test.

We found a correlation between the peak load and the size of the transferred segment of AgNWs most likely based on the crack velocity at the peel initiation. Unfortunately we were unable to measure a accurately for many of those tests due to the absence of a contact impression. This is an issue we hope to resolve in the future.

As was the case for alumina we found that the JKR calculation of G throughout the tests were inadequate. Therefore a correction is needed to the model before we can adequately analyse the energy release rate during the transfer of the nanowires.

Transfer of CNT Films

We discovered that the transfer mechanism for carbon nanotube films was significantly different than for silver nanowires. The silver nanowires are loosely bonded to one another and therefore peel easily from the network. CNTs on the other hand form a highly cohesive network, like a continuous, porous film and need to be fractured before they can transfer to a PDMS tip. The crack velocity alone is not adequate to cause this fracture to occur and transfer only occurs at the point in which the PDMS neck is disengaging with the material. The stress produced by the deformation of the PDMS at this point is enough to fracture the CNT film and the fractured portion adheres to the PDMS. The size of the fractured portion depends on the diameter of the neck at the uncontact point which is in turn prescribed by the peak load of the contact as set by the user. In this way the user can choose the size of the CNT portions being transferred.

The CNT films form porous networks and as such we demonstrated that it is possible to ink multiple CNT layers onto one tip. This stacking of the CNT layers onto the tip is similar to what we saw with the AgNWs. This stacking effect has potential for creating multilayer devices on a tip using porous nanomaterials which can then be printed to another location later on. At low loads in the same location we discovered a "seeding" effect. In this case the tip removes a small amount of CNTs from the network and each subsequent test removes a slightly larger section of CNTs. This suggests that the presence of CNTs on the tip or the absence of them in the CNT matrix changes the neck dynamics during the unload and the uncontact point occurs at larger neck diameters.

This could be because the uncontact occurs slightly earlier due to lower adhesion between tests or that the crack propagation between the tip and material has changed.

Printing and Applications

Printing of the CNT films onto glass and plastic was facilitated by the use of a heat stage. This is due to the rate dependence of the crack velocity on temperature as described in Chapter 1. By increasing the temperature the window for printing is shifted relative to the crack velocity. This experimental work is only in the initial stages at this point and we do not have adequate mechanical data to describe how v changes during the printing process. Therefore we cannot draw conclusions between v and the temperature used. We observed that CNT films will transfer for temperatures of 100 °C whereas the AgNW films never printed using the heat stage in the nanoindenter. Without understanding the contact mechanics during the printing process it is difficult to explain why this is the case. A major goal of our future work will be to understand this mechanism fully.

Interestingly it was possible to print both CNT films and AgNW films to silicon oxide chips which had evaporated gold contacts and we are able to see a contact impression on the silicon oxide which was never observed before. The silicon oxide chip had been treated with hot acetone and oxygen plasma ashing which was followed by photolithography using S-1813. They were developed using MF-319 and evaporation of a nickel adhesion layer and gold contacts followed. The lift-off was then conducted using hot acetone. More work is needed to understand how the processes done on the chip seemed to influence the printing process, even in the absence of heat. The evaporated Au contacts created a two-point probe system and it was possible to measure a current through the AgNWs and the CNT films, showing that they were still conductive even after transfer had occurred. In the future this will be studied in more detail with a view to optimising the conductivity of the films.

AgNW and CNT films were printed onto flexible transparent plastic for electromechanical testing. In this case bulk PDMS stamps were used and the transfer conducted by hand. Contacts were evaporated on to the films and they were connected to a source meter while undergoing mechanical testing. A tensile tester was used to bend the plastic substrates with the films on them. There were two types of testing, compression and tensile and it was found that even after a thousand cycles, the conductivity of the films had decreased only by a few per cent. This means these materials are ideal for flexible electronics applications.

Future Work

There is great scope for future work in this research project. In order to fully understand the contact mechanics of the system and specifically the role of the finite size of the PDMS, we plan to conduct contact mechanics experiments on alumina using small spheres of PDMS in the manner created by Doi *et al* [81]. In this way we can test whether the JKR formulation is valid for use in our nanoindenter experiments. This might also provide a clue as to the kind of correction needed to use the JKR formula for G, or if another theory altogether, such as the DMT theory is more applicable for the confined films. Once we can estimate G accurately, we can formulate a printing and inking curve schematic where G is a function of v as was shown by John Rogers [46] in Chapter 1. Therefore we can test the power-law relationships for G and v using Equation 2.

$$G = G_0(1 + \left(\frac{v}{v^*}\right)^n)$$

The contact impression left by the excess crosslinker has been of great use in our work. However as we have seen it does influence adhesion. For this reason we would like to conduct contact experiments where the excess crosslinker has been removed. In this way we can verify that the contact impression is due to excess crosslinker and not due to cohesive failure of the PDMS itself. It is possible that a very thin layer of PDMS is deposited on the materials after contact. It is also possible that the excess crosslinker could influence the electrical conductivity of the film after transfer which may be undesirable. In order to establish the contact radius using the stiffness during testing however, a contact impression is needed. Therefore we would like to upgrade our optical system so that we can directly measure the contact during the experiments. This could be done by placing a camera underneath the sample. Alumina is reasonably transparent, especially if a strong light is shone through it. Imaging from below is the most desirable as we can track the propagation of the contact edge throughout the test and see if it is uniform. It is hoped that this would also allow us to directly image the transfers occurring, the necking behaviour of the PDMS and the tenting behaviour of CNT films. As well as providing us with direct observations of these fascinating behaviours, optical measurements will allow us to truly understand the contact mechanics processes influencing transfer, allowing us greater control over the transfers in the future. This could give us scope for narrowing down the parameters needed for choosing the size and shape of transferred objects with great accuracy.

We wish to experiment with different configurations of the PDMS stamp. To date we have only worked with spherical tips. PDMS however is easily patterned and it is possible to create a relief of different shapes, squares, triangles and even star-shapes. By trying different geometries of the tip we can examine the possibility of creating cut-outs of different shapes in the nanomaterials. In this way any pattern could be designed and cut-out of the material for use in specific device applications. There are plans also to test the stacking of nanomaterials onto the tips with different

shapes and configurations, as well as mixing materials. For example we could pick up a section of AgNWs, followed by a section of CNTs and then top that off with more AgNWs. This could have use in sensor applications where different materials can test for different gases in one device.

The nanoindenter is currently being upgraded to allow for electrical measurements of the materials during the transfer process. In this case additional channels such as current and resistance will be available alongside the mechanical channels such as load, displacement and stiffness. This will enhance our understanding of the electrical properties of these films and how they respond to the mechanical stress of inking and printing. It will also be possible to compare different materials using a four point probe system. We will be able to compare CNTs and AgNW film directly, and for different thicknesses and porosities. This opens up exciting new possibilities in materials science.

By fully understanding the processes involved in transferring materials it is hoped that we can fully control transfer for *any* material. Conducting these transfer by elastomeric stamps provides and easy, low cost and scalable method for creating devices using materials which exhibit exceptional properties. In this way we can test the materials for their suitability in various applications and there is potential for industry to adapt the techniques for their own needs. The manipulation of complex materials is vital to our desire for ever more powerful and efficient technology in our daily lives.

References

1 McSwain, R. L. & Shull, K. R. Cavity nucleation and delamination during adhesive transfer of a thin viscoelastic film. *Journal of Applied Physics* **99**, 053523-053523-053528 (2006).

2 Zhou, Y., Hu, L. & Gruner, G. A method of printing carbon nanotube thin films. *Applied Physics Letters* **88**, 123109 (2006).
3 Schwarz, U. D. A generalized analytical model for the elastic deformation of an adhesive contact between a sphere and a flat surface. *Journal of Colloid and Interface Science* **261**, 99-106, doi:10.1016/s0021-9797(03)00049-3 (2003).
4 Barthel, E. Adhesive elastic contacts: JKR and more. *Journal of Physics D-Applied Physics* **41**, doi:163001 10.1088/0022-3727/41/16/163001 (2008).
5 Barthel, E. Adhesive contact of a compliant sphere to an elastic coated substrate: The thin film limit. *Journal of Adhesion* **83**, 729-739, doi:10.1080/00218460701585774 (2007).
6 Barthel, E. Adhesive Contact: A Few Comments on Cohesive Zone Models and Self-Consistency. *Journal of Adhesion* **88**, 55-69, doi:10.1080/00218464.2011.611057 (2012).
7 Barthel, E. & Frétigny, C. Adhesive contact of elastomers: effective adhesion energy and creep function. *Journal of Physics D: Applied Physics* **42**, 195302 (2009).
8 Barthel, E. & Haiat, G. Adhesive contact of viscoelastic spheres: A hand-waving introduction. *Journal of Adhesion* **80**, 1-19, doi:10.1080/00218460490276722 (2004).
9 Barthel, E. & Haiat, G. Approximate Model for the Adhesive Contact of Viscoelastic Spheres. *Langmuir* **18**, 9362-9370, doi:10.1021/la025959+ (2002).
10 Gacoin, E., Fretigny, C., Chateauminois, A., Perriot, A. & Barthel, E. Measurement of the mechanical properties of thin films mechanically confined within contacts. *Tribology Letters* **21**, 245-252 (2006).
11 Haiat, G. & Barthel, E. An approximate model for the adhesive contact of rough viscoelastic surfaces. *Langmuir* **23**, 11643-11650, doi:10.1021/la701560n (2007).
12 Ebenstein, D. M. & Wahl, K. J. A comparison of JKR-based methods to analyze quasi-static and dynamic indentation force curves. *Journal of Colloid and Interface Science* **298**, 652-662, doi:10.1016/j.jcis.2005.12.062 (2006).
13 Gerberich, W. W. & Cordill, M. J. Physics of adhesion. *Reports on Progress in Physics* **69**, 2157-2203 (2006).
14 Wahl, K. J., Asif, S. A. S., Greenwood, J. A. & Johnson, K. L. Oscillating adhesive contacts between micron-scale tips and compliant polymers. *Journal of Colloid and Interface Science* **296**, 178-188 (2006).
15 Creton, C., Brown, H. R. & Shull, K. R. Molecular-Weight Effects in Chain Pullout. *Macromolecules* **27**, 3174-3183, doi:10.1021/ma00090a010 (1994).
16 Creton, C. & Lakrout, H. Micromechanics of Flat-Probe Adhesion Tests of Soft Viscoelastic Polymer Films. *Journal of Polymer Science, Part B: Polymer Physics* **38**, 965-979 (2000).
17 Crosby, A. J., Shull, K. R., Lakrout, H. & Creton, C. Deformation and failure modes of adhesively bonded elastic layers. *Journal of Applied Physics* **88**, 2956-2966 (2000).
18 Derks, D., Lindner, A., Creton, C. & Bonn, D. Cohesive failure of thin layers of soft model adhesives under tension. *Journal of Applied Physics* **93**, 1557-1566 (2003).
19 Glassmaker, N. J., Hui, C. Y., Yamaguchi, T. & Creton, C. Detachment of stretched viscoelastic fibrils. *European Physical Journal E* **25**, 253-266, doi:10.1140/epje/i2007-10287-y (2008).
20 Lindner, A., Maevis, T., Brummer, R., Luhmann, B. & Creton, C. Subcritical failure of soft acrylic adhesives under tensile stress. *Langmuir* **20**, 9156-9169, doi:10.1021/la049388s (2004).
21 Baney, J. M. & Hui, C. Y. Viscoelastic crack healing and adhesion. *Journal of Applied Physics* **86**, 4232-4241 (1999).
22 Baney, J. M., Hui, C. Y. & Cohen, C. Experimental Investigations of a Stress Intensity Factor Based Description of the Adhesion of Viscoelastic Materials. *Langmuir* **17**, 681-687 (2001).
23 C. Y. Hui, Y. Y. Lin J. M. Baney E. J. Kramer. The mechanics of contact and adhesion of periodically rough surfaces. *Journal of Polymer Science Part B: Polymer Physics* **39**, 1195-1214 (2001).
24 C. Y. Hui, Y. Y. Lin J. M. Baney The mechanics of tack: Viscoelastic contact on a rough surface. *Journal of Polymer Science Part B: Polymer Physics* **38**, 1485-1495 (2000).

25 Crosby, A. J., Shull, K. R., Lin, Y. Y. & Hui, C. Y. Rheological properties and adhesive failure of thin viscoelastic layers. *Journal of Rheology* **46**, 273-294, doi:10.1122/1.1428316 (2002).
26 Hui, C. Y., Baney, J. M. & Kramer, E. J. Contact Mechanics and Adhesion of Viscoelastic Spheres. *Langmuir* **14**, 6570-6578 (1998).
27 Hui, C. Y., Lin, Y. Y., Baney, J. M. & Jagota, A. The accuracy of the geometric assumptions in the JKR (Johnson Kendall Roberts) theory of adhesion. *Journal of Adhesion Science & Technology* **14**, 1297-1319 (2000).
28 Lin, Y. Y., Hui, C. Y. & Baney, J. M. Viscoelastic contract, work of adhesion and the JKR technique. *Journal of Physics D: Applied Physics* **32**, 2250-2260 (1999).
29 Lin, Y. Y., Hui, C. Y. & Conway, H. D. Detailed elastic analysis of the flat punch (tack) test for pressure-sensitive adhesives. *Journal of Polymer Science, Part B: Polymer Physics* **38**, 2769-2784 (2000).
30 S. Perutz, E. J. Kramer J. Baney C. Y. Hui C. Cohen Investigation of adhesion hysteresis in poly(dimethylsiloxane) networks using the JKR technique. *Journal of Polymer Science Part B: Polymer Physics* **36**, 2129-2139 (1998).
31 Vajpayee, S., Hui, C. Y. & Jagota, A. Model-independent extraction of adhesion energy from indentation experiments. *Langmuir* **24**, 9401-9409, doi:10.1021/la800817x (2008).
32 Johnson, K. L. *Contact Mechanics*. (1985).
33 Johnson, K. L., Kendall, K. & Roberts, A. D. Surface Energy and the Contact of Elastic Solids. *Proceedings of the Royal Society of London. Series A, Mathematical and Physical Sciences* **324**, 301-313 (1971).
34 Langstreth Johnson, K. Contact Mechanics.
35 Kendall, K. Adhesion: Molecules and Mechanics. *Science* **263**, 1720-1725, doi:10.1126/science.263.5154.1720 (1994).
36 Kendall, K., Alford, N. M. & Birchall, J. D. A New Method for Measuring the Surface-Energy of Solids. *Nature* **325**, 794-796 (1987).
37 Maugis, D. Adhesion of Spheres - The JKR-DMT Transition using a Dugdale Model. *Journal of Colloid and Interface Science* **150**, 243-269 (1992).
38 Maugis, D. & Barquins, M. Fracture Mechanics and Adherence of Viscoelastic Bodies. *Journal of Physics D-Applied Physics* **11**, 1989-&, doi:10.1088/0022-3727/11/14/011 (1978).
39 Gent, A. N. Compression of Rubber Blocks. *Rubber Chemistry and Technology* **67**, 549-558 (1994).
40 Gent, A. N. Adhesion and Strength of Viscoelastic Solids. Is There a Relationship between Adhesion and Bulk Properties?†. *Langmuir* **12**, 4492-4496, doi:10.1021/la950887q (1996).
41 Gent, A. N. & Lai, S. M. Interfacial bonding, energy dissipation, and adhesion. *Journal of Polymer Science Part B: Polymer Physics* **32**, 1543-1555, doi:10.1002/polb.1994.090320826 (1994).
42 Gent, A. N. & Lindley, P. B. Internal Rupture of Bonded Rubber Cylinders in Tension. *Proceedings of the Royal Society of London Series a-Mathematical and Physical Sciences* **249**, 195-& (1959).
43 Gent, A. N. & Meinecke, E. A. Compression, Bending and Shear of Bonded Rubber Blocks. *Polymer Engineering and Science* **10**, 48-& (1970).
44 Gent, A. N. & Schultz, J. Effect of Wetting Liquids on Strength and Adhesion of Viscoelastic Materials. *Journal of Adhesion* **3**, 281-&, doi:10.1080/00218467208072199 (1972).
45 Cao, Q. Kim, Hoon-sikPimparkar, NinadKulkarni,JaydeepP.Wang,CongjunShim, MoonsubRoy, KaushikAlam, Muhammad A.
Rogers, John A.. Medium-scale carbon nanotube thin-film integrated circuits on flexible plastic substrates. *Nature* **454**, 495-500 (2008).
46 Feng, X. Meitl, M. A.Bowen, A. M.Huang, Y.Nuzzo, R. G.
Rogers, J. A.. Competing fracture in kinetically controlled transfer printing. *Langmuir* **23**, 12555-12560, doi:10.1021/la701555n (2007).

47 Hsia, K. J. Y. Huang E. Menard J. U. ParkW. Zhou J. Rogers J. M. Fulton. Collapse of stamps for soft lithography due to interfacial adhesion. *Applied Physics Letters* **86**, 154106 (2005).

48 Huang, Y. Y. Zhou, W.Hsia, K. J.Menard, E.Park, J. U.Rogers, J. A. Alleyne, A. G.. Stamp Collapse in Soft Lithography. *Langmuir* **21**, 8058-8068 (2005).

49 John A. Rogers, R. J. J. G. M. W. Microcontact printing and electroplating on curved substrates: Production of free-standing three-dimensional metallic microstructures. *Advanced Materials* **9**, 475-477 (1997).

50 Kang, S. J. Kocabas, C. Kim, H. S.Cao, Q.Meitl, M. A.Khang, D. Y.Rogers, J. A.. Printed multilayer superstructures of aligned single-walled carbon nanotubes for electronic, applications. *Nano Letters* **7**, 3343-3348, doi:10.1021/nl071596s (2007).

51 Meitl, M. A. *et al.* Solution Casting and Transfer Printing Single-Walled Carbon Nanotube Films. *Nano Lett.* **4**, 1643-1647 (2004).

52 Meitl, M. A. Meitl, Matthew A.Zhu, Zheng-TaoKumar, VipanLee, Keon JaeFeng, XueHuang, Yonggang Y.Adesida, IlesanmiNuzzo, Ralph G. Rogers, John A.Transfer printing by kinetic control of adhesion to an elastomeric stamp. *Nat Mater* **5**, 33-38 (2006).

53 Rogers, J. A. Slice and dice, peel and stick: Emerging methods for nanostructure fabrication. *Acs Nano* **1**, 151-153, doi:10.1021/nn7002794 (2007).

54 Rogers, J. A. Bao, ZhenanBaldwin, KirkDodabalapur, AnanthCrone, BrianRaju, V. R.Kuck, ValerieKatz, HowardAmundson, KarlEwing, Jay Drzaic, Paul From the Cover: Paper-like electronic displays: Large-area rubber-stamped plastic sheets of electronics and microencapsulated electrophoretic inks. *PNAS* **98**, 4835-4840, doi:10.1073/pnas.091588098 (2001).

55 Xiao, J. Carlson, A.Liu, Z. J.Huang, Y.Jiang, H.Rogers, J. A. Stretchable and compressible thin films of stiff materials on compliant wavy substrates. *Applied Physics Letters* **93**, 013109-013103 (2008).

56 Ahn, D. & Shull, K. R. JKR studies of acrylic elastomer adhesion to glassy polymer substrates. *Macromolecules* **29**, 4381-4390, doi:10.1021/ma9518924 (1996).

57 Drzal, P. L. & Shull, K. R. Adhesive failure of model acrylic pressure sensitive adhesives. *Journal of Adhesion* **81**, 397-415, doi:10.1080/00218460590944800 (2005).

58 Shull, K. R. Fracture and adhesion of elastomers and gels: Large strains at small length scales. *Journal of Polymer Science, Part B: Polymer Physics* **44**, 3436-3439 (2006).

59 Shull, K. R. Contact mechanics and the adhesion of soft solids. *Materials Science and Engineering: R: Reports* **36**, 1-45 (2002).

60 Shull, K. R., Ahn, D., Chen, W. L., Flanigan, C. M. & Crosby, A. J. Axisymmetric adhesion tests of soft materials. *Macromolecular Chemistry and Physics* **199**, 489-511, doi:10.1002/(sici)1521-3935(19980401)199:4<489::aid-macp489>3.0.co;2-a (1998).

61 Shull, K. R., Flanigan, C. M. & Crosby, A. J. Fingering instabilities of confined elastic layers in tension. *Physical Review Letters* **84**, 3057-3060 (2000).

62 Shull, K. R. Martin, E. F.Drzal, P. L.Hersam, M. C.Markowitz, A. R. McSwain, R. L. Adhesive transfer of thin viscoelastic films. *Langmuir* **21**, 178-186, doi:10.1021/la048120y (2005).

63 Shull, K. R. Martin, E. F.Drzal, P. L.Hersam, M. C. Markowitz, A. R. McSwain, R. L.Adhesive Transfer of Thin Viscoelastic Films. *Langmuir* **21**, 178-186, doi:10.1021/la048120y (2004).

64 Griffith, A. A. Phenomena of Rupture and Flow in Solids. *Asm Transactions Quarterly* **61**, 871-& (1968).

65 Sperling, L. H. *Introduction to Physical Polymer Science*. (1992).

66 Andrews, R. D. & Tobolsky, A. V. Elastoviscous Properties of Polyisobutylene 4. Relaxation Time Spectrum and Calculation of Bulk Viscosity. *Journal of Polymer Science* **7**, 221-242, doi:10.1002/pol.1951.120070210 (1951).

67 Irwin, G. R. Fracture Dynamics.". *Fracture of methals American Society for Metals*, 147-166 (1948).
68 T.L., A. Fracture Mechanics. (1995).
69 Wikipedia.
70 Fichet, M. Dutier, G.Yarovitsky, A.Todorov, P.Hamdi, I.Maurin, I.Saltiel, S.Sarkisyan, D.Gorza, M. P.Bloch, D.
Ducloy, M. Exploring the van der Waals atom-surface attraction in the nanometric range. *Epl* **77**, doi:10.1209/0295-5075/77/54001 (2007).
71 Derjaguin, B. V., Muller, V. M. & Toporov, Y. P. Effect of Contact Deformations on Adhesion of Particles. *Journal of Colloid and Interface Science* **53**, 314-326 (1975).
72 Tabor, D. & Winterto.Rh. Direct Measurement of Normal and Retarded Van der Waals Forces. *Proceedings of the Royal Society of London Series a-Mathematical and Physical Sciences* **312**, 435-&, doi:10.1098/rspa.1969.0169 (1969).
73 Argento, C., Jagota, A. & Carter, W. C. Surface formulation for molecular interactions of macroscopic bodies. *Journal of the Mechanics and Physics of Solids* **45**, 1161-1183 (1997).
74 Jagota, A., Argento, C. & Mazur, S. Growth of adhesive contacts for Maxwell viscoelastic spheres. *Journal of Applied Physics* **83**, 250-259 (1998).
75 N, S. I. *Fourier Transfom*. (New York: McGraw-Hill, 1950).
76 Packham, D. E. Surface energy, surface topography and adhesion. *International Journal of Adhesion and Adhesives* **23**, 437-448 (2003).
77 http://www.doitpoms.ac.uk/tlplib/glass-transition/free-volume.php.
78 Chaudhury, M. K. & Whitesides, G. M. Direct Measurements of Interfacial Interactions between Semispherical Lenses and Flat Sheets of Poly(dimethylsiloxane) and their Chemical Derivatives. *Langmuir* **7**, 1013-1025, doi:10.1021/la00053a033 (1991).
79 Schapery, R. A. Theory of Crack Initiation and Growth in Viscoelastic Media 1. Theoretical Development. *International Journal of Fracture* **11**, 141-159 (1975).
80 Greenwood, J. A. J., K. L. *Philos. Mag. A* **43** (1981).
81 Morishita, Y., Morita, H., Kaneko, D. & Doi, M. Contact Dynamics in the Adhesion Process between Spherical Polydimethylsiloxane Rubber and Glass Substrate. *Langmuir* **24**, 14059-14065, doi:10.1021/la8024155 (2008).
82 Morishita, Y., Morita, H. & Doi, M. Effect of the Contact Line Motion in the Adhesion of Very Soft Sphere. *Journal of the Physical Society of Japan* **78**, doi:114802 10.1143/jpsj.78.114802 (2009).
83 Lakrout, H., Sergot, P. & Creton, C. in *21st Annual Meeting of the Adhesion-Society.* 307-359 (1999).
84 Gent, A. N. & Tompkins, D. A. Nuclean and Growth of Gas Bubbles in Elastomers. *Journal of Applied Physics* **40**, 2520-& (1969).
85 Gent, A. N. & Wang, C. Fracture Mechanics and Caviation in Rubber Like Solids *Journal of Materials Science* **26**, 3392-3395 (1991).
86 Kaelble, D. H. Interfacial morphology and mechanical properties of A-B-A triblock copolymers. *Transactions of the Society of Rheology* **15**, 235-260 (1971).
87 Gay, C. & Leibler, L. Theory of tackiness. *Physical Review Letters* **82**, 936-939 (1999).
88 Iijima, S. Helical microtubules of graphitic carbon. *Nature* **354**, 56 (1991).
89 Radushkevich-lukyanovich. *Soviet Journal of Physical Chemistry* **26** (1952).
90 Monthioux, M. & Kuznetsov, V. L. Who should be given the credit for the discovery of carbon nanotubes? *Carbon* **44**, 1621-1623 (2006).
91 Nanocomp. (2008).
92 Krishnan, A., Dujardin, E., Ebbesen, T. W., Yianilos, P. N. & Treacy, M. M. J. Young's modulus of single-walled nanotubes. *Physical Review B* **58**, 14013 (1998).
93 Popov, V. N. Carbon nanotubes: properties and application. *Materials Science and Engineering: R: Reports* **43**, 61-102 (2004).

94 Bernholc, J., Brenner, D., Buongiorno Nardelli, M., Meunier, V. & Roland, C. Mechanical and electrical properties of nanotubes. *Annual Review of Materials Science* **32**, 347-375 (2002).

95 http://www-ibmc.u-strasbg.fr/ict/vectorisation/vectorisation_eng.shtml.

96 Giordani, S. Bergin, Shane D.Nicolosi, ValeriaLebedkin, SergeiKappes, Manfred M.Blau, Werner J.
Coleman, Jonathan N.Debundling of single-walled nanotubes by dilution: Observation of large populations of individual nanotubes in amide solvent dispersions. *Journal of Physical Chemistry B* **110**, 15708-15718 (2006).

97 Bockrath, M. Cobden, David H.
McEuen, Paul L.Chopra, Nasreen G.Zettl, A.Thess, Andreas
Smalley, R. E.Single-Electron Transport in Ropes of Carbon Nanotubes. *Science* **275**, 1922-1925, doi:10.1126/science.275.5308.1922 (1997).

98 Saito, R., Dresselhaus G., Dresselhaus M.S.,. (1998).

99 Baughman, R. H., Zakhidov, A. A. & de Heer, W. A. Carbon Nanotubes--the Route Toward Applications. *Science* **297**, 787-792, doi:10.1126/science.1060928 (2002).

100 Arnold, M. S., Green, A. A., Hulvat, J. F., Stupp, S. I. & Hersam, M. C. Sorting carbon nanotubes by electronic structure using density differentiation. *Nat Nano* **1**, 60-65 (2006).

101 Lynam, C. Minett, A. I.Habas, S. E.Gambhir, S.Officer, D. L.
Wallace, G. G.Functionalising carbon nanotubes. *International Journal of Nanotechnology* **5**, 331-351 (2008).

102 Stadermann, M. Papadakis, S. J.Falvo, M. R.Novak, J.Snow, E.Fu, Q.Liu, J.Fridman, Y.Boland, J. J.Superfine, R.Washburn, S.Nanoscale study of conduction through carbon nanotube networks. *Physical Review B* **69**, 201402 (2004).

103 http://www.acsmaterial.com/product.asp?CID=43&ID=42.

104 De, S. Higgins, T. M.Lyons, P. E.Doherty, E. M.Nirmalraj, P. N.Blau, W. J.Boland, J. J.Coleman, J. N.Silver Nanowire Networks as Flexible, Transparent, Conducting Films: Extremely High DC to Optical Conductivity Ratios. *Acs Nano* **3**, 1767-1774, doi:10.1021/nn900348c (2009).

105 Tsuji, X. T. a. M. . Syntheses of Silver Nanowires in Liquid Phase, Nanowires Science and Technology, . *Nicoleta Lupu (Ed.), ISBN: 978-953-7619-89-3, InTech, DOI: 10.5772/39491. Available from: http://www.intechopen.com/books/nanowires-science-and-technology/syntheses-of-silver-nanowires-in-liquid-phase* ((2010)).

106 A. T. Tilke F. C. Simmel, H. L., R. H. Blick, and J. P. Kotthaus. Quantum interference in a one-dimensional silicon nanowire. *Physical Review B* **68**.

107 Pethica, J. B., Hutchings, R. & Oliver, W. C. Hardness Measurement at Penetration Depths as small as 20 nm. *Philosophical Magazine a-Physics of Condensed Matter Structure Defects and Mechanical Properties* **48**, 593-606 (1983).

108 Pethica, J. B. & Oliver, W. C. Tip Surface Interactions in STM and AFM. *Physica Scripta* **T19A**, 61-66, doi:10.1088/0031-8949/1987/t19a/010 (1987).

109 Weihs, T. P., & Pethica, J.B. *Mat.Res.Symp.Proc* **Vol. 108,** (1992).

110 Schapery, R. A. Theory of Crack Initiation and Growth in Viscoelastic Media3. Analysis of Continuous Growth. *International Journal of Fracture* **11**, 549-562 (1975).

111 Schapery, R. A. Theory of Crack Initiation and Growth in Viscoelastic Media 2. Approximate Methods of Analysis. *International Journal of Fracture* **11**, 369-388 (1975).

112 Scardaci, V., Coull, R., Lyons, P. E., Rickard, D. & Coleman, J. N. Spray Deposition of Highly Transparent, Low-Resistance Networks of Silver Nanowires over Large Areas. *Small* **7**, 2621-2628, doi:10.1002/smll.201100647 (2011).

113 Ahn, B. Y., Lorang, D. J. & Lewis, J. A. Transparent conductive grids via direct writing of silver nanoparticle inks. *Nanoscale* **3**, 2700-2702 (2011).

114 Bell, N., Dimos, D. Calculation of Hamaker Constants in Nonaqueous Fluid Media. . *MRS Proceedings* **625** ((2000)).

115 Murali, S. Xu, T.Marshall, B. D.Kayatin, M. J.Pizarro, K.Radhakrishnan, V. K.Nepal, D.

Davis, V. A.Lyotropic Liquid Crystalline Self-Assembly in Dispersions of Silver Nanowires and Nanoparticles. *Langmuir* **26**, 11176-11183, doi:10.1021/la101305z (2010).

116 Doherty, E. M. De, SukantaLyons, Philip E.Shmeliov, AlekseyNirmalraj, Peter N.Scardaci, VittorioJoimel, JeromeBlau, Werner J.Boland, John J.Coleman, Jonathan N.The spatial uniformity and electromechanical stability of transparent, conductive films of single walled nanotubes. *Carbon* **47**, 2466-2473, doi:10.1016/j.carbon.2009.04.040 (2009).

117 Williams, J. G. Energy release rates for the peeling of flexible membranes and the analysis of blister tests. *International Journal of Fracture* **87**, 265-288, doi:10.1023/a:1007314720152 (1997).

118 Leterrier, Y. Fischer, C.Medico, L.Demarco, F.Manson, J. A. E.Bouten, P. C. P.De Goede, J.Nisato, G.Nairn, J. A. 169-174 (Society of Vacuum Coaters).